(I) A COUPLED GEOCHEMICAL AND GEODYNAMICAL APPROACH TO SUBDUCTION ZONE MODELING
&
(II) DEVELOPMENT OF COLOR IN GREENISH QUARTZ

Thesis by

Laura Baker Hebert

In Partial Fulfillment of the Requirements

for the Degree of

Doctor of Philosophy

California Institute of Technology

Pasadena, California

2008

(Defended February 15, 2008)

ACKNOWLEDGMENTS

I would like firstly to thank my advisors. Paul Asimow and Mike Gurnis have provided support, guidance, patience, and have great ability to teach as well as to inspire. Their excitement and willingness to explore the gray areas of interdisciplinary geoscience have allowed this work to be done. George Rossman, whose love of science and deep sense of curiosity have been an incredible inspiration, demonstrates every day why teaching is the best job there is.

Secondly, and equally importantly, I would like to thank Paula Antoshechkina, mentor and friend. She and I have worked very closely for over three years in the development of the GyPSM model, and she has provided guidance, advice, and a strict attention to detail that were essential not only to this project, but to my learning how to be a scientist. She was always willing to share her considerable expertise, whether it be regarding geochemistry or a wide range of programming languages, and is an excellent and patient teacher.

Thanks to Chad Hall, who was heavily involved in the early stages of the GyPSM-S project, and to Eh Tan, who provided excellent help with ConMan whenever asked. Thank you to Elizabeth Miura Boyd and to Chi Ma for analytical help. Mike Baker and Jed Mosenfelder were very helpful in the lab with my early work in high-pressure experimental geochemistry.

I am appreciative of the chance to have been a teaching assistant for both George Rossman and John Eiler, both excellent instructors. Additional thanks to John for acting as academic advisor.

I am indebted to my friends: Laura, Julie, Nicole, Brandy, Ryan, Charlie, Sarah, Chris, Lydia, Elisabeth, Liz J., Nathan, Cody, Rhea, and Kris. Thank you to Tessa and Saffie for always being there when I needed them. Thanks to my family for always supporting me on my unconventional higher educational path that started at Peabody Conservatory and is ending at Caltech.

And, finally, I thank Craig, my wonderful husband and best friend, for his sense of humor, for seeing me through all of this, and for always giving me unconditional support, encouragement, and confidence. I thank our son, for making things interesting.

"Nothing is easy.
Nothing good takes 5 minutes."

- GRR lab truisms

ABSTRACT

(I)

We couple a petrological model with a 2D thermal and variable viscosity flow model to describe and compare fundamental processes occurring within subduction zones. We study the thermal state and phase equilibria of the subducting oceanic slab and mantle wedge and constrain fluid flux, presenting model results spanning normal ranges in subduction parameters. Coupling between the chemistry and the dynamics results in the development of a stable slab-adjacent low-viscosity region defined by hydrous phases and higher concentrations of water in nominally anhydrous minerals, bounded by the water-saturated solidus.

Subduction parameters are significant to the position of dehydration reactions within the slab and the geochemistry of fluids initiating flux melting. Modeling of fluid transport mechanisms and potential melt migration processes based on coupled modeling with the addition of fluid-mobile trace elements was performed. There is a progression of geochemical characteristics described in previous studies of arc lava datasets that can be duplicated with these models.

A localized low-viscosity, low-density geometry within the wedge, predicted by coupled modeling of the Izu-Bonin system, is required to match observations of topography, gravity, and geoid anomalies. Based on this, predictions can be made as to specific low-viscosity geometries associated with geophysical signals for other subduction zones based on regional subduction parameters.

(II)

Naturally occurring greenish quartz found within the context of amethyst-bearing deposits is not simply the result of the exposure of amethyst to thermal bleaching. Rather, it can represent a set of distinct color varieties resulting from the changing chemical and thermal nature of the precipitating solution. Greenish quartz occurs at the Thunder Bay Amethyst Mine Panorama, Thunder Bay, Ontario, Canada, in several distinct varieties. Spectroscopic, irradiation, and controlled heating studies show that changes in salinity and temperature of the hydrothermal system that produced the deposit and changes in quartz growth rate are reflected in coloration. As the system evolved, a minor ferric component appears to change position from interstitial to substitutional within specific growth sectors. Greenish colors within the quartz are consistently correlated with the speciation of hydrous components.

TABLE OF CONTENTS

PART I: A COUPLED GEOCHEMICAL AND GEODYNAMICAL APPROACH TO SUBDUCTION ZONE MODELING

PART II: DEVELOPMENT OF COLOR IN GREENISH QUARTZ

FIGURES AND TABLES

Chapter II:

Chapter III:

Chapter IV:

Chapter V:

Chapter I:

Introduction

(PART I)

Observations associated with convergent margins, including analyses of lavas and xenoliths collected at the surface, seismic imaging, and measurements of dynamic topography and gravity and geoid anomalies can be used to remotely detect properties of the mantle wedge and to interpret processes operating within that important region. The story is a complicated one, including fluxing of the mantle by slab-derived components, origins of initial and progressive mantle depletion, a complex pressure and temperature structure, and considerations of melt and fluid migration within the solid flow field. Nevertheless, understanding of first-order processes occurring within the mantle wedge can lead to larger-scale implications including the transport of fluid-modified slab-adjacent material into the deep mantle [1-6], origins of the continental crust [7, 8], time-dependent changes in slab dip angle [9], and controls on back-arc volcanism [10].

There is general agreement that fluids from a dehydrating slab are introduced to the wedge as the slab descends and that the pressure-temperature path, chemical composition, and phase equilibria within the slab determine the locations of water-rich fluid release [2]. The delivery of this water-rich fluid phase into and interaction with the overlying mantle induces hydration reactions within the peridotite and, where temperature is sufficient, water-fluxed melting [11]. Major element abundances in arc lavas are derived from partial melting of the wedge peridotite above the slab, but large-ion lithophile elements (LILE) and other incompatible elements can be traced to slab-derived influences such as sediment melting [12, 13], dehydration of the altered oceanic crust [14], or dehydration of subducting serpentinized lithosphere [2, 15]. In general, convergent margins involve lavas that are enriched in incompatible fluid-mobile elements and depleted in incompatible high field strength elements [16-18; others], suggesting a significant connection between fluid introduction and melt production.

A particular part of the subduction system where strong coupling between mass and energy flows and geophysical and geochemical processes is most important is the mantle wedge immediately adjacent to the slab. Conventional steady-state thermal solutions of subduction indicate that the slab-wedge interface is too cold for even water-saturated melting of peridotite, so the fluids must somehow migrate into hotter areas of the wedge in order for melting to begin [19]. Migration and equilibration of fluids with peridotite can lead to higher concentrations of water in nominally anhydrous minerals (NAM) and to the stabilization of hydrous phases. The effect of increasing water content in NAM is twofold: (i) decreasing solidus temperatures [20, 21] and (ii) water-weakening that reduces the viscosity of the solid material [22]. As such, there is a dual effect of hydrous fluid introduction on the geochemistry of initial melts within the system and on the force balance within the wedge.

The depth interval and the magnitude of fluid release from the subducting plate are a function of parameters such as slab age and convergence velocity as well as the composition of the descending plate [23]. Specifically, the different lithological fluid sources emphasized by different subduction parameters allow for changing fluid addition patterns (mass and fluid-mobile trace element chemistry) along the length of the subducting plate through the upper mantle [23, 24]. These patterns may directly influence the composition and mass fraction of fluxed melts within the wedge, leading to regional variations in arc lava geochemistry. Variations can be compared among different subduction systems, or through cross-arc and along-arc trends within the same subduction system. For example, relative contributions from heterogeneous slab fluid sources can be manifested in diverse chemical characteristics of lavas derived from different depths above the seismic Wadati-Benioff zone (WBZ) [18, 25, 26].

Subduction zones can be generally described as having topographically depressed back-arc regions and overlying plates, long-wavelength geoid highs over slabs, and shorter wavelength geoid lows over trenches [27, 28]. Long-wavelength geoid highs are interpreted as indicative of a radial viscosity structure leading to regional compensation of subducting slabs [29, 30]. However, shorter-wavelength geoid anomalies and the depth of back-arc basins may be resolved by studying viscosity variations caused by thermal or compositional factors within the upper mantle [28]. Along the slab-mantle interface, the viscosity structure is strongly dependent on both temperature and composition (water-weakening) [22]. A localized low-viscosity region in the mantle wedge has been shown to have a substantial effect on the force balance in a subduction zone, and leads to observable signals in topography, state of stress, gravity, and the geoid [28, 31-33]. While the importance of such a region in a subduction zone has been evaluated, the mechanism by which it develops and its detailed geometry have yet to be completely investigated.

Modeling that addresses principally either the force balance or the chemistry, using results from one area to infer behaviors in the other, has succeeded in reaching broad conclusions as to the manner of hydration of the mantle wedge and melting beneath the arc [24, 34-39]. However, when the thermal structure, viscosity, and the solid flow field are addressed within the context of a fully coupled geophysical and geochemical model, emphasizing the importance of interdependent contributions, more detailed interpretations can be made. Therefore, understanding of subduction zones requires a model that accounts for complex interactions between chemical and dynamic features of the system. The evolution of dynamical quantities such as the flow field, entropy, and bulk composition should provide input to thermodynamic calculations, which output chemically-governed quantities such as melt fraction, compositional buoyancy, water speciation, and latent heat contributions to the thermal balance. This forms an essential loop where neither chemistry nor physics are independently evaluated. Indeed, it is the dependence of one on the other that presents insights into the subduction system on a fundamental level. This thesis investigates subduction processes from fluid release to melting within a coupled, internally consistent geochemical and geophysical modeling treatment, emphasizing the origination, development, and implications of hydration features within the wedge as a function of regional subduction parameters.

Chapter 2 is a presentation of GyPSM-S (**G**eod**y**namic and **P**etrological **S**ynthesis **M**odel for **S**ubduction), a self-consistent model that includes the thermodynamic minimization algorithm pHMELTS [20, 40, 41], which takes into account water partitioning into NAM, in conjunction with the 2-D thermal and variable viscosity flow model ConMan [42] and a fluid migration scheme. Evaluation of properties such as the melt fraction, fluid flux, the impact of water in NAM on the viscosity structure and overall flow field, and spatial extent of fluids and melts within the subduction system are all incorporated into GyPSM-S. The significance of the coupled scheme is the detailed tracking of fluids and their rheological and chemical effects from release to initiation of melting. The primary results of the GyPSM-S models confirm the conclusions of earlier models of spatial separation between the slab interface and the regions of melt initiation in addition to introducing the existence of a low-viscosity channel (LVC) within the mantle wedge, the process by which LVCs form, and the limitations on LVC geometry. The low-viscosity region is shown to be a robust feature that is stable over a range of subduction parameters.

In order to demonstrate the applicability of GyPSM-S results to geochemical datasets, a supplemental modeling approach is required to account for the addition of fluid-mobile tracers and to make detailed inferences as to the geochemistry of arc lavas with respect to slab fluid sources and as a function of changing subduction parameters. Chapter 3 presents an extension of the results of GyPSM-S to specific mass tracing. A source-based approach is employed to determine how slab dehydration changes with changing subduction model parameters and how this influences the major and trace element chemistry of fluid-fluxed melts within the wedge. Consequences of different degrees of interaction between fluids and hydrated peridotite within the LVC are investigated, and cross-arc and along-arc variations in regional geochemical datasets are compared to the model results with an emphasis on changing slab fluid-source lithology. Additionally, there is discussion of simple melt migration scenarios which may preserve relative heterogeneities in melts initiated at different locations within the wedge. Interpretations of the results lead to several potential mechanisms to produce hydrous inputs to back-arc source regions.

The influence of the existence of the LVC, and other localized low-viscosity geometries within the wedge, on the overall flow field and force balance can be evaluated by surface observables particular to the viscosity structure, such as the topography and gravity and geoid anomalies [31, 32]. While it is well understood that localized low-viscosity regions may be important to the force balance within mantle wedges, the mechanisms of development of these regions and how the regional geometries change based on changing subduction behaviors have been established only recently (Chapter 2). The logical next step would be to attempt to match observed geophysical signals in a particular locality with a modeled fluid-source-based hydration structure. Chapter 4 presents the impact of GyPSM-S modeled localized low-viscosity regions on the topography and geoid and gravity anomalies for the northern Izu-Bonin subduction system, particularly emphasizing the manner of development of the low-viscosity region as the primary influence on the geometry and comparing model results with observed signals.

(PART II)

A greenish coloration in synthetic quartz can arise from irradiation of quartz, heating of quartz originally of another color, or from the presence of ferrous iron within the structure [43-46]. Upon irradiation, an electron will migrate away, leaving a “hole center,” and the associated charge-compensating cation will migrate away through the structure as well [47]. Heating of quartz can thermally activate color centers and encourage migration of species within the structure. By destroying color centers, heat treatment can selectively eliminate components of coloration associated with exposure to ionizing radiation. The presence of molecular H_2O within the quartz structure has been found to be detrimental to the development of certain colors and may allow other colors to emerge instead [48]. However, natural examples of greenish coloration in quartz are rare [49-51], and have not been fully discussed within the context of their environment of formation or in relation to other associated colors of quartz. Both amethyst and smoky quartz have been found to be closely associated with natural examples of greenish quartz. The violet coloration in amethyst is due to the removal of an electron by high-energy radiation that results in oxidation of ferric iron within the quartz structure to Fe^{4+} [52]. Commonly characterized by a brownish gray hue, smoky quartz represents another color variety of quartz produced by ionizing radiation. The smoky color center is modeled as Al^{3+} substituting into the Si^{4+} tetrahedral site, with associated charge-balance fulfilled by a nearby positively charged ion (such as Li^{+}) in an interstitial site.

The Thunder Bay Amethyst Mine Panorama (TBAMP) deposit is the site of an extinct hydrothermal system that flowed through a fault and led to mineralization primarily by quartz [53]. Although most of the quartz is amethystine, natural greenish quartz has been found in the TBAMP in several distinct varieties. Yellowish green quartz and dark green quartz with purple hues are found as loose detritus within the TBAMP (originating from outcroppings), and pale greenish gray quartz is found as part of an outcropping color-gradational sequence involving macrocrystalline quartz of other colors, including colorless and smoky gray, and chalcedony. The color-gradational sequence occurs solely in a localized zone, which may be the site of initial influx of fluids into the fault. Distally, the color of the *in situ* quartz is dominantly dark violet amethyst. In some cases, this dark violet amethyst, when cut perpendicular to its *c* axis, is found to be composed of alternating sectors of colorless and dark purple quartz. McArthur et al. [53] proposed that greenish coloration at TBAMP was heat-induced “bleaching” of amethyst.

Chapter 5 presents a study involving visual observations and spectroscopic analyses of the different color varieties in the TBAMP system interpreted specifically in association with radiation exposure and heat-treatment experiments. It is important to understand the origin of the greenish color because it is ubiquitously present within a progressive color sequence in quartz. Clues in the chemical and spectroscopic variations within the sequence may provide an increased understanding of the development and persistence of radiation-induced color centers in quartz within the context of changing chemical, thermal, and kinetic factors in a hydrothermal system.

References

[1] T. Elliott et al. (2006) Lithium isotope evidence for subduction-enriched mantle in the source of mid-ocean-ridge basalts. Nature **443**(5), 565-568, http://dx.doi.org/10.1038/nature05144.

[2] M.W. Schmidt and S. Poli (1998) Experimentally based water budgets for dehydrating slabs and consequences for arc magma generation. Earth and Planetary Science Letters **163**, 361–379.

[3] K. M. Cooper et al. (2004) Oxygen isotope evidence for the origin of enriched mantle beneath the mid-Atlantic ridge. Earth and Planetary Science Letters **220**, 297-316.

[4] K. E. Donnelly et al. (2004) Origin of enriched ocean ridge basalts and implications for mantle dynamics. Earth and Planetary Science Letters **226**, 347-366.

[5] J. E. Dixon et al. (2002) Recycled dehydrated lithosphere observed in plume-influenced mid-ocean-ridge basalt. Nature **420**, 385-389.

[6] P. J. le Roux et al. (2002) Mantle heterogeneity beneath the southern Mid-Atlantic Ridge: trace element evidence for contamination of ambient asthenospheric mantle.

Earth and Planetary Science Letters **203**, 479-498.

[7] P. B. Kelemen (1995) Genesis of high Mg# andesites and the continental crust. Contributions to Mineralogy and Petrology **120**, 1-19.

[8] R. L. Rudnick (1995) Making continental crust. Nature **378**, 571-577.

[9] V. Manea and M. Gurnis (2007) Subduction zone evolution and low viscosity wedges and channels. Earth and Planetary Science Letters **264**(1-2), 22-45.

[10] C. H. Langmuir et al. (2006) Chemical systematics and hydrous melting of the mantle in back-arc basins. Geophysical Monograph 166, 87-146.

[11] Y. Tatsumi and S. Eggins (1995) Subduction Zone Magmatism, Blackwell, Cambridge.

[12] T. Plank and C. H. Langmuir (1993) Tracing trace elements from sediment input to volcanic output at subduction zones. Nature **362**, 739-743.

[13] T. Elliott et al. (1997) Element transport from slab to volcanic front at the Mariana arc. Journal of Geophysical Research **102**(B7), 14991-15019.

[14] T. Ishikawa and F. Tera (1999) Two isotopically distinct fluids fluid components involved in the Mariana Arc; evidence from Nb/B ratios and B, Sr, Nd, and Pb isotope systematics. Geology **27**, 83-86.

[15] P. Ulmer and V. Trommsdorf (1995) Serpentine stability to mantle depths and subduction-related magmatism. Science **268**, 858-861.

[16] R. J. Arculus (1994) Aspects of magma genesis in arcs. Lithos **33**, 189-208.

[17] C. Hawkesworth et al. (1997) U-Th isotopes in arc magmas: Implications for element transfer from the subducted crust. Science **276**, 551-555.

[18] R. J. Stern et al. (2006) Subduction factory processes beneath the Guguan cross-chain,

Mariana Arc: no role for sediments, are serpentinites important? Contributions to Mineralogy and Petrology, doi: 10.1007/s00410-005-0055-2.

[19] S. M. Peacock (2003) Thermal Structure and Metamorphic Evolution of Subducting Slabs. Geophysical Monograph 138, 7-22.

[20] P. D. Asimow, J. E. Dixon, C. H. Langmuir (2004) A hydrous melting and fractionation model for mid-ocean ridge basalts: Application to the Mid-Atlantic Ridge near the Azores. Geochemistry, Geophysics, Geosystems **5**(1), Q01E16, doi:10.1029/2003GC000568.

[21] G. A. Gaetani and T. L. Grove (2003) Experimental constraints on melt generation in the mantle wedge. Geophysical Monograph **138**, 107-134.

[22] G. Hirth and D. L. Kohlstedt (1996) Water in the oceanic upper mantle; implications for rheology, melt extraction, and the evolution of the lithosphere. Earth and Planetary Science Letters **144**(1-2), 93-108.

[23] L. H. Rupke et al. (2002) Are regional variations in Central American arc lavas due to differing basaltic versus peridotitic slab sources of fluids? Geology **30**(11), 1035-1038.

[24] H. Iwamori (1998) Transportation of H_2O and melting in subduction zones. Earth and Planetary Science Letters **160**, 65-80.

[25] J. G. Ryan et al. (1995) Cross-arc geochemical variations in Kurile arc as a function of slab depth. Science **270**, 625-627.

[26] A. Hochstaedter et al. (2001) Across-arc geochemical trends in the Izu-Bonin arc: contributions from the subducting slab. Geochemistry, Geophysics, Geosystems 2:2000GC000105.

[27] S. Zhong and M. Gurnis (1992) Viscous flow model of a subduction zone with a faulted lithosphere: Long and short wavelength topography, gravity and geoid. Geophysical Research Letters **19**(18), 1891-1894.

[28] M. I. Billen et al. (2003) Multiscale dynamics of the Tonga-Kermadec subduction zone. Geophysical Journal International **153**, 359-388.

[29] B. H. Hager (1984) Subducted slabs and the geoid: Constraints on mantle rheology and flow. Journal of Geophysical Research **89**(B7), 6003-6015.

[30] L. Moresi and M. Gurnis (1996) Constraints of the lateral strength of slabs from three-dimensional dynamic flow models. Earth and Planetary Science Letters **138**, 15-28.

[31] M. I. Billen and M. Gurnis (2001) A low viscosity wedge in subduction zones. Earth and Planetary Science Letters **193**, 227-236.

[32] M. I. Billen and M. Gurnis (2003) Comparison of dynamic flow models for the Central Aleutian and Tonga-Kermadec subduction zones. Geochemistry, Geophysics, Geosystems **4**(4), 1035, doi:10.1029/2001GC000295.

[33] N. H. Sleep (1975) Stress and flow beneath island arcs. Geophysical Journal International **42**, 827-857.

[34] J. H. Davies and D. J. Stevenson (1991) Physical model of source region of subduction zone volcanics. Journal of Geophysical Research **97**(B2), 2037-2070.

[35] D. Arcay et al. (2005) Numerical simulations of subduction zones: Effect of slab dehydration in the mantle wedge dynamics. Physics of the Earth and Planetary Interiors **149**, 133-153.

[36] M. W. Schmidt and S. Poli (1998) Experimentally-based water budgets for dehydrating slabs and consequences for arc magma generation. Earth and Planetary

Science Letters **163**, 361-379.

[37] M. Spiegelman and D. McKenzie (1987) Simple 2-D models for melt extraction at mid-ocean ridges and island arcs. Earth and Planetary Science Letters **83**, 137-152.

[38] P. E. van Keken et al. (2002) High-resolution models of subduction zones: Implications for mineral dehydration reactions and the transport of water into the deep mantle. Geochemistry, Geophysics, Geosystems **3**(10), 1056, doi: 10.1029/2001GC000256.

[39] S. M. Peacock (1990) Fluid processes in subduction zones. Science **248**, 329-337.

[40] P. M. Smith and P. D. Asimow (2005) Adiabat_1ph: A new public front-end to the MELTS, pMELTS, and pHMELTS models. Geochemistry, Geophysics, Geosystems **6**(2), Q02004, doi:10.1029/2004GC000816.

[41] M. S. Ghiorso and R. O. Sack (1995) Chemical mass transfer in magmatic processes; IV, A revised and internally consistent thermodynamic model for the interpolation and extrapolation of liquid-solid equilibrium magmatic systems at elevated temperatures and pressures. Contributions to Mineralogy and Petrology **119**(2-3), 197-212.

[42] S. King et al. (1990) ConMan; vectorizing a finite element code for incompressible two-dimensional convection in the Earth's mantle. Physics of the Earth and Planetary Interiors **59**(3), 195-207.

[43] G. Lehmann and H. Bambauer (1973) Quarzkristalle und ihre Farben. Angew. Chem. **85**, 281-289; Quartz crystals and their colors. Angew. Chem. Int'l Edn. **12**, 283-291.

[44] A. J. Cohen and F. Hassan (1974) Ferrous and ferric ions in synthetic alpha-quartz and natural amethyst. American Mineralogist **59**, 719-728.

[45] E. Neumann and K. Schmetzer (1984) Mechanism of thermal conversion of colour and colour centres by heat treatment of amethyst. N. Jb. Miner. Mh. **6**, 272-282.

[46] G. R. Rossman (1994) Colored Varieties of the Silica Minerals. In P.J. Heaney, C.T. Prewitt, G.V. Gibbs (eds.), Reviews in Mineralogy, Mineralogical Society of America, Washington, 1994, p. 433.

[47] J. A. Weil (1975) The aluminum centers in alpha-quartz. Radiat. Eff. **26**, 261-265.

[48] R. D. Aines and G. R. Rossman (1986) Relationships between radiation damage and trace water in zircon, quartz, and topaz. American Mineralogist **71**, 1186-1986.

[49] K. Nassau and B. E. Prescott (1977) A unique green quartz. American Mineralogist **62**, 589-590.

[50] T. R. Paradise (1982) The natural formation and occurrence of green quartz. Gems and Gemmology **18**, 39-42.

[51] A. N. Platonov et al. (1992) Natural prasiolite from Lower Silesia, Poland. Z. Dt. Gemmol. Ges. **41**, 21-27.

[52] R. T. Cox (1977) Optical absorption of the d^4 ion Fe^{4+} in pleochroic amethyst quartz. Journal of Physics, C: Solid State Physics **10**, 4631-4643.

[53] J. R. McArthur et al. (1993) Stable-isotope, fluid inclusion, and mineralogical studies relating to the genesis of amethyst, Thunder Bay Amethyst Mine, Ontario. Canadian Journal of Earth Sciences **30**, 1955-1969.

Chapter II:

Emergence of a Low-Viscosity Channel in Subduction Zones Through the Coupling of Mantle Flow and Thermodynamics

Laura Baker Hebert, Paula Antoshechkina, Paul Asimow, and Michael Gurnis

For submission to Earth and Planetary Science Letters

Abstract

We couple a petrological model (pHMELTS) with a 2D thermal and variable viscosity flow model (ConMan), to describe and compare fundamental processes occurring within subduction zones. We study the thermal state and phase equilibria of the subducting oceanic slab and adjacent mantle wedge and constrain fluid flux. Using a Lagrangian particle distribution to perform thousands of thermodynamically equilibrated calculations, the chemical composition of the domain is continuously updated. Allowing the buoyancy and viscosity to be compositionally and thermally dependent permits a consistent linkage between the effect of water addition to and flow within the mantle wedge, leading to predictions as to the fate of hydrated material as subduction proceeds. We present seven model cases that span normal ranges in subducting slab age, convergence velocity, and slab dip angle. In all models, the coupling between the chemistry and the dynamics results in behavior previously unresolved, including the development of a continuous, slab-adjacent low-viscosity channel (LVC) defined by hydrous mineral stability and higher concentrations of water in nominally anhydrous minerals and bounded by the water-saturated solidus. The LVC develops due to fluid ingress into the mantle wedge from the dehydrating slab, and can be responsible for slab decoupling, large-scale changes in the wedge flow field, and a mechanism by which hydrated slab-adjacent mantle material can be transported to the deep mantle. Changing model parameters indicate that slab age and slab dip angle exert primary control over variations in LVC shape and thickness, due to changing fluid release patterns within the slab. Slab convergence velocity appears to exert a secondary control over LVC shape. Younger slabs tend to have thinner, more uniform LVCs, while older slabs tend to have a thinner LVC at shallow depths with a large increase in LVC thickness at ~100 km depth, followed by a gradual thinning deeper in the model domain as material is advected down.

Keywords: subduction, low-viscosity channel, coupled models, Costa Rica, Izu-Bonin, Mariana

1. Introduction

A complete understanding of subduction zones requires a model that accounts for complex interactions between chemical and dynamic features of the system. Modeling that addresses principally either the force balance or the chemistry, using results from one direction to infer behaviors in the other, has succeeded in reaching broad conclusions as to the manner of hydration of the mantle wedge and melting beneath the arc [1-7]. However, when the thermal structure, viscosity, and the solid flow field are addressed within the context of a fully coupled geophysical and geochemical model, emphasizing the importance of interdependent contributions, more detailed interpretations can be made. The evolution of dynamical quantities such as the flow field, entropy, and bulk composition should provide input to thermodynamic calculations, which output chemically-governed quantities such as melt fraction, compositional buoyancy, water speciation, and latent heat contributions to the thermal balance. This forms an essential loop where neither chemistry nor physics are independently evaluated. Indeed, it is the dependence of one on the other that presents insights into the subduction system on a fundamental level.

A particular part of the subduction system where strong coupling between mass and energy flows and geophysical and geochemical processes is most important is the mantle wedge adjacent to the slab. There is general agreement that fluids from the dehydrating slab are introduced to the overlying mantle as the slab descends and that the pressure-temperature path, chemical composition, and phase equilibria within the slab determine the locations of water-rich fluid release [4]. The delivery of this water-rich fluid phase into and interaction with the overlying mantle induces hydration reactions within the peridotite and, where temperature is sufficient, water-fluxed melting [8]. Conventional steady-state thermal solutions of subduction indicate that the slab-wedge interface is too cold for even water-saturated melting of peridotite, so the fluids must somehow migrate into hotter areas of the wedge in order for melting to begin [9]. However, the mechanism by which wedge hydration proceeds and the pathways by which water-rich fluids are introduced to the sites of melting remain speculative [2, 4]. Previous modeling studies have specifically addressed the role of water in the subduction system together with dynamical considerations, emphasizing the role of hydrous minerals in acting as transport agents and/or sources of water and using phase diagrams for consideration of the peridotite solidus. Davies and Stevenson [1] propose a model where water released from the basaltic slab at 2.3 GPa is transferred into the wedge and stabilizes amphibole. Advection with the solid flow field results in a net horizontal transport of water along the amphibole-out boundary until the water-saturated peridotite solidus is crossed and melting begins. The model of Iwamori [2] improves upon [1] by adding the potential stabilization of additional hydrous phases within the wedge into the model. This method results in nearly all the water expelled during primary dehydration from the altered oceanic crust being hosted within a slab-adjacent layer of hydrated peridotite (serpentine and chlorite). Secondary dehydration of this hydrated layer allows the formation of fluid columns leading to zones of active melting. Arcay et al. [3], using non-Newtonian rheology, include the presence of lithospheric serpentinite in the down going slab as a major contributor to the water budget, and discuss a process by which the entire mantle wedge can experience hydration as the slab subducts. However, these studies do not include a full evaluation of water stability in nominally anhydrous minerals or changing bulk composition of the peridotite due to melt extraction. In addition to contributing to the stability of hydrous phases and the initiation of melting, the influx of fluid induces partitioning of hydrogen into defect sites within nominally anhydrous minerals (NAM) such as olivine. Recent investigations introduce the potential importance of these minerals in both the water budget and the dynamics of subduction zones [10-12], and this study aims to improve upon previous modeling by including water partitioning in NAM in the mantle wedge as the primary focus of a coupled geochemical and geodynamic model which emphasizes the origination and development of hydration features within the wedge in an internally consistent treatment.

There is a dual impact on the viscosity structure along the slab-mantle interface due to temperature dependence and compositional dependence (water-weakening) [10]. The implications of the reduction of viscosity of the mantle due to slab-related hydration have been considered [13, 14]. For example, a low-viscosity mantle wedge has been shown to have a substantial effect on the force balance in a subduction zone, and leads to observable signals in topography, state of stress, gravity, and the geoid [13, 15]. The viscosity of the wedge may be at least a factor of 10 smaller than the surrounding mantle lithosphere and asthenosphere [13], consistent with estimates from seismic dissipation [16] and rock deformation experiments [10]. The low-viscosity wedge potentially resolves the over-prediction of back-arc basin depths by several kilometers [13]. In models that successfully fit the observed geoid, the addition of a low-viscosity wedge changes the state of stress in the over-riding plate from compression to extension [13]. Such a wedge may play an important role in controlling the presence of back-arc spreading. While the importance of a localized low-viscosity region in a subduction zone has been evaluated, the mechanism by which it develops and its detailed geometry have yet to be considered.

We present GyPSM-S (**G**eod**y**namic and **P**etrological **S**ynthesis **M**odel for **S**ubduction), a self-consistent model that includes the thermodynamic minimization algorithm pHMELTS [17-19], which takes into account water partitioning into nominally anhydrous minerals, in conjunction with the 2-D thermal and variable viscosity flow model ConMan [20] and a fluid migration scheme. Evaluation of properties such as the melt fraction, fluid flux, the impact of water in NAM on the viscosity structure and overall flow field, and spatial extent of fluids and melts within the subduction system are all incorporated into GyPSM-S. It is important to mention that the overall structure of GyPSM can be adapted for other tectonic regimes such as mid-ocean ridges (GyPSM-R, [85]).

2. Model Formulation

2.1. Component programs

The two primary component programs used within the GyPSM-S computational scheme are (1) ConMan, a two-dimensional thermal and variable viscosity numerical flow model [20], and (2) pHMELTS, a thermodynamic energy minimization algorithm that can calculate water partitioning into nominally anhydrous minerals [17-19].

ConMan solves equations for incompressible buoyant viscous flow using the finite element method (FEM) in two dimensions. While an extension to three-dimensional flow is important to fully model variables that may contribute to along-arc observables, it is beneficial to first consider the consequences of a two-dimensional approach. A penalty formulation is used to enforce incompressibility in the solution of the momentum equation [20]. The dynamics are controlled by conservation equations of mass, momentum, and energy, with the Boussinesq approximation. The non-dimensional equations for mass and momentum are:

$$\nabla \cdot v' = 0 \qquad \text{and} \tag{1}$$

$$\nabla P' - \nabla \cdot \left(\eta' \nabla v' \right) = RaT' \hat{k} \quad , \tag{2}$$

where v' is the dimensionless velocity, T' is the dimensionless temperature, P' is the dimensionless pressure, η' is dimensionless viscosity, and $\hat{k}$ is a unit vector in the direction of gravity. The dimensionless Rayleigh number combines all the material properties:

$$Ra = \frac{g \alpha \rho \Delta T d^3}{\kappa \eta} \quad , \tag{3}$$

where g is the acceleration due to gravity, α is the coefficient of thermal expansion, ΔT is the temperature drop across the box, d is the depth of the box (Table 3), κ is the thermal diffusivity, and η is the dynamic viscosity (Table 1).

The effects of latent heats of melting, hydration, and dehydration can be better evaluated in pressure-entropy space, where an isentropic calculation can result in an increase or decrease in temperature depending on melting or crystallization. Consequently, compared to the normally-posed convection problem ConMan was designed to solve [20], we have modified the energy equation such that entropy is advected instead of temperature. Our non-dimensional energy equation is:

$$\frac{\partial S'}{\partial t'} = -v' \cdot \nabla S' + \frac{C_P'}{T'} (\nabla^2 T') \qquad , \tag{4}$$

where S' is the dimensionless entropy, C_P' is the dimensionless heat capacity, and t' is dimensionless time. A streamline upwind Petrov-Galerkin method [21] is used to solve (4). In the model formulation of GyPSM-S, we employ a near-fractional melting scheme that accounts for the instantaneous removal of all melt above a certain residual porosity (MINF, Table 1). Because of this, we do not allow the melt to subsequently interact with or crystallize in the lithosphere, which negates the possibility of increases in temperature there due to crystallization of melt.

For all of the results presented here, the computational grid consists of 2×10^4 uniformly sized bilinear quadrilateral elements: 100 in the vertical direction and 200 in the horizontal direction (20301 Eulerian nodes). All numerical experiments use the same number of elements, and as such the different model grids have slightly different resolutions from one to another, as the width of the model domain varies among experiments. The dimensional grid resolutions and dimensions of the calculation domains of all models are presented in Table 3.

The viscosity law is both temperature and composition dependent, as influenced by water in nominally anhydrous minerals, specifically olivine [10]:

$$\eta' = \frac{\eta}{\eta_0} = \exp\left[\left(\frac{Q}{RT_0}\right) * \left(\left(\frac{T_0}{T}\right) - 1\right)\right] * \left(\frac{XH_2O}{XH_2O_{crit}}\right)^{-1} \quad , \qquad (5)$$

where $XH_2O > XH_2O_{crit}$, η_0 is the reference viscosity, Q is the activation energy, R is the gas constant, T_0 is the model reference temperature, XH_2O is the water content in olivine, and XH_2O_{crit} is the critical value for water weakening (Table 1). The law was determined empirically from experimental results for dislocation creep of hydrated olivine aggregates [22] and is relatively simplistic, meant to account for a large range of pressures, temperatures, and water contents well outside current experimental bounds. The possible compounding effects of the hydration of other NAM are neglected in the viscosity formulation. The viscosity of the thermal lithosphere and the slab depends on temperature and has a maximum value of 1.0×10^{24} Pa s for the coldest regions ($10^3 \times$ reference viscosity, Table 1). Within the models, we expect variations in temperature of 1500 degrees and water in olivine contents up to ~2000 ppm at the highest pressures. As such, we observe that the viscosity law as stated results in a range of potential viscosities of 5.5×10^{19} to 1.0×10^{27} Pa s (with the maximum value seen in the model results set at 1.0×10^{24} Pa s). This model maximum viscosity restricts the range of solid viscosities found within the model to approximately 5 orders of magnitude (Fig. 1). For comparison, Kelemen et al. [23] show that there is a variation in viscosity of three orders of magnitude from temperature dependence alone.

The initial and boundary conditions within the model are summarized in Figure 2. The subducting slab velocity as well as the velocity of all material subjacent to the slab is kinematically imposed and the magnitude is dependent on the rate of convergence of the model being calculated (Table 3). The velocity boundary conditions on the left-side and the base of the wedge domain are imposed by an analytical solution for corner flow (equation 4.8.23, [24]), while the velocities within the wedge itself are allowed to respond dynamically. The top surface is isothermal (273 K), and the thickness of the over-riding plate and the thermal age of the down-going slab define the initial thermal conditions within the model. The initial particle distribution within the convecting portion of the mantle is assigned a temperature based on a pHMELTS-calculated adiabatic gradient. A prescribed potential temperature and an imposed adiabatic gradient on the sidewalls (Table 1) determine the temperature of incoming material for the duration of the calculation. Specifically, temperatures and entropies along the sidewalls are fixed and determined by independent pHMELTS calculations based on the position of the intersection of the convective (adiabatic) asthenosphere with the conductive thermal lithosphere [80 and references therein]. This explicit treatment of the thermal boundary layer discourages melting of the peridotite immediately upon entering the model domain, and we do not include decompression melting associated with a back-arc in any model. The initial composition-space spanned by the model includes depleted peridotite solved for by pHMELTS (with some supplemental calculations required where pressure and temperature conditions restrict pHMELTS applicability, see below for discussion), hydrated altered oceanic crust (AOC) within the slab, and hydrated lithospheric serpentinite also within the slab. The latter two compositions are *not* solved within pHMELTS, but refer to phase diagrams [25] for dehydration reaction locations within pressure-temperature space. This is due to the fact that the calibration of pHMELTS does not encompass the full spectrum of lithologies within the model domain. Within the slab, we impose a layered structure. The first layer is composed of AOC (basaltic, 2 km, and gabbroic, 5 km) modeled after [25], which treats the entire oceanic crust as basalt and gabbro of MORB composition (Table 2b) and initially contains ~5.0 wt. % H_2O. The second layer is composed of a serpentinite lithology (5 km) and is modeled on the hydrated harzburgite phase diagram in [25], initially containing 14.8 wt. % H_2O. Within the wedge, we use an initial depleted peridotite composition which includes an initial bulk water content of 110 ppm (Table 2a) [26]. There is no K_2O included, which effectively suppresses formation of mica within pHMELTS, but results in a more realistic melt productivity. Equilibration of the original peridotite composition, mass-normalized to 100.0 g, occurs at 3.3 GPa, 1424.56 °C and f_{O_2} = NNO, which is then used as the starting composition within the pHMELTS algorithm. In selecting a single depleted mantle composition, we are not specifically accounting for the range of source compositions presumably encountered within subduction zone wedges, which can include depletion due to extraction of melt at a back-arc, or larger-scale mantle source variations. While mineral-melt trace element partitioning is included, pHMELTS cannot currently calculate trace elements within the fluid phase itself, making it impossible to directly include the fluid-mobile trace element composition of the slab lithologies in the fully-coupled experiments. Supplemental modeling done independently using GyPSM-S results is required to address this (Chapter 3).

pHMELTS can be used to calculate water partitioning among hydrous minerals, nominally anhydrous minerals, melt, and free water, and the effect of such partitioning on melt productivity. The underlying thermodynamic model behind pHMELTS is pMELTS [27]. This is calibrated for peridotite bulk compositions between 1 and 4 GPa. In pMELTS, water is treated as an oxide component accommodated only in melt, vapor, or hydrous mineral phases, whereas in pHMELTS the effects of storage of water in nominally anhydrous minerals are approximately modeled [19]. The pHMELTS calculation uses trace element partitioning to distribute water between the system-consisting of melt, pure vapor, or hydrous minerals-and a hidden reservoir within the nominally anhydrous minerals. Although the algorithms used to calculate thermodynamic equilibria are powerful and generally reliable, especially when melt is present, there are situations where they fail to converge to a correct solution. The pHMELTS starting solutions are carefully constructed to avoid many of these potential pitfalls, but where they do occur, and also in regions outside of the calibrated pressure-temperature-composition range of pHMELTS, we use a heat-capacity polynomial formulation for entropy [28] with pMELTS-calculated end-member parameters, in conjunction with an equation of state for water [29]. pHMELTS uses the Birch-Murnaghan equation of state for the melt phase, but a polynomial expression for the solid volumes [28]. We do not allow the system to re-equilibrate above 5.3 GPa, but use an extrapolation of the equation of state and the heat capacity formulation of assemblages at 5.3 GPa that is continuous in volume and its first derivatives. Liquids are only calculated at pressures below 4 GPa.

2.2.Code coupling and tracer particles

The adiabat_1ph interface to pHMELTS [17] uses scripts to invoke subroutine versions of the (pH)MELTS program, which has the advantage over the graphical user interface (GUI) version of allowing almost complete automation of the calculation process. GyPSM-S uses an extension of adiabat_1ph that can be exploited with parallel processing. Bulk density is computed by pHMELTS from the equations of state of the constituent phases and the equilibrium phase assemblage and is a function of temperature, pressure, and composition. The latest estimates of water solubility in olivine are included [30].

The component programs are executed and controlled by scripts governing the parallel computing process (Fig. 3). Within GyPSM-S, quantities such as temperature, entropy, volatile content in nominally anhydrous minerals, and water content are passed in a loop structure which includes the component programs until the model reaches a state independent of its initial conditions. A network of Lagrangian particles, acting as chemical tracers, provide iterative feedback among the component programs and are advected within ConMan using a predictor-corrector method [31]; for one convective overturn (about twice the residence time of a particle in our calculations), the particles accumulate a spatial error $O(10^{-5})$. The particle set includes an initial distribution of approximately 4×10^4 particles (Fig. 4a), with four particles randomly introduced per element within the area of interest and one particle per node in rigid regions and in regions of relatively uniform bulk composition (beyond the extent of water introduction from the slab). In areas where single particles are on the nodes, because of the uniformity of bulk composition and the redundancy of pHMELTS calculations, we do not allow the particles to advect with the flow field (Fig. 2a). We chose this particle distribution in order to maximize computational efficiency and minimize errors due to interpolation and interference with boundaries (see below).

Particles within the model have several different compositional "tags" that determine lithology. As the experiment proceeds, the particles can be advected across the boundaries of the model domain. In order to keep a uniform particle density, new particles are added at the boundaries (the right sidewall and the interface between high and low particle densities, Fig. 2a) as older particles are advected out of the model domain. The temperature of new particles is interpolated from fixed boundary values along the sidewalls. The criterion for adding particles is a particle summation test within the elements along the boundaries. If an element has become empty, then four more particles are introduced in a random configuration within that element. The type of particle added is appropriate to its initial position: peridotite within the wedge (for particles entering the left boundary within the convecting region and along the right sidewall beneath the 12 km hydration depth), AOC (for particles entering along the right sidewall within 7 km of the top of the slab), and serpentinite (for particles entering along the right sidewall between 7 km and 12 km from the top of the slab). Throughout the computation, the wedge remains well-resolved (Fig. 4b). Encroachment of streamlines against the interface between the convecting and rigid parts of the mantle results in the necessity for a random "kick" given to particles to prevent clumping. Each peridotite-composition particle is associated with a full pHMELTS calculation, translating into thousands of thermodynamically equilibrated calculations per iteration. This allows for a continuously updating dataset and a strong chemical feedback mechanism into the dynamics, provided by particle-to-node and node-to-particle interpolations at each time step. The particle-to-node step is performed using a triangle-based linear interpolation scheme for smoothly-varying quantities such as temperature, but a bilinear scheme for interpolation of available fluid (particles in the four surrounding bilinear quadrilateral elements all contribute an area-weighted value to each node) in order to conserve mass. The node-to-particle step is performed using a bilinear interpolation method (area-weighted value at the particle position within an element calculated from quantities at the four surrounding nodes). It has been suggested that, for area-weighted bilinear methods, 5 particles per element represents the optimal load for high resolution interpolation [32]. We tested three interpolation methods (bilinear, triangle-based linear, and bi-cubic triangulated) with particle densities of up to 9 particles per element and ultimately chose to use 4 particles per element as the slight improvement in resolution presented by the increased particle density was offset by the high computational cost (pHMELTS). Over the model duration, there is a slight numerical diffusion that results in overall cooling of tens of degrees due to the interpolations. This appears to be unavoidable, and we have chosen the scheme and particle distribution that minimizes it while maximizing computational efficiency. Errors in temperature are highest in areas of high thermal gradients, namely in the wedge corner and along the slab interface, and the triangulation scheme appears to perform best at minimizing errors in these areas.

Prior to coupling, the finite element program is used independently (with only temperature-dependent viscosity) to achieve a quasi-steady-state thermal structure (approximately 56 million years of subduction); this is then used as our thermal initial condition for the coupled GyPSM calculations. These nodal values for temperature are interpolated onto the particle set, with pressure and compositional information (e.g., depleted peridotite, altered oceanic crust, lithospheric serpentinite, etc.), including initial water content, being assigned (or "tagged") based on the position of each particle within the dimensional domain (200 km depth, variable width, see Table 3, Fig. 4a).

This first set of pHMELTS calculations involves an isothermal thermodynamic minimization: inputs being temperature and pressure, and outputs being entropy and water content in nominally anhydrous minerals, along with chemical information such as melt presence and composition, water content, trace element abundance, solid phase mode and mineral compositions, and melt and solid density. Each subsequent pHMELTS calculation will be isentropic. At each ConMan timestep, the chemical information is returned to the FEM, influencing the viscosity and energy fields. The appropriate particles move with the updated velocity field, into a new pressure-entropy state, which then becomes the condition sent to the next set of pHMELTS calculations. The energy equation is an advection-diffusion formulation in entropy terms, dependent upon the temperature state of the system. Key variables are updated accordingly, including the water content in nominally anhydrous minerals and the density of the residue. The total duration of the coupled computations in dimensional model time are typically two to five million years of subduction. This is sufficient to approach a state independent of initial conditions, judged by the complete progression of original particles from the top of the model slab to its base.

We use a near-fractional melting scheme, employed such that after every iteration all but a small residual porosity of melt (MINF, Table 1) is instantaneously removed. As the equations governing the finite element calculation assume incompressibility and single-phase flow, we do not allow the removed melt to interact with the remaining solid residue (amounting to an assumption of perfect chemical isolation of migrating melts).

Additionally, we do not account for any impact the remaining porosity has on the solid flow field or the viscosity. However, a small but finite residual porosity helps to stabilize the pHMELTS calculation. Melt extraction depletes the residue (changes the bulk composition of sources for future melts), which changes the solidus temperature. When a packet of mantle peridotite residue (that has experienced melting due to fluid fluxing) is advected along slab-parallel streamlines, encountering new fluid sources from the slab, the temperature of the solidus of the residue should be slightly higher than for the original peridotite composition, influencing where melting will initiate (Table 2a). In order to account for this, pHMELTS retains knowledge of the changing bulk composition of each particle. The bulk composition of the residue, plus any residual liquid, is re-summed to 100.0 g of material so that the extensive quantities calculated by pHMELTS (such as entropy and volume) can be readily incorporated into the finite element model, which deals with intensive quantities (such as density).

2.3. Water migration

The hydrated slab is progressively dehydrated as it moves deeper into the mantle, with slab particles advected into increasing temperature and pressure conditions. We use the hydrous mineral stability calculations of [25] to approximate the amount of free water liberated from slab hydrous mineral phases upon crossing univariant reactions, solving for slab dehydration during subduction as thermobaric conditions change. We assume an initial hydration depth into the slab of 12 km, including both an AOC layer and a lithospheric serpentinite layer, as mentioned previously. A serpentinite layer has been observed in Alpine ophiolites [33, 34] and seafloor exposures and is presumed to be formed by the introduction of fluids at the ridge crest or along normal faults occurring during plate bending [35]. We do not, however, include a sediment layer, assuming that most sediment water is lost to compaction early in slab descent [79]; sediments probably do not contain enough water to be significant water sources at these depths [36]. However, this assumption disallows sediment melting, which may be significant in certain subduction zones as sources of chemical slab tracers [37]. We assume that the initial state of the slab is water-saturated, resulting in an immediate vertical flux of water into the wedge (running the model long enough so that this initial transient is passed). There is the possibility that temperature changes associated with phase changes, melting, or hydration/dehydration reactions in the mantle wedge can progressively heat or cool the slab, influencing the flux of water at each subsequent iteration. However, because we rely on phase diagrams to predict reactions within the AOC and serpentinite lithologies, we cannot directly account for the thermodynamics of slab dehydration reactions within the model. We do account for the movement of entropy with the fluid phase.

The evolved pure water (water that is not bound by NAM, melt, or hydrous phases) is advected vertically by Darcy's law, taking into account the estimated domain permeability:

$$\left(v_{water} - v_{solid}\right) = \frac{Kg\Delta\rho}{\eta_W} \qquad \text{and} \tag{6}$$

$$K = \frac{d_m^2 \varphi^n}{C} \quad , \tag{7}$$

where K is the permeability, d_m is the characteristic spacing of transport tubules (on the order of grain size), φ is the mean fluid fraction, $\Delta\rho$ is the density difference between fluid and solid, η_W is the fluid viscosity, n is a constant parameter indicating the type of pore geometry, and C is a geometrical constant [38] (Table 1). We estimate the fluid velocity to be approximately 2×10^{-8} m/s (63 cm/yr) with the current parameters. The choice of $n = 2$ includes a fundamental assumption that flow is occurring within an isotropic network of cylindrical pores of uniform size. Experimental investigation of natural systems indicates that the pore geometry may differ significantly from this idealized case in natural systems, with $n = 3$ [39, 40], and may be anisotropic [41]. The simplifications used in our models can be justified by the lack of information available for conditions at depth. However, we consider the range of fluid velocities dependent on grain size and on the value of n to assess the impact on the model results. Changing n from 2 to 3 effectively extends the time in which it takes water to migrate through the LVC to reach the zone of active melting, however, the LVC geometry and the orientation of the zone of active melting remain the same. At each iteration (dimensionally ~8,000-14,000 years), we assume that chemical equilibrium between the fluid and the solid matrix is attained, such that the water may be bound in nominally anhydrous minerals or in hydrous minerals such as chlorite and/or amphibole, or freely move through water-saturated regions up into the hotter regions of the wedge, where it may be partitioned into a melt phase. We do not account for the solubility of silicate components in our hydrous fluid, which may be of importance to phase relations, as the second critical endpoint beyond which H_2O-rich fluids and silicate melts forms a single supercritical phase exists within the bounds of our models (approximately 3.8 GPa and 1000 ºC) [42].

2.4.Model input parameters

Subduction parameters such as slab convergence velocity, slab dip angle, and slab thermal age vary on Earth over ranges of 10-100 mm/yr, 10-70º, and 10-160 Ma, respectively [43]. To evaluate the role of changing physical characteristics on the thermal and chemical development of the LVC, we have varied the subduction variables (Table 3) convergence velocity, slab dip, slab thermal age, and crustal thickness among seven models, spanning significant ranges of convergence velocities (47.5-90 mm/yr), slab dip angles (30-60º), and slab thermal structures (incoming plate age 15-165 Ma). Four of the models are immediately applicable to two geographical regions (and two sub-regions within each): (i) the Costa Rica-Nicaragua segment of the Central American subduction zone and (ii) the Izu-Bonin-Mariana subduction zone, and the model results can be used to specifically match physical and chemical datasets.

The Central American subduction zone involves relatively young lithosphere (15-25 Ma) of the Cocos Plate subducting beneath the Caribbean Plate [44]. The convergence rate increases slightly towards the southeast, but the primary difference between the Central Costa Rican (CCR) and Southeastern Costa Rican (SCR) models is the slab dip, which changes from 45º to 30º, respectively. The Izu-Bonin-Mariana (IBM) subduction zone involves relatively mature lithosphere of the western Pacific Plate subducting beneath the eastern Philippine Sea Plate [45], allowing us to evaluate the possible effects of a significantly older slab and a slower convergence rate, as compared to the CCR and SCR cases. The primary difference between the Northern Izu-Bonin (NIB) and Northern Marianas (NMAR) models is the slab dip, which changes from 45º to 60º, respectively. Model ADD1 addresses fast subduction of an older plate, while ADD2 is a slow-subducting young plate. Model ADD3 involves slow subduction of a mature slab with a thicker overlying lithosphere. All additional models have slab dips of 45º, allowing an evaluation of slab age and slab convergence velocity at a constant dip angle (compared with models CCR and NIB).

3. Model Results

3.1.Development of the low-viscosity channel and controls on its shape

For a young, moderately fast subducting plate, we summarize the results for the process of slab-adjacent mantle wedge hydration (Fig. 5). The pressure-temperature path of the descending slab allows the release of water in distinct locations along the slab surface (Fig. 5c), corresponding to the crossing of dehydration reaction boundaries [25] of particles within the basalt-gabbro and the serpentinite layers (within the slab). At the early stages of this model, the majority of the shallow water release (< 100 km) is due to reactions within the AOC layer (jadeite lawsonite blueschist → lawsonite amphibole eclogite, lawsonite amphibole eclogite → amphibole eclogite, and amphibole eclogite → zoisite eclogite) [25]. Reactions within the serpentinite layer account for fluids coming from ~110 km depth (rock containing serpentine chlorite brucite → serpentine chlorite dunite; lithologic descriptions from [25]) and from ~170 km depth (chlorite harzburgite → garnet harzburgite) [25]. As the initial fluid transient dissipates, the primary sources of fluid become shallow sources within the AOC (60-80 km depth) and a source around 140 km depth within the serpentinite layer (chlorite harzburgite → garnet harzburgite). The flux of water from the slab interacts with the nominally anhydrous minerals (NAM) such as olivine, pyroxene, and garnet in the overlying wedge. There is a substantial increase in the water content of these minerals in a region of the wedge adjacent to the slab (Fig. 5c). Through the viscosity formulation (Eq. 5), this creates a strong variation (a reduction of 10-100 times, due to water-weakening) in wedge viscosity within ~25 kilometers of the slab surface (Fig. 5d). Despite discontinuous point sources of water influx, the low-viscosity zone is extended into a continuous layer that is further advected downward by entrainment in the slab-dominated velocity field. Ultimately, the low-viscosity layer extends from 50 kilometers depth to the base of our model region (200 km) and results in a non-uniform low viscosity channel (LVC) (Fig. 5f). The difference in hydration between the ambient mantle wedge and the LVC increases with depth, leading to a strong variation in viscosity that extends perpendicular to the slab. There is a lack of fluid release at the highest pressures beyond the initial transient (in contrast to other models, see below) that results in an LVC thickness at 200 km that is primarily a result of advection of hydrated material from lower pressures, thinned slightly relative to the LVC at lower pressures directly above the fluid sources. The flow field changes with the development of the LVC as seen in the difference in the streamlines within the wedge (Fig. 5a versus Fig. 5e). There is a stronger component of upward flow across the boundary between the nominally anhydrous mantle wedge and the hydrated LVC.

In addition to the hydration of NAM, there is the concurrent appearance of hydrous phases within the hydrated region of the slab-adjacent wedge. Amphibole appears at pressures below 2.1 GPa, and chlorite appears as a stable slab-adjacent phase at pressures from 2.0 GPa to ~5.3GPa, where chlorite breaks down by the reaction clinochlore +

enstatite → forsterite + pyrope + H_2O [46-48], leading to a continuous hydrous phase layer above the slab surface and below the 1000 K isotherm within the wedge (Fig. 6a). Small amounts of deep chlorite (> 5.3 GPa) are an artifact of pHMELTS not including a high-P hydrous phase such as Mg-sursassite or phase A. An evaluation of the position and extent of melting reveals a localized slab-adjacent region of hydrous melt production formed by water-fluxed wedge melting that extends deeper than 100 km. Instantaneous low-degree fractional melts bound the top of the LVC (water-saturated solidus). Water transport occurs solely within the hydrous fluid phase, and therefore, as melting initiates, and water partitions strongly into the melt phase, the activity of water drops below unity and the fluid phase disappears, preventing further transport of water and additional flux melting. The region of melting is therefore thin (~6 km) as measured normal to the LVC surface and is restricted to the top of the LVC, but displaced from the slab-wedge interface due to the thermal structure. In areas with quasi-continuous dehydration from the slab, the melting region is oriented at a slight angle to the slab-wedge interface with depth, as progressive depletion of the advecting slab-adjacent mantle by melting results in a displacement of the water-saturated solidus further into the wedge to higher temperatures. Indeed, melt initiation provides the limitation on the geometry of the hydrated region as demonstrated in a comparison calculation with the silicate liquid phase suppressed in pHMELTS (Fig. 6c). If melting is suppressed, fluid continues to react with the wedge peridotite, hydrating NAM and moving through the wedge until it enters the overlying rigid lithosphere. A sharp, upper boundary (Fig. 6b, c) is imposed to prevent water from entering low-temperature and low-pressure regions where pHMELTS is not stable.

The development of a low-viscosity channel within a subduction zone is a consequence of the dehydration of the subducting slab and progressive hydration of the overlying mantle wedge below the water-saturated solidus. The thickness of the LVC is determined by the thermal structure of the wedge, in that initiation of flux melting effectively restricts further transport of fluid in a hydrous phase within the system and forms an upper boundary to the hydrated low-viscosity region, controlling the channel geometry. We do not observe hydrous phases (amphibole and chlorite) restricting water transport as a fluid phase to the active melting region. If melting is not present within the wedge, for whatever reason, then a low-viscosity "wedge" geometry may prevail. Due to our assumption of purely vertical fluid flow, initiation of melting appears discontinuous, controlled primarily by the spatial position of water influx, and the presence of active melting can be transient, depending on a consistent influx of water. As mentioned earlier, we do not include a back-arc spreading region, and take care to avoid melting of the peridotite source prior to its introduction into the wedge corner. Latent heat of melting results in net cooling of the residue before turning the corner in the wedge, potentially counter-acting the incorporation of temperature-dependent viscosity variations, which allow for higher slab-adjacent temperatures than an isoviscous rheology [45].

3.2.Model comparison (Table 3)

The influence that slab age and convergence velocity have on the LVC and flow geometry are illustrated with four models at a constant slab dip angle (45º) with different slab ages (18 Ma versus 135 Ma) and different convergence velocities (50 mm/yr versus 87 mm/yr) (Fig. 7). LVC shape changes substantially with changing subduction parameters.

The cases involving a younger slab have thinner, more uniform LVCs. Cases involving older slabs show a very different geometry: a very thin LVC at shallow depths and a large increase in LVC thickness around 100 km depth, followed by the gradual thinning of the LVC towards 200 km depth as the hydrated material is advected out of the model domain. The abrupt truncations at the base of the LVC (Fig. 7a, b) at 220 km from the trench (x-axis) are due to a change in particle distribution (Fig. 2a), and the upper limit of fluid migration (Fig. 7b) is imposed by the position of the overlying lithosphere. The thick hydrated envelope in models with older, colder slabs originates from stronger fluid sources at greater depths than the models with young, warm slabs, which rely on fluid sources from the slab at < 130 km depth. In the case of the older slabs, the streamlines show a marked kink upwards as they cross the thick region of lower viscosity, and the temperature structure is also decidedly influenced, resulting in significant cooling associated with zones of melting. This is a consequence of the latent heat of melting. In regions of high water flux at higher pressures, which occur in models with colder thermal structures due to subduction of older slabs, the melting column is longer, and time-dependent cooling of the wedge occurs. This results in an upward retreat of the water-saturated solidus and an extension of the fluid pathways, allowing fluid from dominantly serpentinite lithology to interact with a shallow melting region. Over time, the zone of melting retreats vertically and stalls below the thermal lithosphere, reducing to direct fluid transport into the overlying lithosphere (similar to the water transport columns of [2]) and melting restricted to the edges of the hydrated region (Fig. 9). The differences in the LVC shape among the models with younger slabs (and likewise among the models with older slabs) can be attributed to variations in slab velocity. Increasing convergence velocity with other parameters held relatively constant results in a colder thermal regime, and so changes the locations of dehydration reactions within the slab. For the younger slab models, there is melting at 100 km depth in both models as a result of the dehydration of lithospheric serpentinite (chlorite harzburgite → garnet harzburgite), but additional releases at lower pressures (50 mm/yr convergence) and at higher pressures (87 mm/yr convergence) determine the overall shape of the LVC, with the model with more rapid convergence velocity having a slightly thicker LVC due to the deeper fluid release. In terms of comparing lateral variations in viscosity at higher pressures, the slower converging case then involves a greater contrast between the ambient nominally anhydrous mantle wedge and the LVC due to the thinner LVC shape. The overall thinning at higher pressures is a result of the continuation of the LVC solely by advection of hydrated material down-dip, without strong additional fluid sources. For the more mature slab models, the case with the faster convergence velocity likewise involves a slightly deeper fluid source and a somewhat thicker LVC at the base of the model domain. Notably, this is reflected in the position of the melting region (Fig. 9) in that melts for the faster converging case are further down-dip from the trench.

Slab dip has a major control on the geometry of wedge hydration. Models comparing variations in slab dip from 45º are shown in Fig. 8. Fig. 8a and b compare a slab dip shallowing from 45º to 30º, with all other parameters remaining relatively constant. Fig. 8c and d compare a slab dip steepening from 45º to 60º, again with all other parameters remaining relatively constant. The primary observation with regard to the shallowing of the slab dip angle is that while the uniformity of the LVC remains, the thickness of the LVC increases. In the case of the steepening slab dip, the fluid pathways become closer to slab-parallel, decreasing the thickness of the LVC along the slab and resulting in a sharp thinning of the LVC at 200 km depth, leading to large lateral variations in viscosity as the overprinting of the cold boundary layer adjacent to the slab is not as extensive as in other models. While deep fluid sources are influencing shallower melting via a long fluid pathway, the melting region is closer to the trench due to the near-slab-parallel fluid trajectory, reflecting a narrower trench-perpendicular region of melting. The locations of fluid release remain relatively constant throughout the experiment, except for the initial transient.

Instantaneous melt fractions in all cases are low (<1%) (Fig. 9) as a consequence of the size of the time-step between extractions (and therefore the corresponding change in pressure and addition of water). However, using residual compatible trace element abundances to map cumulative melt fraction results in total melt fractions of up to 20%, comparable to petrological estimates of arc magma fractions. The shape of the instantaneous melting region is complex, as melting relates closely to the positions of fluid release from the slab, and is thin, as a function of our fluid migration scheme (vertical transport, water transport in a hydrous fluid only). However, for a batch melting case, the melt layer can be more continuous and the thickness of the melting region will increase. The influence of the latent heat of melting on the thermal regime (and slight additional cooling due to numerical diffusion from the interpolation algorithms) within the wedge is to thicken the LVC (Fig. 9g-i). Specifically, the position of the melting region produced by fluid releases at high pressures transits vertically into the wedge as the wedge cools, leading to longer fluid pathways. The displacement of the solidus could be exaggerated by the presence of prior depletion due, perhaps, to melting at the back-arc, and would result in even thicker LVCs.

The thickness of the LVC is related to the distribution and magnitude of fluid resulting from dehydration reactions within the slab (a function of the slab age and convergence velocity), to the degree of melt extraction (cooling and prior melt depletion due to flux melting or to potential back-arc spreading), and to the slab dip angle. The variations in shape of the LVC indicate that changing slab thermal age and slab dip angle exert a primary control over the degree to which the slab is viscously decoupled from the overlying wedge, judging by the continuity of the LVC along the length of the slab and the extension of the hydration region into the wedge. Changing convergence velocity exerts a secondary control, mainly in terms of variations in LVC shape and position of the melting region within the wedge. Subduction of older slabs emphasizes shallow melts from deeper fluid sources (serpentinite). Steeper-dipping slabs (> 45°) allow for melting regions closer to the trench. Shallower dipping and younger slabs emphasize shallower melts and shallower fluid sources (AOC). As the AOC and serpentinized lithosphere have different fluid-mobile trace element chemistries, fluids from different sources should manifest themselves in different trace element patterns in arc lavas from different regions (Chapter 3). Additionally, the greater extent of the low-viscosity region in ADD1 and NIB (subduction of older, colder slabs) has a significant impact of the force balance, manifesting itself in geophysical observables such as the geoid, gravity, and topography (Chapter 4). Despite differences in shape, the development of the spatially-restricted LVC geometry occurs across the range of model parameters evaluated.

4. Discussion

4.1.The low-viscosity channel (LVC)

In all models we observe the development of a spatially-restricted layer of hydration present continuously along the slab-mantle interface. This layer can extend from the slab-wedge interface vertically into the wedge to the overlying lithosphere, up to 100 km in some cases (Fig. 10), and is comprised of hydrous phases (chlorite and hornblende) and nominally anhydrous minerals with high water contents (olivine up to ~1400 ppm, clinopyroxene up to ~5700 ppm, orthopyroxene up to ~2800 ppm, and garnet up to ~600 ppm as the solubility of water in NAM increases with pressure). As there is a fundamental assumption of a pure water phase, we can discuss water contents in terms of solubility, as opposed to storage capacity. This layer is responsible for a large reduction in viscosity (10^1 to 10^2 ×) due to water-weakening along the slab, and can therefore be referred to as a low-viscosity channel (LVC). The development of the specific geometry of the LVC is affected by slab age, convergence velocity, and dip angle through the specific pressure-temperature evolution of the slab, resulting in differing dehydration patterns for different subduction parameters. The hydrated layer defining the LVC is initiated and thickened by fluid release from the slab and is also advected downward with the slab-dominated velocity field, resulting in a continuous extension of the hydrated layer along the slab-mantle interface. This smearing out by the sub-solidus flow in the wedge counteracts the discontinuous pattern of water release from the slab. Our models are restricted in vertical dimension due to the pressure limitations of pHMELTS, but we observe the persistence of the hydrated layer to the base of our domain, and reasonably assume that it can persist deeper. The increasing solubility of water in olivine with pressure may allow for an even greater influence on viscosity with depth, assuming that the slab has not been completely dehydrated. Indeed, for models with subduction of older slabs, the lithospheric serpentinite layer still contains as much as 6.8 wt. % H_2O as it exits the model domain. The peak water content in NAMs in the LVC, as it reflects a water-saturated zone, is primarily a reflection of the solubility of water at a particular temperature and pressure, and therefore the peak hydration does not vary significantly among the models tested. The extent of the LVC into the mantle wedge is governed by the position of the water-saturated solidus within the specific thermal structure defined by the subduction parameters of a particular model and the degree of melt extraction and prior depletion. As soon as melting initiates, the activity of water drops as water is strongly partitioned into the melt. In the absence of a hydrous fluid phase, water transport ceases, and melting is restricted to a thin zone immediately above slab fluid sources.

We do not see the formation of Rayleigh-Taylor instabilities (cold diapirs) along the surface of the hydrated LVC, in contrast to [49], because of lower density contrasts across that boundary predicted by our models. There are like to be two reasons for the lower density contrasts. Firstly, we do not include a very low-density sediment layer in our slab lithology and do not assume mechanical (solid) mixing between slab lithologies and the overlying mantle wedge peridotite (which decreases the density of the hydrated peridotite and therefore increases the density contrast between that hydrated layer and anhydrous peridotite above it). Secondly, we do not observe the presence of serpentinized wedge peridotite against ambient nominally anhydrous peridotite. The position of the hydrated peridotite solidus in pHMELTS is sufficient to allow some distance between the upper stability limits of the hydrous phases and the water-saturated peridotite solidus. Compositional limitations within pHMELTS result in a restriction in the range of hydrous minerals that can be stabilized in the wedge. Along the slab interface, pHMELTS stabilizes hornblende at lower pressures and chlorite at higher pressures (Fig. 6a). There is residual amphibole present in the shallowest melt source regions, but along the majority of the slab surface, chlorite is the only stable hydrous phase and is restricted to within ~10 km of the slab surface due to breakdown above 1000 K. Coincident with the sharp drop in water content along the top of the LVC boundary, we observe slight density contrasts increasing from water-saturated peridotite in the LVC to ambient nominally anhydrous peridotite ($\Delta\rho \sim$ 20-50 kg/m^3), which are much less than those predicted by [49] for the diapir-source region ("mixed" hydrated layer vs. anhydrous peridotite) along the top of the slab. The thermal conditions of our model predict a much thicker hydrated channel before water-saturated melting begins. Therefore, we never see fully-serpentinized (implying stability of chrysotile and antigorite) mantle lithology adjacent to the nominally anhydrous region above it. Finally, the hydrated channel in our models is capped by the initiation of melting. At lower pressures (~1.5 GPa), melting of a fully-saturated assemblage results in a higher density residue and a lower density melt phase. The residue density is comparable to the anhydrous density, but is slightly lower. At higher pressures (~4.0 GPa) there are even smaller density contrasts between fully-saturated peridotite and residues of melting. The low density contrasts across the top of the LVC compared to the contrasts of [49] across the top of their thinner hydrated layer ultimately inhibit the formation of Rayleigh-Taylor instabilities in this model at the pressures evaluated.

Iwamori [2] presents a numerical model that describes the generation and migration of fluids from the slab with consequent equilibration with the overlying convecting mantle solids, producing hydration and melting. Similar to our results, there is a stable slab-adjacent layer of chlorite within the wedge and a displacement of the region of melting into the wedge. In contrast to our results, their chlorite layer [2] is able to absorb the majority of the water released from the slab and dehydration of the chlorite around 150 km depth allows for a singular fluid source, transporting water to the melting region. Our results, which include consideration of water stability in NAM, indicate that fluid is able to both hydrate the slab-adjacent layer of chlorite and an overlying thickness of NAM. Successive fluid flux through this saturated zone produces melting at multiple depths within the wedge, ultimately producing a discontinuous slab-parallel melting region that is displaced into the wedge. Our melting region looks very similar to the disequilibrium transport case of [2], in which water is allowed to "leak" from the slab-adjacent hydrated layer at depths less than 150 km.

Independent of results presented here, time-dependent models of subduction with a parameterized wedge viscosity show that slab dip can be substantially influenced by a low-viscosity channel geometry with a thickness of tens of kilometers and a viscosity contrast of a factor of two [50]. In such models, a low viscosity channel generally leads to increased slab dips as the suction force drawing the slab upward is reduced. Our model provides a self-consistent mechanism to generate such a low-viscosity channel geometry, however, we are unable to demonstrate the effect changing slab dip would have on an existing LVC because we did not include dynamical feedback to the slab. We can estimate the effect that a changing slab dip may have based on our model results encompassing a range of slab dip angles. Initiation of subduction at a shallow dip angle would result in a continuous LVC to at least 200 km depth of roughly uniform thickness. If the formation of this LVC leads to increasing slab dip angles [50], the LVC would most likely remain as a continuous channel, but the thickness may change, and, more importantly, the positions of the melting region within the wedge would change. This may lead to observable increases in lava flux from the volcanic arc as melts are produced further from the trench initially (perhaps feeding the rear-arc), and then closer with time as the slab dip angle changes. The trenchward progression could also be mapped by signals in fluid-mobile trace elements consistent with lithospheric serpentinite dehydration as opposed to dehydration from AOC proceeding from the rear-arc to the volcanic front with time (Chapter 3).

Although we do not specifically include prior melt depletion at a back-arc into GyPSM-S, we note that it can potentially impact the character of melts produced in the models with time as a function of position in the mantle wedge. For example, considering subduction of an older, cold slab, the melting region influenced by the deep fluid sources changes position in the wedge with time, driven by cooling of the mantle wedge due to latent heat of melting (Fig. 11). At the beginning of the experiment, the source region for these melts is relatively fertile. There is a displacement of the melting region into the wedge away from the residues of the shallow melts traveling along the slab-parallel flow field, and therefore no prior source depletion due to episodes of flux melting earlier along the streamline. Additionally, the position of these melts in relation to the flow field and potential prior depletion from the back-arc melting region implies that they are relatively fertile as well. As the experiment continues, the deep-sourced melting region shallows, and while the fluid-mobile trace elements are still consistent with a deep source (serpentinite), the extent of potential prior depletion due to a back-arc increases, potentially changing the values of trace element indicators such as Zr/Nb with time. Shallowing of the deep-sourced melting region also produces even greater depletion signatures for the shallow-sourced melts, as the two melting regions are aligned along streamlines within the wedge.

Our use of pHMELTS allows for a self-consistent application to the problem of a changing bulk composition (source depletion) due to melting and for the partitioning of water into NAM. Hydrous phases such as amphibole and chlorite are present, but do not dictate the transport of fluid to the active melting region, and while they act as effective "sponges," they do not inhibit the flux of a hydrous fluid phase. Instead, fluid migrates vertically into the wedge, progressively saturating a layer of NAM and hydrous phases. As mentioned previously, we do not see the stability of hydrous phases up to the zone of active melting except in the case of very low pressures. Once the layer is saturated, water can move through to the melting region (water-saturated solidus of peridotite), where it is partitioned into the melt phase and effectively removed from the system.

4.2. Water mobility: recycling to deep mantle and timing of transport to active melting region

The formation of enriched mid-ocean-ridge basalts (E-MORB) at normal mid-ocean ridges hints at the presence of chemical heterogeneities in the mantle which may have been generated by recycling of material at subduction zones [51-55]. Geochemical arguments exist for the relative importance of the slab-adjacent mantle, metasomatized by either slab-derived fluids or small-degree slab melts, rather than recycled oceanic crustal materials or sediments themselves [52, 53]. Analyses of basaltic glasses from the mid-Atlantic ridge (MAR) near the Azores reveal evidence (high $\delta^{18}O$, La/Sm, Ce/Pb, and $^{87}Sr/^{86}Sr$ and low $^{143}Nd/^{144}Nd$) for an enriching agent [52]. However, bulk incorporation of sediments or altered oceanic crust to the ridge melting source region will not reproduce observed geochemical trends [52]. A two-stage model of the slab-adjacent mantle, modified by either fluids or slab-derived small-degree melts, and then mixed with ambient mantle to form a mixed, enriched source region for partial melting allows for erupted E-MORB lavas with major element systematics similar to normal MORB, isotopic ratios reflecting long-term enrichment of the source region, and the required trace element fractionations and concentrations [53]. Additionally, high lithium isotope ratios in enriched East Pacific Rise lavas may be explained by enrichment by fluid-modified recycled wedge material instead of altered oceanic crust itself [36]. The slab-adjacent mantle is carried down with the subducting slab, but, as opposed to altered oceanic crust, may be more efficiently mixed in with ambient upper mantle to produce enriched source regions for normal upwelling and melting beneath ridges.

In these models, the LVC emerges as a stable zone of fluid-modified slab-adjacent mantle material and trapped low-degree melts that is transported with the slab-dominated flow field, presumably to depths beyond our model region, where it may, at some point, separate from the denser oceanic crust and mix with surrounding upper mantle material. The persistence of the LVC to great depths is due to it being spatially limited by the water-saturated solidus. As the subducting slab descends, although water solubility in NAM increases, the pressure-temperature path of the LVC will not cross the solidus, allowing a mechanism for the recycling of water and slab-adjacent water-rich wedge material deep into the mantle, as well as possibly affecting the solid flow and contributing to slab decoupling. Excluding hydrous phases (as pHMELTS does not stabilize realistic hydrous phases near 200 km depth), and assuming a peridotite assemblage of 57% olivine, 8% garnet, 16% orthopyroxene, and 16% clinopyroxene, the LVC can potentially transport ~2200 ppm H_2O into the deeper mantle in NAM alone, providing a significant, robust, water source.

The presence of the LVC has implications for the timing of fluid-bearing element transport from the slab to the arc. It has been hypothesized that two separate mantle wedge enrichment mechanisms result in the ^{238}U excesses observed at the Mariana arc: an episode of sediment-derived (uranium-rich) fluid addition to the mantle source followed by >350ky of radiogenic ingrowth as the solid flow advects the material deeper, and then a second episode of (aqueous) fluid influx from the dehydrating altered oceanic crust [37]. Timing from this second release of fluid to the eruption of lavas is on the order of tens of thousands of years, a time-frame which necessarily includes melt migration and lower crustal processing, and the rapidity of this process suggests that the fluids themselves are the trigger for the initiation of significant mantle wedge melting [37]. The LVC, defined by tens of kilometers of water-saturated mantle material, may allow fairly rapid fluid transport with minimal chemical water-rock equilibration, resulting in direct delivery to the melting region and immediate triggering of melting. With the model fluid velocity ($d = 100$ μm, $n = 2$), it would take < 50 kyr for the fluids to penetrate to the active melting region with an LVC thickness of 25 km, a sufficiently short timeframe that would correspond to the U-series timescale for the second (and applicable, considering a lack of sediment) fluid influx to the wedge from the AOC. Changing these parameters (i.e., $n = 3$) results in timescales of fluid transport on the order of 1.5 Ma for a similar LVC thickness.

4.3. Melting

In all models, there is a distinct spatial region of melt production within the mantle wedge. We find that the dominant factor in subduction systems for controlling this melt distribution is the amount and spatial location of dehydration and free water release within the slab. Not only do fluids carry slab signatures, but the spatial location (pressure and temperature) of their release has implications for the resulting fluxed melt composition. Additionally, although we do not account for the influence of melt on viscosity, the presence of a melt lens may serve to either increase the effective thickness of the LVC, or to smooth out the sharpness of the viscosity transition from the LVC into the interior of the mantle wedge. In contrast to our near-fractional melt extraction scheme, melt migration at depths greater >90 km may be consistent with porous/reactive flow [56]. This would add an additional transport mechanism for water in the system: allowing hydrous melts to react with solids as they migrate will re-distribute water within NAM beyond the LVC, leading to a smoothly decreasing activity of water upwards and a finite extension of the hydration region and a wedge-type low-viscosity geometry.

A number of geochemical and petrological studies have suggested that partial melting of subducting slab components (sediment and/or altered oceanic crust) is a possibility in many arc systems. This is due to recycling of trace elements such as Th that are considered relatively fluid-immobile but can be partitioned strongly into partial melts of metasediments and metabasalt [37, 57-59] and by the similarities between trace element patterns of partial melts of eclogite with primitive arc andesites [60-64]. Plots of slab-wedge interface pressures and temperatures for the models alongside the water-saturated MORB solidus of [25] (i.e., 650-700 deg. C from 1-3 GPa) show that we would not reasonably expect melting of the AOC to occur in any of the models (Fig. 12). If, indeed, melting of the oceanic crust were to occur, as suggested by some thermal models incorporating temperature-dependent [23] and temperature and stress-dependent viscosity [6], the implications for the development of the LVC could be significant. Melting of the slab (sediment and/or AOC) would encourage partitioning of water into the melt phase, reducing the capacity of fluid for transport into the wedge. In this case, relying on a fluid phase to initiate melting may be incorrect, as the fluid could be taken up wholly in NAM and hydrous phases. We would then rely on the migration of the hydrous slab melts as the transport mechanism for water, and a more complicated fluxing process to initiate peridotite melting.

We note that the observation of the volcanic front forming at nearly constant globally-averaged height (~105 km) above the Wadati-Benioff zone [43] does not appear to be fulfilled by a discontinuous melt lens that extends along the slab surface (Fig. 9). However, we do not take into account melt migration processes that may serve to focus the melt, or may exploit the channel geometry for flow reversals back up the slab. Porous flow driven by pressure gradients as a mechanism of melt focusing towards the wedge corner [5], diapirism of melts towards the overlying lithosphere [65], or fracture propagation as a mechanism of melt extraction [66] have all been invoked as potential melt migration processes within subduction zones. We assume vertical fluid transport, immediately moving fluid into the mantle wedge upon release. Accounting for up-dip migration of fluids along the slab-wedge interface to lower pressures may concentrate melting within the wedge. Despite the simplistic approach to melt migration in our models, we can infer quite a lot from the positions of the zones of active melting. Seismic tomographic studies in northeastern Japan show an inclined, slab-parallel seismic low-velocity and high-attenuation zone in the mantle wedge [67, 68]. These discontinuous inclined regions exist at depths less than 150 km, are separated from the upper surface of the slab by ~50 km, and show very similar geometries to melting regions calculated by GyPSM-S in that the regions are inclined towards the position of the arc (Fig. 9).

Latent heat of melting appears to be the cause of the significant cooling of the mantle wedge. Since we remove melt completely from the system (above a certain porosity), we do not allow for crystallization of that melt within the wedge, which may also counteract wedge cooling by latent heat of crystallization. The calculated solidi from pHMELTS show a systematic offset from values calculated by [69]. At pressures less than 1 GPa, pHMELTS predicts lower solidus temperatures, while it gives significantly higher temperatures at higher pressures with a steeper dT/dP solidus curve, (1150 ºC vs. 800-1000 ºC at 3 GPa) (Fig. 13). This may lead to an over-extension of the zone of active melting into the wedge in our models, especially at pressures in excess of 3 GPa, as well as the lack of a contact between the chlorite stability field and the zone of active melting. However, the overall relationship between fluid migration, hydration of NAM, and displacement of the inclined zone of melting away from the slab with increasing pressure should remain the same.

4.4. Impact of LVC on seismic wave propagation

Seismic velocity and attenuation studies have interpreted a hydrated region directly adjacent to the slab. From regionally detected body-wave phases, low velocity layers (LVLs) exist above seismically fast slabs with thicknesses of 5-10 km in the Mariana, Japan [70], Kurile, Nicaragua [71], and Aleutian arcs. However, the LVL may be up to 20 km thick in parts of Alaska [72]. The Japan results suggest that the LVL extends down to 300 km depth with substantial velocity reduction. The P-wave velocity reduction could be as much as 14% if the thickness of the LVL is only 10 km, but only 4% if the layer is 30 km thick [70], suggesting a thick zone of hydrated phases. In addition, studies of seismic attenuation (with lower spatial resolution than the velocity models) suggest that there are broad zones of high attenuation (low Q) above slabs in Tonga [73], Alaska [74], and elsewhere.

It has been shown that the presence of hydrous phases can have a direct impact on seismic properties, and estimates of low-velocity anomalies along the slab-wedge interface in subduction zones have been hypothesized to be due to a continuous layer of hydrous phases [72, 82]. While hydrous phases can certainly hold more water than NAM, it remains true that NAM can account for significant amounts of water (in olivine alone as much as 0.6-0.9 wt. % can be held at 12 GPa [30, 75]) with steadily increasing solubility with increasing pressure and may have an indirect effect on seismic properties. The LVC is defined by an increased water content in NAM, present as hydrogen-related defects, which can enhance anelasticity and lead to an increase in attenuation and a reduction in seismic wave velocities [76-78,16]. Therefore, our results for a continuous channel of high water content in NAM may be consistent with regionally detected body-wave phase results showing low velocity layers (LVLs) of order tens of kilometers thickness above slabs [70].

5. Conclusions

As our models show, the ability to simultaneously explain geophysical and geochemical observations is essential to demonstrate certain behaviors such as the development of boundary features along the slab-mantle interface. The spatial extent of the low-viscosity region of the wedge may be a large-scale volume extending from the slab-mantle interface to the back-arc (e.g., [13]) or a relatively thin, continuous channel defined by water-saturated NAM and hydrous phases along the slab-mantle interface, depending on subduction parameters (slab age, convergence velocity, slab dip angle). The development of the LVC is a consequence of the vertical migration of fluids into the mantle wedge and reaction with peridotite to produce hydrous phases and higher water contents in NAM. Its extent is limited by the onset of melting and is therefore dependent on the position of the water-saturated solidus, which changes spatial position within the wedge due to source depletion (prior melt extraction) and/or the thermal evolution of the wedge (progressive melt extraction). The zone of active melting exists at the upper surface of the LVC, and the thickness and instantaneous melt fraction are restricted in our models by the assumptions of near-fractional melt extraction and the limitation of water transport to the hydrous fluid phase. Despite changing subduction parameters, the geometry of the melting regions are quite similar in all models: discontinuous lenses inclined to the slab surface and displaced from it by tens of kilometers. The persistence of the LVC would provide a mechanism by which hydrated slab-adjacent mantle material (consisting of a significant reservoir of water and potentially very low-degree mantle melts) is transported to the deep mantle without melting, providing a source for enriched OIB magmas such as the Azores. The LVC is also significant because of the effect it has on the large-scale flow field within the wedge, possibly leading to slab decoupling [13] and changes in slab dip [50]. Additional evidence for the existence of the LVC includes seismic wave propagation and attenuation and recent studies showing the significant displacement of the active melting region from the slab-wedge interface [67, 68].

Acknowledgments

The authors would like to especially thank Chad Hall for his substantial early work on code and concept development. This work benefited from helpful discussion with V. Manea, M. Chen, B. Hacker, and S. Kidder and from very constructive comments by two anonymous reviewers and editor C. Jaupart. Support provided through the Caltech Tectonics Observatory by the Gordon and Betty Moore Foundation. All calculations carried out on the Caltech Geosciences Supercomputer Facility partially supported by NSF EAR-0521699.

References

[1] J. H. Davies and D. J. Stevenson (1991) Physical model of source region of subduction zone volcanics. Journal of Geophysical Research **97**(B2), 2037-2070.

[2] H. Iwamori (1998) Transportation of H_2O and melting in subduction zones. Earth and

Planetary Science Letters **160**, 65-80.

[3] D. Arcay et al. (2005) Numerical simulations of subduction zones: Effect of slab dehydration in the mantle wedge dynamics. Physics of the Earth and Planetary Interiors **149**, 133-153.

[4] M. W. Schmidt and S. Poli (1998) Experimentally-based water budgets for dehydrating slabs and consequences for arc magma generation. Earth and Planetary Science Letters **163**, 361-379.

[5] M. Spiegelman and D. McKenzie (1987) Simple 2-D models for melt extraction at mid-ocean ridges and island arcs. Earth and Planetary Science Letters **83**, 137-152.

[6] P. E. van Keken et al. (2002) High-resolution models of subduction zones: Implications for mineral dehydration reactions and the transport of water into the deep mantle. Geochemistry, Geophysics, Geosystems **3**(10), 1056, doi: 10.1029/2001GC000256.

[7] S. M. Peacock (1990) Fluid processes in subduction zones. Science **248**, 329-337.

[8] Y. Tatsumi and S. Eggins (1995) Subduction Zone Magmatism, Blackwell, Cambridge.

[9] S. M. Peacock (2003) Thermal Structure and Metamorphic Evolution of Subducting Slabs. Geophysical Monograph 138, 7-22.

[10] G. Hirth and D. L. Kohlstedt (1996) Water in the oceanic upper mantle; implications for rheology, melt extraction, and the evolution of the lithosphere. Earth and Planetary Science Letters **144**(1-2), 93-108.

[11] S. Mei and D. L. Kohlstedt (2000) Influence of water on plastic deformation of olivine aggregates 2. Dislocation creep regime. Journal of Geophysical Research **105**(21), 21471-21481.

[12] E. H. Hauri et al. (2006) Partitioning of water during melting of the Earth's upper

mantle at H_2O-undersaturated conditions. Earth and Planetary Science Letters **248**, 715-734.

[13] M. I. Billen and M. Gurnis (2001) A low viscosity wedge in subduction zones. Earth and Planetary Science Letters **193**, 227-236.

[14] M. I. Billen and M. Gurnis (2003) Comparison of dynamic flow models for the Central Aleutian and Tonga-Kermadec subduction zones. Geochemistry, Geophysics, Geosystems **4**(4), 1035, doi:10.1029/2001GC000295.

[15] N. H. Sleep (1975) Stress and flow beneath island arcs. Geophysical Journal International **42**, 827-857.

[16] S. Karato and H. Jung (1998) Water, partial melting, and the origin of the seismic low velocity and high attenuation zone in the upper mantle. Earth and Planetary Science Letters **157**(3-4), 193-207.

[17] P. M. Smith and P. D. Asimow (2005) Adiabat_1ph: A new public front-end to the MELTS, pMELTS, and pHMELTS models. Geochemistry, Geophysics, Geosystems **6**(2), Q02004, doi:10.1029/2004GC000816.

[18] M. S. Ghiorso and R. O. Sack (1995) Chemical mass transfer in magmatic processes; IV, A revised and internally consistent thermodynamic model for the interpolation and extrapolation of liquid-solid equilibrium magmatic systems at elevated temperatures and pressures. Contributions to Mineralogy and Petrology **119**(2-3), 197-212.

[19] P. D. Asimow, J. E. Dixon, C. H. Langmuir (2004) A hydrous melting and fractionation model for mid-ocean ridge basalts: Application to the Mid-Atlantic Ridge near the Azores. Geochemistry, Geophysics, Geosystems **5**(1), Q01E16,

doi:10.1029/2003GC000568.

[20] S. King et al. (1990) ConMan; vectorizing a finite element code for incompressible two-dimensional convection in the Earth's mantle. Physics of the Earth and Planetary Interiors **59**(3), 195-207.

[21] A. N. Brooks and T. J. R. Hughes (1982) Streamline Upwind Petrov-Galerkin Formulations for Convection Dominated Flows with Particular Emphasis on the Incompressible Navier-Stokes Equations. Computer Methods in Applied Mechanics and Engineering **32**(1-3), 199-259.

[22] G. Hirth and D. Kohlstedt (2003) Rheology of the Upper Mantle and the Mantle Wedge: A View from the Experimentalists. Geophysical Monograph 138, 83-105.

[23] P. B. Kelemen et al. (2003) Thermal Structure due to Solid-State Flow in the Mantle Wedge. Geophysical Monograph 138, 293-311.

[24] G. K. Batchelor (1967) An Introduction to Fluid Dynamics. Cambridge University Press.

[25] B. R. Hacker, G. A. Abers, and S. M. Peacock (2003) Subduction factory-1. Theoretical mineralogy, densities, seismic wave speeds, and H_2O contents. Journal of Geophysical Research-Solid Earth **108**(B1), http://dx.doi.org/10.1029/2001JB001129.

[26] R. K. Workman and S.R. Hart (2005) Major and trace element composition of the depleted MORB mantle (DMM). Earth and Planetary Science Letters **231**(1-2), 53-72, http://dx.doi.org/10.1016/j.epsl.2004.12.005.

[27] M. S. Ghiorso et al. (2002) The pMELTS: A revision of MELTS from improved calculation of phase relations and major element partitioning related to partial

melting of the mantle to 3GPa. Geochemistry, Geophysics, Geosystems **3**, 10.1029/2001GC000217.

[28] R. G. Berman (1988) Internally consistent thermodynamic data for minerals in the system Na_2O-K_2O-CaO-MgO-FeO-Fe_2O_3-Al_2O_3-SiO_2-TiO_2-H_2O-CO_2: representation, estimation, and high temperature extrapolations. Journal of Petrology **89**, 168-183.

[29] K. S. Pitzer and S. M. Sterner (1994) Equations of state valid continuously from zero to extreme pressures for H_2O and CO_2. Journal of Chemical Physics **101**(4), 3111-3116.

[30] J. L. Mosenfelder et al. (2006) Hydrogen incorporation in olivine from 2-12 GPa. American Mineralogist **91**(2), 285-294, http://dx.doi.org/10.2138/am.2006.1943.

[31] I. Sidorin and M. Gurnis (1998) Geodynamically consistent seismic velocity predictions at the base of the mantle, in M. Gurnis, M. Wysession, E. Knittle, and B. Buffett, eds. The Core Mantle Boundary Region, American Geophysical Union, Washington, D.C., 209-230.

[32] P. J. Tackley and S. D. King (2003) Testing the tracer ratio method for modeling active compositional fields in mantle convection simulations. Geochemistry, Geophysics, Geosystems **4**(4).

[33] L. H. Rupke et al. (2004) Serpentine and the subduction water cycle. Earth and Planetary Science Letters **223**, 17-34.

[34] M. Scambelluri et al. (2004) The fate of B, Cl, and Li in the subducted oceanic mantle and in the antigorite breakdown fluids. Earth and Planetary Science Letters **222**, 217-234.

[35] P. Ulmer and V. Trommsdorf (1995) Serpentine stability to mantle depths and subduction-related magmatism. Science **268**, 858– 861.

[36] T. Elliott et al. (2006) Lithium isotope evidence for subduction-enriched mantle in the source of mid-ocean-ridge basalts. Nature **443**(5), 565-568, http://dx.doi.org/10.1038/nature05144.

[37] T. Elliott et al. (1997) Element transport from slab to volcanic front at the Mariana arc. Journal of Geophysical Research **102**(B7), 14991-15019.

[38] M. G. Braun, G. Hirth, and E. M. Parmentier (2000) The effect of deep damp melting on mantle flow and melt generation beneath mid-ocean ridges. Earth and Planetary Science Letters **176**, 339-356.

[39] D. A. Wark and E. B. Watson (1998) Grain-scale permeabilities of texturally equilibrated, monomineralic rocks. Earth and Planetary Science Letters **164**, 591-605.

[40] D. A. Wark et al. (2003) Reassessment of pore shapes in microstructurally equilibrated rocks, with implications for permeability of the upper mantle. Journal of Geophysical Research **108**(B1).

[41] M. E. Zimmerman et al. (1999) Melt distribution in mantle rocks deformed in shear. Geophysical Research Letters **26**(10), 1505-1508.

[42] K. Mibe et al. (2007) Second critical endpoint in the peridotite-H_2O system. Journal of Geophysical Research **112**, B03201, doi: 10.1029/2005JB004125.

[43] E. M. Syracuse and G. A. Abers (2006) Global compilation of variations in slab depth beneath arc volcanoes and implications. Geochemistry, Geophysics, Geosystems **7** (5), Q05017, doi: 10.1029/2005GC001045.

[44] S. M. Peacock et al. (2005) Thermal structure of the Costa Rica-Nicaragua subduction zone. Physics of the Earth and Planetary Interiors **149**(1-2), 187-200.

[45] R. J. Stern et al. (2003) An Overview of the Izu-Bonin-Mariana Subduction Factory. Geophysical Monograph 138, 175-222.

[46] T. L. Grove et al. (2006) The influence of H_2O on mantle wedge melting. Earth and Planetary Science Letters **249**, 74-89.

[47] P. M. Smith et al. (2007) Coupled Petrological and Geodynamic Models of Mantle Flow in Subduction Zones; the Importance of Chlorite in the Emergence of a Low-Viscosity Channel. Eos Trans. AGU, **88**(52), Fall Meet. Suppl., Abstract V43D-1637.

[48] A. Pawley (2003) Chlorite stability in mantle peridotite: the reaction clinochlore+enstatite=forsterite+pyrope+H_2O. Contributions to Mineralogy and Petrology **144**, 449-456.

[49] T. V. Gerya and D. A. Yuen (2003) Rayleigh-Taylor instabilities from hydration and melting propel 'cold plumes' at subduction zones. Earth and Planetary Science Letters **212**, 47-62.

[50] V. Manea and M. Gurnis (2007) Subduction zone evolution and low viscosity wedges and channels. Earth and Planetary Science Letters **264**(1-2), 22-45.

[51] M.W. Schmidt and S. Poli (1998) Experimentally based water budgets for dehydrating slabs and consequences for arc magma generation. Earth and Planetary Science Letters **163**, 361– 379.

[52] K. M. Cooper et al. (2004) Oxygen isotope evidence for the origin of enriched mantle beneath the mid-Atlantic ridge. Earth and Planetary Science Letters **220**, 297-316.

[53] K. E. Donnelly et al. (2004) Origin of enriched ocean ridge basalts and implications for mantle dynamics. Earth and Planetary Science Letters **226**, 347-366.

[54] J. E. Dixon et al. (2002) Recycled dehydrated lithosphere observed in plume-influenced mid-ocean-ridge basalt. Nature **420**, 385-389.

[55] P. J. le Roux et al. (2002) Mantle heterogeneity beneath the southern Mid-Atlantic Ridge: trace element evidence for contamination of ambient asthenospheric mantle. Earth and Planetary Science Letters **203**, 479-498.

[56] J. Nakajima et al. (2005) Quantitative analysis of the inclined low-velocity zone in the mantle wedge of northeastern Japan: A systematic change of melt-filled pore shapes with depth and its implications for melt migration. Earth and Planetary Science Letters **234**, 59-70.

[57] T. Plank and C. H. Langmuir (1993) Tracing trace elements from sediment input to volcanic output at subduction zones. Nature **362**, 739-743.

[58] T. Plank and C. H. Langmuir (1998) The chemical composition of subducting sediment and its consequences for the crust and mantle. Chemical Geology **145**, 325-394.

[59] M. C. Johnson and T. Plank (1999) Dehydration and melting experiments constrain the fate of subducted sediments. Geochemistry, Geophysics, Geosystems **1**, 1999GC000014.

[60] G. M. Yogodzinski and P. B. Kelemen (1998) Slab melting in the Aleutians: implications of an ion probe study of clinopyroxene in primitive adakite and basalt. Earth and Planetary Science Letters **158**, 53-65.

[61] M. J. Defant and P. Kepezhinskas (2001) Evidence suggests slab melting in arc

magmas. EOS **82**, 65-69.

[62] T. L. Grove et al. (2002) The role of an H_2O-rich fluid component in the generation of primitive basaltic andesites and andesites from the Mt. Shasta region, N. California. Contributions to Mineralogy and Petrology **142**(4), 375-396.

[63] Y. Tatsumi et al. (2001) Tectonic setting of high-Mg andesite magmatism in the SW Japan Arc: K-Ar chronology of the Setouchi volcanic belt. Geophysical Journal International **144**(3), 625-631.

[64] G. M. Yogodzinski et al. (2001) Geochemical evidence for the melting of subducting oceanic lithosphere at plate edges. Nature **409**, 500-504.

[65] P. Hall and C. Kincaid (2001) Diapiric flow at subduction zones: A recipe for rapid transport. Science **292**, 2472-2475.

[66] F. Furukawa (1993) Magmatic processes under arcs and formation of the volcanic front. Journal of Geophysical Research **98**, 8309-8319.

[67] A. Hasegawa et al. (2005) Deep structure of the northeastern Japan arc and its implications for crustal deformation and shallow seismic activity. Tectonophysics **403**, 59-75.

[68] D. P. Zhao et al. (2001) Seismological structure of subduction zones and its implications for arc magmatism and dynamics. Physics of the Earth and Planetary Interiors **127**, 197-214.

[69] T. L. Grove et al. (2006) The influence of H_2O on mantle wedge melting. Earth and Planetary Science Letters **249**, 74-89.

[70] M. Chen et al. (2007) Waveform modeling of the slab beneath Japan. Journal of Geophysical Research-Solid Earth **112**(B02305), doi: 10.1029/2006JB004394.

[71] G. A. Abers et al. (2003) The wet Nicaraguan slab. Geophysical Research Letters **30** (2), 1098. http://dx.doi.org/10.1029/2002GL015649.

[72] A. Ferris et al. (2003) High-resolution image of the subducted Pacific plate beneath central Alaska, 50-150km depth. Earth and Planetary Science Letters **214**(3-4), 575-588. http://dx.doi.org/10.1016/S0012-821X(03)00403-5.

[73] E. G. Roth, D. A. Wiens, and D. P. Zhao (2000) An empirical relationship between seismic attenuation and velocity anomalies in the upper mantle. Geophysical Research Letters **27**(5), 601-604. http://dx.dot.org.10.1029/1999GL005418.

[74] J. C. Stachnik, G. A. Abers, and D. H. Christensen (2004) Seismic attenuation and mantle wedge temperatures in the Alaska subduction zone. Journal of Geophysical Research-Solid Earth **109**(B10). http://dx.doi.org/10.1029/2004JB003018.

[75] J. R. Smyth et al. (2006) Olivine hydration in the deep upper mantle: Effects of temperature and silica activity. Geophysical Research Letters **33**(L15301), doi: 10.1029/2006GL026194.

[76] S. Karato (2003) Mapping Water Content in the Upper Mantle. Geophysical Monograph 138, 135-152.

[77] S. Karato et al. (1986) Rheology of synthetic olivine aggregates: influence of grain size and water. Journal of Geophysical Research **91**, 8151-8176.

[78] S. Mei and D. L. Kohlstedt (2000) Influence of water on plastic deformation of olivine aggregates 2. Dislocation creep regime. Journal of Geophysical Research **105**(21), 21471-21481.

[79] L. H. Rupke et al. (2002) Are regional variations in Central American arc lavas due to differing basaltic versus peridotitic slab sources of fluids? Geology **30**(11), 1035-

1038.

[80] D. McKenzie and M. J. Bickle (1988) The volume and composition of melt generated by extension of the lithosphere. Journal of Petrology **29**(3), 625-679.

[81] D. W. Peate and J. A. Pearce (1998) Causes of spatial compositional variations in Mariana arc lavas: Trace element evidence. The Island Arc **7**, 479-495.

[82] H. Kawakatsu and S. Watada (2007) Seismic evidence for Deep-Water Transportation in the Mantle. Science **316**, 1468-1471.

[83] A. Hochstaedter et al. (2001) Across-arc geochemical trends in the Izu-Bonin arc: contributions from the subducting slab. Geochemistry, Geophysics, Geosystems 2:2000GC000105.

[84] A. Audetat and H. Keppler (2004) Viscosity of fluids in subduction zones. Science **303**, 513-516.

[85] P. M. Smith et al. (2005) Integrating Geodynamic and Petrological Numerical Models; Mid-Ocean Ridge Flow Dynamics Revisited. Eos Trans. AGU, **86**(52) Fall Meet. Suppl., Abstract V33D-03.

Figure Captions

Figure 1: Range in viscosity produced from Eq. 5 implemented in GyPSM-S for the model water in olivine contents (0-2000 ppm) and model temperatures (0-1500 ºC in 100 ºC intervals). The range spans 5 orders of magnitude in viscosity when the maximum viscosity cut-off is imposed.

Figure 2: (a) Initial conditions and (b) boundary conditions imposed within the GyPSM-S model domain. See text for details.

Figure 3: Computational organization and data flow of the GyPSM-S model.

Figure 4: (a) Initial particle distribution for the wedge corner region of model SCR. The particles are arranged by composition and by temperature: peridotite (green), altered oceanic crust (black), and serpentinite (blue). The particle density is increased for the mantle wedge, the area of interest. (b) Final particle distribution after run completion for the wedge corner region of model SCR.

Figure 5: Development of LVC for model CCR: (a) initial thermal structure and streamfunction (with arrows showing direction of flow), resulting from an uncoupled ConMan calculation approaching steady-state; (b) initial viscosity structure, calculated immediately after the first coupled iteration with pHMELTS such that the water content of the ambient mantle is reflected in the viscosity structure as well as temperature-dependent contributions; (c) increase in water in olivine above the ambient background as fluid from the dehydrating slab rises vertically into the wedge and then reacts with the peridotite to form hydrous phases and hydrated NAM. A thin zone of melting is illustrated at the top of the hydrated channel where the white contour indicates melting > 1%; (d) viscosity structure corresponding to panel c, showing the marked decrease in viscosity of the solid matrix due to water-weakening from hydration of nominally anhydrous olivine; (e) advection of the slab-adjacent wedge peridotite results in the development of a hydrated

channel, bounded at the top by a thin melt lens. The solid flow streamlines shows a marked change in trajectory upon impacting the hydrated channel, with an increasing upward component; (f) the hydrated channel is defined by high concentrations of water in NAM, which influence the viscosity through the flow law, and result in the low-viscosity channel (LVC). Note that the contour interval of the stream function in the slab and descending mantle is twice the value in the wedge.

Figure 6: (a) Distribution of hydrous phases within model CCR. Hornblende (red) is present at lower pressures (< 2.5 GPa), while chlorite (green) is stable at pressures up to ~5 GPa, and temperatures < 1000 K. This stability field results in the formation of a continuous channel of hydrous minerals to depths of ~175 km within the LVC and bounding the slab surface. (b) Water in olivine (which defines the LVC). (c) An experiment with melting suppressed within the pHMELTS model, to test the impact of melting as the primary restriction on the thickness of the LVC. Note that the contour interval of the stream function in the slab and descending mantle is twice the value in the wedge.

Figure 7: Influence of slab age and convergence velocity on the development of the LVC as shown by the resulting viscosity structure. Models with a 45° slab dip are compared, arranged such that the effects of increasing slab age and increasing slab convergence velocity can be evaluated at constant slab dip angle. Fig. 7a (NIB) and b (ADD1) represent the subduction of old, cold slabs (thermal age 135 Ma), differentiated primarily by slow (50 mm/yr) and fast (87 mm/yr) convergence velocity. Fig. 7c (ADD2) and d (CCR)

represent the subduction of young, warm slabs (thermal age 18 Ma), and slow and fast velocities, respectively (Table 3).

Figure 8: Influence of the impact of changing slab dip on the geometry of the LVC. (a-b) CCR-SCR: shallowing slab dip from 45º to 30º. (c-d) NIB-NMAR: steepening slab dip from 45º to 60º.

Figure 9: Instantaneous melt fraction (color) and fluid release from the slab (blue contours), showing that melting is generally restricted to a thin (~6 km) lens immediately above fluid release locations within the slab for models (a) CCR, (b) NIB, (c) ADD2, (d) NMAR, (e) SCR, and (f) ADD1. Panels (g-i) illustrate the evolution of the melting region and the changing fluid release locations over time for model ADD1.

Figure 10: Thickness of the LVC vertically from the slab surface as a function of distance along the slab for (a) CCR (red), NIB (blue), ADD1 (black), ADD2 (purple), (b) NMAR (green), and (c) SCR (pink) models.

Figure 11: Schematic of the low-viscosity channel (LVC) geometry, including hydrous melt layer for the NIB model case. Dehydration reactions in the down-going slab release water, which rises into the overlying mantle wedge and reacts with peridotite to form hydrous phases and to hydrate nominally anhydrous minerals (NAM), such as olivine. Locations of water release from slab dehydration reactions showing the discontinuous nature of the water release due to crossing of reaction boundaries. The shallower

dehydration reactions are due to reaction boundaries in the altered oceanic crust, while the deeper reactions are in the lithospheric serpentinite layer. Once saturated, water can rise through the hydrated NAM layer into the hotter regions of the wedge, where it induces water-fluxed melting.

Figure 12: Pressure-temperature trajectories of the slab-wedge interface for the six models with the water-saturated MORB solidus from [19]. We neglect slab melting in our models, which refers to melting of the altered oceanic crust, as sediments are not included. The only model that approaches the water-saturated MORB solidus is ADD2, around 4.0 GPa.

Figure 13: Solidus relations for the model peridotite wedge starting composition (Table 1) with variable H_2O contents predicted by pHMELTS and the estimates of solubility of water in nominally anhydrous minerals (NAM) given by [30], similar to the construction of Figure 1 from [19], but with the primary difference being the higher estimates of water able to go into NAM relative to values originally given by [10]. The upper heavy black curve is the anhydrous solidus ($a_{H_2O} = 0.0$); the lowermost heavy black curve is the water-saturated solidus ($a_{H_2O} = 1.0$). The blue contours are lines of constant activity of water on the solidus in increments of 0.1 in a_{H_2O}. The black curves labeled 50, 300, 700, 1200, and 2000 show the solidus predicted for these bulk H_2O contents in parts per million by weight. The gray lines indicates the stability limits of garnet and plagioclase on the solidus, respectively. The green boundary shows the stability of hornblende on the solidus.

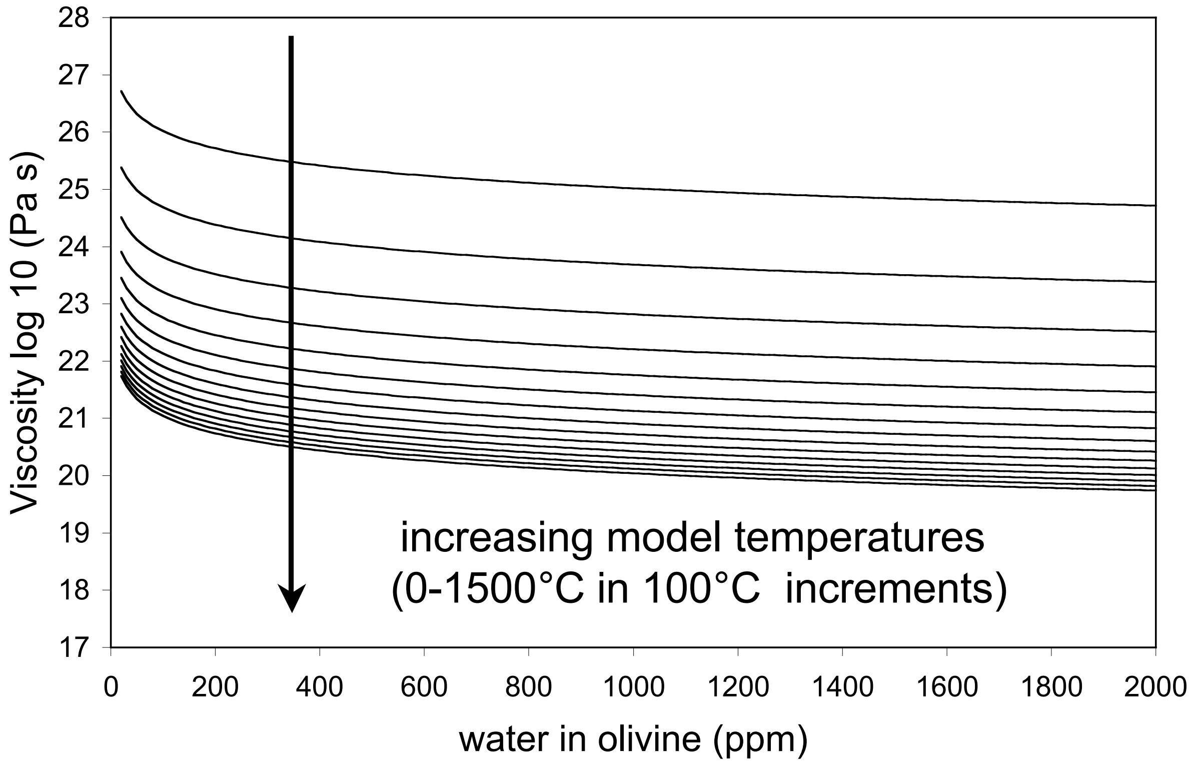
Viscosity log 10 (Pa s)
28
27
26
25
24
23
22
21
20
19
18
17
0
200
400
600
800
1000
1200
1400
1600
1800
2000
water in olivine (ppm)
increasing model temperatures
(0-1500°C in 100°C increments)

Figure 1.

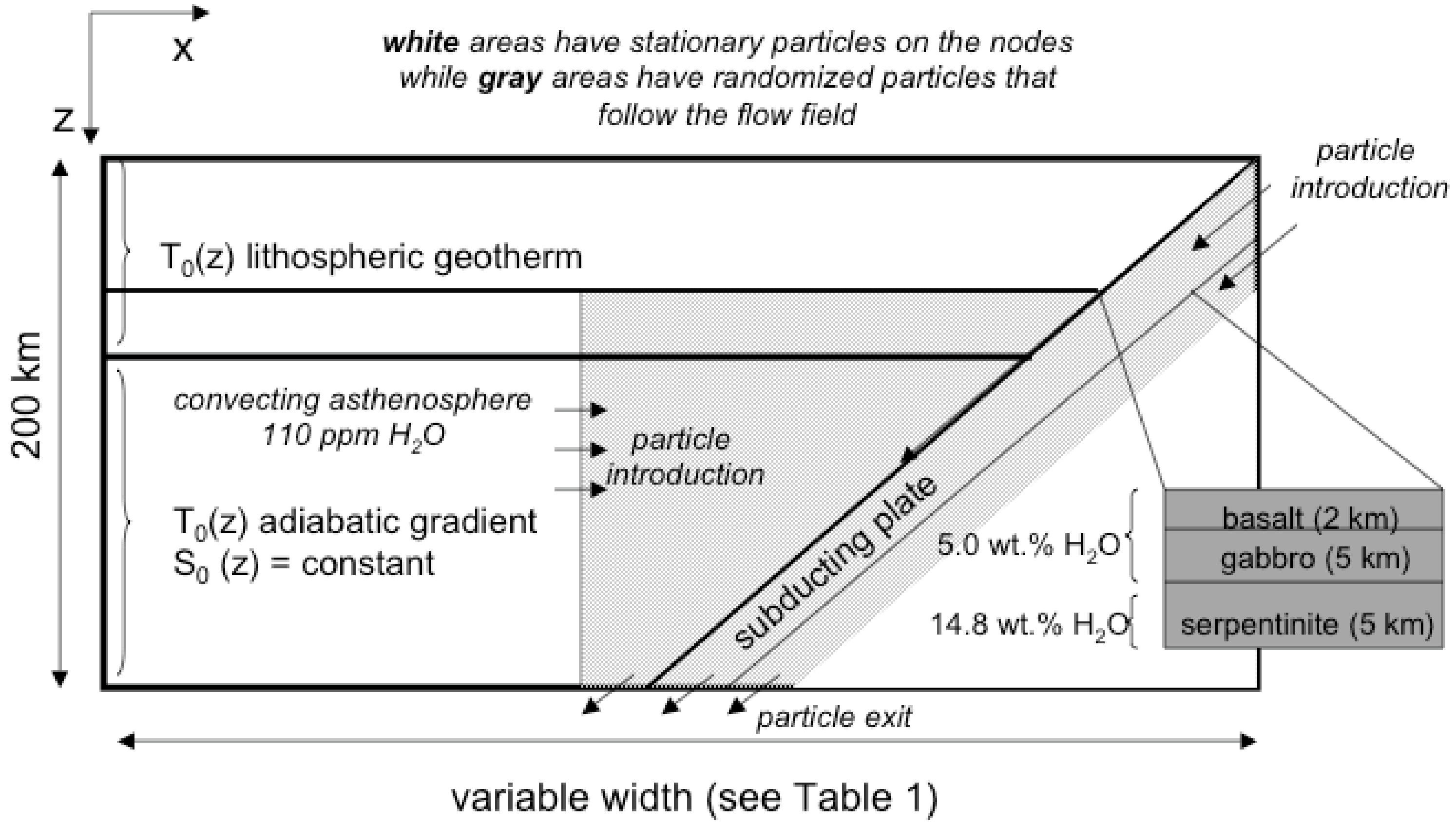
x
z
white areas have stationary particles on the nodes
while **gray** areas have randomized particles that
follow the flow field
particle
introduction
200 km
T$_0$(z) lithospheric geotherm
convecting asthenosphere
110 ppm H$_2$O
particle
introduction
T$_0$(z) adiabatic gradient
S$_0$ (z) = constant
subducting plate
5.0 wt.% H$_2$O
14.8 wt.% H$_2$O
basalt (2 km)
gabbro (5 km)
serpentinite (5 km)
particle exit
variable width (see Table 1)

Figure 2a.

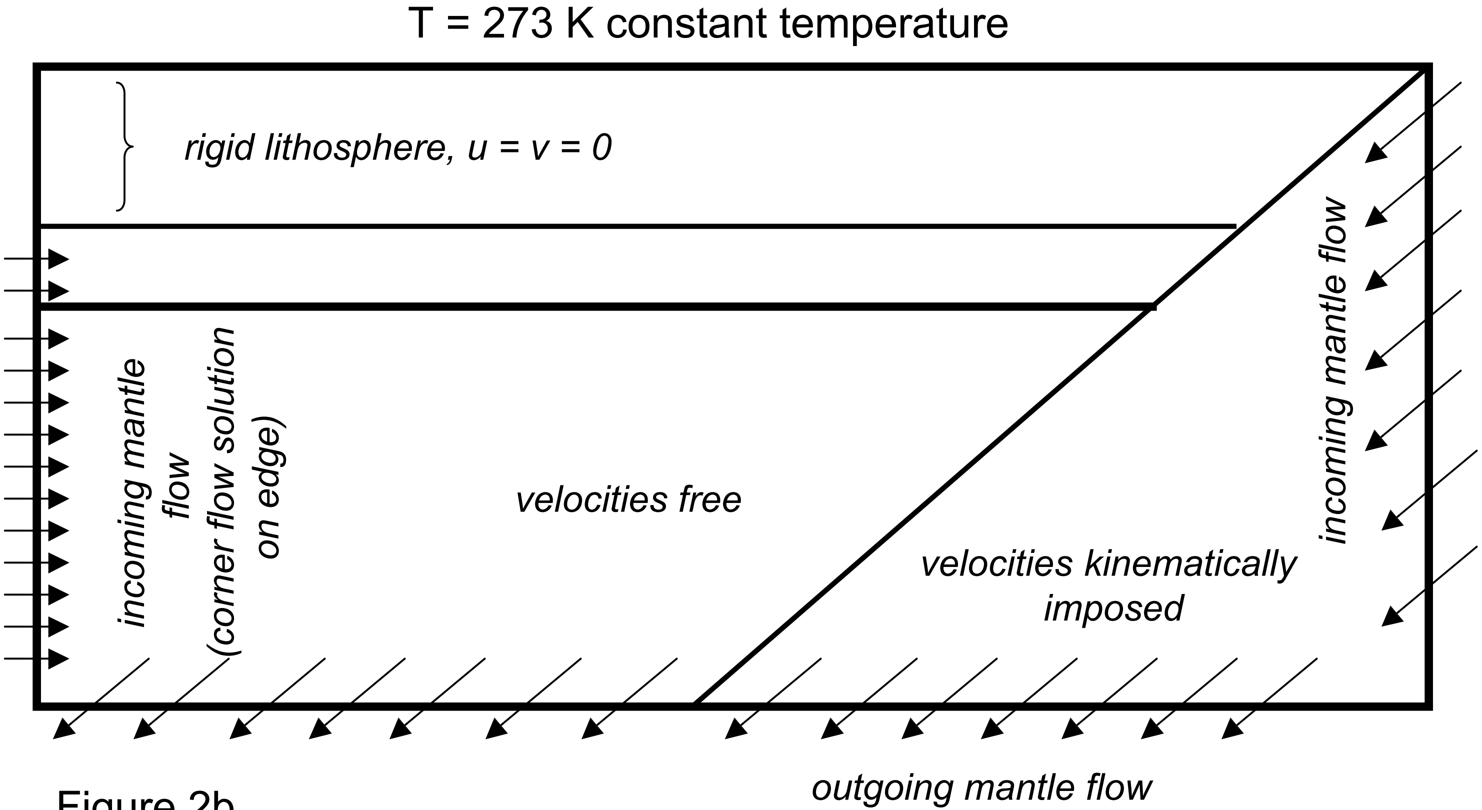
T = 273 K constant temperature
rigid lithosphere, u = v = 0
incoming mantle flow (corner flow solution on edge)
velocities free
velocities kinematically imposed
incoming mantle flow
outgoing mantle flow

Figure 2b.

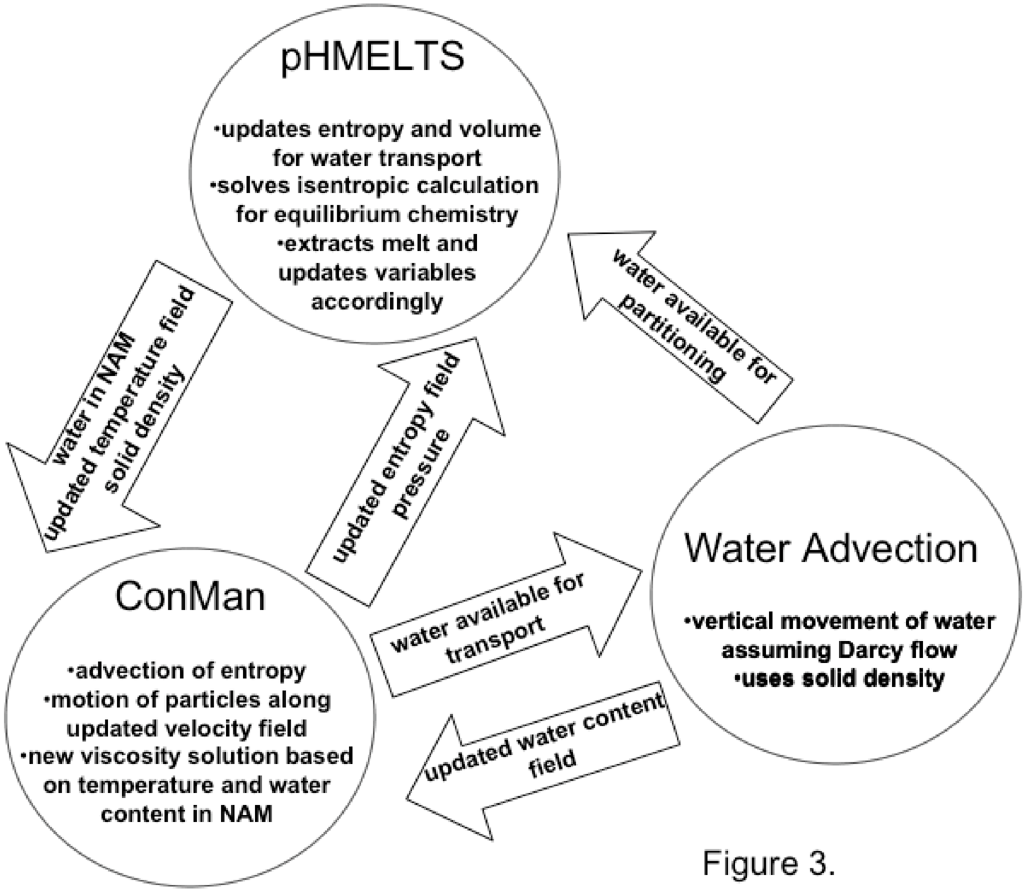
pHMELTS
•updates entropy and volume for water transport
•solves isentropic calculation for equilibrium chemistry
•extracts melt and updates variables accordingly
water in NAM
updated temperature field
solid density
updated entropy field
pressure
water available for partitioning
ConMan
•advection of entropy
•motion of particles along updated velocity field
•new viscosity solution based on temperature and water content in NAM
water available for transport
Water Advection
•vertical movement of water assuming Darcy flow
•uses solid density
updated water content field

Figure 3.

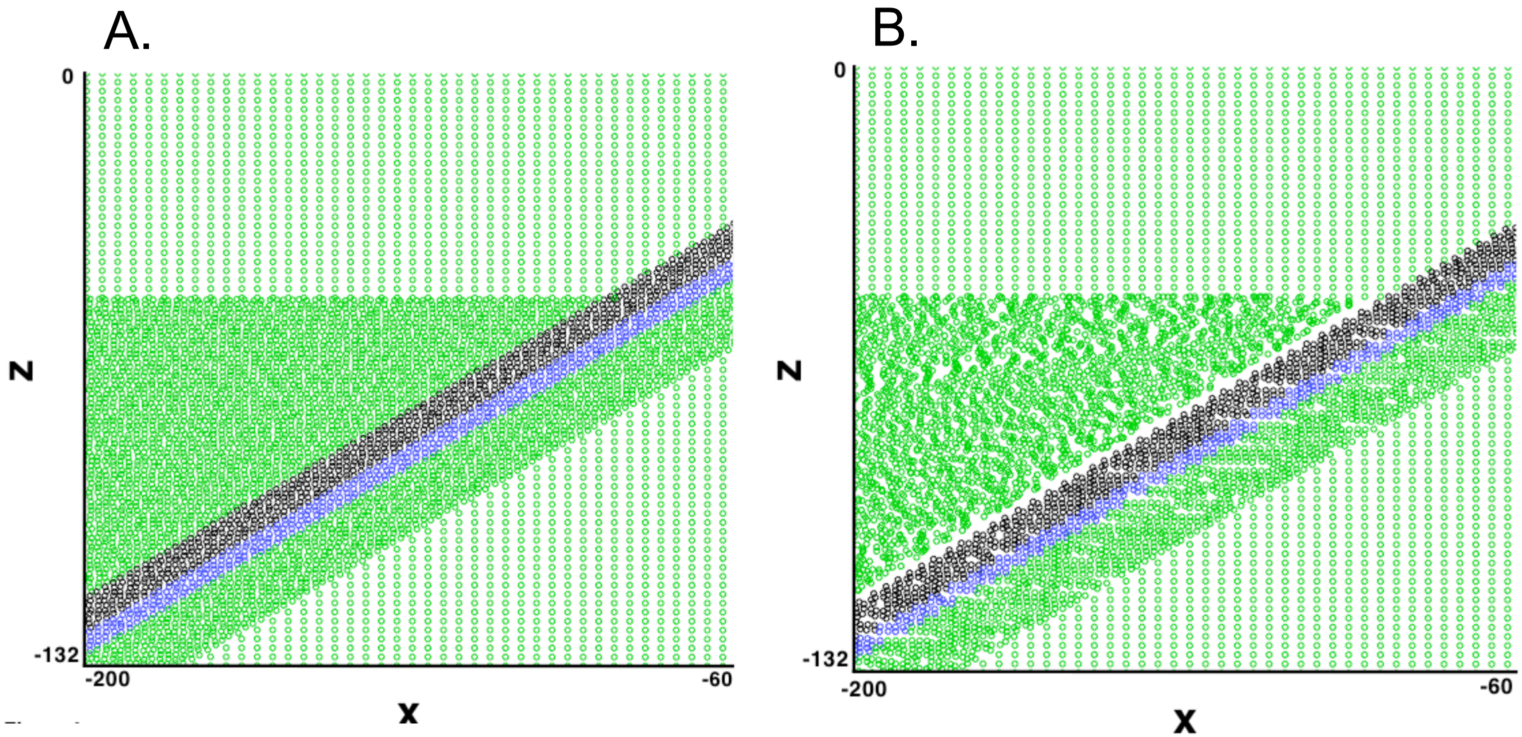

Figure 4.

Figure 5.

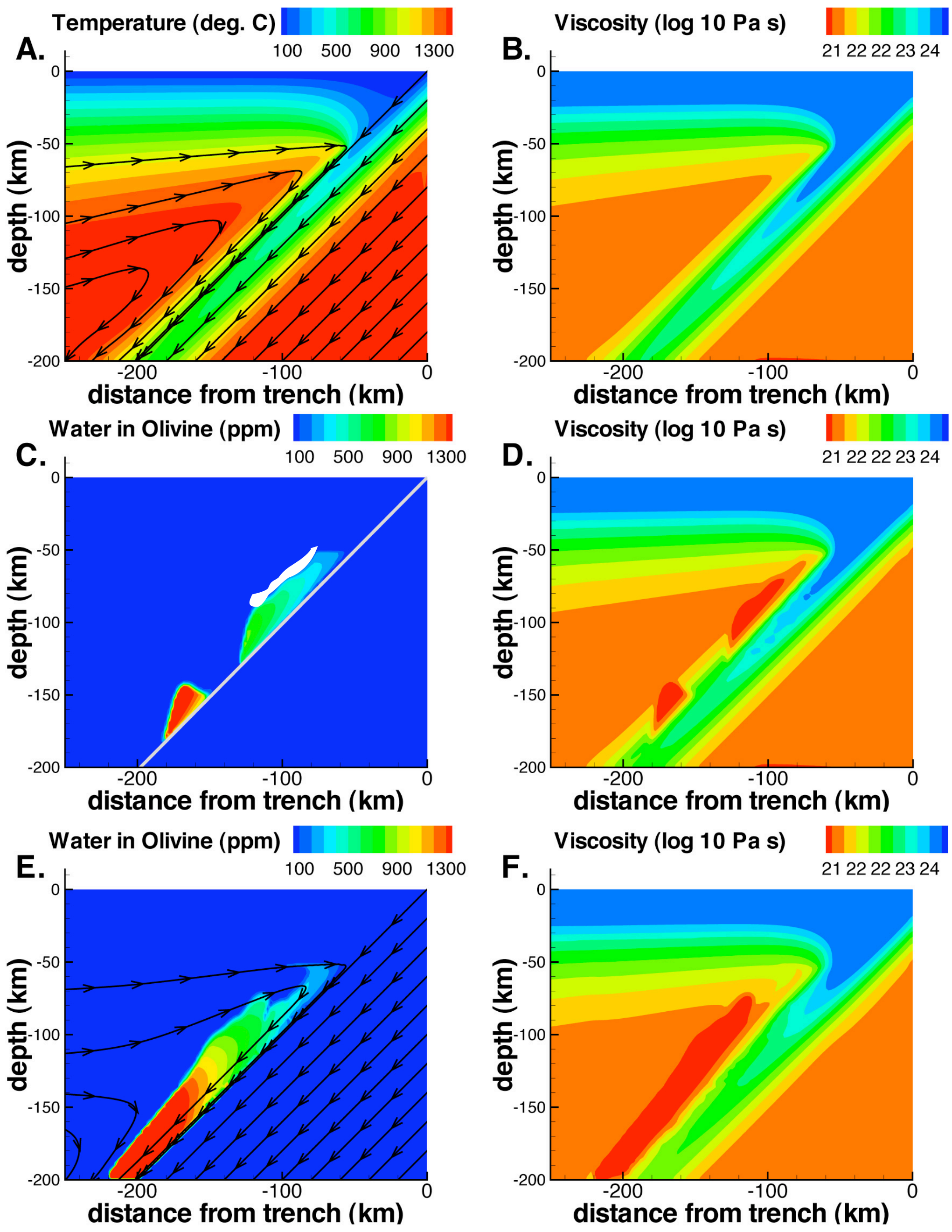
Temperature (deg. C)
100 500 900 1300
A.
Viscosity (log 10 Pa s)
21 22 22 23 24
B.
Water in Olivine (ppm)
100 500 900 1300
C.
Viscosity (log 10 Pa s)
21 22 22 23 24
D.
Water in Olivine (ppm)
100 500 900 1300
E.
Viscosity (log 10 Pa s)
21 22 22 23 24
F.
depth (km)
0
-50
-100
-150
-200
distance from trench (km)
-200
-100
0

Figure 6.

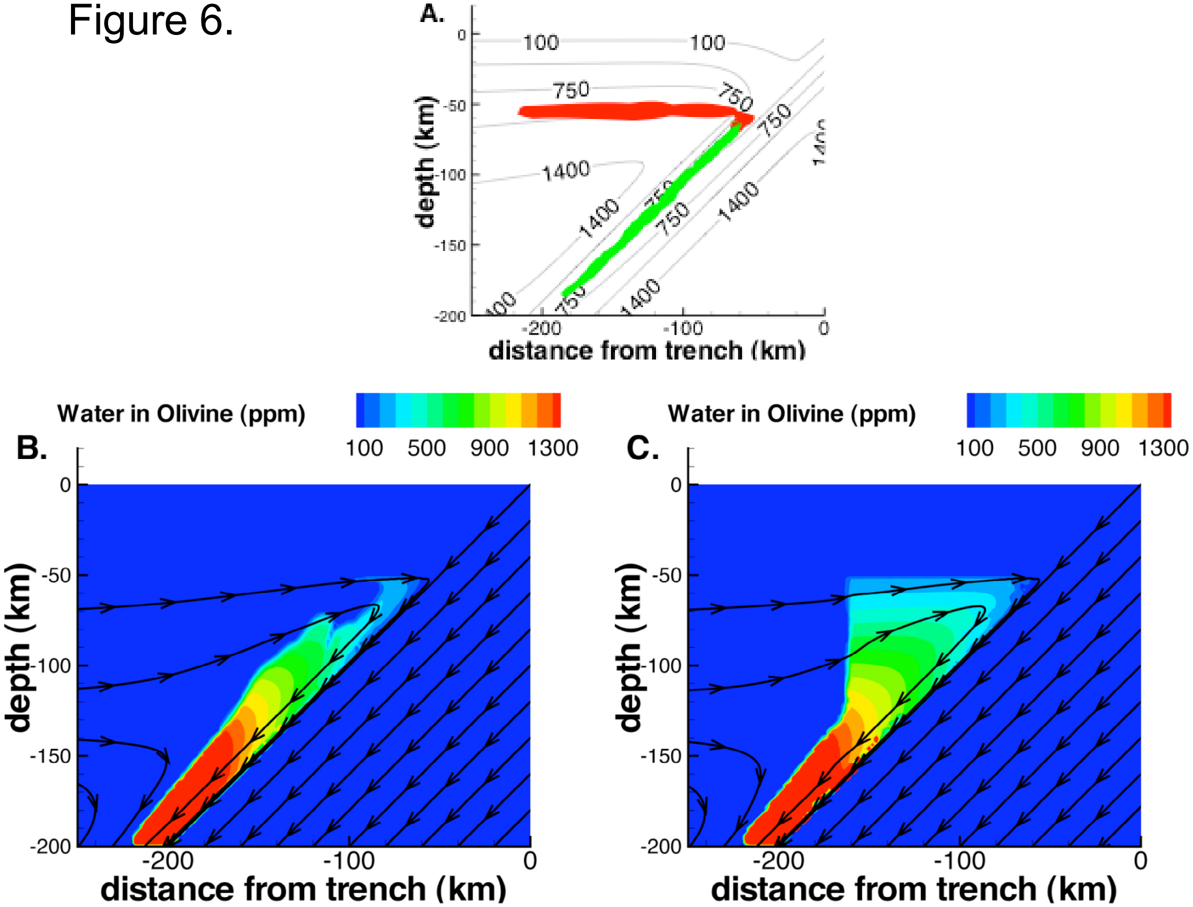
A.
depth (km)
0
-50
-100
-150
-200
distance from trench (km)
-200
-100
0
100
750
1400
B.
C.
Water in Olivine (ppm)
100
500
900
1300
depth (km)
0
-50
-100
-150
-200
distance from trench (km)
-200
-100
0

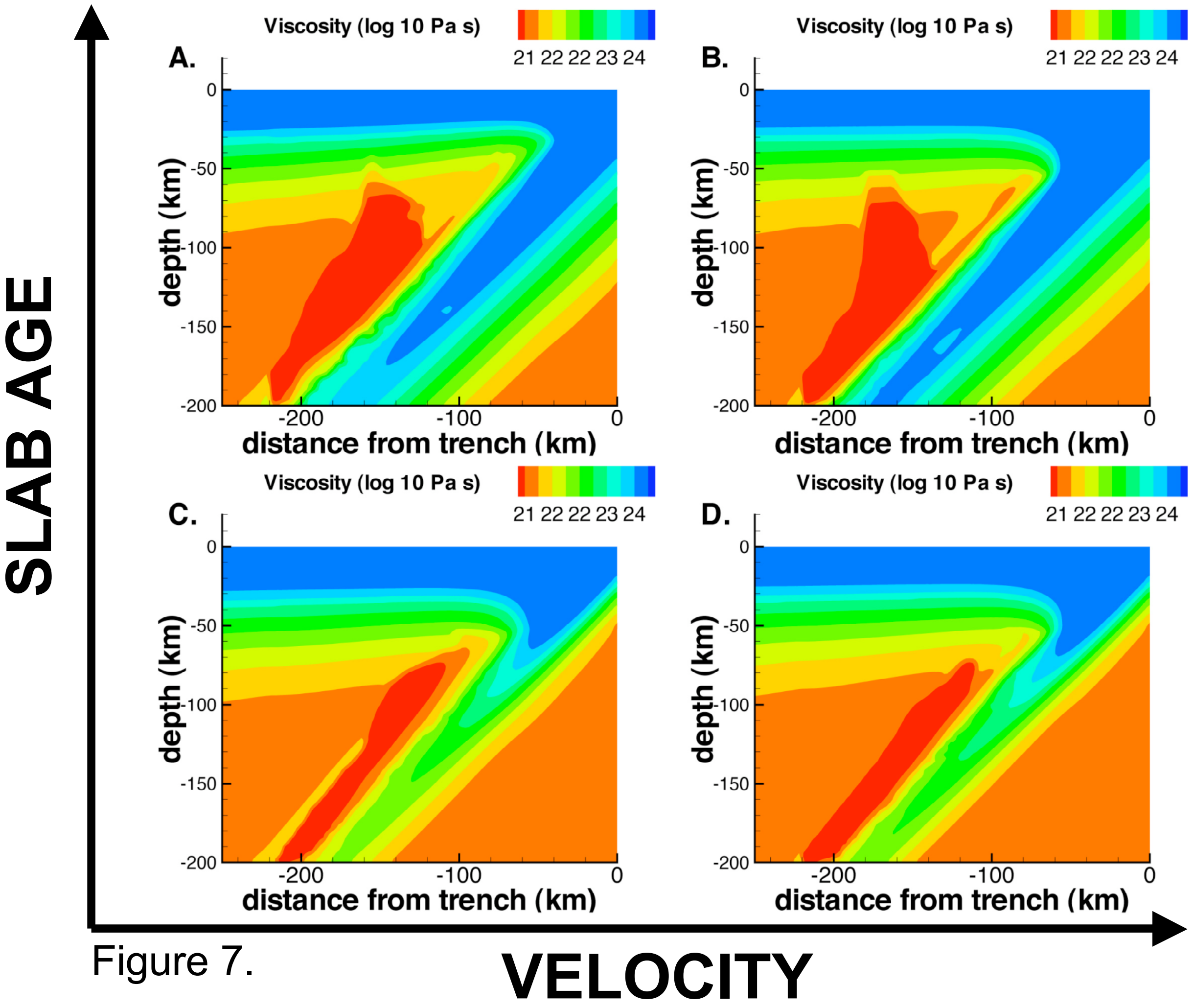
SLAB AGE
VELOCITY
A.
B.
C.
D.
Viscosity (log 10 Pa s)
21 22 22 23 24
depth (km)
0
-50
-100
-150
-200
distance from trench (km)
-200
-100
0

Figure 7.

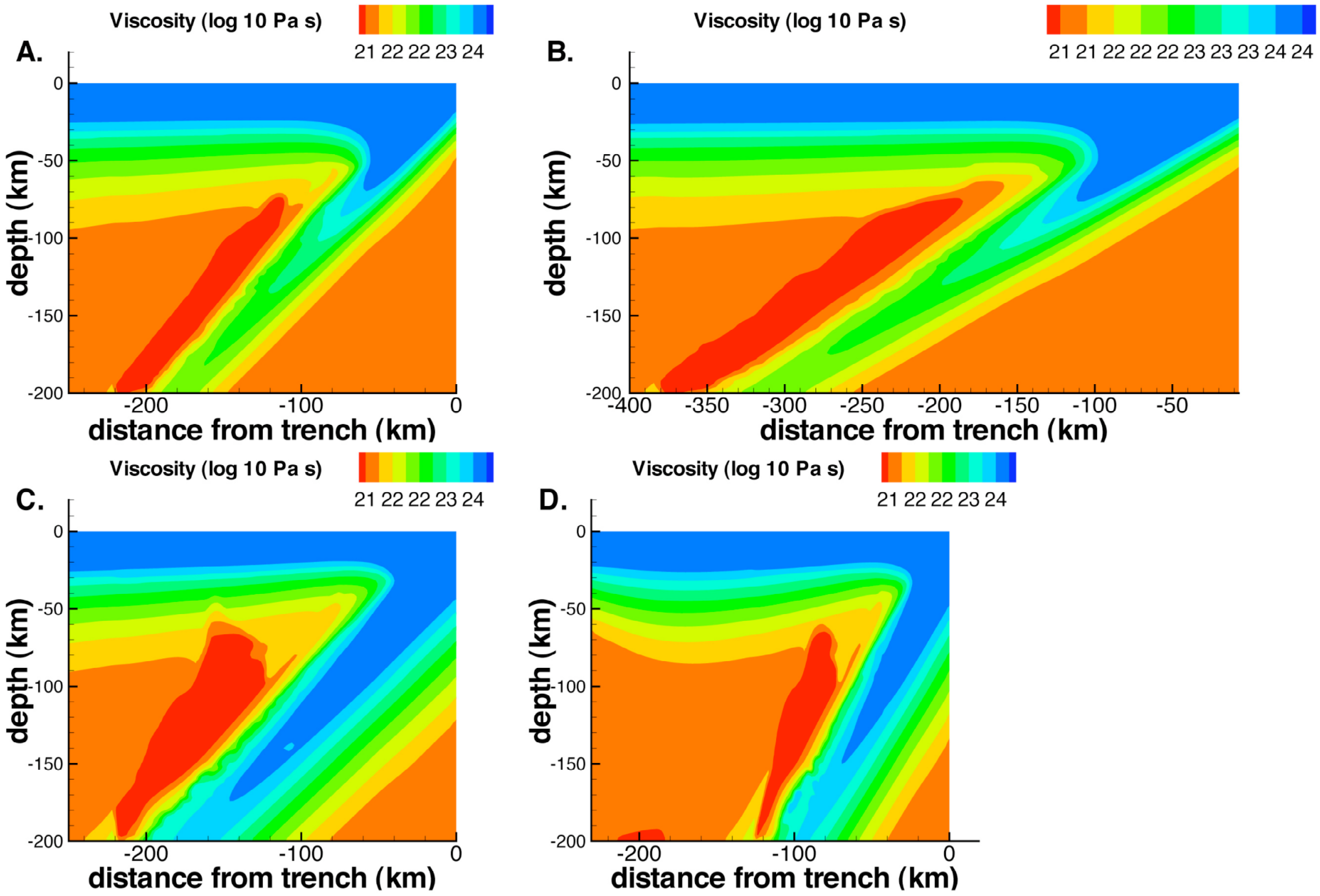
A.
Viscosity (log 10 Pa s)
21 22 22 23 24
0
-50
-100
-150
-200
depth (km)
-200
-100
0
distance from trench (km)
B.
Viscosity (log 10 Pa s)
21 21 22 22 22 23 23 23 24 24
0
-50
-100
-150
-200
depth (km)
-400
-350
-300
-250
-200
-150
-100
-50
distance from trench (km)
C.
Viscosity (log 10 Pa s)
21 22 22 23 24
0
-50
-100
-150
-200
depth (km)
-200
-100
0
distance from trench (km)
D.
Viscosity (log 10 Pa s)
21 22 22 23 24
0
-50
-100
-150
-200
depth (km)
-200
-100
0
distance from trench (km)

Figure 8.

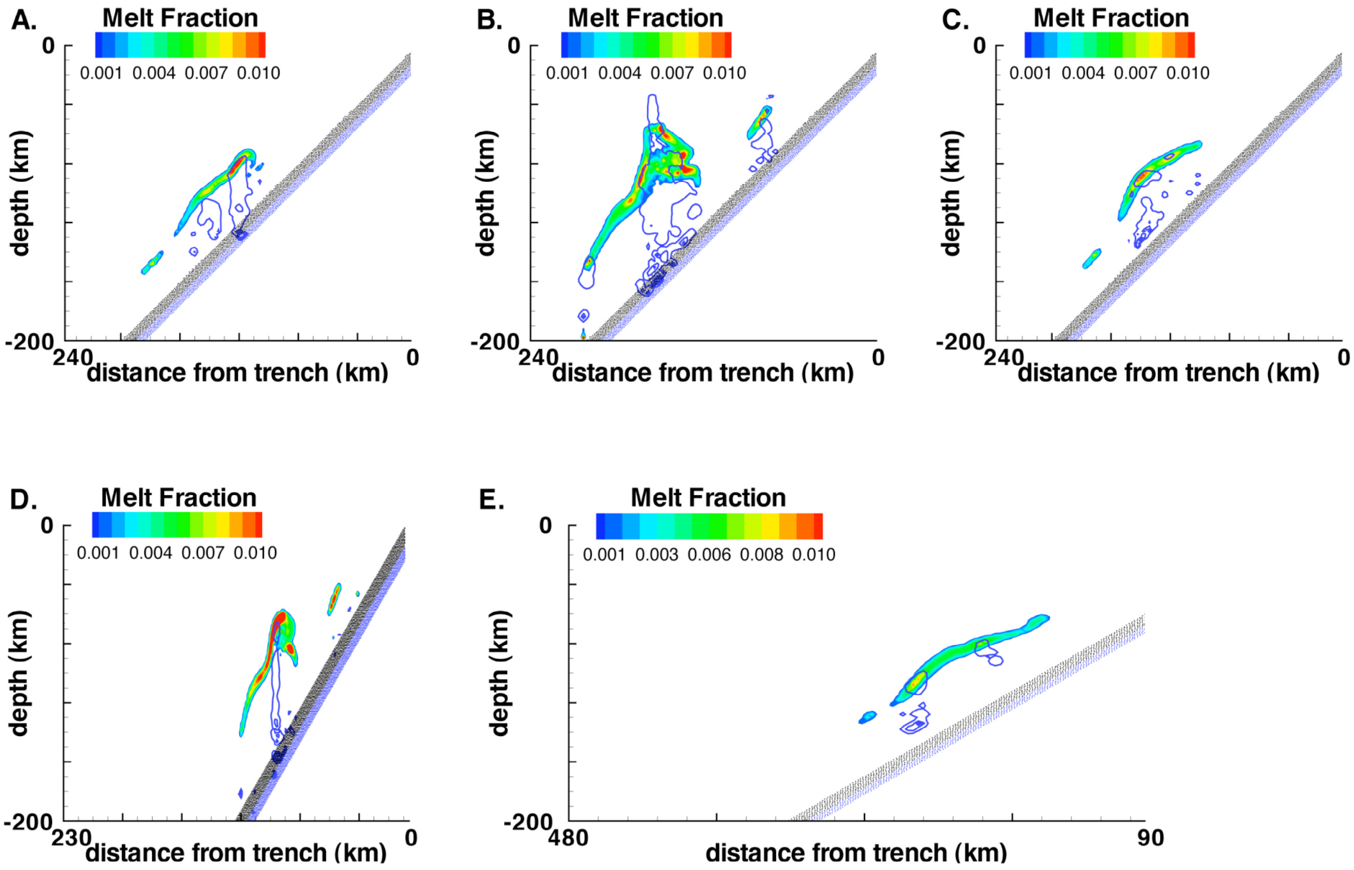
A.
Melt Fraction
0.001 0.004 0.007 0.010
0
-200
depth (km)
240
0
distance from trench (km)
B.
Melt Fraction
0.001 0.004 0.007 0.010
0
-200
depth (km)
240
0
distance from trench (km)
C.
Melt Fraction
0.001 0.004 0.007 0.010
0
-200
depth (km)
240
0
distance from trench (km)
D.
Melt Fraction
0.001 0.004 0.007 0.010
0
-200
depth (km)
230
0
distance from trench (km)
E.
Melt Fraction
0.001 0.003 0.006 0.008 0.010
0
-200
depth (km)
480
90
distance from trench (km)

Figure 9.

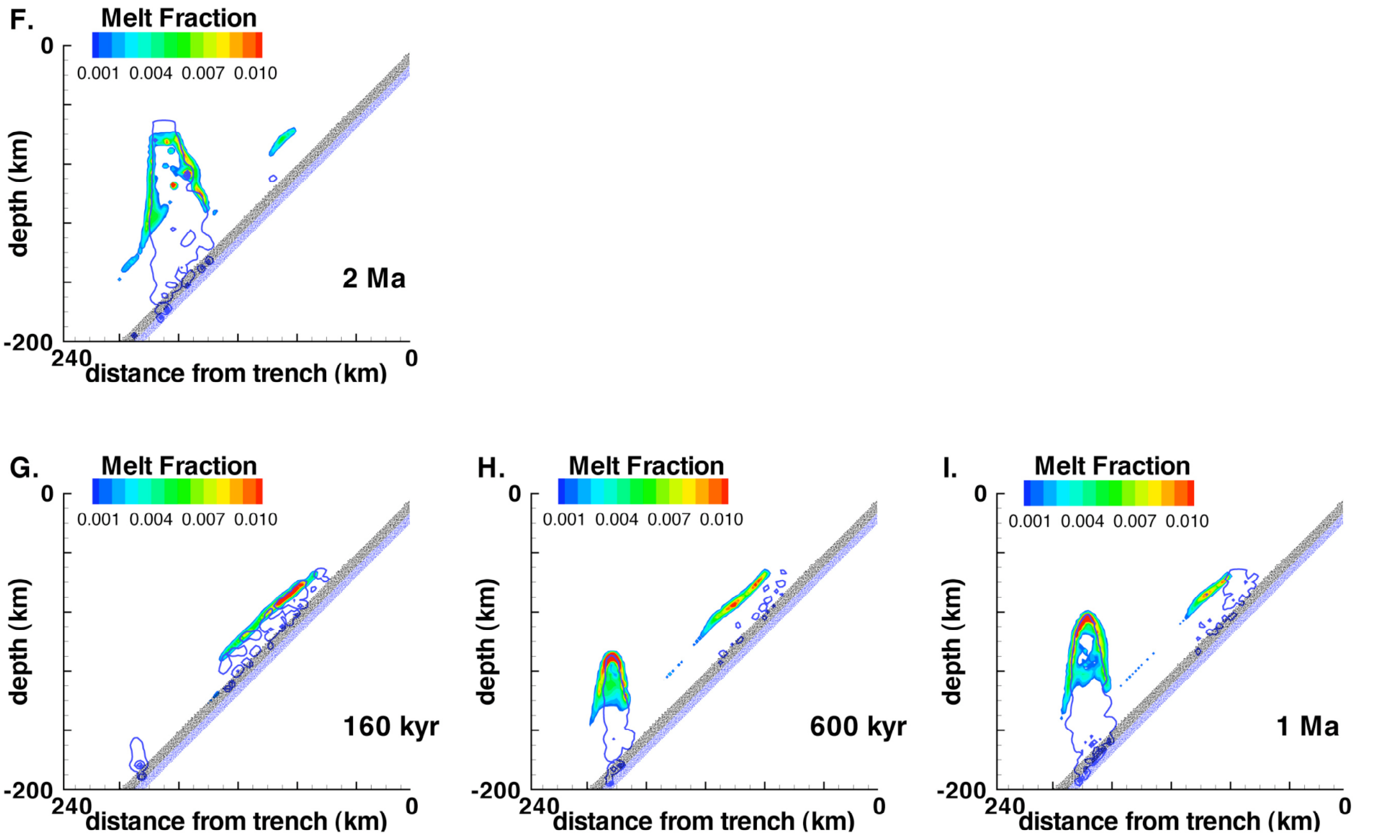
F.
Melt Fraction
0.001 0.004 0.007 0.010
0
-200
depth (km)
240
distance from trench (km)
0
2 Ma
G.
Melt Fraction
0.001 0.004 0.007 0.010
0
-200
depth (km)
240
distance from trench (km)
0
160 kyr
H.
Melt Fraction
0.001 0.004 0.007 0.010
0
-200
depth (km)
240
distance from trench (km)
0
600 kyr
I.
Melt Fraction
0.001 0.004 0.007 0.010
0
-200
depth (km)
240
distance from trench (km)
0
1 Ma

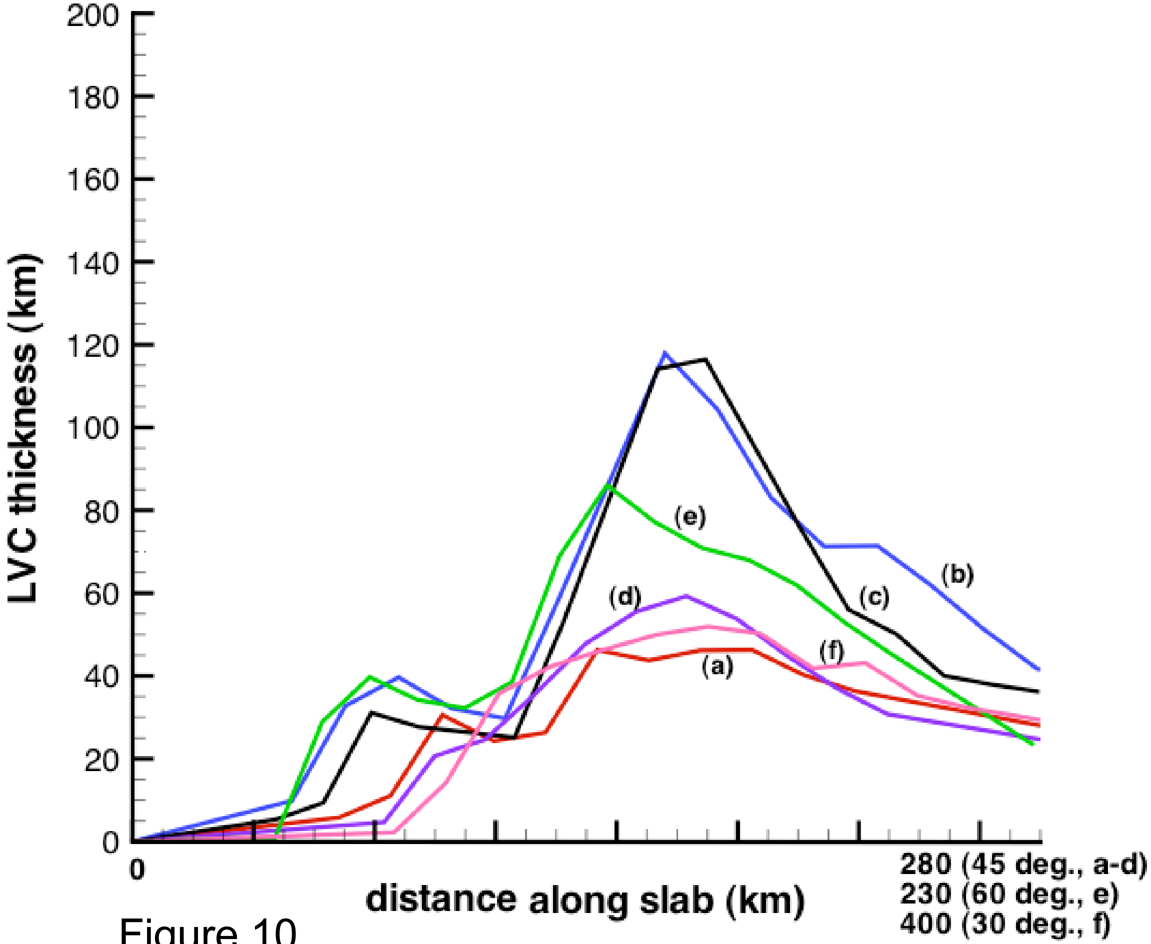
LVC thickness (km)
200
180
160
140
120
100
80
60
40
20
0
0
distance along slab (km)
280 (45 deg., a-d)
230 (60 deg., e)
400 (30 deg., f)
(a)
(b)
(c)
(d)
(e)
(f)

Figure 10.

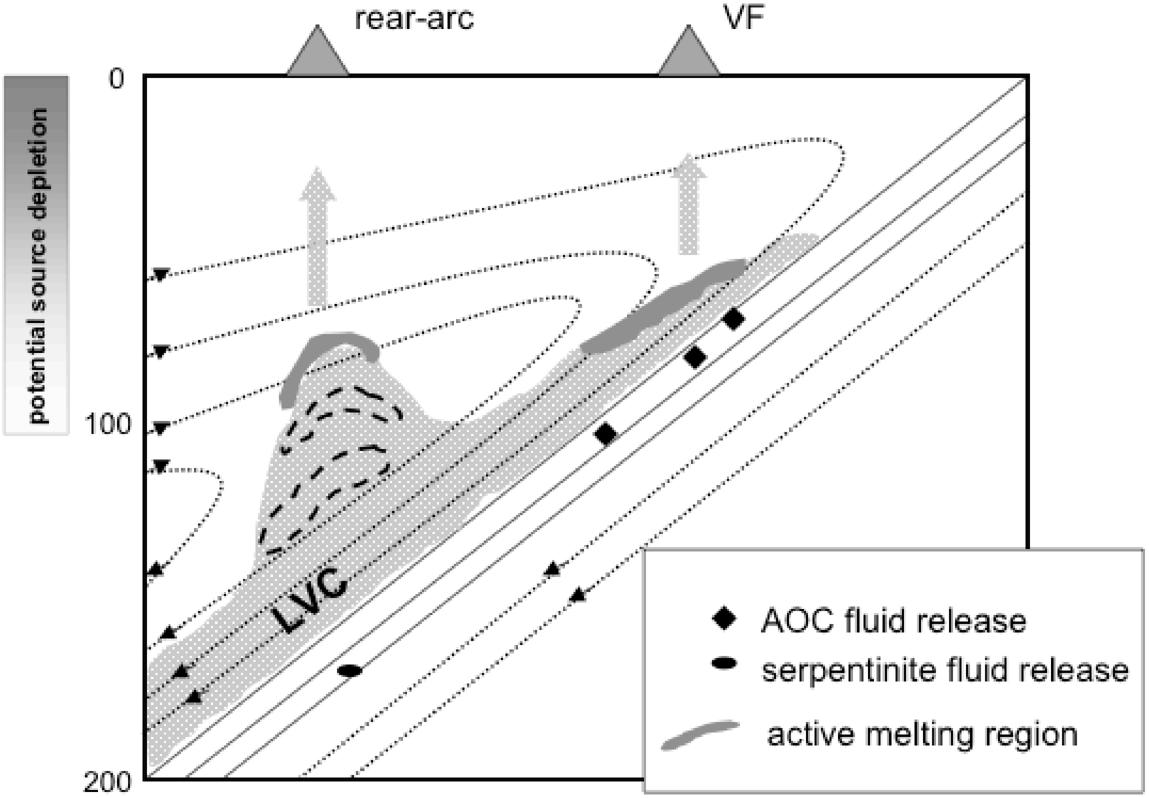
rear-arc
VF
potential source depletion
0
100
200
LVC
AOC fluid release
serpentinite fluid release
active melting region

Figure 11.

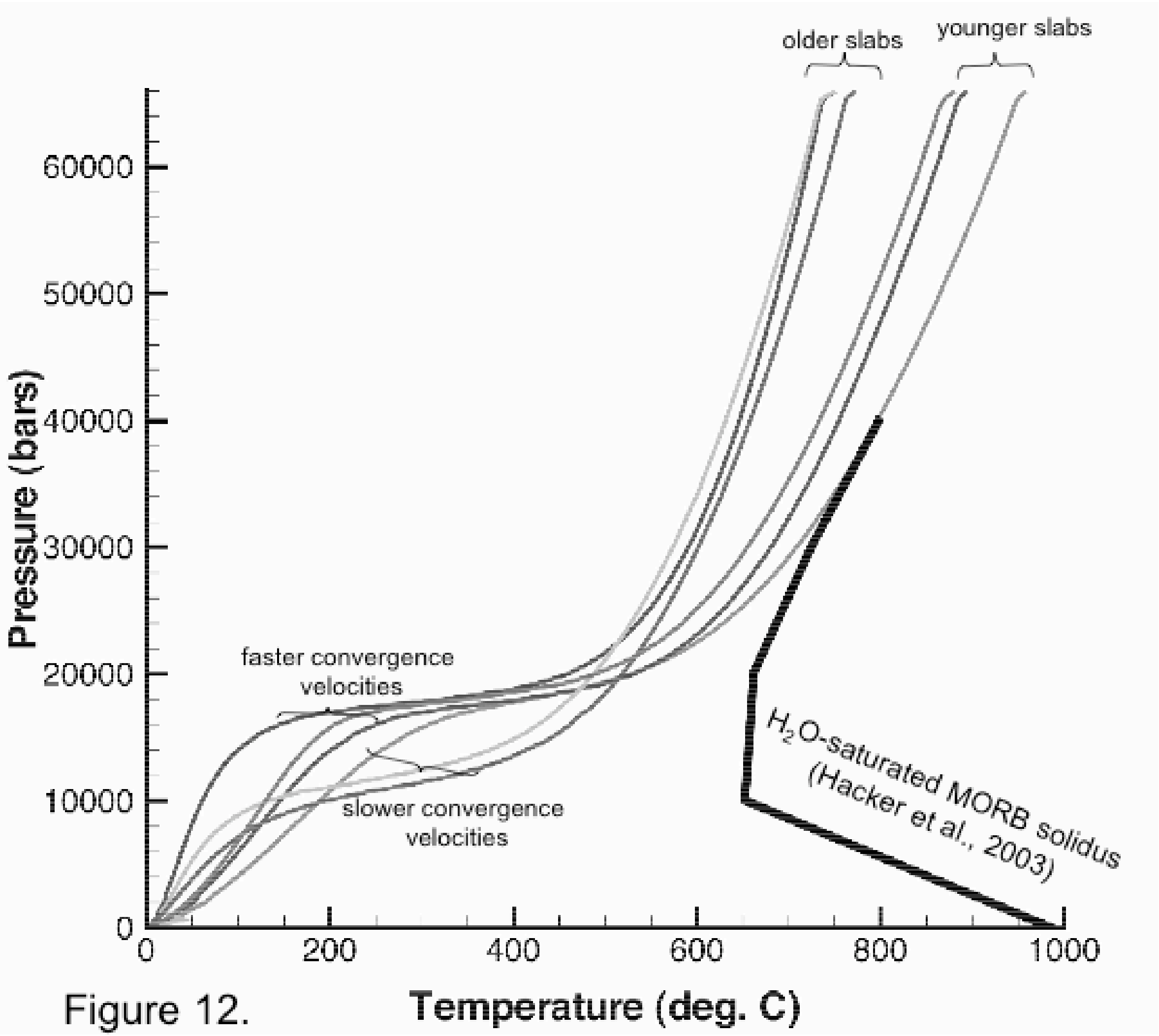
older slabs
younger slabs
Pressure (bars)
60000
50000
40000
30000
20000
10000
0
faster convergence velocities
slower convergence velocities
H_2O-saturated MORB solidus (Hacker et al., 2003)
0
200
400
600
800
1000
Temperature (deg. C)

Figure 12.

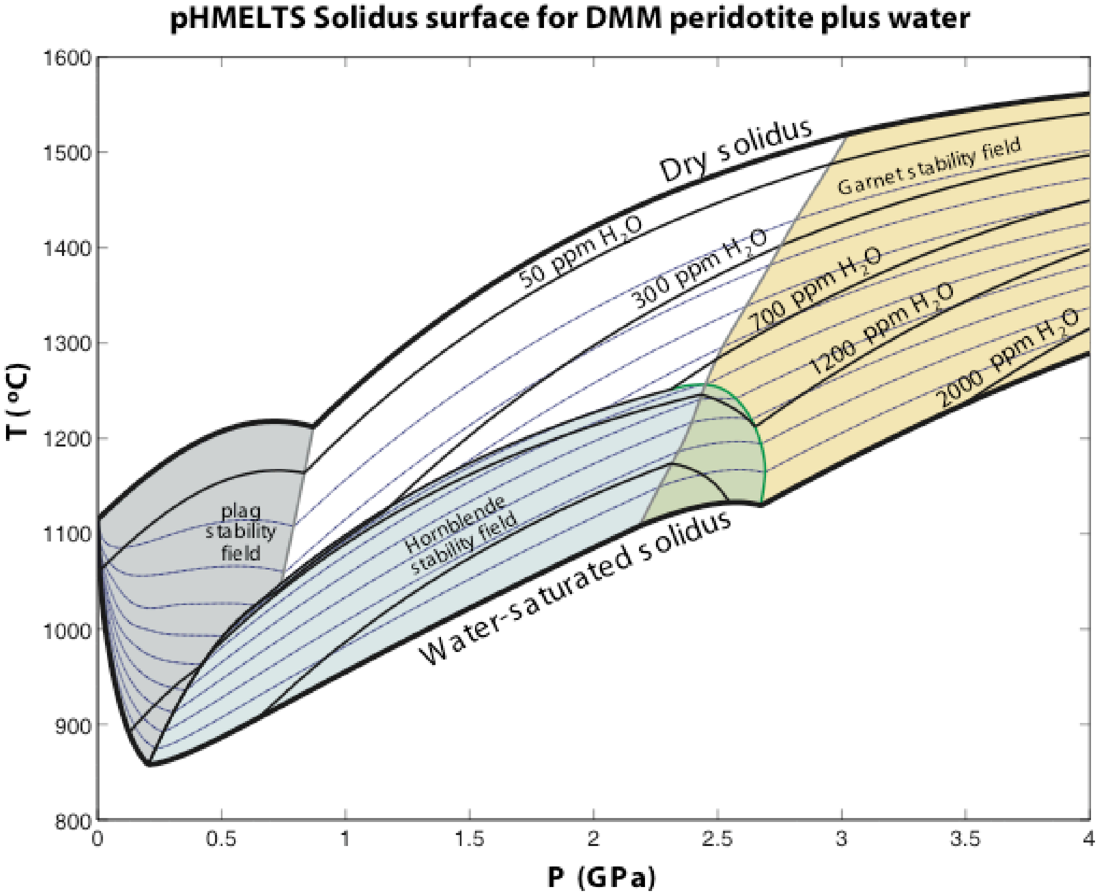

pHMELTS Solidus surface for DMM peridotite plus water

Figure 13.

Table 1: Model parameters held constant

parameter	*value*	*units*
T_0	1773	K
ΔT	1500	K
Ra	1.0E+04	*
η_0	1.0E+21	Pa s
R	8.31	J/K mol
XH2O_crit	100	ppm
Q	500	kJ/mol
n	2 [38]	*
C	1.2E+04 [38]	*
η_W	1.0E-03 [84]	Pa s
d_m	1.0E-04	m
φ	0.03 [38]	*
κ	1.0E-06	m^2/s
α	2.5E-05	K^{-1}
g	10.0	m/s^2
MINF	0.005	*
adiabatic gradient	0.7	ºC/km

** indicates non-dimensional quantity*
square brackets indicate references

Table 2a: pHMELTS starting composition

oxide	***initial value (weight percent)***
SiO_2	44.80
TiO_2	0.13
Al_2O_3	3.99
Fe_2O_3	0.41
Cr_2O_3	0.57
FeO	7.83
MgO	38.81
CaO	3.18
Na_2O	0.28
tracer	***initial value (ppm)***
H_2O	110.00
K	60.00
Rb	0.05
Ba	0.56
Th	0.01
U	0.0032
Nb	0.15
Ta	0.01
La	0.19
Ce	0.55
Pb	0.02
Pr	0.11
Nd	0.58
Sr	7.66
Zr	5.08
Hf	0.16
Sm	0.24
Eu	0.10
Ti	716.30
Gd	0.36
Tb	0.07
Dy	0.51
Ho	0.12
Y	3.33
Er	0.35
Yb	0.37
Lu	0.06

Adapted from Workman and Hart [26]

Table 2b: Altered MORB starting composition

oxide	***initial value (weight percent)***
SiO_2	48.70
TiO_2	1.30
Al_2O_3	16.60
FeO*	9.60
MgO	7.10
CaO	13.70
Na_2O	2.20
K_2O	0.6

After Hacker et al. [25]

Table 3: A summary of subduction zone model parameters

approximate subduction region	Central Costa Rica	Southeastern Costa Rica	Northern Izu-Bonin	Northern Mariana	Additional Model 1	Additional Model 2	Additional Model 3
abbreviation	CCR	SCR	NIB	NMAR	ADD1	ADD2	NIB
latitude	~8-11° N	~8-11° N	~32° N	~23° N	N/A	N/A	N/A
longitude	~275-277° E	~276-278° E	~135-143° E	~143-145° E	N/A	N/A	N/A
rate of convergence (mm/yr)	87 [44]	90 [44]	50 [45]	47.5 [45]	87.00	50.00	50.00
slab dip (degrees)	45 [44]	30 [44]	45 [45]	60 [45]	45	45	45
slab thermal age (Ma)	18 [44]	15 [44]	135 [45]	165 [45]	135	18	135
rigid lithospheric thickness (km)	50 [44]	50 [44]	32 [81]	32 [81]	50	50	50
thermal lithospheric thickness (km)	88	88	66	66	88	88	88
dimensional grid resolution (z, x)	2.0 km, 2.0 km	2.0 km, 3.4641 km	2.0 km, 2.0 km	2.0 km, 1.1547 km	2.0 km, 2.0 km	2.0 km, 2.0 km	2.0 km, 2.0 km
dimensions of model domain (z, x)	200 km, 400 km	200 km, 692.8 km	200 km, 400 km	200 km, 230.9 km	200 km, 400 km	200 km, 400 km	200 km, 400 km

numbers in square brackets are references

Chapter III:

Fluid Source-based Modeling of Melt Initiation within the Subduction Zone Mantle Wedge: Implications for Geochemical Trends in Arc Lavas

Laura Baker Hebert and Paul Asimow

Abstract

This study supplements GyPSM-S modeling (Chapter 2) with a focus on the influences of slab fluid source lithology and fluid transport mechanisms on melt geochemistry, the implications of mantle source depletion related to fluid fluxing, and potential melt migration processes. Slab age and convergence velocity, which contribute to the slab thermal structure, are significant for the locations of dehydration reactions within the different lithological layers of the slab. The fluid source lithology determines the fluid flux and the fluid-mobile trace element input to the wedge. Through an investigation of changing fluid inputs based on changing subduction model parameters, there is a progression of geochemical characteristics described in studies of cross-arc and along-arc lavas that can be duplicated assuming (i) limited fluid-rock interaction within the mantle wedge and (ii) melt migration preserves the spatial distinction among melts initiated in different areas of the wedge. Specifically, volcanic front lavas have significant contributions from shallower slab fluid sources, and rear-arc lavas have significant contributions from deeper slab fluid sources. Evidence for limited fluid-rock interaction could imply either a rapid fluid transport mechanism or a fluid-dominated trace element budget within the low-viscosity channel (LVC). Although we do not explicitly include a back-arc in these models, interpretations of the results lead to several potential mechanisms to explain hydrous inputs to back-arc source regions.

Keywords: Costa Rica, Izu-Bonin, subduction, volcanic front, cross-arc trends, trace element, GyPSM-S

1. Introduction

Melt initiation within the mantle at plate boundaries is an important problem that has been addressed through analyses of lavas and xenoliths collected at the surface, interpretations of seismic imaging results, and experimental investigations [1-5]. Spreading centers at divergent boundaries represent the most accessible environment, due to well-established estimates of N-MORB-source mantle composition and decompression pathways, a lack of significant crustal contamination, and agreement amongst experimental results [6, 7]. At convergent boundaries, the story is complicated by fluxing of the mantle by components derived from heterogeneous slab sources, the potential for significant crustal contamination, sources of initial and progressive mantle source depletion, and a more complex pressure and temperature structure.

Major element abundances in arc lavas are derived from partial melting of the wedge peridotite above the slab, but large-ion lithophile elements (LILE) and other incompatible elements can be traced to slab-derived influences such as sediment melting [8, 9], dehydration of the altered oceanic crust (AOC) [10], and/or dehydration of subducting serpentinized lithosphere [11, 12]. In general, convergent margins involve lavas that are enriched in incompatible fluid-mobile elements (Rb, Ba, U, K, Sr, Pb) and depleted in incompatible high field strength elements (HFSE) (Nb, Zr, Ta) and heavy rare-earth elements (HREE) [13-15; others], suggesting a significant connection between fluids, mantle source bulk composition, and melt production. However, interpretation of the geochemistry can be somewhat obscured by the complexity of slab sources.

The depth interval and the magnitude of fluid release from the subducting plate are a function of parameters such as slab age and convergence velocity (Chapter 2) as well as the composition of the descending plate [16]. Specifically, the different lithological fluid sources emphasized by different subduction parameters allow for changing fluid addition patterns (mass and fluid-mobile trace element chemistry) along the length of the subducting plate through the upper mantle [16, 17]. These patterns may directly influence the composition and mass fraction of fluxed melts within the wedge, leading to regional variations in arc lava geochemistry. Variations can be compared among different subduction systems, or through cross-arc and along-arc trends within the same subduction system. For example, relative contributions from heterogeneous slab fluid sources can be manifested in diverse chemical characteristics of lavas derived from different depths above the seismic Wadati-Benioff zone (WBZ) [15, 18, 19].

Interpretations of arc lava geochemistry include the potential for re-melting of previously depleted sources as an explanation for significant HFSE and HREE depletions. Sequential melting within the system, such as at a back-arc spreading center, has been invoked as a cause; however, some systems, such as the northern Izu-Bonin subduction zone, do not involve current back-arc spreading and still maintain such depletions [33]. It has been proposed that hydrous fluid addition process alone may be somehow responsible for these trends [68].

GyPSM-S (**G**eod**y**namic and **P**etrological **S**ynthesis **M**odel for **S**ubduction, Chapter 2) involves the dehydration of a subducting slab and the impact of fluid release on the shallow (< 200 km) mantle wedge, assuming an equilibrium-based interaction. The primary model observation is the development of a water-saturated low-viscosity channel (LVC), which arises due to the partitioning of water into nominally-anhydrous minerals

(NAM), the thermal structure of the mantle wedge, and the down-dip advection of near-slab material (Chapter 2). Water in NAM has two consequences: reduction of the peridotite solidus [5, 20], and reduction of solid matrix viscosity [21]. The thickness of the LVC, which can reach tens of kilometers, separates the slab-wedge interface from the water-saturated peridotite solidus. Similar displacements between the slab surface and the zone of active melting have been imaged seismically, and are well established by previous models [16, 17, 22]. In GyPSM-S, the locations of melting are strongly determined by the positions of fluid release from dehydration reactions within hydrated slab layers, given a vertical buoyancy-driven fluid migration path.

The use of the pHMELTS algorithm [20, 27, 28] in the structure of GyPSM-S allows for major and trace element analyses of melts and residues and includes a treatment of water (H_2O) as a trace element. However, analyses are somewhat limited in that pHMELTS cannot yet account for fluid-mobile trace elements carried with the hydrous species from the slab. Additionally, specific tracing of fluids as direct influences on melt composition is complicated by the slight smearing within GyPSM-S due to iterative particle-to-node interpolation steps, mostly observed in water mass and leading to lower instantaneous melt fractions (Chapter 2). In order to demonstrate the applicability of GyPSM-S results to actual datasets, a supplemental modeling approach is required to account for the addition of these important fluid-mobile tracers and to make detailed inferences as to the geochemistry of arc lavas with respect to slab fluid sources and as a function of changing subduction parameters.

Melt migration processes are neglected in the current formulation of GyPSM-S, which assumes a near-fractional melt extraction scheme and a lack of interaction of extracted melt with the solid matrix. However, theoretical treatment of the extracted melts through the established pressure-temperature structure of the wedge is possible. Past studies have suggested mechanisms by which melt generated within the mantle at plate boundaries can transit to the surface. Within the context of convergent boundaries, Spiegelman and McKenzie [23] describe porous flow driven by pressure gradients as a mechanism of melt focusing towards the wedge corner, Hall and Kincaid [24] invoke diapirism of melts towards the overlying lithosphere, and Furukawa [25] proposes fracture propagation as a mechanism of melt extraction. Kelemen et al. [26, and references therein] additionally discuss the role of dissolution channels in melt migration at mid-ocean ridges, resulting in a combination of rapid, chemically-isolated melt flow and porous reactive flow. The processes of melt migration can be very significant with regard to understanding trends observed within subduction systems, considering the locations of melt initiation within the wedge and geochemistry of the inital melts as strongly dependent on the identity of slab-derived fluid sources (Chapter 2) [2].

This study represents an extension of a fully-integrated geochemical and geodynamical approach (GyPSM-S) to specific mass tracing. A fluid source-based approach is employed to determine how slab dehydration changes with changing subduction model parameters and how this influences the major and trace element chemistry of fluid-fluxed melts within the wedge. In addition to a fully-equilibrated pathway of fluid migration, we also consider the consequences of less-interactive fluid paths through the near-slab wedge. Cross-arc and along-arc variations in regional geochemical datasets are compared to the model results, with an emphasis on changing slab fluid-source lithology. Additionally, we offer a discussion of simple melt migration scenarios which may preserve relative heterogeneities in melts initiated at different locations within the wedge.

2. Model Parameters and Regional Significance

Results from GyPSM-S modeling indicate that the first-order control on the locations of fluid release from the slab (and therefore, the locations of melt production in the mantle wedge) is the slab thermal structure, primarily defined by slab age and secondarily by convergence velocity. More mature slabs have significantly different patterns of fluid release than younger slabs (Chapter 2). While examining the dehydration structures produced by GyPSM-S over a range of subduction parameter space, we chose to focus this study on two systems with different slab thermal structures to more closely examine the potential implications of the different fluid release patterns for melt production and chemistry.

The Northern Izu-Bonin intra-oceanic subduction system (NIB, Table 3) involves the mature Pacific plate (135 Ma) subducting beneath the Philippine Sea plate at a relatively moderate convergence velocity (~5.0 cm/yr) and a moderate dip angle of 45º [29]. The arc itself includes a volcanic front, extensional zones, and seamount chains towards the rear-arc trending into the Shikoku Basin [19]. The history of the arc involves a multi-stage process [30-33]. There are two periods of arc formation associated with the IBM system: Eocene-Oligocene volcanism and mid-Miocene to present [31]. A hiatus of around 7.5 Ma between these periods [34] involved rifting associated with the Shikoku Basin [31]. The end of the Oligocene marks the end of boninitic lava appearance within the arc record, and the completion of the sub-arc mantle "replacement" stage from an ultra-depleted mantle to depleted Indian MORB-source mantle [31]. With resumption of volcanic activity in the mid-Miocene, a quasi-steady-state flow was established within the wedge characterized by (i) continuous advection of Indian MORB-source mantle from the rear-arc that is (ii) continuously fluxed by hydrous slab components, leading to (iii) constancy within temporal trends of major element oxides [31]. Straub [31] therefore suggests that melt formation processes and the source composition are relatively constant in this system and that the thin (~7-22 km) crust does not seem to have a significant impact on lava chemistry. The volcanic front (VF) of the Izu-Bonin arc is one of the most depleted of all volcanic arcs, and there exist significant cross-arc variations in the geochemistry of erupted lavas, including ε_{Nd}, Ba/Nb, U/Nb, and $^{87}Sr/^{86}Sr$ [19]. Additionally, there is a lack of evidence of slab-derived sediment melting influence to the shallow (< 175 km depth) wedge [19, 35] which emphasizes the role of fluids in the production and geochemistry of melts.

The central Costa Rican subduction system (CCR, Table 3), on the southeastern end of the Central American arc, involves the subduction of the relatively young Cocos plate beneath the Caribbean plate along the Middle America Trench at moderately fast convergence velocity (~9.0 cm/yr) and a moderate dip angle of 45° [36]. The Central American system involves systematic along-arc variations in many geochemical indicators such as $\delta^{18}O$ [37], U/Th, Ba/La, and $Na_{6.0}$. These variations have been linked to geophysical parameters such as slab dip, crustal thickness, and slab composition that vary along arc strike [16, 38-41]. Specifically, it has been concluded that the concentration of trace elements contributed by the slab-derived fluids reaches a minimum beneath the Costa

Rican segment [39, 42, 43] and that the degree of melting is relatively lower beneath Costa Rica [39]. Rupke et al. [16] speculate on the basis of geodynamic modeling that there is a lack of a strong serpentinite-derived fluid release beneath Costa Rica, contributing to the along-arc geochemical differences.

3. Method

3.1. Initial GyPSM-S calculation of the shallow hydrated wedge

We used GyPSM-S (see Chapter 2 for full model description) to describe the thermal structure and locations of slab dehydration for subduction model parameters (slab age, convergence velocity, slab dip angle) approximating six regional systems, respectively (Table 3). Results for each model were taken from a GyPSM-S iteration representing ~160-280 kyr of subduction, upon water-saturation of the LVC and initiation of active melting regions, to avoid potential errors due to nodal smearing. The initial fluid transient is avoided, and the locations of fluid release from the slab have been shown not to change appreciably over full model run durations (two to five million years).

3.2. Construction of calculation columns

In order to address the important issue of fluid-mobile tracers that are carried with the hydrous fluid phase and are neglected in the current formulation of pHMELTS, as well as to achieve a more detailed examination of the melting region and the impact of the fluid migration scheme without the consequences of iterative particle-to-node interpolation steps, we add a supplemental modeling step of one-dimensional calculation columns through the mantle wedge for the NIB and CCR models (Fig. 1). Columns originate at the slab-mantle interface immediately above the locations of fluid release, rise through the mantle wedge thermal field, and end where the activity of water in the peridotite drops below unity. If the result of a calculation is water-saturation, the excess fluid moves on to the next step (pressure-temperature point). The endpoint corresponds to water under-saturation due to preferential partitioning of water into the melt phase. The columns mimic the dimensional set-up of the GyPSM-S model in that steps between the vertically rising fluid and the wedge peridotite occur in intervals of 2 km along the vertical axis and the pressure and temperature of these equilibration steps are mapped directly from GyPSM-S output on the Eulerian mesh.

At the start of the model, the steps along the column have the same bulk composition [44] (Table 1). Prior source depletion due to melting at a back-arc or along a decompression trajectory associated with the solid flow field, is neglected. The columns begin water-saturated up to the respective solidus, which allows the fluid to arrive at the location of melting with negligible loss (loss may be due to stabilization of additional water in NAM as the material advects from lower to higher pressures, due to the increasing solubility of water in NAM with pressure). The first calculation involves the column associated with the lowest pressure fluid release. If melting is present, the bulk composition at that step along the column is then depleted. This depletion is carried along the flow field to the next column calculation, whereby the residues from the first column calculation become the starting compositions for the second column calculation and so on, assuming advection of the solid down slab-parallel trajectories (Fig. 1a). Calculations to test for melting are performed by individual isothermal, isobaric pHMELTS equilibrations using the adiabat_1ph user interface [28]. We do not account for changes to the overall GyPSM-S-calculated temperature structure due to hydration or melting within the columns.

We consider fluid migration through the near-slab wedge in two ways: (i) using a fundamental assumption that at each interval fluid is fully equilibrated with mantle material (similar to the GyPSM-S calculation) and (ii) incorporating an assumption that fluids do not equilibrate with the already hydrated peridotite at each step, but carry the original fluid-mobile trace element composition with them until they reach a point at which melting begins. The difference in these two schemes is manifested within the fluid-mobile trace elements only, and represents two end-member possibilities for fluid transport within the near-slab region. For the full-equilibration sequence, if the column calculation is not the initial (lowest-pressure), the fluid-modified trace element composition of the peridotite from the previous column is used as a starting point to equilibrate with the fluid moving along the current column. For the isolated fluid transport case, the fluid retains its original trace element composition (a function of slab source lithology and initial fluid mass release) until reaching a zone of potential melting. At this point, the fluid-mobile trace element composition is added to the bulk peridotite composition which is then equilibrated by pHMELTS. If a calculation results in a very low-degree melt and water-saturation, the excess fluid mass is moved to the next column, assuming that the fluid trace element composition is preserved, but the amount of water able to move has decreased.

3.3. Slab dehydration and fluid release

Within the context of GyPSM-S, compositionally-tagged Lagrangian particles within the slab carry lithological information and are the fluid sources in the model (Chapter 2). As the slab descends, the particles advect to higher pressures and temperatures, crossing univariant phase boundaries and dehydrating to produce a hydrous fluid, effectively acting as point sources. The dehydration reactions are controlled by the MORB and harzburgite phase diagrams of [45] (Fig. 2). We assume a hydration depth into the slab of 12 km, including 7 km of altered oceanic crust (AOC), and 5 km of fully-serpentinized mantle lithosphere. The serpentinization process is hypothesized to occur at the outer rise of subduction zones, where ocean water has the potential to penetrate down large normal faults into the mantle lithosphere, reacting with the lithospheric peridotite to produce hydrous phases such as antigorite and chrysotile [46]. Seismic surveys show the potential for hydration along lithospheric faults to up to 10 km depth [46], however, little is known about the average degree of serpentinization. We do not include sediments within this model, assuming that they dewater significantly by 50 km depth [16]. For the column models, we assume that dehydration of a particle within a slab element is representative of the total volume of that element such that the fluid mass released upon crossing a phase boundary (1.0 to 8.6 wt. % H_2O) represents the effective fluid mass released into the first volume of wedge peridotite at the slab-mantle interface (the start of the column calculation). This is a maximum fluid flux, compared to the values resulting from the GyPSM-S calculation, and results in a maximum melt fraction.

3.4. Trace element composition of migrating hydrous fluids (Table 2)

The missing part of the puzzle is the addition of fluid-mobile trace elements, as pHMELTS is sufficient for calculating melt/residue trace element partitioning (including H_2O). Forward modeling allows the generation of fluid-mobile trace element contributions from the AOC and the lithospheric serpentinite using published partition coefficients, initial concentrations, and the batch melting equation. Of course, the quality of the partition coefficient dataset limits the precision of the models, and the partition coefficients are assumed to remain constant for the respective bulk lithologies over a range of temperatures and pressures, and bulk compositions. We calculate the initial trace element content of the fluid for specific fluid-mobile tracers (Ba, Th, U, Pb, and Sr) based on equilibration of a mass of fluid (the release mass described above) with the slab source lithology using the following mass balance equation for each element:

$$\frac{C_{fluid}}{C_{initial}} = \frac{1}{D(1-F)+F} \quad , \tag{1}$$

where C_{fluid} is the concentration of a tracer in the fluid, $C_{initial}$ is the concentration of a tracer in the bulk starting material, D is the rock/fluid partition coefficient, and F is the fluid fraction expressed as a weight percent. We used rock/fluid partition coefficients for fluid in equilibrium with eclogite ($D^{eclogite/fluid}$) from Brenan et al. [47] and for fluid in equilibrium with serpentinite ($D^{serpentinite/fluid}$) from Tenthorey and Hermann [48]. The values for $D^{eclogite/fluid}$ were calculated assuming a 60:40 garnet:clinopyroxene assemblage. The source chemistry for eclogite is from the altered oceanic crust composition from McCulloch and Gamble [49]. The source chemistry for the serpentinite lithology is the serpentinized peridotite ETF1 (antigorite + olivine + diopside + chlorite + magnetite + Ti-clinohümite) from Erro-Tobbio, Western Alps, NW Italy, analyzed by Scambelluri et al. [50]. Notably, the lithospheric serpentinite composition, compared with the eclogite, is relatively depleted in LILE (Table 2).

For the fully-equilibrated scheme, in each subsequent subsolidus step, we equilibrate the fluid-mobile tracers with a peridotite source lithology based on partition coefficients for fluid in equilibrium with lherzolite ($D^{\mathrm{lherzolite/fluid}}$) [47], assuming 60:30:10 by mass olivine:orthopyroxene:clinopyroxene. The peridotite compositions are carried down from previous columns as described earlier. Errors may be introduced due to the changing bulk composition of the peridotite as it melts and is advected, especially as some melting steps lead to cpx-exhaustion. The resultant fluid-mobile contents from the fluid (including water as a trace element) are added to the bulk trace element composition of the peridotite prior to a pHMELTS equilibration, relative to the mass proportion of fluid added. After the calculation, any excess water is then given a fluid-mobile trace element content based on its mass fraction and is moved along to the next pressure-temperature point (see Notes to Table 2). Melts calculated by pHMELTS at the top of the column thus include the fluid-mobile trace elements added by the hydrous fluid phase. In the isolated transport case for fluid, the fluid interacts with the peridotite source lithology at the top of the column only, such that the resultant fluid-mobile elements are added to the bulk trace element composition of the peridotite prior to a pHMELTS equilibration, relative to the mass proportion of fluid added. Within the GyPSM-S model, fluid is transported using Darcy flow. For these simple models, we necessarily impose that fluid moves fast enough such that it will reach the top of the calculation column before advection of the solid would move the column to new P-T conditions.

3.5. Melt transport

The GyPSM-S calculation assumes a divergence-free, incompressible flow field and near-fractional melting, such that the melts are isolated immediately upon formation and have no further physical or chemical effect on the solid flow field. Realistic melt flow beneath subduction zones is most likely to be at least two-dimensional [23]; however, one-dimensional models can provide some insight. In the context of the columns introduced above, we examine the compositions of the melts as they are initiated and address the fate of melts initiated at different depths and distances into the wedge in the context of near-vertical buoyant transport towards the surface. Near-vertical transport allows for the least complicated manner of equating melts initiated at different depths to different locations in a cross-arc sense. Two end-member possibilities for melt-solid interaction along this type of trajectory are evaluated.

The fate of the melt can theoretically fit into one of two categories: (i) chemically isolated transport (perhaps along unreactive channels, or along fractures) and (ii) reactive transport (porous flow). Both scenarios can be addressed within the column configuration. During the original calculation, described above, information as to the pressure, temperature, composition, and mass fraction of melts generated along a column is provided. However, the original column assumes the transport of water in a hydrous fluid only, and the calculation ends when the activity of water drops below unity. The melting calculation employs an extension of the original column, further mapping pressures and temperatures at each point from the GyPSM-S mesh. A single initial melt composition from each original column, representing the maximum melt fraction experienced for that column, is extracted. In the case of chemically isolated transport, we examine the situation in which these melts continue to travel along their respective column extensions in chemical isolation from the surrounding peridotite (scaling the melt mass to 100.0 g of material). If a calculation results in the persistence of the melt phase, the melt is extracted and moved to the next point along the column extension. This is a case of closed system transport, where there is no exchange of mass. In the case of reactive transport, we examine an open system in which the melt continues to move along the column, but with complete equilibration with the surrounding peridotite at each step. In both cases, there is complete physical separation of the melt and residue after each step, such that it is the melt phase alone that moves up the column. For both cases, the extended column calculation continues until the melt fraction drops to zero or the limits of pHMELTS stability are reached.

4. Results

4.1. Dehydration patterns as a function of subduction parameters

Due to the specification of vertical fluid transport through the mantle wedge, the locations of melt initiation are controlled by the positions of the dehydration reactions within the different lithologic layers within the slab [45]. These reactions generate different dehydration patterns in different models due to the changing thermal structure of the model slabs. In all models, there appears to be a roughly bimodal distribution of fluid sources and an overall evolution in the host reservoir with distance along the slab (Fig. 3). In subduction zones defined by a younger slab, the AOC layer and the serpentinite layer completely dehydrate by the time they exit the base of the model domain (200 km). The AOC layer dehydrates over a pressure range of ~1 GPa before 100 km depth. The serpentinite layer dehydrates in a series of reactions starting ~3 GPa and ending ~6 GPa (rock containing serpentine chlorite brucite → serpentine chlorite dunite; serpentine chlorite dunite → chlorite harzburgite; chlorite harzburgite → garnet harzburgite; Fig. 2; lithologic descriptions from [45]). In models defined by subduction of a more mature slab, the AOC layer dehydrates over a longer pressure range (~2 GPa) extending to greater depths. The serpentinite layer crosses a single phase boundary and exits the model domain with 6.8 wt. % H_2O. Increasing the downgoing slab thermal age results in a very strong fluid source from the serpentinite layer at higher pressures (≥ 5.9 GPa), as opposed to a relatively weak fluid source from the serpentinite layer associated with younger slabs at lower pressures. This is due to the change in the thermal structure of the slab, resulting in altering the P-T trajectory across phase boundaries (Fig. 2).

The primary effect of increasing slab velocity at a similar convergence angle is a relative deepening of the serpentinite reactions, as a faster slab leads to an overall cooler thermal structure. Changing the convergence angle does not seem to impact the fluid release pattern with depth, but does have a significant impact on the horizontal (arc-normal) expanse of the melting region [39]. Increasing slab dip (45° to 60°) allows the strong serpentinite-derived fluid source to approach the melting region associated with AOC-derived fluid sources. Decreasing slab dip (45° to 30°) increases the horizontal extent of the melting region, distributing fluids over a wider interval (Fig. 3e, f). This has a primary influence on the ultimate geometry of the hydrated region within the wedge.

We have modeled the dehydration of both AOC and serpentinite as point sources associated with crossing of sharp univariant boundaries, but recognize that in reality the AOC at least is likely to experience more continuous dehydration associated with reactions of higher variance. Serpentinite, being a relatively simple compositional system with more limited solid solution, is expected to behave in a manner closer to the point source approximation. The fluid flux from the slab increases with depth for the models with older slabs as a function of the capacity of the deeper-dehydrating serpentinite minerals and the position of the phase boundary. For younger slab models this is not the case, and the majority of the fluid is released from the interval ~2.5-3.5 GPa. Mid-pressure fluid release (< 4.0 GPa) from younger slabs is primarily a product of the serpentinite layer, while for more mature slabs it is the AOC layer.

Especially in the case of the younger slabs, very shallow fluid release results in the hydration of the peridotite wedge without melting, and the fluid continues to migrate up into the overlying lithosphere. Shallow fluid release into the near-slab mantle immediately adjacent to the wedge corner is all that is necessary to initiate the LVC, as the thermal structure inhibits release of water from the NAM along slab-parallel streamlines.

4.2. Time-dependent consequences of dehydration patterns

Based on GyPSM-S results (Chapter 2), the deepest serpentinite-derived fluid sources from mature slabs lead to a strong continuous flux to the deeper melt region. As a result of the latent heat of melting, significant continuous cooling of the active melting region can occur, and the position of the water-saturated solidus may ultimately retreat into the wedge, producing a longer fluid pathway leading to shallower melting associated with the serpentinite fluid source. This mechanism is a way to generate hydrous melts derived from deep slab fluid sources at relatively low pressures. Younger slabs do not exhibit this behavior, primarily due to the lack of a similar strong fluid source at depth. Instead, models with younger slabs maintain the uniform-thickness channel configuration throughout the model duration.

4.3. Melt characteristics

The positions and relative strengths of the fluid sources are important for the fluid-mobile trace element chemistry of the resulting melts. As shown in Table 2, the fluid-mobile trace element compositions of the fluids derived from the lithospheric serpentinite are more depleted than those originating from the AOC layer, resulting in different melt trace element signatures depending on the direct fluid source to a specific melting region. Thus, the serpentinite provides a significantly greater fluid source without a corresponding increase in fluid-mobile components (Fig. 4) [15]. There is a strong control on the initiation of melting with the influx of fluid, and all initial melts are very hydrous, with 8-15 wt.% H_2O (higher pressure initial melts have less water). There is not a simple pressure-dependent trend of instantaneous melt fraction (f) of the initial melts that appear in the system. Single columns can produce multiple degrees of f, and in some cases, particularly at shallower melting regions, multiple melts with significantly different concentrations of indicators of source depletion, such as HFSE, and significantly different major element compositions.

The cumulative melt fraction (*F*) experienced by a packet of mantle within the calculation column as it moves past the base of the model domain (Fig. 5) changes dramatically between the model with the younger slab and the model with the more mature slab. Larger fluid flux from the mid-pressure serpentinite fluid releases within the younger slab result in very high *F* (> 35 wt. %) in the center of the column. Higher fluid flux leads to higher extents of melting for mid-pressure melts. For the mature slab case, the maximum *F* experienced at mid-pressures is ~20 wt. %, with a significant tail (up to 10 wt. %) appearing at higher pressures, extending further into the wedge. This is due to the relatively lesser fluid mass released from the mid-pressure AOC layers for this model case. In all cases, the activity of water rapidly drops below unity as the water is partitioned into the melt phase (Fig. 6). Restricting water transport to a hydrous fluid phase results in a sharp boundary in the water content of NAM and in solid density ($\Delta\rho \sim$ 20-50 kg/m^3) between the LVC and the ambient mantle above the melting region. These density contrasts are not enough to initiate Rayleigh-Taylor instabilities leading to diapirism of the hydrated solid (e.g. [52]); however, the water content boundary leads to strong lateral variations in solid viscosity which have an impact on the flow field as well as geophysical surface observables (Chapter 4).

4.4. Changing bulk composition-melt depletion patterns within the wedge flow field

A combination of changing bulk composition due to melting along previous columns, and of the gradual divergence of the pressure-temperature path of the slab surface from the water-saturated solidus, causes the active melting region to occur as a thin lens that appears at a greater distance from the slab interface with increasing depth. In most cases, material is not being progressively depleted by melting, but rather fluid migration occurs through previously melt-depleted regions to less-depleted (or non-depleted) sources towards the interior of the wedge. Therefore, there is an overall combination of melts produced from fertile sources and melts produced from depleted sources. Melts associated with deeper fluid releases are uniformly from more fertile sources.

In real subduction systems, there is the potential for sequential melting of mantle peridotite as it advects along streamlines within the wedge, including upwelling beneath a back-arc, melting beneath rear-arc volcanoes, and then beneath the magmatic front itself [15, 19, 49, 64]. However, in this study, previous depletions due to such factors are neglected, and depletion trends in the trace elements can be seen solely as a consequence of proximity of fluid sources in the low- to mid-pressure regions, leading to certain cases of additional fluxing of material previously depleted by melting. This is particularly appropriate for the NIB system, which has very depleted arc lavas, yet no active back-arc spreading [33]. As demonstrated by the results presented here, and as suggested by [68], hydrous fluxing alone may maintain the depletion of arc sources. Even if the presence of a back-arc is considered, the solid flow pattern is such that more wedge-interior streamlines may not have passed through melting regions feeding the back-arc melting region, leading to a general trend of melts from less depleted sources associated with deeper fluid releases (Fig. 7). This leads to an apparent paradox: the most fertile sources receive the most depleted fluids.

4.5. Melt chemistry

Incompatible element ratios that reflect source depletion vary with spatial location within the wedge and are not significantly affected by the method in which fluids transit the hydrated region. These ratios show a bimodal distribution correlated with pressure of initial melting. For example, Zr/Nb increases with source depletion [15], and the highest values are found in low- to mid-pressure melting regions (Fig. 8a), influenced by more closely-spaced fluid sources. Melts become more depleted with pressure, as residues from previous melting events are advected down-dip and additionally melt. However, these melts are generally low melt fraction, and do not result in water-undersaturation. Fluids tend to continue to move through to fertile sources immediately above the depleted sources, resulting in additional melting with significantly higher melt fractions in the same column. The residues from the low- to mid-pressure melting region do not influence the deepest melts, and as such the deep source region is less depleted overall. Thus, Zr/Nb decreases with increasing pressure of melting overall. Nb/Yb decreases as the mantle source becomes more depleted [53] (Fig. 8b) and increases with pressure of melting, overall. These model data imply that the most depleted melts are associated with low- to mid-pressure fluid sources: the AOC (eclogite) layer in the case of mature slabs and the serpentinized lithosphere in the case of younger slabs.

Geochemical tracers carried with slab-derived fluids are affected by the mechanism of fluid transport (fully-equilibrated or isolated) through the hydrated near-slab wedge. Ba shows the most dramatic difference, as its concentration in the fully-equilibrated case rapidly increases within the LVC (a consequence of the low $D^{lherzolite/fluid}$ for Ba and of the fluid carrying more Ba due to consecutive equilibration with a peridotite composition carrying more Ba). Indeed, concentrations of Ba in the peridotite become unrealistic in the fully-equilibrated fluid transport end-member. In contrast, the method of isolated transport of the fluid, with interaction only at the top of the column, results in trace element ratios within the range of regional datasets. The fully-equilibrated fluid path results in slight enrichments of Pb in the initial melts at all pressures and U and Sr at low- to mid-pressures relative to the limited interaction fluid path. Th contents in the initial melts are not significantly affected by the choice of fluid transport scheme.

Plots of Zr/Nb vs. U/Th (Fig. 8d, e) show the depletion trends together with the degree of hydration. Higher U/Th is expected for mantle sources metasomatized by hydrous fluids, whereas higher Zr/Nb is expected for depleted mantle sources, as mentioned previously. Values for the melts associated with young slab serpentinite fluid release and mature slab AOC fluid release appear to most closely match the real datasets, potentially indicating that the regions of highest melt production (mid-pressure) are most readily represented at the arc front, and that changing subduction parameters result in changing fluid source lithology responsible for the mid-pressure fluid release .

The La/Yb ratio represents the mantle source's enrichment in incompatible elements, generally relating to the amount of melting [15, 16], and the Ba/La ratio represents the slab-derived fluid's contribution, or the relative slab signal [16]. Plots of La/Yb vs. Ba/La (Fig. 8f, g) show that in both models, melts influenced by AOC-derived fluids have lower La/Yb and higher Ba/La. The model melts influenced by serpentinite-derived fluids are closer fitting to the dataset for Costa Rica, while the model melts influenced by AOC-derived fluids are closer fitting to the Izu-Bonin dataset. It should be noted that the Carr dataset [55] for Costa Rica has anomalously high values for La/Yb, derived from Galapagos-like mantle in the area [42, 56].

Some ratios of fluid-mobile incompatible elements to HFSE (generally assumed not to be mobile in fluids), such as Ba/Nb, can be indicative of the total subduction component that is added to the arc magma source [53] (Fig. 9). Ba/Nb ratios in these models range from > 200.0-2100.0 for lower pressure melts to < 200.0-600.0 for higher pressure melts. These values are all much higher than for N-MORB (Ba/Nb ~ 4), reflecting the influence of the slab-related fluid sources [54]. For the NIB model, Ba/Nb decreases with increasing pressure. Plots of Ba/Th and U/Th (Fig. 9c, d) comparing the Carr dataset with model melts show that the serpentinite-derived fluids from CCR more closely match the data from Costa Rica.

The major element composition of the initial melts are shown in Table 4. The initial melts are very hydrous, as mentioned previously. Overall, initial melts at low- to mid-pressures have higher SiO_2, Al_2O_3, and H_2O and lower TiO_2 contents than higher pressure melts. Na_2O varies primarily by melt fraction.

4.6. Simple models for melt extraction

We attempt two column-based tests of melt extraction: full equilibration of the melt along the column pressure-temperature conditions, and isolated transport of the melt along the column pressure-temperature conditions. When melt is fully equilibrated with ambient peridotite at each additional step along the column, two trends emerge (Fig. 10). For initial melts that have formed at relatively shallow depths, equilibration up the column results in the progressive dehydration of resultant melts and increasing activity of water in the system, with concurrent increases in the water content of NAM along the column. Ultimately, around 1.35 GPa, hornblende is added to the assemblage. The additional column calculation ends with the activity of water reaching unity (second boiling) and melting ceasing around 1.15 GPa. There is a very abrupt contrast between the conditions at the top of this column and the ambient conditions in terms of water activity and solid density (a_{H_2O} = 1.0 versus 0.3; ρ_{solids} = 3.16 versus 3.28 g/cm^3). For initial melts that have formed at higher pressures, the column extension is much longer, yet involves much lower melt fractions. Hornblende stability is never reached, due to the higher pressures. Instead, water is progressively partitioned into the NAM, with water activity and solid density decreasing to ambient levels (a_{H_2O} = 0.08; ρ_{solids} = 3.27 g/cm^3). Interestingly, the situation of complete melt equilibration along a path results in an extension of the hydrated layer beyond the original thickness of the LVC. For the case of isolated transport of melt along the pressure-temperature path specified by an extension of the original column, second boiling occurs at relatively greater depths (~1.25 GPa).

For a test of directly matching the model-derived initial melt compositions with real lava chemistry from the northern Izu-Bonin system, we attempted a "direct-delivery" model. We calculated a primary magma composition for a local volcano (Miyakejima, Table 5) based on fractionation pathways that matched analyzed lava compositions [72] under conditions of isobaric cooling in a hypothetical magma chamber at 500 bars, with f_{O_2} = QFM+0.5 (Fig. 11). We find that none of the individual modeled NIB melt compositions provided a match for the calculated Miyakejima primary magma composition. Indeed, neither did a direct combination of the modeled NIB melts as investigated by a singular value decomposition (SVD) analysis. However, this is an extremely idealized approach, assuming no melt-residue interaction and the result is not surprising.

5. Discussion

5.1. Fluid transport within the LVC and potential consequences of a lack of sediment

Fluid transport modeling with the assumption of full equilibration of the fluid with peridotite along the entire thickness of the LVC is not matched by the fluid-mobile trace element datasets for either region. In fact, it is the assumption of equilibration of the fluid with peridotite only at the top of the transport pathway that appears to be more valid. These end-member results could be indicative of limited interaction of the fluids with the hydrated peridotite along the pathway, not necessarily only near the melting region. As the LVC is initiated near the wedge corner, at the shallowest locations of fluid release, and water in NAM is quite stable within the LVC throughout its transit to (at least) the base of the model domain (200 km depth), the primary impact of the equilibration of fluid is to increase the water content, and perhaps thicken the LVC. A more limited interaction will not negate the presence or persistence of the LVC, and will act to more readily preserve the differences in fluid-mobile trace element chemistry derived from particular source lithologies along the slab, leading to discernible influences on the initial melt chemistry that vary spatially within the wedge. If these differences are preserved, and a melt migration scheme acts to prevent significant mixing of magmas within the wedge, such that melts associated with higher-pressure-derived slab fluids will erupt separately from melts associated with lower-pressure-derived slab fluids, cross-arc variations in lava trace element chemistry become significant for depth tracing of initial melts.

The concept of a changing fluid-source slab lithology manifested in rear-arc to arc geochemical trajectories has been proposed by previous studies [15, 19]. The Guguan cross-arc chain represents the fluid-fluxed end-member of the intraoceanic Mariana arc and involves subduction of a mature slab [9, 63]. Stern et al. [15] propose that changing slab sources of metasomatic fluids with depth lead to variations in the fluid-mobile trace element concentrations in the lavas in this system (Fig. 7), concluding that there may be an increasing role of serpentinite-derived fluids at greater depths leading to rear-arc volcanism due to the appearance of a weakening slab signature with increasing distance to the WBZ. As hypothesized by [15], this could simply be due to the relative lack of LILE in subducting serpentinized lithosphere. Notably, the water contents of rear-arc lavas are not shown to change markedly from volcanic front lavas, further suggesting a changing slab fluid source to serpentinite, which provides a significant fluid flux [15]. If the fluid source-derived geochemical differences are preserved, changing subduction parameters (such as slab dip) may produce changing lava geochemistry, as different fluid sources are emphasized. For example, volcanic front lavas along the Central American subduction system demonstrate that trace element data may preserve information about the relative influences of fluid-source lithology as ratios associated with a slab signal vary with respect to changing subduction parameters [16].

This study neglects sediment-derived fluid contributions to the fluid budget, as well as sediment melts, or melts of the AOC [57]. We assume that sediment-derived fluids are expelled at shallower depths than the convecting mantle wedge [16], but the lack of sediment melting may be significant. At present, modeling of slab-derived components encompasses selected fluid-mobile trace elements only. Melting of sediment allows for the bulk addition of elements concentrated in the sediment layer to the mantle wedge that may not be effectively added through fluid-dominated transport alone, due to the very low mobility of certain elements within a fluid. These elements include the HFSE (Nb, Ta, Zr, and Hf), REE, and possibly Th [9, 47, 58]. Neglecting sediment melting effectively results in the potential for higher concentrations of these elements than predicted by this study.

5.2. Comparison of model results with regional datasets

5.2.1 Costa Rica (CCR)

Rupke et al. [16] use a 2-D dynamic model to track the evolving sources of fluid release from the downgoing slab in the Costa Rican subduction zone. The results show that sediments dewater by 75% during shallow (< 50 km) subduction, the AOC (the most significant source of the slab-derived fluid flux) dewaters over an interval 100-140 km depth, and serpentinites dewater over an interval 130-150 km depth. Our results show a similar overlap between AOC and serpentinite dehydration, but that serpentinite is the major source of mid-pressure (80-130 km depth) fluid flux. Significantly, the fluid sources for the CCR model in this study and the model of [16], despite the fundamental difference in fluid-source lithology, feed into similar spatial melting regions. These mid-pressure melts represent the result of the highest fluid flux in the CCR model, as well as the highest melt fraction, and can thus be considered to be the primary input towards the volcanic front. Lithospheric serpentinite is relatively depleted in fluid-mobile elements compared to subducting AOC. The reason the concentration of trace elements added to the melting region from the dehydrating slab decreases beneath Costa Rica as opposed to neighboring regions with different subduction parameters [16, 39, 42, 43] may be this change in fluid source lithology. The range of melting expected beneath Costa Rica is 5-25% [39], which is significantly lower than the maximum degree of melting produced by the column modeling of this study, but is not inconsistent with the overall range of melting produced by the columns (Fig. 5). The upper value is probably a consequence of a maximum fluid flux to the active melting region in the column modeling.

Carr et al. [59] argues that regional along-arc variation in Ba/La in the Central American subduction system is a result of the manner of fluid delivery and its impact on melt production. Specifically, Carr et al. [59] contends that the steeper-dipping, slightly older slab beneath the Nicaraguan segment involves more concentrated fluid delivery, leading to higher Ba/La, while more diffuse fluid introduction in Costa Rica, a function of the more moderately-dipping slab, leads to lower Ba/La ratios. Modeling of a steeper-dipping slab by GyPSM-S agrees with the potential for a more concentrated fluid flux to mid-pressure regions feeding the volcanic front as fluids from depth transit pathways approaching the same melting region as influenced by shallower fluid release. However, an additional factor for consideration may be the fluid-source lithology. Fluids derived from the slab AOC layer tend to result in melts with higher Ba/La ratios, while fluids derived from the slab serpentinized lithospheric layer tend to result in melts with lower

Ba/La. Perhaps there is a change from mid-pressure AOC-derived fluid flux under Nicaragua to mid-pressure serpentinite-derived flux beneath Costa Rica, a function of the slightly different slab age. This would not preclude the arguments of [37], which lead to the conclusion that there is a strong slab-derived fluid source designated by a low-$\delta^{18}O$ water-rich component beneath Nicaragua. We suggest that it is the deeper AOC layers that would be dehydrating at the mid-pressure ranges, and hydrothermally-altered lower oceanic crust and hydrothermally-altered ultramafic rocks both have similar ranges for oxygen isotope values ($\delta^{18}O_{SMOW}$ = 0-6‰) [60-62].

5.2.2 Izu-Bonin

Izu-Bonin arc tephra geochemistry indicates minimal contribution from subducted sediment, a dominantly fluid-based slab component transport scheme, and a highly depleted mantle source for the volcanic arc [32]. Additionally, there is a cross-arc distribution of chemical characteristics that indicates that the melt transport systematics can be described relatively simply [19] and shows evidence for a lack of crustal contamination [31]. We propose that there is a maximum contribution at the volcanic front from primary magmas fluxed by mid-pressure fluid release from dehydrating slab AOC layers and that rear-arc lavas (Western Seamounts) involve significant contributions from primary magmas fluxed by fluids released at higher pressures from the dehydrating slab serpentinite layer.

Hochstaedter et al. [19] note significant cross-arc trends for the Izu-Bonin system, including increasing Nb/Zr (decreasing mantle source depletion) and decreasing Ba/Nb and SiO_2 with distance from the volcanic front to the rear-arc. These trends agree with the results of this study, assuming a melt migration pathway allowing melts initiated by fluids released lower pressures to influence the volcanic front, and melts initiated by fluids released at higher pressure to influence the rear-arc. Specifically, with regard to the end-member results for limited fluid interaction, the values for Ba/Nb for the low- to mid-pressure melts and the higher-pressure melts match very closely the data from [19], for volcanic front lavas and rear-arc lavas, respectively (Fig. 9b). Additionally, we observe a trend of decreasing SiO_2 with increasing pressure among initial modeled melts, and trace element indicators of mantle source depletion show that melts associated with low- to mid-pressures are the most depleted in HFSE, a pattern that matches the data from [19] indicating that the volcanic front lavas are the most depleted of the arc system (Fig. 8). Stern et al. [15] additionally observe increasing mantle source depletion with decreasing distance to the WBZ.

Hochstaedter et al. [19] propose that a mechanism of fluid depletion can explain the cross-arc variation, such that a "fertile" (higher in fluid-mobile elements) fluid is released at lower pressures, and a then more "depleted" fluid (a result of the earlier fluid release) is released at higher pressures. We suggest that instead of a progressively-dehydrating singular slab-source that evolves with regard to concentrations of fluid-mobile elements, there is a condition of progressive dehydration from heterogeneous slab lithologies defined by different initial fluid-mobile trace element compositions and varying fluid fluxes, a situation similar to that modeled by [16] and suggested by [15].

GyPSM-S results for the subduction of a mature slab indicate that there is a time-dependent evolution of the hydrated low-viscosity region from a channel into a more extensive wedge-type geometry (Chapter 2). This is a consequence of the strong, deep serpentinite-derived fluid flux in mature slabs and the effect of the latent heat of melting. Progressive cooling associated with the active melting region may eventually lead to the retreat of the solidus into the wedge and a lengthening of the deeply originating fluid pathway over time. This should not effect the overall trace element chemistry of the low- to mid-pressure melts presented in this study. For the melts influenced by the deeply-derived fluid source, the lower degree of prior depletion relative to certain melts derived from low- to mid-pressure fluid releases should remain the same, and if the hypothesis of limited interaction with the wedge peridotite is correct, the fluid-mobile trace element composition of these melts should remain consistent with the results presented here.

5.3. End-member results for vertical melt transport

We find a close spatial agreement with the GyPSM-S modeled locations of melt initiation and seismic imaging results for low-velocity zones within the wedge [2, 3, 66], indicating that models of the active melting region are successful. However, in order to preserve the spatial heterogeneity of initial melts as described in previous studies of cross-arc geochemistry, a nearly-vertical melt migration model is required. This model should readily allow the arrival of melts fluxed by fluids derived from lower pressures towards the arc front versus melts fluxed by fluids derived from higher pressures towards the rear-arc. The rear-arc lavas in the Guguan chain show higher pressures and temperature of equilibration [15], an indication that deeper melts may tend to influence volcanism towards the rear of the arc as opposed to the volcanic front itself. There also appear to be lower degrees of melting experienced as depth to the WBZ increases in the Guguan chain (shown from variations in alkali content [15]), a similar result to the column modeling, where deeper melting of less depleted sources results in lower melt fractions (Fig. 5).

This study involves the investigation of two end-member interaction scenarios involving the implications of vertical melt transport originating at the zone of active melting and continuing through the mantle wedge. A scenario in which melts remain isolated from the surrounding peridotite matrix results in a short additional transit of the melt before it results in second boiling. In the case of an "infinitely permeable" scenario defined by batch melting, melt migrates along vertical paths, with a full equilibration with ambient peridotite at each step. The possibility of high water contents in NAM is extended further from the slab into the wedge, providing a potential mechanism to generate a more extensive low-viscosity geometry. Melts continue to react along the column to the point of freezing out (higher-P) or stabilizing hornblende (lower-P). Because melts have to approach the surface in order to result in arc lavas, an infinitely permeable scenario can only work for part of the transport process (< 40 km depth), and only for shallower melts. The deepest melts in the models may end up as source enriching agents rather than coherent melts passing through the long potential melting column to eruption. In both end-member cases, the column calculation ends well before the depth of potential shallow magma chambers feeding the arc, resulting in the conclusion that neither of these interaction mechanisms by itself defines the entire melt extraction pathway.

5.4. Implications for slab-component transport rates

The stability of the slab-adjacent hydrated zone (LVC) and the separation of the slab-wedge interface from the melting region has been established through GyPSM-S. Studies of slab-fluid component transport to the arc using U-series isotopes indicate a timeframe of transport from fluid release to eruption between 30,000 and 120,000 years, allowing for a fluid transport rate of 1-4 m/yr [14], and implying the probability of a rapid transport pathway. Current GyPSM-S parameters for fluid transport allow for 0.63 m/yr as a fluid velocity, on the lower end of that estimate. From comparison with regional datasets, the results presented in this study indicate that fluids responsible for flux melting may preserve the trace element signatures of the original dehydrating lithology with little modification along their pathway through the LVC to the melting region. This suggests either a potential rapid transport scenario that prevents significant fluid-mantle interaction or a fluid-dominated trace element budget. Perhaps hydraulic fracture plays an subordinate role in the slab-adjacent mantle wedge, allowing for a more or less direct delivery of fluid to melting region [65].

5.5. Implications for back-arc basin basalt (BABB) sources

There is a critical role of water, originating presumably at the slab-wedge interface, evident in the petrogenesis of basalts erupted at back-arc basins [67-69]. However, the pathways of water delivery from the slab to the back-arc melting region have not been clearly established. In this study, we do not include a back-arc spreading region and cannot therefore offer a unique solution. Despite this, we can infer potential hydrous pathways leading to melting beneath the back-arc from the results presented here.

5.5.1 Direct delivery of fluids to the shallow-level wedge

Previous investigation of BABB geochemistry invokes mixing between dry, fractional melts and hydrous melts that have been equilibrated at low pressures [51]. The hydrous end-member is associated with fluid influx from the slab, and requires low-pressure equilibration in order to explain aspects of the geochemistry of BABBs such as low $Fe_{8.0}$ and the lack of a garnet signature [51].

The model domain in GyPSM-S extends to 200 km depth, and dehydration reactions within the slab over that depth range lead to active melting that can explain trace element variations evident in cross-arc lavas. Rupke et al. [70] hypothesize that serpentinite dehydration reactions within the slab, and possibly within the hydrated near-slab mantle, can occur at even greater depths, allowing for melting to initiate further inboard from the arc, perhaps extending beneath a back-arc. Deeper sources may eventually translate into longer serpentinite-derived fluid pathways to shallower melting regions beneath the back-arc, similar to the mature slab GyPSM-S results (Chapter 2). This could potentially translate into low-pressure hydrous melting beneath the back-arc as required by [51] (Fig. 12a).

5.5.2 Diapirism

Even if fluid pathways did not reach directly into the BABB source region, fluids generated by deep serpentinite dehydration result in hydrous melting further into the mantle wedge than at shallower areas, removing the active melting region farther from the down-dip influence of the slab-parallel solid flow field. The density differences between the initial melts and solid residue are significant ($\Delta\rho$ = 400-500 kg/m^3), and could result in buoyant transport of hydrous melts as diapirs vertically into the BABB source region, as suggested by [51] (Fig. 12b).

5.5.3 Transport of enriched material along solid flow streamlines

Porous flow of relatively low-degree melts at depth may result in an extension of wedge hydration above the zone of fluid delivery to the active melting region. The concentrations of water in NAM are increased in the solid residue due to equilibration with the migrating hydrous melt. Ultimately, the melt will freeze out in this process, but the remaining solid along its migration path may then be carried as hydrous enrichments with the flow field towards the back-arc source region (Fig. 12c).

6. Conclusions

This study involves a supplement to original GyPSM-S modeling of systems with varying subduction parameters in order to demonstrate the applicability of GyPSM-S results to regional geochemical datasets. Changing patterns of fluid release from dehydration reactions within slab lithologic layers as a function of distance along the slab were investigated and related to the influence of changing parameters such as slab age and convergence velocity. Modeling of fluid migration through hydrated peridotite within the LVC provides evidence for a limited fluid-rock interaction, preserving the fluid-mobile trace element chemistry associated with the original slab lithology to the active melting region. This suggests the potential for either a rapid fluid transport scenario or a fluid-dominated trace element budget within the LVC. Comparison with interpretations of along-arc trends suggests that changing subduction parameters significantly affect the dehydration pattern within the subducting slab, leading to changes in reaction location within the slab and a varying fluid flux and fluid chemistry reaching the active melting region, which can be manifested in erupted lavas. By comparison with regional datasets and interpretations of cross-arc and along-arc trends, we find that a simple melt migration scheme which preserves spatial heterogeneity of initial melts towards eruption is likely. Specifically, that melts associated with low- to mid-pressure fluid release will erupt towards the volcanic front and melts associated with higher-pressure fluid release will erupt towards the rear-arc. Although we do not explicitly include a back-arc in these models, interpretations of the results lead to several potential mechanisms to explain hydrous inputs to back-arc source regions.

Acknowledgments

The authors would like to thank P. Antoshechkina and M. Gurnis for collaboration in the GyPSM-S modeling effort. Support provided through the Tectonics Observatory by the Gordon and Betty Moore Foundation.

References

[1] T. Plank and C. H. Langmuir (1988) An evaluation of the global variations in the major element chemistry of arc basalts. Earth and Planetary Science Letters **90**(4), 349-370.

[2] A. Hasegawa et al. (2005) Deep structure of the northeastern Japan arc and its implications for crustal deformation and shallow seismic activity. Tectonophysics **403**, 59-75.

[3] D. P. Zhao et al. (2001) Seismological structure of subduction zones and its implications for arc magmatism and dynamics. Physics of the Earth and Planetary Interiors **127**, 197-214.

[4] G. A. Gaetani and T. L. Grove (1998) The influence of water on melting of mantle peridotite. Contributions to Mineralogy and Petrology **131**(4), 323-346.

[5] G. A. Gaetani and T. L. Grove (2003) Experimental constraints on melt generation in the mantle wedge. Geophysical Monograph 138, 107-134.

[6] E. M. Stolper (1980) A phase diagram for mid-ocean ridge basalts. Contributions to Mineralogy and Petrology **74**, 13-27.

[7] E. M. Klein and C. H. Langmuir (1987) Global correlations of ocean ridge basalt chemistry with axial depth and crustal thickness. Journal of Geophysical Research **92**(B8), 8089-8115.

[8] T. Plank and C. H. Langmuir (1993) Tracing trace elements from sediment input to volcanic output at subduction zones. Nature **362**, 739-743.

[9] T. Elliott et al. (1997) Element transport from slab to volcanic front at the Mariana arc. Journal of Geophysical Research **102**(B7), 14991-15019.

[10] T. Ishikawa and F. Tera (1999) Two isotopically distinct fluids fluid components

involved in the Mariana Arc; evidence from Nb/B ratios and B, Sr, Nd, and Pb isotope systematics. Geology **27**, 83-86.

[11] P. Ulmer and V. Trommsdorf (1995) Serpentine stability to mantle depths and subduction-related magmatism. Science **268**, 858-861.

[12] M. W. Schmidt and S. Poli (1998) Experimentally based water budgets for dehydrating slabs and consequences for arc magma generation. Earth and Planetary Science Letters **163**, 361-379.

[13] R. J. Arculus (1994) Aspects of magma genesis in arcs. Lithos **33**, 189-208.

[14] C. Hawkesworth et al. (1997) U-Th isotopes in arc magmas: Implications for element transfer from the subducted crust. Science **276**, 551-555.

[15] R. J. Stern et al. (2006) Subduction factory processes beneath the Guguan cross-chain, Mariana Arc: no role for sediments, are serpentinites important? Contributions to Mineralogy and Petrology **151**(2), 202-221, doi: 10.1007/s00410-005-0055-2.

[16] L. H. Rupke et al. (2002) Are regional variations in Central American arc lavas due to differing basaltic versus peridotitic slab sources of fluids? Geology **30**(11), 1035-1038.

[17] H. Iwamori (1998) Transportation of H_2O and melting in subduction zones. Earth and Planetary Science Letters **160**, 65-80.

[18] J. G. Ryan et al. (1995) Cross-arc geochemical variations in Kurile arc as a function of slab depth. Science **270**, 625-627.

[19] A. Hochstaedter et al. (2001) Across-arc geochemical trends in the Izu-Bonin arc: contributions from the subducting slab. Geochemistry, Geophysics, Geosystems

2:2000GC000105.

[20] P. D. Asimow, J. E. Dixon, C. H. Langmuir (2004) A hydrous melting and fractionation model for mid-ocean ridge basalts: Application to the Mid-Atlantic Ridge near the Azores. Geochemistry, Geophysics, Geosystems **5**(1), Q01E16, doi:10.1029/2003GC000568.

[21] G. Hirth and D. L. Kohlstedt (1996) Water in the oceanic upper mantle; implications for rheology, melt extraction, and the evolution of the lithosphere. Earth and Planetary Science Letters **144**(1-2), 93-108.

[22] J. H. Davies and D. J. Stevenson (1991) Physical model of source region of subduction zone volcanics. Journal of Geophysical Research **97**(B2), 2037-2070.

[23] M. Spiegelman and D. McKenzie (1987) Simple 2-D models for melt extraction at mid-ocean ridges and island arcs. Earth and Planetary Science Letters **83**, 137-152.

[24] P. Hall and C. Kincaid (2001) Diapiric flow at subduction zones: A recipe for rapid transport. Science **292**, 2472-2475.

[25] F. Furukawa (1993) Magmatic processes under arcs and formation of the volcanic front. Journal of Geophysical Research **98**, 8309-8319.

[26] P. B. Kelemen et al. (1997) A review of melt migration processes in the adiabatically upwelling mantle beneath oceanic spreading ridges. Phil. Trans. R. Soc. Lond. A **355**, 283-318.

[27] M. S. Ghiorso and R. O. Sack (1995) Chemical mass transfer in magmatic processes; IV, A revised and internally-consistent thermodynamic model for the interpolation and extrapolation of liquid-solid equilibrium magmatic systems at elevated temperatures and pressures. Contributions to

Mineralogy and Petrology **119**(2-3), 197-212.

[28] P. M. Smith and P. D. Asimow (2005) Adiabat_1ph: A new public front-end to the MELTS, pMELTS, and pHMELTS models. Geochemistry, Geophysics, Geosystems **6**(2), Q02004, doi:10.1029/2004GC000816.

[29] R. J. Stern et al. (2003) An Overview of the Izu-Bonin-Mariana Subduction Factory. Geophysical Monograph 138, 175-222.

[30] B. Taylor (1992) Rifting and the volcanic-tectonic evolution of the Izu Bonin-Mariana Arc. Proc. Ocean Drill. Program Sci. Results **126**, 627-651.

[31] S. M. Straub (2003) The evolution of the Izu Bonin-Mariana volcanic arcs (NW Pacific) in terms of major element chemistry. Geochemistry, Geophysics, Geosystems **4**(2), 1018, doi: 10.1029/2002GC000357.

[32] C. J. Bryant et al. (2003) The geochemical evolution of the Izu-Bonin arc system: A perspective from tephras recovered by deep-sea drilling. Geochemistry, Geophysics, Geosystems **4**(11), 1094, doi: 10.1029/2002GC000427.

[33] A. G. Hochstaedter et al. (2000) Across-arc geochemical trends in the Izu Bonin arc: Constraints on source composition and mantle melting. Journal of Geophysical Research **105**, 495-512.

[34] Y. Xu and S. W. Wise (1992) Middle Eocene to Miocene calcareous nanofossils of Leg 125 from the western Pacific Ocean. Proc. Ocean Drill. Program Sci. Results **125**, 43-70.

[35] T. Plank and K. Kelley (2001) Contrasting Sediment Input and Output at the Izu and Mariana Subduction Factories. EOS, Transactions, American Geophysical Union, **82** (47), p. 1155.

[36] S. M. Peacock et al. (2005) Thermal structure of the Costa Rica-Nicaragua subduction zone. Physics of the Earth and Planetary Interiors **149**(1-2), 187-200.

[37] J. M. Eiler et al. (2005) Oxygen isotope constraints on the sources of Central American arc lavas. Geochemistry, Geophysics, Geosystems **6**(7), Q07007, doi: 10.1029/2004GC000804.

[38] M. J. Carr (1984) Symmetrical and segmented variation of physical and geochemical characteristics of the Central American volcanic front. Journal of Volcanological and Geothermal Research **20**, 231-252.

[39] M. J. Carr et al. (1990) Incompatible elements and isotopic evidence for the tectonic control of source mixing and melt extraction along the Central American arc. Contributions to Mineralogy and Petrology **105**, 369-380.

[40] M. J. Carr et al. (2004) Volcanism and geochemistry in Central America: Progress and problems. Geophysical Monograph 138, 153-174.

[41] G. A. Abers et al. (2003) The wet Nicaraguan slab. Geophysical Research Letters **30** (2), 1098, doi: 10.1029/2002GL015649.

[42] W. P. Leeman et al. (1994) Boron geochemistry of the Central American volcanic arc: Constraints on the genesis of subduction-related magmas. Geochimica et Cosmochimica Acta **58**, 149-168.

[43] L. C. Patino et al. (2000) Local and regional variations in Central American arc lavas controlled by variations in subducted sediment input. Contributions to Mineralogy and Petrology **138**, 265-283.

[44] R. K. Workman and S. R. Hart (2005) Major and trace element composition of the depleted MORB mantle (DMM). Earth and Planetary Science Letters **231**(1-2), 53-

72, http://dx.doi.org/10.1016/j.epsl.2004.12.005.

[45] B. R. Hacker et al. (2003) Subduction factory-1. Theoretical mineralogy, densities, seismic wave speeds, and H_2O contents. Journal of Geophysical Research-Solid Earth **108**(B1), http://dx.doi.org/10.1029/2001JB001129.

[46] C. R. Ranero et al. (2003) Bending-related faulting and mantle serpentinization at the Middle America trench. Nature **425**, 367-373.

[47] J. M Brenan et al. (1995) Mineral-aqueous fluid partitioning of trace elements at 900ºC and 2.0 GPa: Constraints on the trace element chemistry of mantle and deep crustal fluids. Geochimica et Cosmochimica Acta **59**(16), 3331-3350.

[48] E. Tenthorey and J. Hermann (2004) Composition of fluids during serpentinite breakdown in subduction zones: Evidence for limited boron mobility. Geology **32** (10), 865-868, doi: 10.1130/G20610.

[49] M. T. McCulloch and A. J. Gamble (1991) Geochemical and geodynamical constraints on subduction zone magmatism. Earth and Planetary Science Letters **102**, 358-374.

[50] M. Scambelluri et al. (2001) Fluid and Element Cycling in Subducted Serpentinite: A Trace-Element Study of the Erro-Tobbio High-Pressure Ultramafites (Western Alps, NW Italy). Journal of Petrology **42**(1), 55-67.

[51] C. H. Langmuir et al. (2006) Chemical systematics and hydrous melting of the mantle in back-arc basins. Geophysical Monograph 166, 87-146.

[52] T. V. Gerya and D. A. Yuen (2003) Rayleigh-Taylor instabilities from hydration and melting propel 'cold plumes' at subduction zones. Earth and Planetary Science Letters **212**, 47-62.

[53] J. A. Pearce et al. (2005) Geochemical mapping of the Mariana arc-basin system:

implications for the nature and distribution of subduction components. Geochemistry, Geophysics, Geosystems **6**(7), doi:10.1029/2004GC000895.

[54] A. W. Hofmann (1988) Chemical differentiation of the Earth: the relationship between mantle, continental crust, and oceanic crust. Earth and Planetary Science Letters **90**, 297-314.

[55] *http://www-rci.rutgers.edu/~carr/index.html*

[56] E. A. Herrstrom et al. (1995) Variations in lava composition associated with flow of asthenosphere beneath southern Central America. Geology **23**(7), 617-620.

[57] P. B. Kelemen et al. (2003) Thermal Structure due to Solid-State Flow in the Mantle Wedge. Geophysical Monograph 138, 293-311.

[58] H. Keppler (1996) Constraints from partitioning experiments on the composition of subduction-zone fluids. Nature **380**, 237-240.

[59] M. J. Carr et al. (2007) Element fluxes from the volcanic front of Nicaragua and Costa Rica. Geochemistry, Geophysics, Geosystems **8**(6), doi: 10.1029/2006GC001396.

[60] J. C. Alt et al. (1986) An oxygen isotopic profile through the upper kilometer of the oceanic crust, DSDP hole 504B. Earth and Planetary Science Letters **80**, 217-229.

[61] H. Staudigel et al. (1995) Large-scale isotopic Sr, Nd and O isotopic anatomy of altered oceanic crust-DSDP/ODP sites 417/418. Earth and Planetary Science Letters **130**, 169-185.

[62] M. Magaritz and H. P. Taylor (1974) Oxygen and hydrogen isotope studies of serpentinization in Troodos Ophiolite complex, Cyprus. Earth and Planetary Science Letters **23**, 8-14.

[63] J. D. Woodhead et al. (2001) Hafnium isotope evidence for 'conservative' element

mobility during subduction zone processes. Earth and Planetary Science Letters **192**, 331-346.

[64] J. D. Woodhead et al. (1993) High field strength and transition element systematics in island arc and back-arc basin basalts: evidence for multi-phase melt extraction and depleted mantle wedge. Earth and Planetary Science Letters **114**, 491-504.

[65] J. H. Davies and A. Rowland (1997) Importance of temperature-dependent viscosity and hydraulic fracture on physical models of subduction zone magmatism. Geological Society of Australia Abstracts **45**, 17-20.

[66] J. Nakajima et al. (2005) Quantitative analysis of the inclined low-velocity zone in the mantle wedge of northeastern Japan: A systematic change of melt-filled pore shapes with depth and its implications for melt migration. Earth and Planetary Science Letters **234**, 59-70.

[67] E. M. Stolper and S. Newman (1994) The role of water in the petrogenesis of Mariana Trough magmas. Earth and Planetary Science Letters **121**, 293-325.

[68] B. Taylor and F. Martinez (2003) Back-arc basin basalt systematics. Earth and Planetary Science Letters **210**, 481-497.

[69] K. A. Kelley et al. (2006) Mantle melting as a function of water content beneath back-arc basins. Journal of Geophysical Research **111**(B9), B09301.

[70] L. H. Rupke et al. (2004) Serpentine and the subduction zone water cycle. Earth and Planetary Science Letters **223**, 17-34.

[71] D. W. Peate and J. A. Pearce (1998) Causes of spatial compositional variations in Mariana arc lavas: Trace element evidence. The Island Arc **7**, 479-495.

[72] *http://georoc.mpch-mainz.gwdg.de/georoc/*

Figure Captions

Figure 1: (a) Schematic view of the GyPSM-S model calculation space. Sample columns are shown, as well as locations of fluid release and melt initiation. The layered structure of the subducting crust is detailed in addition to initial water content. (b) Schematic view of a single calculation column showing a phase boundary within the slab and the effective water release point (P_S, T_S) as a dark blue filled circle. The successive equilibration points above the inclined slab-wedge interface are filled black circles labeled (P_0,T_0)...(P_n,T_n), where the final point (red) represents melt initiation where the activity of water drops below unity for the equilibrium assemblage.

Figure 2: Simplified phase diagrams for MORB (a) and harzburgite (b) from [45] with example pressure-temperature trajectories for slab particles from the NIB model case (yellow) and the CCR model case (red). The trajectories for the different models cross different phase boundaries due to the different thermal structures experienced by the slab, respectively. For the MORB case, I: prehnite-pumpellyite facies, containing 4.5 wt. % H_2O; II: lawsonite blueschist, containing 5.0 wt. % H_2O; III: lawsonite amphibole eclogite, containing 3.0 wt. % H_2O; IV: amphibole eclogite, containing 1.0 wt. % H_2O; V: amphibolite, containing 1.3 wt. % H_2O; VI: epidote amphibolite, containing 2.0 wt. % H_2O; VII: greenschist facies, containing 3.0 wt. % H_2O. For the harzburgite case, I: rock containing serpentine chlorite brucite, with 14.8 wt. % H_2O; II: assemblage containing high-pressure hydrous phase A, containing 6.8 wt. % H_2O; III: serpentine chlorite dunite,

containing 6.2 wt. % H_2O; IV: chlorite harzburgite, containing 1.4 wt. % H_2O; V: garnet harzburgite, containing 0.0 wt. % H_2O.

Figure 3: Results from GyPSM-S calculations showing the thermal structure and example particle fluid release points for models (a) ADD1, (b) NIB, (c) ADD2, (d) CCR, (e) SCR, and (f) NMAR (Table 3). Fluid mass releases (in ppm) are noted for all models (see Fig. 2 for dehydration reaction information), and the calculation columns for this study are noted for the NIB and CCR models. Pressures (in bars) are noted on the left-hand side of the figures and arrows indicate lateral extents of fluid infiltration in (e, f).

Figure 4: Initial concentrations of fluid-mobile elements used in this study (Ba, Th, U, Pb, and Sr) for immediate fluid releases calculated in equilibrium with serpentinized lithosphere (gray) or AOC (black) source lithologies. Different lines indicate different initial fluid masses released from different reactions within the slab (see Fig. 2 and 3).

Figure 5: Plot of total degree of melting (F) experienced by the advecting mantle material at different distances from the slab for CCR (black) and NIB (gray). The maximum melt fractions are extracted from ~15-25 km vertical distance from the slab, initiated from mid-pressure fluid-releases.

Figure 6: Plots of the changing activity of water in the system for (a) the NIB model and (b) the CCR model. The thickness of the hydrated channel adjacent to the slab (LVC) is water-saturated (a_{H_2O} = 1.0). When melting initiates, water partitions into the melt phase,

and the activity of water rapidly decreases after that point. The initial activities are all equal to 1.0, but are spread out slightly in the y-direction on the plot for clarity.

Figure 7: Cartoon of the LVC, slab fluid releases, and melting regions for an example mature-slab model with a moderate slab dip angle. Indicated are potential simple melt migration pathways that would allow deeper melts to impact rear-arc lava chemistry and shallower melts to impact volcanic front (VF) lava chemistry. The trends observed by [15, 19] for cross-arc variations reflecting distance to WBZ are shown.

Figure 8: Plots of modeled trace element ratios for the limited fluid interaction case: (a, b) indicators of progressive mantle source depletion as a function of slab fluid source lithology and dehydration pressure (MORB value for Zr/Nb ~30 [15] and for Nb/Yb ~0.92 [54]); (c-e) indicators of degree of hydration (U/Th) versus dehydration pressure and degree of mantle source depletion as a function of slab fluid source lithology and compared to regional datasets [55, 72]; (f, g) indicators of mantle source enrichment (La/Yb) versus indicators of slab fluid contribution (Ba/La) as a function of slab fluid source lithology and compared to regional datasets.

Figure 9: Plots of modeled trace element ratios for the limited fluid interaction case: (a, b) ratios of fluid-mobile elements to HFSE as a function of slab fluid source lithology and dehydration pressure and (c-f) versus indicators of slab fluid contribution and compared to regional datasets [55, 72].

Figure 10: Schematic diagrams for the extension of the calculation column for the fully-equilibrated case at lower pressures (a, b) and at higher pressures (c, d). The columns for the two cases are not extended the same vertical distance.

Figure 11: Fractionation paths for a calculated primary Miyakejima magma composition, plotted with the Miyakejima lava dataset [72].

Figure 12: Schematic models for transport of fluids and/or melts to the back-arc melting region: (a) in this model, which is similar to the ultimate development of the mature slab system (Chapter 2), continuous fluxing of the deep melt region by a strong serpentinite-derived fluid source results in progressive lengthening of the fluid pathway such that low-pressure, hydrous melts can be generated by direct delivery of fluids to the base of the BABB melting region. (b) Diapiric rise of hydrous melts generated at depth transport material to the base of the BABB melting region. (c) Melt transport along a vertical path beyond the water-saturated solidus results in a freezing of the melt into an enriched mantle packet, which is transported along solid streamlines to the base of the BABB melting region.

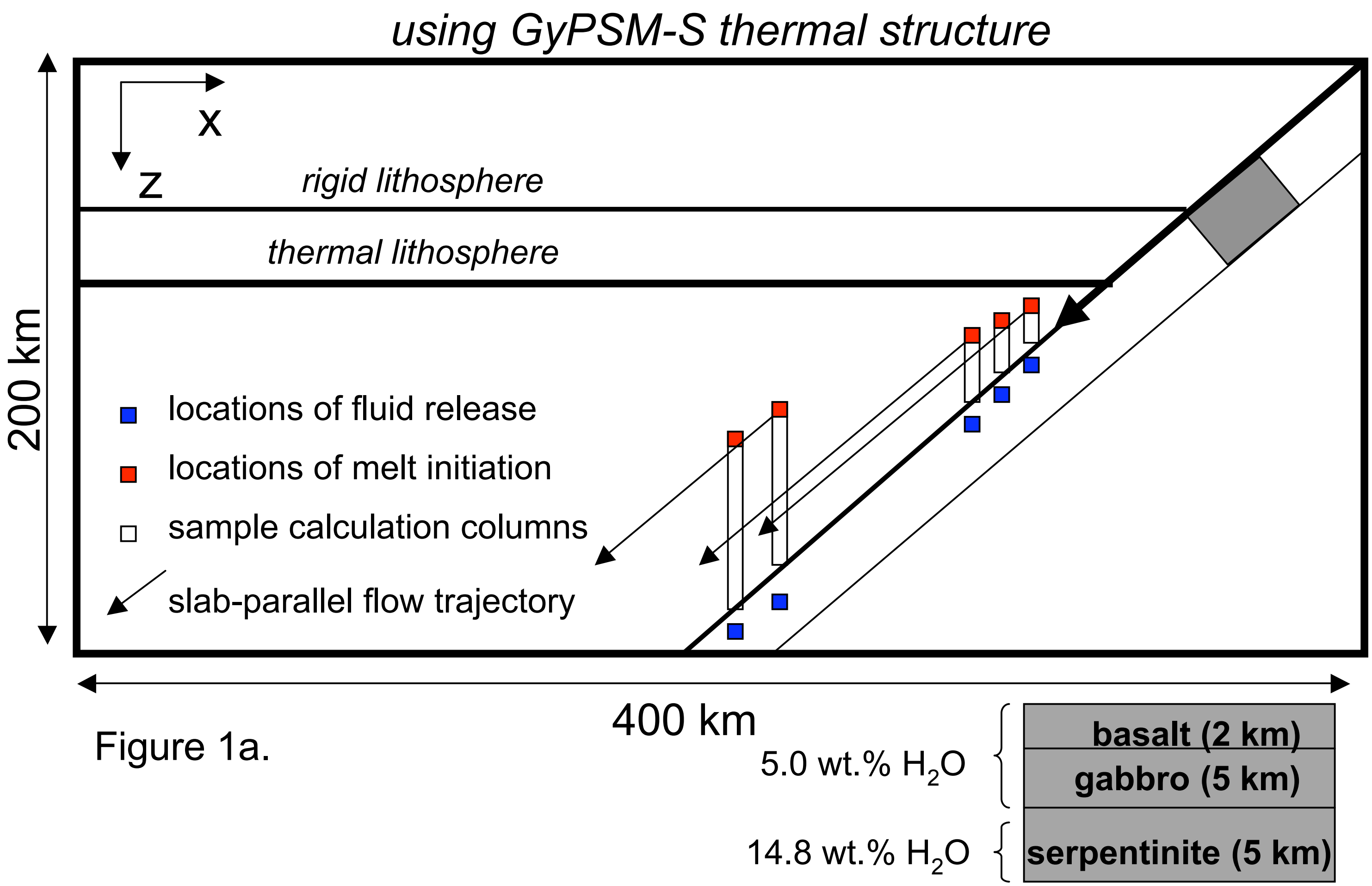
using GyPSM-S thermal structure
x
z
rigid lithosphere
thermal lithosphere
200 km
400 km
🟦 locations of fluid release
🟥 locations of melt initiation
☐ sample calculation columns
slab-parallel flow trajectory
5.0 wt.% H_2O
14.8 wt.% H_2O
basalt (2 km)
gabbro (5 km)
serpentinite (5 km)

Figure 1a.

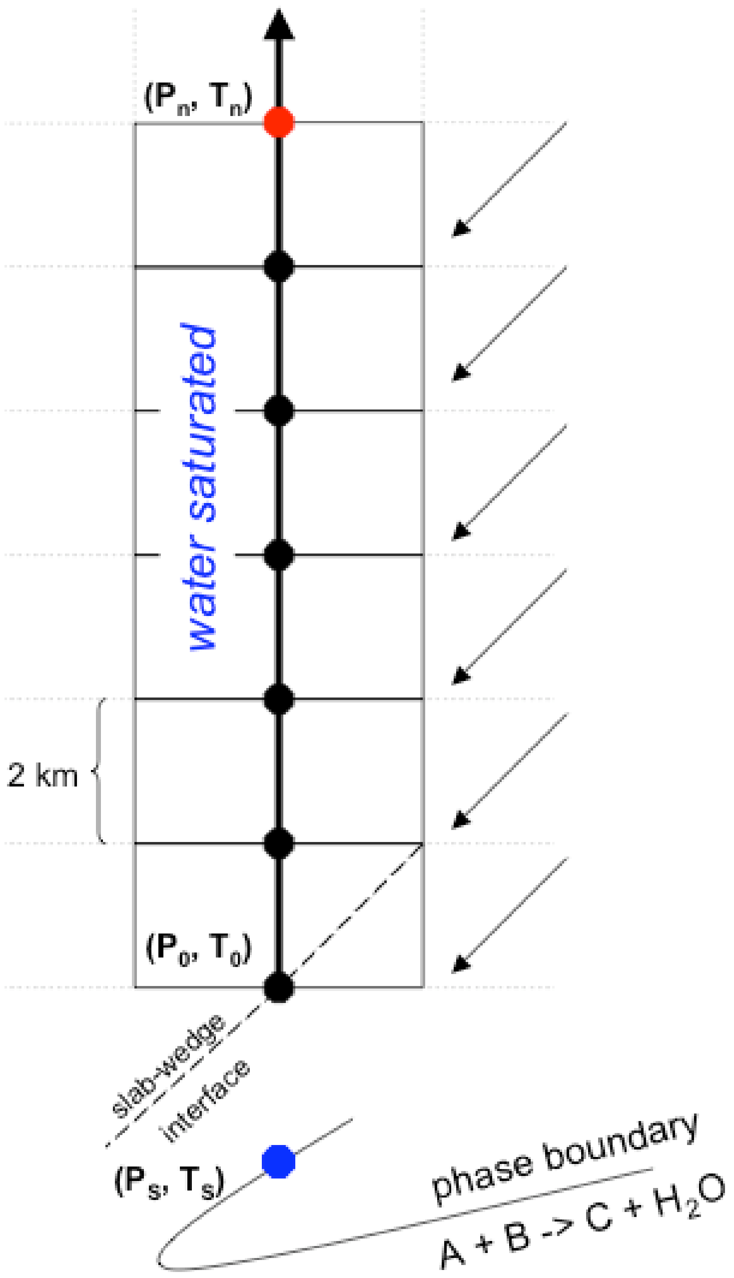
(P$_n$, T$_n$)
water saturated
2 km
(P$_0$, T$_0$)
slab-wedge interface
(P$_S$, T$_S$)
phase boundary
A + B -> C + H$_2$O

Figure 1b.

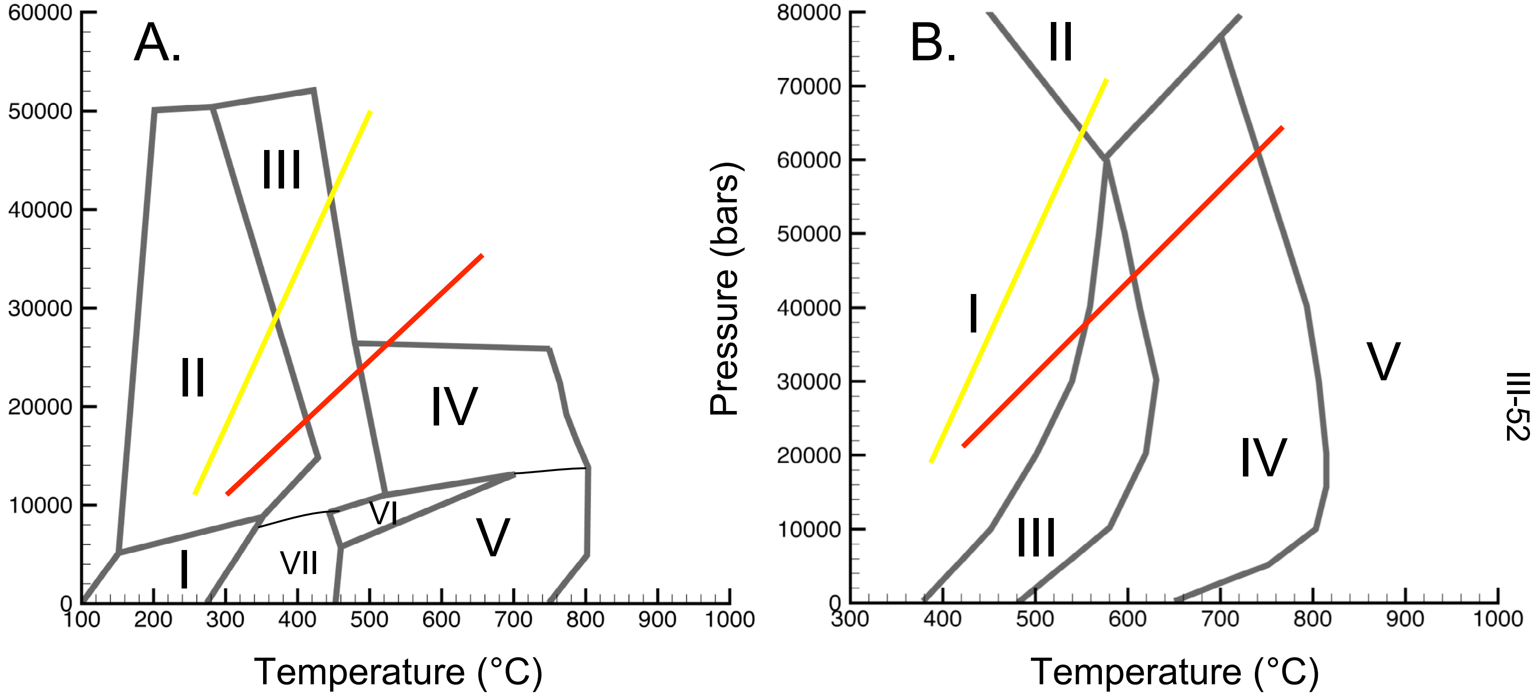
A.
60000
50000
40000
30000
20000
10000
0
100
200
300
400
500
600
700
800
900
1000
Temperature (°C)
I
II
III
IV
V
VI
VII
B.
80000
70000
60000
50000
40000
30000
20000
10000
0
300
400
500
600
700
800
900
1000
Pressure (bars)
Temperature (°C)
I
II
III
IV
V

Figure 2.

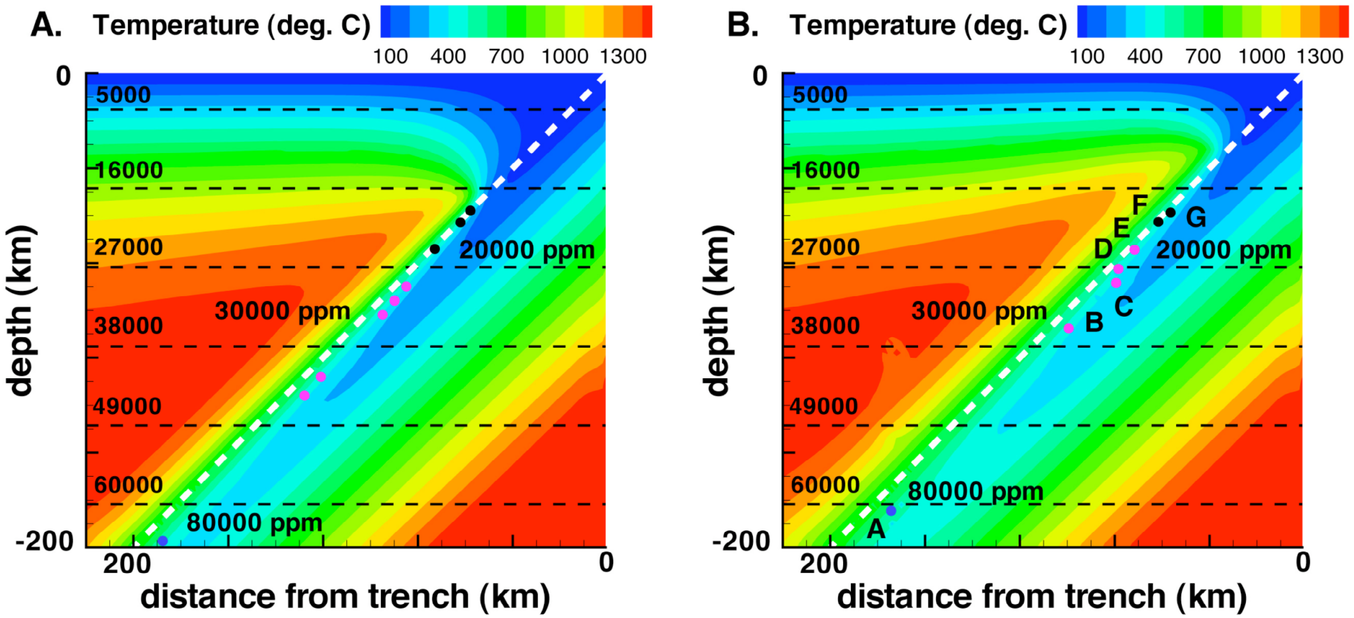
A.
Temperature (deg. C)
100
400
700
1000
1300
0
-200
depth (km)
5000
16000
27000
38000
49000
60000
20000 ppm
30000 ppm
80000 ppm
200
0
distance from trench (km)
B.
Temperature (deg. C)
100
400
700
1000
1300
0
-200
depth (km)
5000
16000
27000
38000
49000
60000
F
G
E
D
20000 ppm
C
30000 ppm
B
80000 ppm
A
200
0
distance from trench (km)

Figure 3.

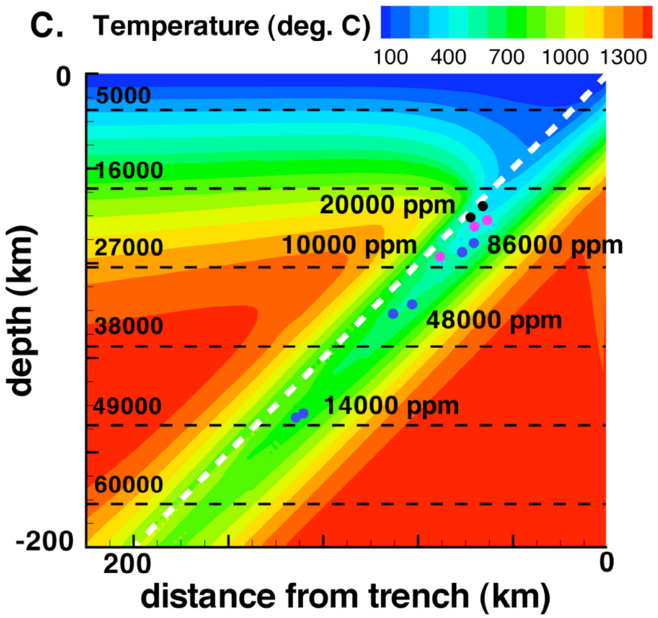
C.
Temperature (deg. C)
100
400
700
1000
1300
0
-200
depth (km)
5000
16000
27000
38000
49000
60000
20000 ppm
10000 ppm
86000 ppm
48000 ppm
14000 ppm
200
0
distance from trench (km)

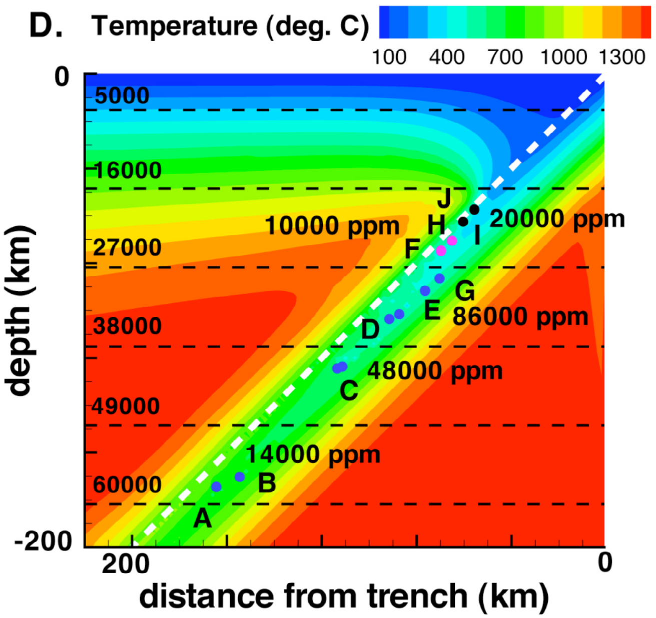
D.
Temperature (deg. C)
100
400
700
1000
1300
0
-200
depth (km)
5000
16000
27000
38000
49000
60000
J
10000 ppm
H
20000 ppm
I
F
G
E
86000 ppm
D
48000 ppm
C
14000 ppm
B
A
200
0
distance from trench (km)

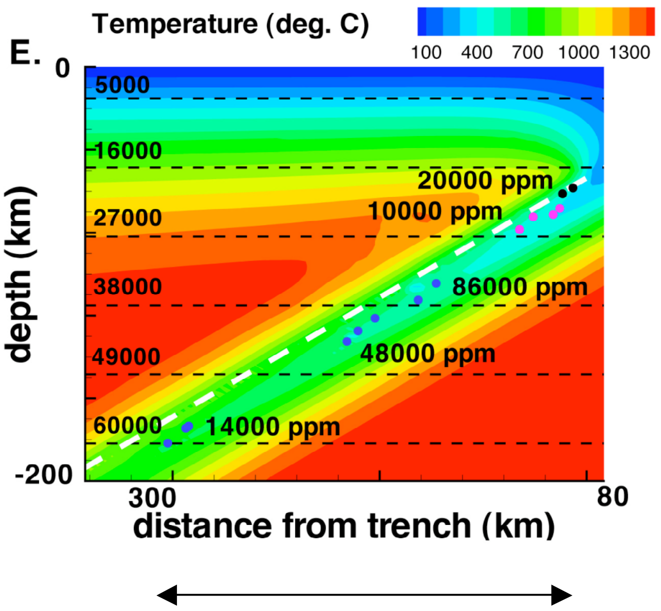
E.
Temperature (deg. C)
100
400
700
1000
1300
0
-200
depth (km)
300
80
distance from trench (km)
5000
16000
27000
38000
49000
60000
20000 ppm
10000 ppm
86000 ppm
48000 ppm
14000 ppm

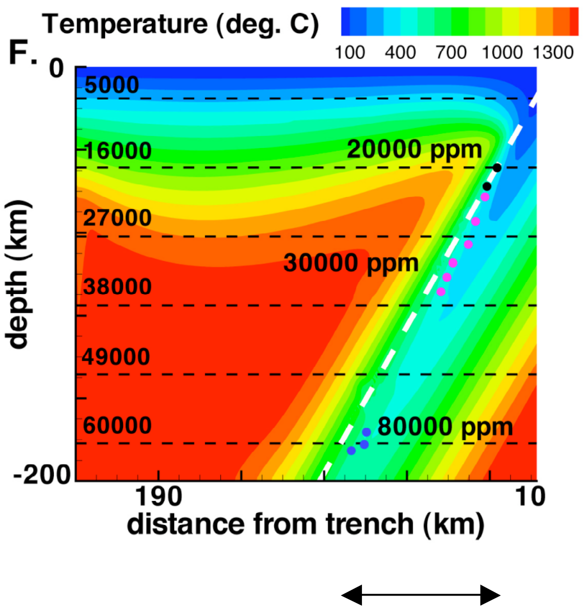
F.
Temperature (deg. C)
100
400
700
1000
1300
0
-200
depth (km)
190
10
distance from trench (km)
5000
16000
27000
38000
49000
60000
20000 ppm
30000 ppm
80000 ppm

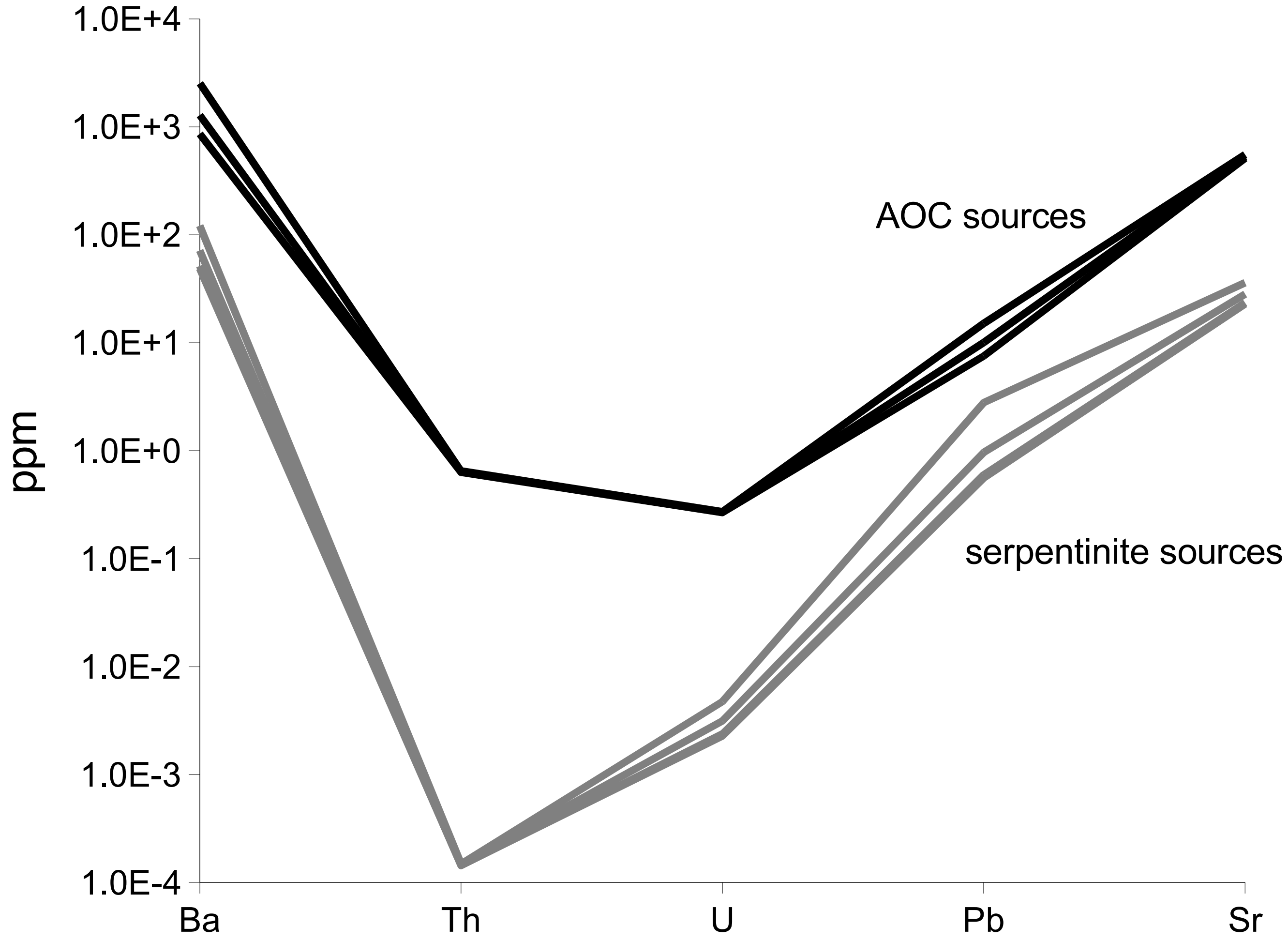
1.0E+4
1.0E+3
1.0E+2
1.0E+1
1.0E+0
1.0E-1
1.0E-2
1.0E-3
1.0E-4
ppm
Ba
Th
U
Pb
Sr
AOC sources
serpentinite sources

Figure 4.

Figure 5.

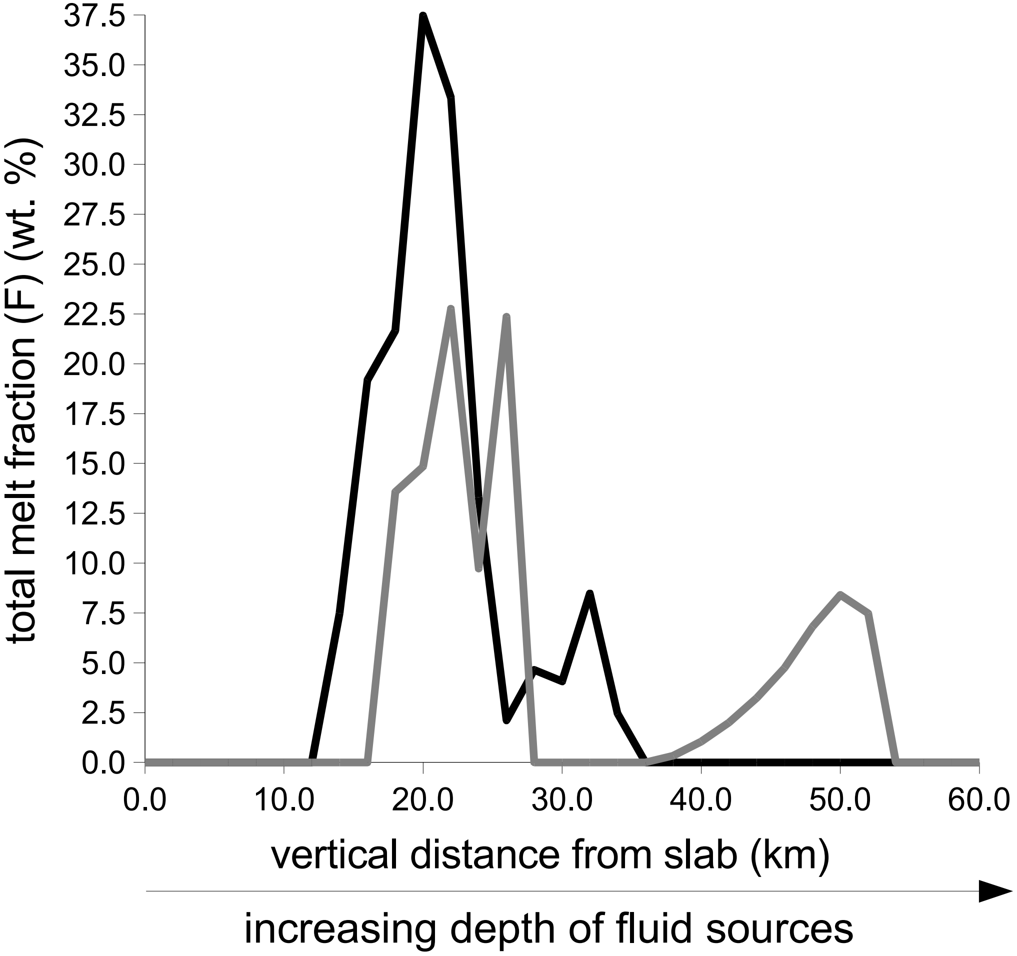
total melt fraction (F) (wt. %)
37.5
35.0
32.5
30.0
27.5
25.0
22.5
20.0
17.5
15.0
12.5
10.0
7.5
5.0
2.5
0.0
0.0
10.0
20.0
30.0
40.0
50.0
60.0
vertical distance from slab (km)
increasing depth of fluid sources

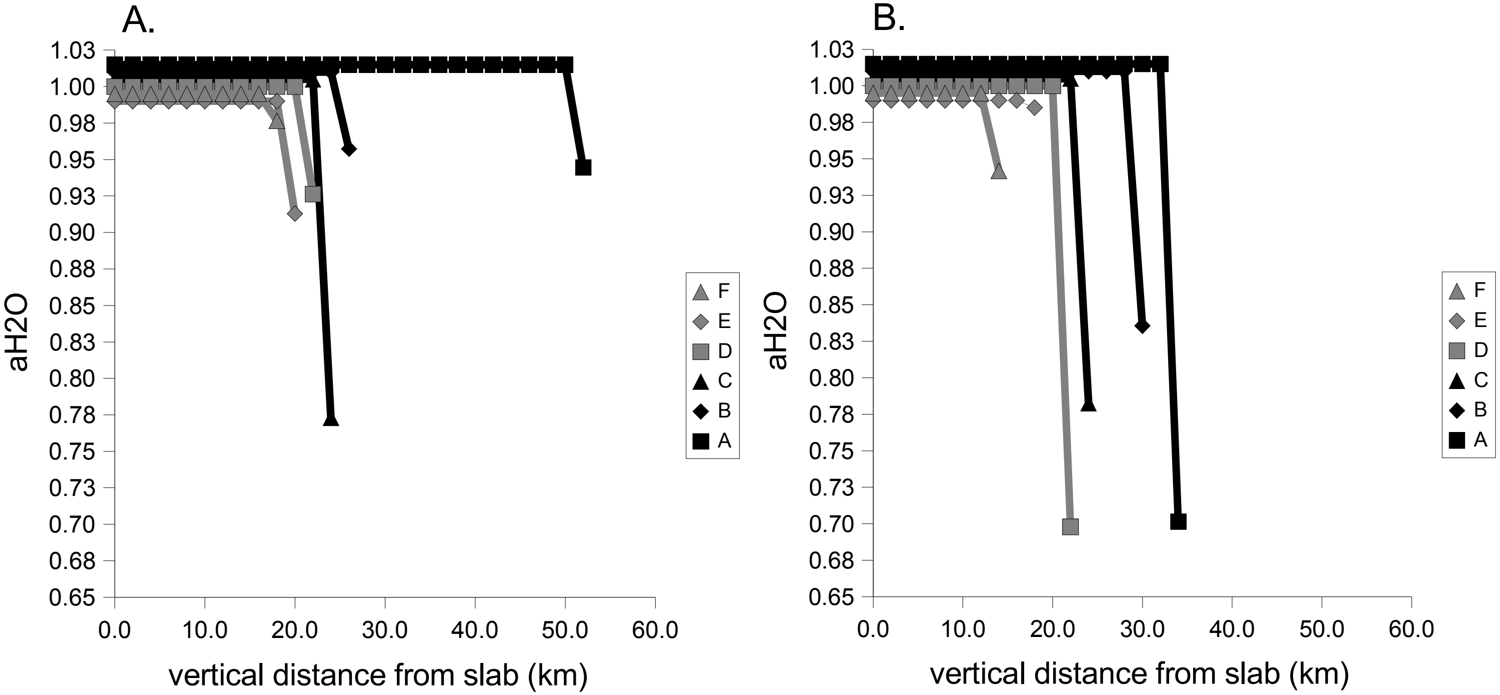
A.
B.
aH2O
1.03
1.00
0.98
0.95
0.93
0.90
0.88
0.85
0.83
0.80
0.78
0.75
0.73
0.70
0.68
0.65
0.0
10.0
20.0
30.0
40.0
50.0
60.0
vertical distance from slab (km)
F
E
D
C
B
A

Figure 6.

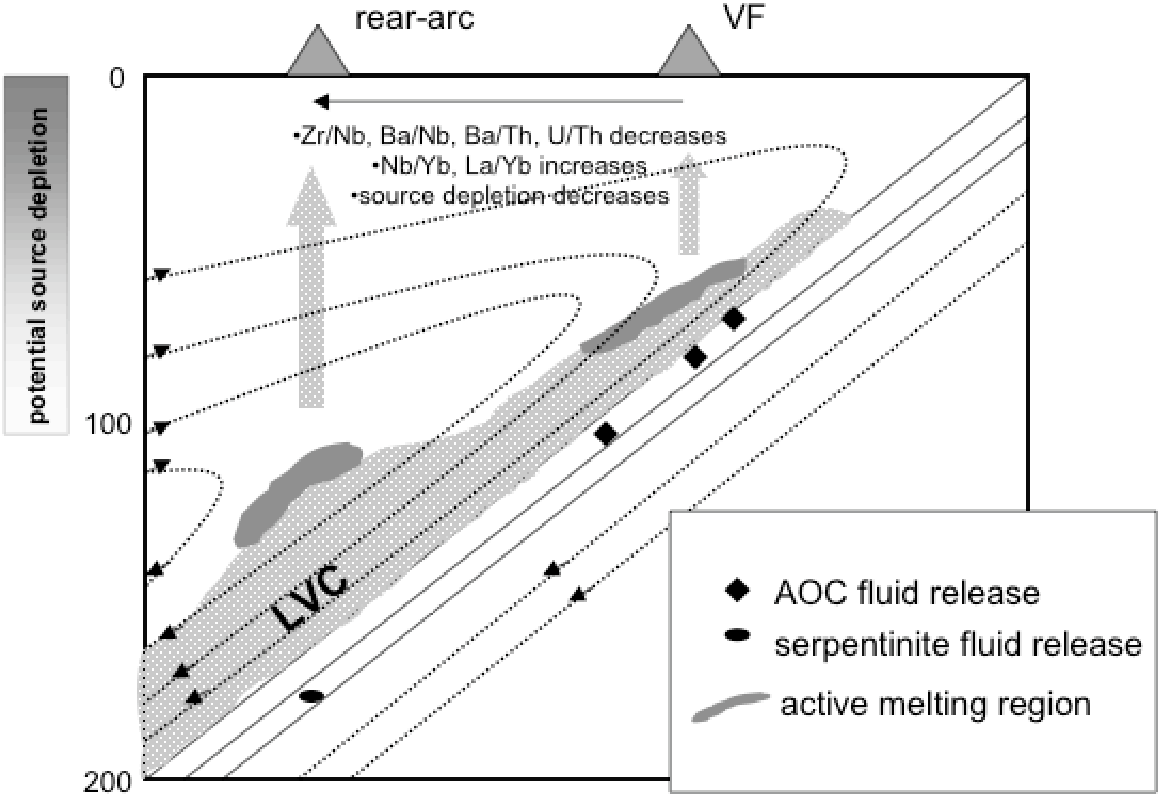
rear-arc
VF
0
100
200
potential source depletion
•Zr/Nb, Ba/Nb, Ba/Th, U/Th decreases
•Nb/Yb, La/Yb increases
•source depletion decreases
LVC
◆ AOC fluid release
● serpentinite fluid release
active melting region

Figure 7.

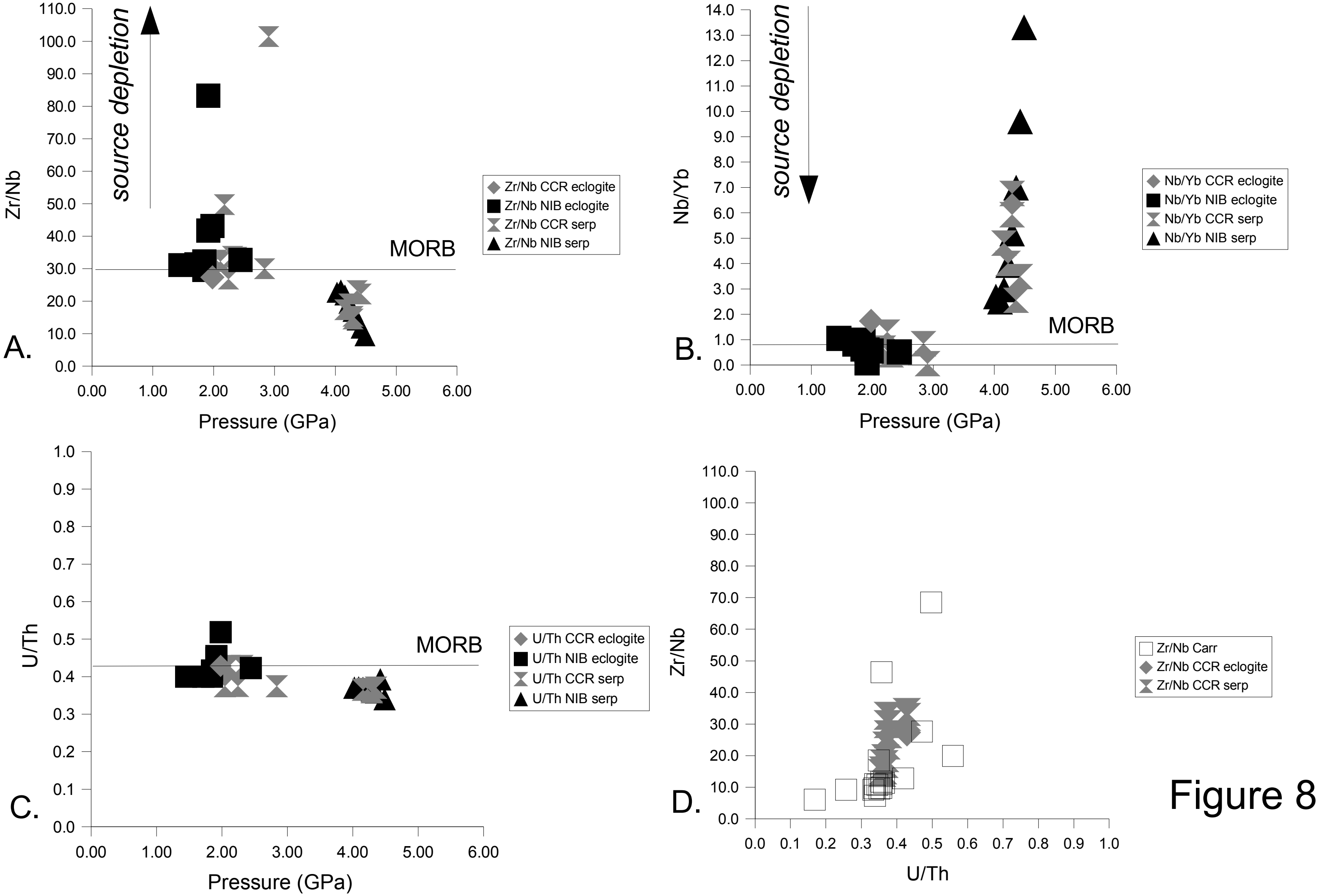
A.
Zr/Nb
source depletion
MORB
Pressure (GPa)
0.0
10.0
20.0
30.0
40.0
50.0
60.0
70.0
80.0
90.0
100.0
110.0
0.00
1.00
2.00
3.00
4.00
5.00
6.00
◆ Zr/Nb CCR eclogite
■ Zr/Nb NIB eclogite
⧗ Zr/Nb CCR serp
▲ Zr/Nb NIB serp
B.
Nb/Yb
source depletion
MORB
Pressure (GPa)
0.0
1.0
2.0
3.0
4.0
5.0
6.0
7.0
8.0
9.0
10.0
11.0
12.0
13.0
14.0
0.00
1.00
2.00
3.00
4.00
5.00
6.00
◆ Nb/Yb CCR eclogite
■ Nb/Yb NIB eclogite
⧗ Nb/Yb CCR serp
▲ Nb/Yb NIB serp
C.
U/Th
MORB
Pressure (GPa)
0.0
0.1
0.2
0.3
0.4
0.5
0.6
0.7
0.8
0.9
1.0
0.00
1.00
2.00
3.00
4.00
5.00
6.00
◆ U/Th CCR eclogite
■ U/Th NIB eclogite
⧗ U/Th CCR serp
▲ U/Th NIB serp
D.
Zr/Nb
U/Th
0.0
10.0
20.0
30.0
40.0
50.0
60.0
70.0
80.0
90.0
100.0
110.0
0.0
0.1
0.2
0.3
0.4
0.5
0.6
0.7
0.8
0.9
1.0
☐ Zr/Nb Carr
◆ Zr/Nb CCR eclogite
⧗ Zr/Nb CCR serp

Figure 8.

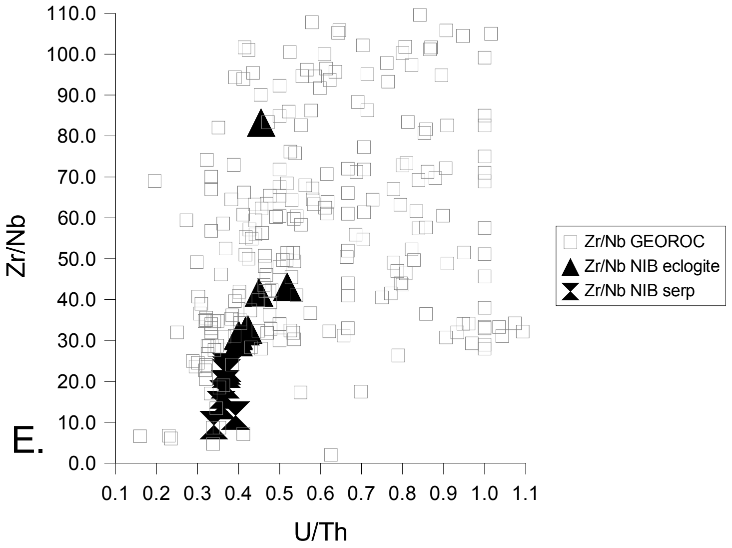
E.
Zr/Nb
110.0
100.0
90.0
80.0
70.0
60.0
50.0
40.0
30.0
20.0
10.0
0.0
0.1
0.2
0.3
0.4
0.5
0.6
0.7
0.8
0.9
1.0
1.1
U/Th
Zr/Nb GEOROC
Zr/Nb NIB eclogite
Zr/Nb NIB serp

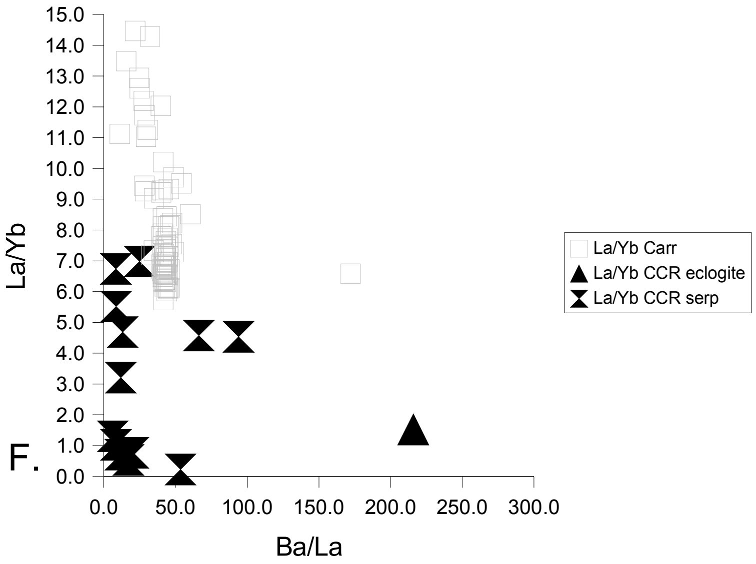
F.
La/Yb
15.0
14.0
13.0
12.0
11.0
10.0
9.0
8.0
7.0
6.0
5.0
4.0
3.0
2.0
1.0
0.0
0.0
50.0
100.0
150.0
200.0
250.0
300.0
Ba/La
La/Yb Carr
La/Yb CCR eclogite
La/Yb CCR serp

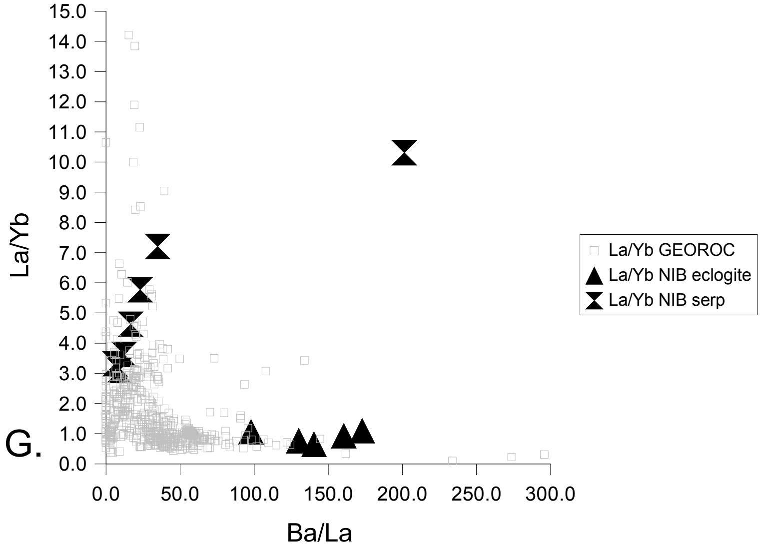
G.
La/Yb
15.0
14.0
13.0
12.0
11.0
10.0
9.0
8.0
7.0
6.0
5.0
4.0
3.0
2.0
1.0
0.0
0.0
50.0
100.0
150.0
200.0
250.0
300.0
Ba/La
La/Yb GEOROC
La/Yb NIB eclogite
La/Yb NIB serp

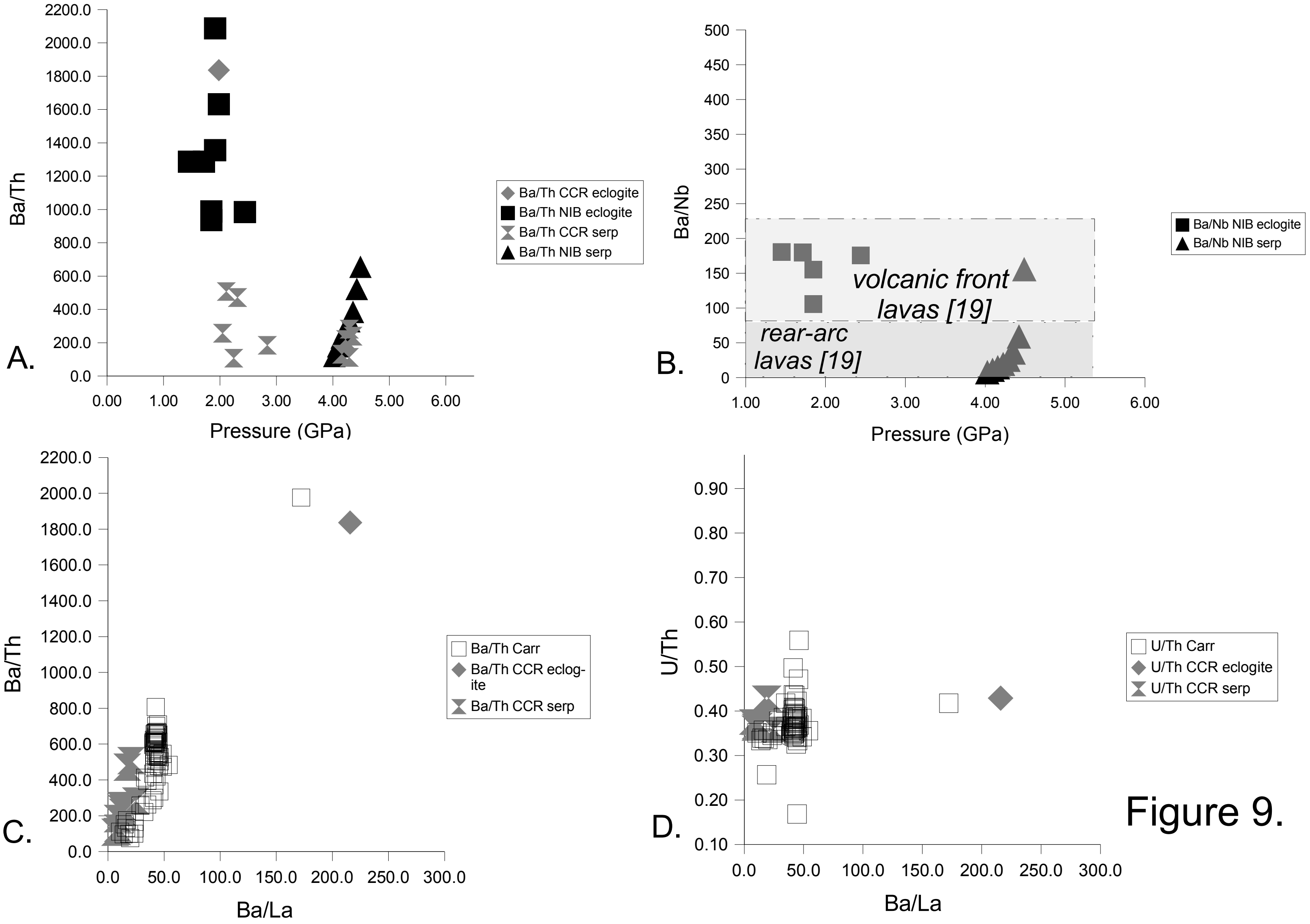
A.
Ba/Th
Pressure (GPa)
2200.0
2000.0
1800.0
1600.0
1400.0
1200.0
1000.0
800.0
600.0
400.0
200.0
0.0
0.00
1.00
2.00
3.00
4.00
5.00
6.00
Ba/Th CCR eclogite
Ba/Th NIB eclogite
Ba/Th CCR serp
Ba/Th NIB serp
B.
Ba/Nb
Pressure (GPa)
500
450
400
350
300
250
200
150
100
50
0
1.00
2.00
3.00
4.00
5.00
6.00
volcanic front lavas [19]
rear-arc lavas [19]
Ba/Nb NIB eclogite
Ba/Nb NIB serp
C.
Ba/Th
Ba/La
2200.0
2000.0
1800.0
1600.0
1400.0
1200.0
1000.0
800.0
600.0
400.0
200.0
0.0
0.0
50.0
100.0
150.0
200.0
250.0
300.0
Ba/Th Carr
Ba/Th CCR eclog-ite
Ba/Th CCR serp
D.
U/Th
Ba/La
0.90
0.80
0.70
0.60
0.50
0.40
0.30
0.20
0.10
0.0
50.0
100.0
150.0
200.0
250.0
300.0
U/Th Carr
U/Th CCR eclogite
U/Th CCR serp

Figure 9.

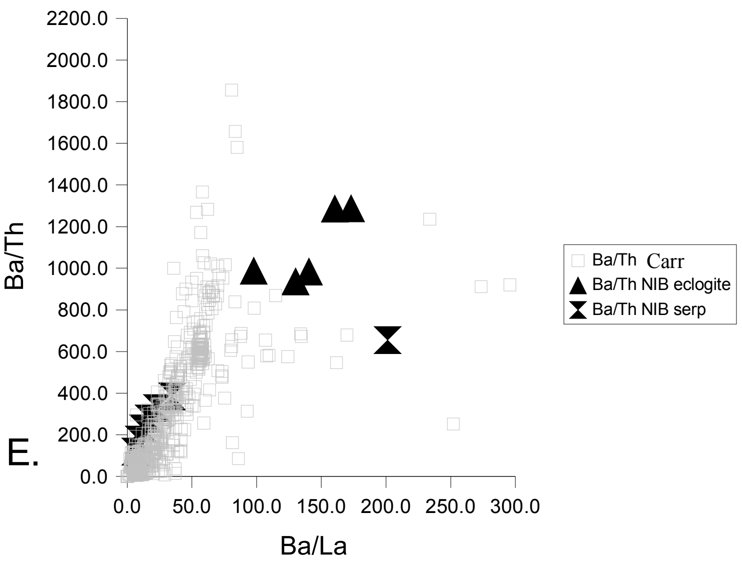
E.
Ba/Th
2200.0
2000.0
1800.0
1600.0
1400.0
1200.0
1000.0
800.0
600.0
400.0
200.0
0.0
0.0
50.0
100.0
150.0
200.0
250.0
300.0
Ba/La
Ba/Th Carr
Ba/Th NIB eclogite
Ba/Th NIB serp

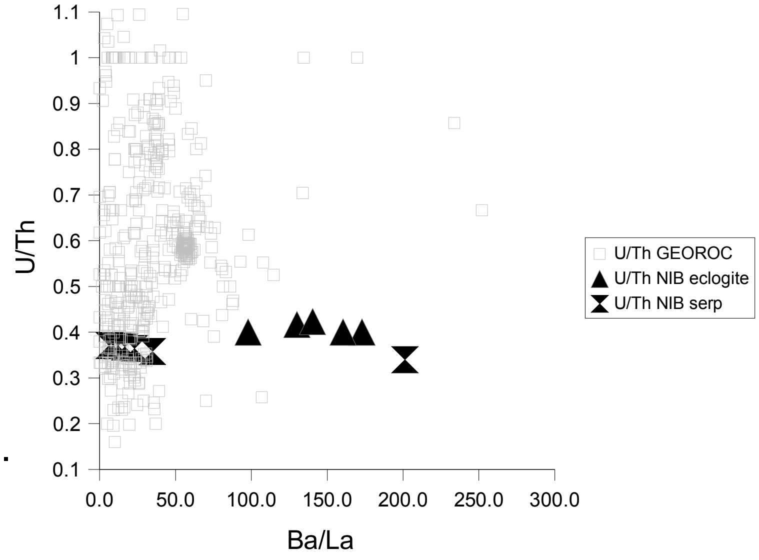
F.
U/Th
1.1
1
0.9
0.8
0.7
0.6
0.5
0.4
0.3
0.2
0.1
0.0
50.0
100.0
150.0
200.0
250.0
300.0
Ba/La
U/Th GEOROC
U/Th NIB eclogite
U/Th NIB serp

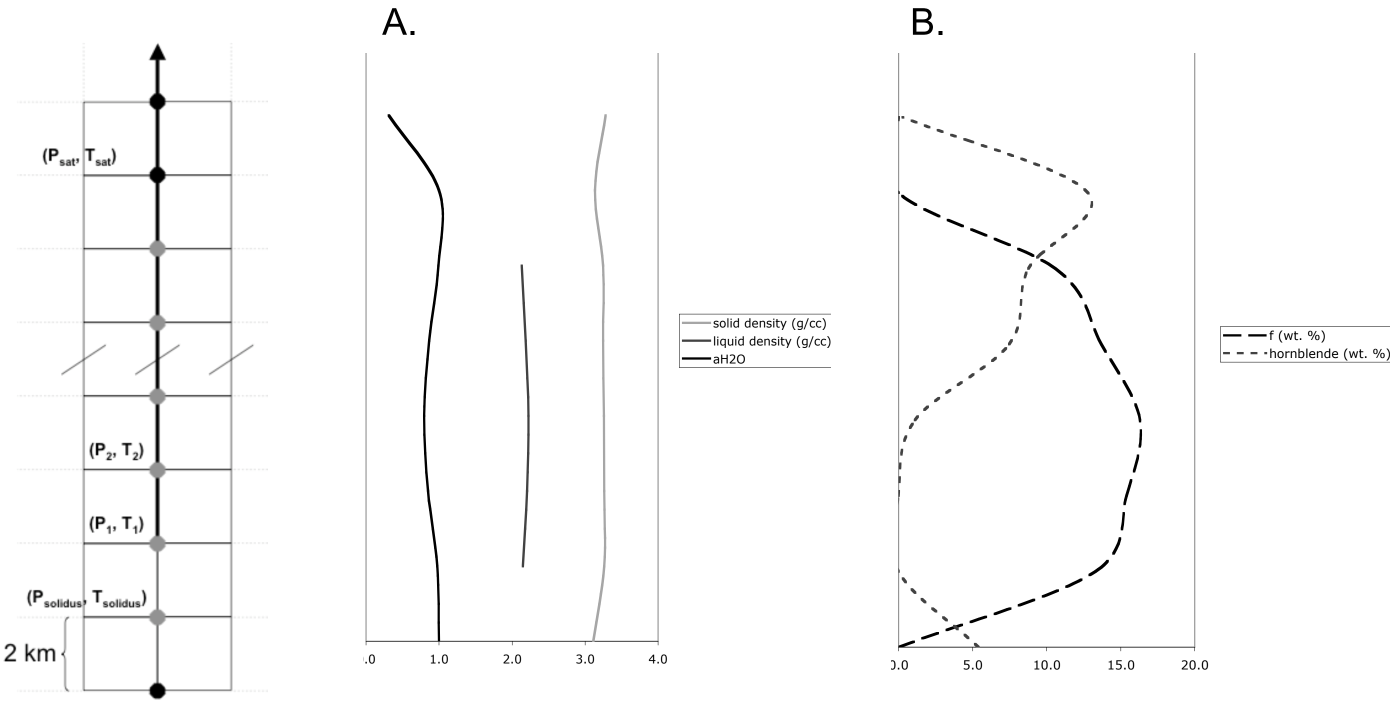
(P_sat, T_sat)
(P_2, T_2)
(P_1, T_1)
(P_solidus, T_solidus)
2 km
A.
solid density (g/cc)
liquid density (g/cc)
aH2O
.0
1.0
2.0
3.0
4.0
B.
f (wt. %)
hornblende (wt. %)
0.0
5.0
10.0
15.0
20.0

Figure 10.

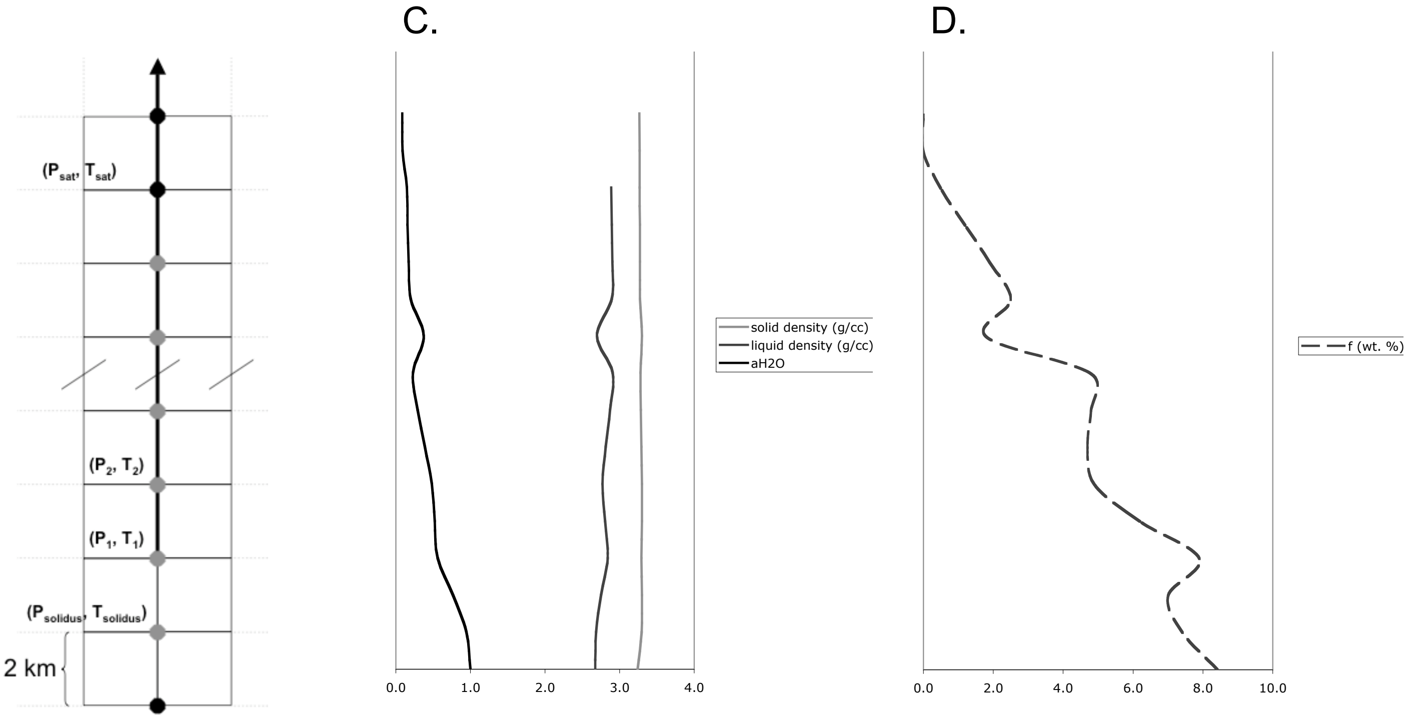
(P$_{sat}$, T$_{sat}$)
(P$_2$, T$_2$)
(P$_1$, T$_1$)
(P$_{solidus}$, T$_{solidus}$)
2 km
C.
0.0
1.0
2.0
3.0
4.0
solid density (g/cc)
liquid density (g/cc)
aH2O
D.
0.0
2.0
4.0
6.0
8.0
10.0
f (wt. %)

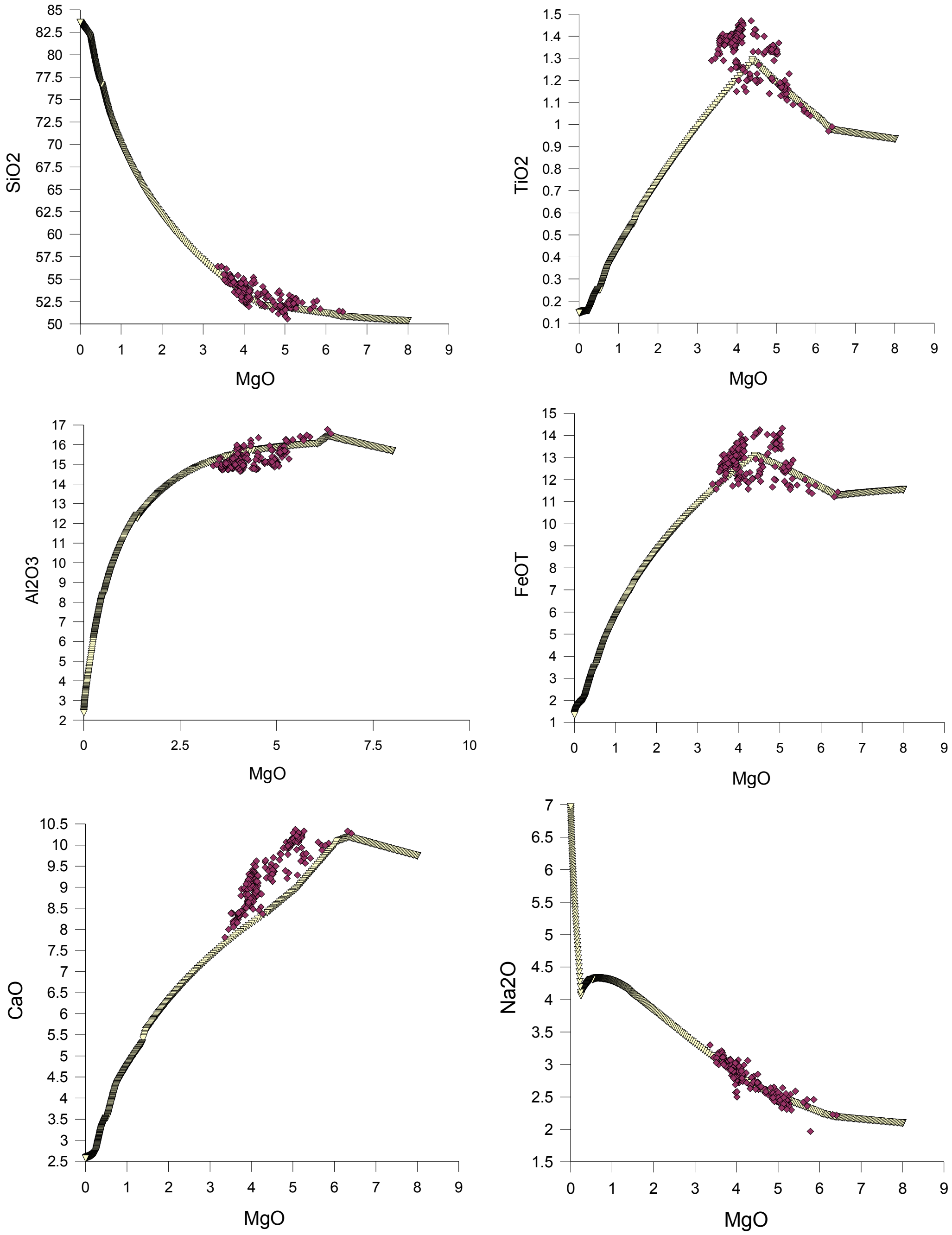
SiO2
85
82.5
80
77.5
75
72.5
70
67.5
65
62.5
60
57.5
55
52.5
50
0 1 2 3 4 5 6 7 8 9
MgO
TiO2
1.5
1.4
1.3
1.2
1.1
1
0.9
0.8
0.7
0.6
0.5
0.4
0.3
0.2
0.1
0 1 2 3 4 5 6 7 8 9
MgO
Al2O3
17
16
15
14
13
12
11
10
9
8
7
6
5
4
3
2
0 2.5 5 7.5 10
MgO
FeOT
15
14
13
12
11
10
9
8
7
6
5
4
3
2
1
0 1 2 3 4 5 6 7 8 9
MgO
CaO
10.5
10
9.5
9
8.5
8
7.5
7
6.5
6
5.5
5
4.5
4
3.5
3
2.5
0 1 2 3 4 5 6 7 8 9
MgO
Na2O
7
6.5
6
5.5
5
4.5
4
3.5
3
2.5
2
1.5
0 1 2 3 4 5 6 7 8 9
MgO

Figure 11.

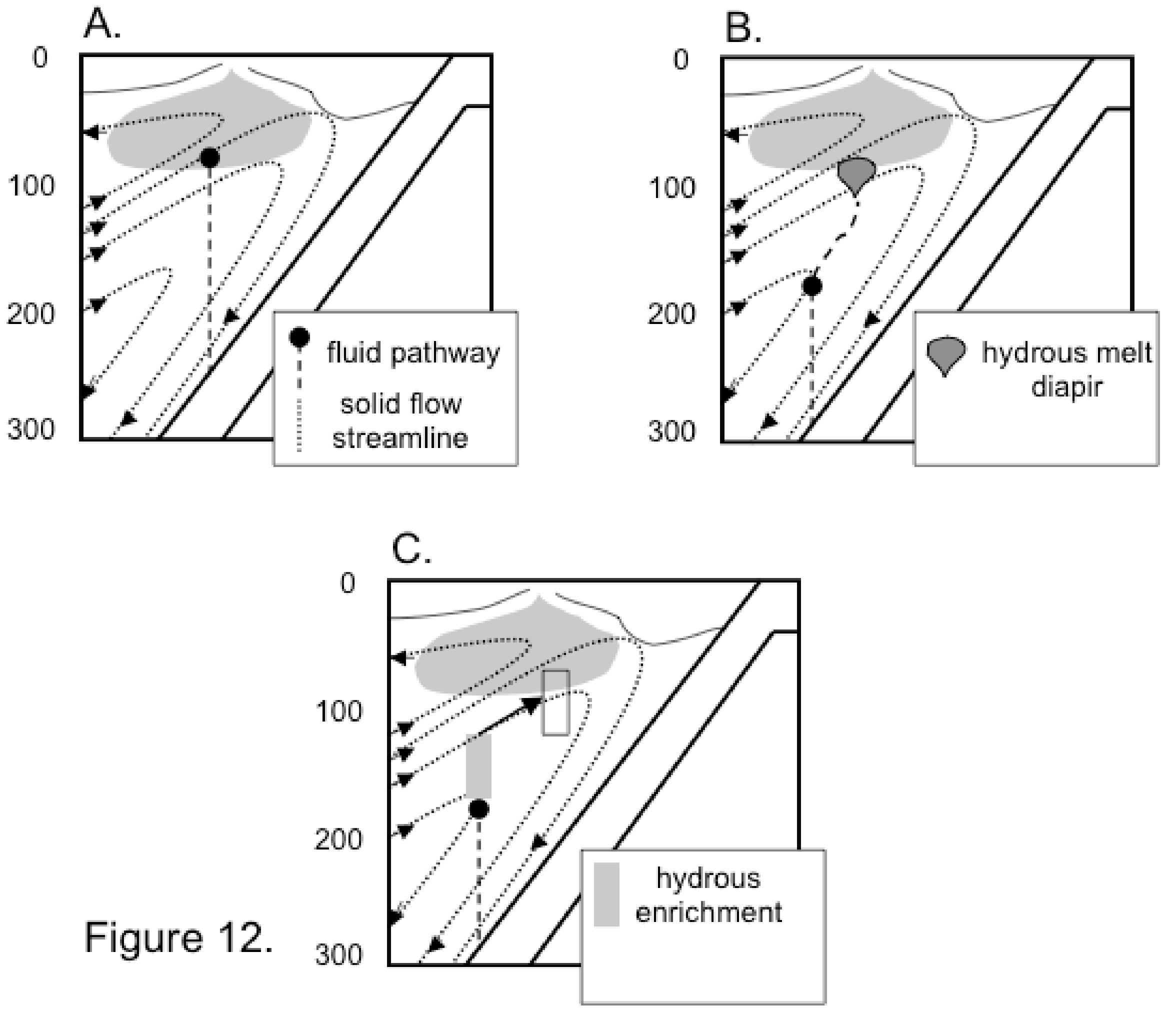
A.
0
100
200
300
fluid pathway
solid flow
streamline
B.
0
100
200
300
hydrous melt
diapir
C.
0
100
200
300
hydrous
enrichment

Figure 12.

Table 1: pHMELTS starting composition

oxide	***initial value (weight percent)***
SiO_2	44.80
TiO_2	0.13
Al_2O_3	3.99
Fe_2O_3	0.41
Cr_2O_3	0.57
FeO	7.83
MgO	38.81
CaO	3.18
Na_2O	0.28
tracer	**initial value (ppm)**
H_2O	110.00
K	60.00
Rb	0.05
Ba	0.56
Th	0.01
U	0.0032
Nb	0.15
Ta	0.01
La	0.19
Ce	0.55
Pb	0.02
Pr	0.11
Nd	0.58
Sr	7.66
Zr	5.08
Hf	0.16
Sm	0.24
Eu	0.10
Ti	716.30
Gd	0.36
Tb	0.07
Dy	0.51
Ho	0.12
Y	3.33
Er	0.35
Yb	0.37
Lu	0.06

Adapted from Workman and Hart [44]

Table 2: Partition coefficients and sample column calculation

---

trace elements (fluid-mobile)	initial ppm serpentinite	initial ppm AOC	$D^{serpentinite/fluid}$	$D^{eclogite/fluid}$	$D^{lherzolite/fluid}$
Ba	5.7000	26.0000	0.0333	0.0002	7.60E-005
Th	0.0001	0.2700	0.6667	0.4100	0.0890
U	0.0003	0.1400	0.0500	0.5100	0.0250
Pb	0.0500	0.3000	0.0040	0.0100	3.10E-003
Sr	4.0500	110.0000	0.1000	0.1900	0.0430
reference	(a)	(b)	(c)	(d)	(e)

Notes: Fluids are assumed to be released in trace element equilibrium from the source lithology (assuming to start with 100.0 g). For example, 0.5 wt. % (0.5 g) fluid fraction released from the AOC layer, using Equation (1) and the values for $D^{eclogite/fluid}$ given above, will result in a fluid carrying approximately 4972.41 ppm Ba, 0.65 ppm Th, 0.27 ppm U, 20.07 ppm Pb, and 566.86 ppm Sr.

If this fluid (0.5 g) is then added to 100.0 g of water-saturated subsolidus lherzolite at (P_0, T_0) (Table 1, assuming the composition has not been subject to prior melt depletion), the resulting bulk fluid-mobile trace element composition of the lherzolite + fluid assemblage (100.5 g) will include 25.3 ppm Ba, 0.01 ppm Th, 0.005 ppm U, 0.118 ppm Pb, and 10.46 ppm Sr.

This fluid, after equilibrating with the lherzolite, is then moved along to the next equilibration point (P_1, T_1). Using Equation (1) and the values for $D^{lherzolite/fluid}$ given above, the bulk composition of the 0.5 g of fluid equilibrated at (P_0,T_0) and removed to (P_1, T_1) is 4984.61 ppm Ba, 0.107 ppm Th, 0.167 ppm U, 14.60 ppm Pb, and 218.90 ppm Sr.

If this fluid (0.5 g) is then added to 100.0 g of lherzolite at (P_1, T_1), the resulting bulk fluid-mobile trace element composition of the lherzolite + fluid assemblage (100.5 g) will include 25.36 ppm Ba, 0.008 ppm Th, 0.004 ppm U, 0.091 ppm Pb, and 8.72 ppm Sr.

This is repeated to ($P_{solidus}$, $T_{solidus}$) when the water-saturated solidus is crossed, and melting initiates. At that point, pHMELTS calculates the melt and residue trace element composition based on the lherzolite+fluid bulk composition.

(a) serpentinite ETF1 from Scambelluri et al. [50] Supp. Mat.
(b) altered oceanic crust composition from McCulloch and Gamble [49]
(c) Tenthorey and Hermann [48] best estimates of partition coefficients, U and Sr are lower estimates
(d) Brenan et al. [47] calculated eclogite/fluid partition coefficients
(e) Brenan et al. [47] calculated lherzolite/fluid partition coefficients

Table 3: A summary of subduction zone model parameters

approximate subduction region	Central Costa Rica	Southeastern Costa Rica	Northern Izu-Bonin	Northern Mariana	Additional Model 1	Additional Model 2
abbreviation	CCR	SCR	NIB	NMAR	ADD1	ADD2
latitude	~8-11° N	~8-11° N	~32° N	~23° N	N/A	N/A
longitude	~275-277° E	~276-278° E	~135-143° E	~143-145° E	N/A	N/A
rate of convergence (mm/yr)	87 [36]	90 [36]	50 [29]	47.5 [29]	87.00	50.00
slab dip (degrees)	45 [36]	30 [36]	45 [29]	60 [29]	45	45
slab thermal age (Ma)	18 [36]	15 [36]	135 [29]	165 [29]	135	18
rigid lithospheric thickness (km)	50 [36]	50 [36]	32 [71]	32 [71]	50	50
thermal lithospheric thickness (km)	88	88	66	66	88	88
dimensional grid resolution (z, x)	2.0 km, 2.0 km	2.0 km, 3.4641 km	2.0 km, 2.0 km	2.0 km, 1.1547 km	2.0 km, 2.0 km	2.0 km, 2.0 km
dimensions of model domain (z, x)	200 km, 400 km	200 km, 692.8 km	200 km, 400 km	200 km, 230.9 km	200 km, 400 km	200 km, 400 km

numbers in square brackets are references

Table 4: Major element chemistry of modeled initial melts

Major Oxides (wt. %)	**CCR_F14L**	**CCR_E14L**	**CCR_E16L**	**CCR_E18L**	**CCR_D18L**	**CCR_D20L**	**CCR_D22L**	**CCR_C22L**	**CCR_C24L**	**CCR_B26L**	**CCR_B28L**	**CCR_B30L**	**CCR_A30L**	**CCR_A32L**	**CCR_A34L**
SiO_2	42.45	40.61	42.51	43.49	41.01	43.57	41.84	39.65	38.99	36.54	36.68	37.15	36.56	37.00	37.45
TiO_2	0.24	0.26	0.32	0.34	0.41	0.32	0.35	0.33	0.41	0.91	0.83	0.88	0.89	0.73	0.96
Al_2O_3	18.00	17.11	14.69	14.17	12.52	10.08	15.62	9.11	11.58	2.49	2.72	3.02	2.05	2.31	2.58
Fe_2O_3	0.55	0.67	0.80	0.82	1.03	0.86	0.70	0.87	0.97	1.65	1.77	1.78	1.98	1.70	1.83
Cr_2O_3	0.41	0.41	0.60	0.61	0.58	0.80	0.26	0.61	0.33	0.79	0.62	0.56	0.55	0.52	0.52
FeO	5.42	6.37	6.08	5.87	7.63	6.62	7.93	9.00	10.39	15.51	15.63	15.85	16.60	15.72	16.55
MgO	8.62	9.87	10.63	10.54	13.04	14.00	12.42	18.63	17.50	21.92	23.40	23.43	24.32	25.40	24.05
CaO	6.18	6.68	7.65	7.86	8.33	8.12	7.65	8.98	8.57	4.42	5.37	5.22	5.16	5.95	4.79
Na_2O	3.03	2.21	1.28	1.15	0.86	0.69	3.24	0.25	1.74	5.79	3.75	4.38	3.47	2.45	5.01
H_2O	15.10	15.81	15.44	15.15	14.59	14.94	9.98	12.56	9.53	9.98	9.23	7.73	8.43	8.21	6.26
Temperature (deg. C)	1116.59	1137.11	1153.33	1153.95	1201.91	1213.20	1234.69	1295.70	1312.51	1359.62	1379.62	1396.22	1395.51	1408.88	1419.34
Pressure (bars)	19800.00	21780.00	21120.00	20460.00	23760.00	23100.00	22440.00	29040.00	28380.00	42900.00	42240.00	41580.00	44220.00	43560.00	42900.00

(a)

Major Oxides (wt. %)	**NIB_F18L**	**NIB_E20L**	**NIB_D20L**	**NIB_D22L**	**NIB_C20L**	**NIB_C22L**	**NIB_C24L**	**NIB_B26L**	**NIB_A38L**	**NIB_A40L**	**NIB_A42L**	**NIB_A44L**	**NIB_A46L**	**NIB_A48L**	**NIB_A50L**	**NIB_A52L**
SiO_2	47.83	45.83	43.54	45.15	42.97	45.11	44.86	40.89	36.55	36.53	36.53	36.58	36.68	36.85	36.98	37.10
TiO_2	0.22	0.28	0.29	0.32	0.30	0.38	0.30	0.34	0.94	0.95	0.93	0.89	0.83	0.76	0.70	0.72
Al_2O_3	18.19	16.83	16.36	15.26	16.11	13.17	16.83	12.79	1.91	2.08	2.27	2.48	2.72	2.99	3.28	3.57
Fe_2O_3	0.59	0.69	0.73	0.78	0.74	0.91	0.67	0.85	1.20	1.46	1.66	1.76	1.77	1.70	1.62	1.65
Cr_2O_3	0.49	0.45	0.55	0.52	0.57	0.62	0.31	0.55	1.24	0.97	0.79	0.68	0.61	0.57	0.56	0.54
FeO	3.48	4.74	5.28	5.30	5.52	5.63	5.80	7.58	14.79	15.39	15.72	15.78	15.63	15.29	14.91	14.94
MgO	6.25	8.27	8.91	9.44	9.21	10.17	9.70	13.71	19.76	21.05	22.09	22.88	23.45	23.96	24.09	23.82
CaO	6.27	7.29	7.04	7.81	6.90	8.33	7.79	8.49	3.05	3.69	4.31	4.87	5.39	5.93	6.29	6.27
Na_2O	1.71	1.64	1.54	1.30	1.82	0.42	2.27	1.12	9.56	7.54	5.90	4.64	3.70	2.90	2.49	2.71
H_2O	14.97	13.98	15.77	14.11	15.85	15.26	11.47	13.68	11.00	10.34	9.81	9.43	9.21	9.05	9.09	8.70
Temperature (deg. C)	1049.55	1114.18	1115.12	1139.98	1121.71	1144.74	1168.48	1221.36	1332.97	1349.68	1362.99	1373.08	1380.33	1386.66	1387.76	1389.42
Pressure (bars)	14520.00	17160.00	19140.00	18480.00	19800.00	19140.00	18480.00	24420.00	44880.00	44220.00	43560.00	42900.00	42240.00	41580.00	40920.00	40260.00

(b)

Table 5: Calculated Miyakejima primary magma composition

Major Oxides (wt. %)	
SiO_2	51.19
TiO_2	0.95
Al_2O_3	15.94
FeO*	11.74
MgO	8.13
CaO	9.91
Na_2O	2.13
H_2O	1.50

Chapter IV:

Geophysical Implications of Izu-Bonin Mantle Wedge Hydration from Chemical Geodynamic Modeling

Laura Baker Hebert and Michael Gurnis

For submission to The Island Arc

Abstract

Using two-dimensional (2-D) dynamic models of the Northern Izu-Bonin (NIB) subduction zone, we show that a particular localized low-viscosity ($\eta_{LV} = 3.3\times10^{19}$-$4.0\times10^{20}$ Pa s), low-density ($\Delta\rho \sim -10$ kg/m^3 relative to ambient mantle) geometry within the wedge is required to match surface observations of topography, gravity, and geoid anomalies. The hydration structure resulting in this low-viscosity, low-density geometry was produced via coupled geochemical and geodynamic modeling of the NIB subduction system with GyPSM-S (**G**eod**y**namic and **P**etrological **S**ynthesis **M**odel for **S**ubduction, Chapter 2). First-order controls on the geometry of hydration within the wedge arise from the thermal structure of the down going slab (mostly a function of slab age), slab dip angle, the mechanism of fluid transport within the wedge, and the spatial position of the water-saturated solidus within the wedge. Slab convergence velocity is a second-order control on the geometry of the hydrated region. On the basis of this modeling, predictions can be made as to the specific low-viscosity geometries associated with geophysical surface observables for other subduction zones based on regional subduction parameters.

Keywords: viscosity, topography, geoid, gravity, Izu-Bonin, water, nominally anhydrous minerals, wedge, GyPSM-S

1. Introduction

Convergent margin volcanism can be explained in terms of the addition of volatiles from the dehydrating slab to the overlying mantle wedge, leading to water-fluxed melting. The locations of dehydration reactions within the slab are dependent on the thermal structure, which is defined primarily by the age of the plate (Chapter 3). Infiltration and equilibration of hydrous fluids with the wedge peridotite allows for increasing amounts of water to be stabilized in nominally anhydrous minerals (NAM) such as olivine, garnet, orthopyroxene, and clinopyroxene [1], as well as for the appearance of hydrous phases such as amphibole, antigorite, chrysotile, and chlorite [2-5]. The effect of increasing water content in NAM is twofold: (i) decreasing solidus temperatures [6, 7] and (ii) water-weakening that reduces the viscosity of the solid material [8]. As such, there is a dual effect of hydrous fluid introduction on the geochemistry of initial melts within the system (Chapter 3) and on the force balance within the wedge. Previous modeling studies [2, 4, 9, 10] have addressed the role of water and wedge hydration in the subduction system together with dynamical considerations, emphasizing the role of hydrous minerals in acting as transport agents and/or sources of water and using phase diagram parameterization to approximate the chemical variables within the system. However, these studies do not include a full evaluation of water stability in NAM or the changing bulk composition of the peridotite due to melt extraction. A coupled approach is necessary to fully address the problem, which includes melting, water in hydrous and nominally anhydrous phases, water-weakening, and a changing bulk composition due to melting.

GyPSM-S (**G**eod**y**namic and **P**etrological **S**ynthesis **M**odel for **S**ubduction)

(Chapter 2) is used to constrain the development of hydrated regions within the mantle wedge of a subduction zone from a coupled perspective. It involves iterative interaction between ConMan, a two-dimensional thermal and variable viscosity numerical flow model [11], and pHMELTS, a thermodynamic energy minimization algorithm that can calculate water partitioning into NAM [6, 12, 13]. The significance of the coupled scheme is the detailed tracking of fluids and their rheological and chemical effects from release to initiation of melting. The primary results of the GyPSM-S models demonstrate the existence of a low-viscosity channel (LVC) within the mantle wedge, the process by which LVCs form, and the limitations on the LVC geometry (Chapter 2).

The LVC is effectively a zone of water saturation that develops immediately adjacent to the subducting slab and extends into the wedge to variable distances depending on subduction parameters. It consists of hydrous phases and NAM with high water contents (water solubility increases with pressure, and can approach thousands of ppm at the base of the model domain when all NAM phases are considered). The thickness of the zone is limited at the base by the subducting plate and at the top by the spatial position of the water-saturated peridotite solidus within the wedge. Variations in thickness of the LVC from model to model depend on the thermal structure within the wedge and the intensity and location of fluid sources from the slab. Due to assumptions of vertical fluid transport within GyPSM-S, active melting initiates almost directly over fluid sources, and is confined to a relatively thin layer (~6 km) immediately above the LVC. This restriction on the thickness of the melting region is a function of the near-fractional melting scheme employed within GyPSM-S as well as the assumption that water transport can only occur within a hydrous fluid, as opposed to a hydrous migrating melt. As water is partitioned strongly into the melt phase, once the water-saturated solidus is crossed, the water activity in the system drops below unity and no water is available for further transport in a hydrous fluid phase, resulting in the cessation of melting. Seismic tomography has allowed imaging of inclined low-velocity zones sub-parallel to the slab within the mantle wedge, coincident with the instantaneous melting regions predicted by GyPSM-S [14]. In pressure-temperature space, the peridotite solidus is a function of composition. With the near-fractional melting scheme implemented in pHMELTS, melts are removed above a certain residual porosity, and therefore the bulk composition of the advecting solids changes (becoming more depleted in incompatible elements) along with the solidus temperature.

LVCs exist over a large range of subduction parameter space (slab age, convergence velocity, slab dip angle) and can be important for considering the initiation of melting within the wedge, the state of stress within the wedge, and for changing slab dip angle [15] as well as for transport of hydrated, relatively fertile near-slab material into the deep mantle [5, 16-20]. The influence of the existence of the LVC and other localized low-viscosity geometries within the wedge on the overall flow field and force balance can be examined through surface observations sensitive to the viscosity structure, such as dynamic topography and gravity and geoid anomalies [21, 22]. The geoid measurement represents a combination of contributions from internal density variations (thermal and mineralogical) and from boundary deformations induced by the flow field [23, 24]. Subduction zones can be characterized by having long-wavelength (10^3 - 10^4 km) geoid highs over slabs and shorter wavelength (10^2 km) geoid lows over trenches [25, 26]. Long-wavelength geoid highs are interpreted as indicative of a radial viscosity structure where the viscosity of the upper mantle (η_{UM}) is less than the viscosity of the lower mantle (η_{LM}), leading to regional compensation of subducting slabs [24, 27]. However, shorter-wavelength geoid anomalies and the depth of back-arc basins may be resolved by studying viscosity variations caused by thermal or compositional variations within the upper mantle [26]. Numerical models have demonstrated that stresses are transmitted through viscous coupling in the wedge from the subducting slab to the overlying lithosphere [25, 28, 29]. Billen and Gurnis [21] demonstrated that a localized region of low viscosity within the upper mantle rather than an overall change in asthenospheric viscosity was required to match the topography and geoid signal on the overlying plate, as a reduction in wedge viscosity reduces the coupling between the slab and the overlying plate, resulting in a less negative dynamic topography. Billen and Gurnis [22] then successfully investigated the relative sizes and shapes of low-viscosity, low-density regions necessary to match signals in the Tonga-Kermadec and Central Aleutian subduction zones. While it is thus well understood that localized low-viscosity regions may be important to the force balance within mantle wedges, the mechanisms of development of these regions and how the regional geometries change based on changing subduction behaviors have only recently been established (Chapter 2). The next logical step would be to attempt to match observed geophysical signals in a particular locality with a modeled fluid-source-based hydration structure. Accordingly, in this study, we present the impact of GyPSM-S modeled localized low-viscosity regions on geophysical signals (topography and geoid and gravity anomalies) from the northern Izu-Bonin subduction system (32 ºN latitude, ~136-146 ºE longitude), particularly emphasizing the manner of development of the low-viscosity region as the primary influence on the geometry.

The northern Izu-Bonin (NIB) subduction system can be described by the descent of relatively old (~135 Ma) Pacific lithosphere beneath the younger Philippine Sea Plate at a moderate convergence velocity of around 5.0 cm/yr and a convergence angle of 45° (Fig. 1) [30]. The Izu-Bonin arc crust between the Izu-Ogasawara trench and the Shikoku Basin is relatively thin (~20 km), and is defined by a narrow (~300 km in width) topographic high over the arc of ~3 km with an associated gravity high of ~100 mGal. The trench is defined by a topographic low of ~ -3 km and a gravity low of ~ -280 mGal. Seismic investigation has determined a velocity structure that can be interpreted as different lithological layers within the arc crust [31-34], most notably a middle crustal layer with *P*-wave velocities approximating mean continental crustal velocities (6.4 km/s [35]). To the west of the arc (Shikoku back-arc basin), and to the east of the trench (Pacific plate), the oceanic crust is uniformly ~8 km in thickness [32]. The relative offset in the bathymetry on either side of the arc-trench area is due to the difference in ages of the two converging oceanic plates. The geoid, filtered from degree and order 2 to 70, is described by a broad high over the arc complemented by a low over the trench. The close proximity of the Kyushu trench and arc to the west leads to a somewhat lower amplitude high and a general decrease towards the west. Altogether, the change in height of the geoid is on the order of ~20 meters. Seismicity within the slab extends to depths of ~475 km, and there is seismic evidence for flattening of the slab within the transition zone [36-40].

2. Method

2.1.Initial GyPSM-S calculation of the shallow hydrated wedge

We used the GyPSM-S model (see Chapter 2 for full GyPSM-S model description) to describe the shallow wedge structure (< 200 km depth) for the NIB system (Fig. 2, Tables 1, 2). This allows an investigation of the development of the hydrated region immediately adjacent to the slab, from initiation to a state independent of the initial conditions and the initial fluid transient.

2.2.Extension of model domain for calculation of geophysical signals

Upon obtaining the GyPSM-S result for the shallow mantle wedge for NIB, a separate, uncoupled model for calculation of topography and geoid and gravity anomalies is constructed using ConMan (Fig. 3a) [12]. A penalty formulation is used to enforce incompressibility in the solution of the momentum equation [12]. The dynamics are controlled by conservation equations of mass, momentum, and energy with the Boussinesq approximation. The non-dimensional equations for mass and momentum are:

$$\nabla \cdot v' = 0 \qquad \text{and} \tag{1}$$

$$\nabla P' - \nabla \cdot (\eta' \nabla v') = RaT' \hat{k} \qquad , \tag{2}$$

where v' is the dimensionless velocity, T' is the dimensionless temperature, P' is the dimensionless pressure, η' is dimensionless viscosity, and $\hat{k}$ is a unit vector in the direction of gravity. The dimensionless Rayleigh number combines all the material properties:

$$Ra = \frac{g\alpha\rho\Delta T d^3}{\kappa\eta} \quad , \qquad (3)$$

where g is the acceleration due to gravity, α is the coefficient of thermal expansion, ΔT is the temperature drop across the box, d is the depth of the box, κ is the thermal diffusivity, and η is the dynamic viscosity (Table 1). The non-dimensional energy equation is:

$$\frac{\partial T'}{\partial t'} = -v' \cdot \nabla T' + \nabla^2 T' \quad , \qquad (4)$$

where t' is dimensionless time. A streamline upwind Petrov-Galerkin method [43] is used to solve Eq. (4). The model domain was extended vertically and horizontally in order to account for the long-wavelength features in the geoid signal. The model domain, 9000 km in width, extends from the surface to the core-mantle boundary (3000 km). The refined computational grid consists of 45000 bilinear quadrilateral elements: 150 in the vertical direction and 300 in the horizontal, and element resolution ranges from (40 km × 40 km) to (10 km × 10 km). A refined zone that includes the GyPSM-S subdomain has the highest resolution (10 km × 10 km). We do not explicitly include a fault. The initial thermal structures of the subducting slab and of the overlying lithosphere are defined by a half-space cooling model for each plate based on age, and the top and bottom surfaces of the model domain have isothermal, no-slip boundary conditions. The wedge flow field consists of analytical corner flow [44], and the thermal structure for the wedge is determined by solving the advection-diffusion equation (Eq. 4) with the fixed flow field to steady-state. Instantaneous flow is driven by internal thermal and chemical buoyancy forces. The slab contributes the primary thermal variation. Imposed chemical heterogeneities such as crustal layering, mineralogical phase transformations, and variations in the degree of wedge hydration are introduced as density variations and represent sources of buoyancy. The slab velocities are kinematically imposed, and slab dip in the upper mantle is a constant 45º, with a flattening to near-horizontal within the transition zone.

2.3.Internal density variations and background radial viscosity

The area of interest is restricted to the Izu-Ogasawara trench, the arc edifice, and oceanic crust immediately to the west and east (~136-146 ºE longitude). We do not account for additional structures further to the west and east in the extended model domain. A lower density island arc could contribute to topographic and gravity highs [28, 55]. Therefore, we include low-density crustal layering in the models. Arc crustal structure is defined by density anomalies interpreted from seismic velocities from the Shikoku Basin to the Izu-Ogasawara Trench [31, 32]. The along-arc variation of the crustal structure in the NIB system is distinguished by the presence of three layers: (i) upper crust interpreted as sediments and basalts with velocities that increase with depth from 1.5 km/s to 5.6 km/s over 5 km, (ii) middle crust with *P*-wave velocities of 6.1-6.3 km/s, corresponding to intermediate (andesitic to tonalitic) plutonic rocks that are close to the mean velocity of continental crust (~6.4 km/s [35]), and (iii) thick lower crust with *P*-wave velocities of 7.1-7.3 km/s, interpreted to be gabbroic igneous underplating [32]. The arc crustal thickness varies from 18 km below the forearc to 20 km beneath the central rift zone 260 km from the trench [32].

The crustal structure of the subducting Pacific plate is ~8 km thick and can be subdivided into three layers: (i) an upper crustal layer with two defining velocity characteristics: upper layer with *P*-wave velocities ranging from 1.6-1.8 km/s, and a lower layer with velocities of 3.0-4.3 km/s, (ii) middle layer with velocities of 4.7-5.7 km/s, and (iii) a lower layer with velocities 6.4-6.5 km/s [32]. For simplicity, we assume that the crust of the Shikoku Basin is the same as the Pacific plate. We are somewhat limited by the resolution of the model (10 km vertical increments along the topmost elements) in re-constructing a realistic density structure within the crust, however, we attempt to include the most important density variations despite the restrictions in resolution.

The exothermic phase transformation from olivine to wadsleyite ($\alpha \rightarrow \beta$) is represented by a density increase of 7.2% at 410 km depth, and the endothermic phase transformation from ringwoodite (γ) to perovskite plus magnesiowüstite is represented by a density increase of 8.4% at 670 km depth [50], with deflections above and below these depths associated with the cold subducting slab. The basalt to eclogite transition within the slab is accounted for by a 6% density increase within the altered oceanic crustal (AOC) layer of the down going plate. Despite evidence that including the effects of phase transformations near the transition zone in the calculation of the dynamic topography and the geoid is insignificant considering the overwhelming effect of the radial viscosity structure [51], we include these effects as part of a comprehensive approach.

The radial background viscosity structure consists of several layers: lithosphere, upper mantle, transition zone, and lower mantle. Viscosity is both temperature- and composition-dependent, with the viscosity in each layer defined with respect to a reference viscosity (η_0) with a value of 3.0×10^{20} Pa s: upper mantle ($\eta_{UM} = 1\times\eta_0$), transition zone ($\eta_{TZ} = 100\times\eta_0$), lower mantle ($\eta_{LM} = 300\times\eta_0$), and lithosphere ($\eta_{LITH} < 100$ km depth, $1000\times\eta_0$). The maximum viscosity of the slab at all depths is $1000\times\eta_0$. Parameterized regions (Fig. 3b) of hydration within the upper mantle are included based on output from the GyPSM-S model, where reductions in viscosity within the hydration zones are due to higher concentrations of water in NAM and the superposition of the thermal structure in the wedge. A depth of 400 km is considered a probable maximum for the parameterized hydrated regions in this system because of the flattening of the slab in the transition zone.

2.4. Calculation of geophysical surface observables

Calculated topography (h), geoid height (ΔN), and gravity anomalies (Δg) are compared with observations to assess the appropriateness of the viscosity and buoyancy models. We evaluate not only the preferred parameterization, which includes an extended LVC region (ELVC), but also other models (no LV region, uniform thickness LVC, and LVW) (Fig. 4). We additionally evaluate the impact of different degrees of hydration of the low-viscosity zone, leading to different magnitudes of lateral viscosity contrast within the wedge, and we evaluate different magnitudes of density contrast between the hydrated zones and the ambient nominally anhydrous wedge. The treatment in the GyPSM-S model is to use water content in olivine as the sole compositional influence on the viscosity law:

$$\eta' = \frac{\eta}{\eta_0} = \exp\left[\left(\frac{Q}{RT_0}\right) * \left(\left(\frac{T_0}{T}\right) - 1\right)\right] * \left(\frac{XH_2O}{XH_2O_{crit}}\right)^{-1} \quad , \qquad (5)$$

where $XH_2O > XH_2O_{crit}$, η_0 is the reference viscosity, Q is the activation energy, R is the gas constant, T_0 is the model reference temperature, XH_2O is the water content in olivine, and XH_2O_{crit} is the critical value for water weakening (Table 1). At upper mantle pressures and temperatures, olivine is the dominant mineral in the solid matrix, and experimental studies have focused on dislocation creep in hydrated olivine aggregates as a mantle proxy [8, 45]. However, substantial amounts of water can also go into other NAM, such as the pyroxenes and garnet.

The dynamic topography (*h*) balances the the normal stress on the top surface and becomes:

$$h = \frac{\eta_0 \kappa}{\Delta\rho\, g d^2} \sigma'_z \quad , \qquad (6)$$

where σ'_z is the non-dimensional stress, $\Delta\rho$ is the density difference across the top of the domain (representing the contrast between lithosphere and water, as we assume the top surface of the domain is covered by water), and d is the depth of the model domain (Table 1). We calculate topography using the consistent boundary flux (CBF) method [46]. We match our model topography results with the residual topography, which is the topography that results when the normal subsidence of the oceanic lithosphere is removed from the observed bathymetry (Fig. 1), using:

$$h_T = h_0 - (2600 + 220\,(A)^{1/2}) \quad , \qquad (7)$$

where h_T is the residual depth in meters, A is the age of the oceanic lithosphere in Myr (Table 1), and h_0 is the observed bathymetry in meters [47, 48]. We compute the predicted geoid height in the wavenumber domain and include contributions from topography on the top surface and density anomalies within the model domain, assuming no density anomalies outside the domain (density anomalies within the domain are converted into mass sheets at each layer of nodes within the model, and topography along the top surface is likewise converted to a mass sheet and summed to form the surface response). To account for the difference in model plate ages, the topography is shifted by a mean value along the edge of the domain before computing geoid height. Testing of the topography and geoid calculations against established benchmarks [49] was performed (Appendix IV-A). Gravity anomalies are also computed in the wavenumber domain. The gravity and geoid results were both subjected to low bandpass filters in order to attenuate frequencies higher than were represented in the regional datasets.

3. Modeling Results

3.1.GyPSM-S modeling of NIB shallow wedge structure

The NIB model results (Fig. 2) show the development of the hydrated wedge due to the subduction of a mature slab at a moderately slow convergence velocity (Chapters 2, 3).

The locations of the dehydration reactions within the slab layers are determined by the relatively cool thermal structure and result in a bimodal distribution. Low- to mid-pressure fluid releases are dominantly from the AOC layers (from increasing depths into the slab), and strong, high-pressure fluid release originates in the lithospheric serpentinite slab layer. The fluid release from the serpentinite layer results in a continuous cooling of the melting region, due to the effects of latent heat of melting. This cooling culminates in a retreat of the water-saturated solidus into the wedge, and a lengthening of the deeply-originating fluid transport pathway, leading to the development of a long hydration corridor through the wedge. Ultimately, with advection of this hydrated region by corner flow towards the slab, the shallow hydrated region approaches the shape of a wedge (LVW), or a very thick channel (ELVC), where the left boundary of the hydrated geometry is controlled by the deepest location of fluid release from the slab, assuming a vertical fluid trajectory. The higher-pressure extension of the ELVC is in the form of a uniformly-thick LVC, as the flow field continues along near-slab-parallel streamlines. This particular shape is in contrast to the relatively uniformly thick low-viscosity channels (LVC) associated with the subduction of relatively younger slabs, or when the slab dip angle is steeper, resulting in narrowing of the region of fluid infiltration into the wedge.

Through water-weakening, these regions of water-saturation translate into low-viscosity zones relative to the ambient solid matrix. In this end-member case of vertical fluid transport, it is the interplay between the slab dip angle and the deepest location of slab fluid release that determines the lateral extent of the wedge geometry. The depth extent of the GyPSM-S model is controlled by the stability of pHMELTS (< 200 km). However, there is evidence for the deeper stability of hydrous phases, such as phase-A, which may result in deeper fluid releases and a wider wedge geometry (LVW). The hydrated NAM, as opposed to hydrous mineral phases, are stable, and can transport water to great depths (Chapter 2), the basis for the theoretical continuation of the LVC to the transition zone. We investigate the response of surface observables for several geometries of varying upper mantle lateral viscosity (no LV, LVC, ELVC, and LVW) (Table 3).

As a result of the viscosity formulation (Eq. 5), the viscosity calculated is a function of both temperature and composition, specifically, water content in olivine. Therefore, the viscosity within the hydrated regions (parameterized by an average $XH_2O_{olivine}$), while significantly reduced relative to an anhydrous value, is non-uniform due to the superimposed thermal structure. Density variations produced by the GyPSM-S calculation for the low-viscosity regions relative to ambient nominally anhydrous mantle wedge are on the order of $\Delta\rho \sim -50$ to -20 kg/m^3. However, previous modeling [22] investigated the range $\Delta\rho \sim -50$ to 0 kg/m^3, and we therefore include this range in the geophysical modeling for completeness (Table 3). The low-viscosity regions calculated by GyPSM-S effectively increase the upward component of flow as material crosses the boundary between the nominally anhydrous mantle wedge and the hydrated region.

3.2. Topography

Incorporation of the low-viscosity region has the primary influence of increasing the topography associated with the arc edifice. Without a low-viscosity region (no LV, Fig. 5e), the calculated topography for the arc is too low and too narrow as compared with that observed, and the trench depth is underestimated. When a low-viscosity channel is added (LVC1, Fig. 5f), fore-arc topography increases to more closely match that observed and trench depth increases to match that observed. The incorporation of the wedge-type structure (ELVC4, Fig. 5g) generates a peak in the arc topography associated with the maximum horizontal extent of the hydrated region in the shallow mantle wedge, more closely matching the amplitude of the observed dataset in that area. Increasing the relative viscosity difference between the ambient mantle wedge and the low-viscosity region by increasing the amount of water in olivine (ELVC5) results in a further increase in the calculated topography by 280 m and an increase in the trench depth.

Increasing the lateral and depth extent of the ELVC to approach a true wedge (LVW2, Fig. 5h) has a significant influence on the shape of the calculated topography. The lateral extent of the ELVC/LVW corresponds to the deepest point of slab dehydration, assumed to result in a long fluid pathway similar to the NIB GyPSM-S model result (Chapter 2, Fig. 2). As the lateral extent of the ELVC increases from the nominal LVC width (50 km), the topography changes from a smooth top to one that peaks within the arc, followed by the smooth top again as the increases in calculated topography due to the low-viscosity zone are added away from the highs associated with the arc edifice (Fig. 6a). The peak is caused by the sharp edge to the low-viscosity region that results in a concentration in stress [26]. Therefore, the peaks in the topography over the relatively narrow (~300 km) Izu-Bonin arc edifice require a low-viscosity region directly beneath it. Because the maximum width LVW (LVW2, 400 km) does not result in a peaked signal, this calculation cannot constrain a maximum depth of fluid release. However, the calculation can be very useful in determining shallower depths of fluid release from the slab, most likely between 100 and 250 km depth and involving dehydration of a lithospheric serpentinite slab source.

Adding, and then changing, the shape of the low-viscosity region (LVC to ELVC) increases trench depth, and more closely predicts of the trench depth compared with that observed. Changing the density within the low-viscosity regions to match GyPSM-S output has an additional significant effect on the calculated topography (Fig. 6b, c). Decreasing the density in the ELVC due to water-saturation by 20 kg/m^3 (the lower end of the value predicted by GyPSM-S modeling) relative to the ambient nominally anhydrous wedge results in a very close match of the calculated topography and that observed by increasing both the maximum height of the model topography (by ~2.3 km) and the width of the model topography. Decreasing the density by the maximum value (50 kg/m^3) results in a considerable over prediction of topographic height (by ~3.4 km). Based on the calculated topography, the preferred parameters, which result in a close match to the amplitude and width of the regional dataset as judged by the NRMS deviation (Fig. 7a), involve the horizontal extension of the shallow wedge hydration region to ~200-350 km and include a density contrast within the LV zone of -30 to -10 kg/m^3, which is on the lower end of the range predicted by [22].

3.3.Gravity anomalies and geoid height

Prediction of the gravity associated with the Izu-Bonin trench and arc system, but with no low-viscosity region, results in a slight under prediction of trench depth and near-trench variations (Fig. 5i). Similar to the results for topography, introduction of an LVC produces a larger amplitude high near the trench, providing a better match to that observed (LVC1, Fig. 5j), particularly in the fore-arc region. Lateral extension of the LVC in the shallow wedge results in an increasing amplitude for the gravity anomaly away from the trench, and significant over predictions relative to the regional dataset (Fig. 5k, Fig. 6d). However, extension of the low-viscosity region into an LVW geometry, where hydration is produced at depths beyond the arc edifice, provides a better match to that observed (LVW2, Fig. 5l).

Introducing a density variation within the modeled low-viscosity regions results in a similar effect as in the topography, specifically an increase in amplitude (Fig. 6e, f). As the topography in the arc region increases, due to a lessening of the dynamic depression of the arc, the gravity anomaly increases. Varying the density contrast from -50 to 0 kg/m^3 between the low-viscosity region and the ambient mantle wedge in conjunction with the lateral extent of the LV zone shows that the best fit to the regional gravity profile is actually given by $\Delta\rho$ = -10 to 0 kg/m^3 over a range of lateral extents, or an LVC geometry with $\Delta\rho$ = -30 to 0 kg/m^3 (Fig. 7b).

Calculation of the model geoid height without a low-viscosity region results in a broad high over the arc and a broad low over the trench, with a similar shape to the observed dataset (Fig. 5a). The amplitude for the height over both the arc and the trench is larger than that of the regional dataset. Addition of a low-viscosity region increases the amplitude over the arc (Fig. 5b-d), and increasing the relative viscosity contrast by increasing the average water in olivine content has no apparent effect. In fact, besides the initial perturbation seen with the introduction of the LVC from the case lacking any low-viscosity zone, changing geometry of the low-viscosity region does not have a significant effect on the geoid height.

4. Discussion

4.1.Subduction parameters and LV zone geometry

It is apparent from the modeling results in this, and previous [21, 22, 26], studies that the particular geometry of the localized low-viscosity zone is important, and can be reflected in surface observations of geophysical quantities over subduction zones. Previous investigations have alluded to the role of fluids in producing the low-viscosity region, and have imposed specific geometries to match regional observations of the dynamic topography, geoid and gravity anomalies [22]. However, this study is based on the results from coupled geochemical and geodynamic modeling that tracks fluids from sources within the slab through reaction of the fluids with the slab-adjacent wedge material to melt production, resulting in the development of hydrated regions within the wedge (Chapter 2). Variations in the geometry of the hydrated regions result from changing subduction parameters such as slab dip, convergence velocity, and slab age and the time-dependence of the hydration process. We therefore are able to link fundamental aspects in subduction zones such as the depth of fluid transport within the slab, the dehydration pattern, fluid flux, and fluid migration pathways with the resulting size and depth extent of low-viscosity regions within the wedge. This study compares the results of modeling a particular subduction region (NIB) to surface observations of topography, gravity and geoid anomalies, to test the ability of the coupled model to determine the low-viscosity geometry.

The primary influence on the geometry of the LVC are the fluid release pattern from the slab, which, in turn, depends on the thermal structure of the slab mostly determined by slab age, and the slab dip, as steeper-dipping slabs lead to narrower regions of fluid infiltration. Slab convergence velocity has a secondary influence on fluid release pattern and is therefore a second-order control on LVC geometry. More mature slabs, such as seen in the NIB model, allow for shallower fluid releases from the AOC layers within the slab, and a strong, deep fluid release from the serpentinite layer within the slab. The strong, deep fluid release may result in the time-dependent lengthening of the deep fluid pathway, and an eventual ELVC structure. Limitations on the depth extent of the GyPSM-S model domain restrict modeled dehydration to less than 200 km, but it is possible for even deeper dehydration reactions to occur either within the slab serpentinite layer or within hydrous phases stabilized within the hydrated slab-adjacent wedge. Assuming a similar lengthening of the fluid pathways, LVW structures with a greater lateral extent may form from even deeper slab fluid sources. In NIB, however, comparison of the observed topography and gravity signals with computed values results in the conclusion that fluid release occurs within the interval 150-350 km depth, with an associated density reduction within the LV zone of ~ -10 kg/m^3 (Fig. 7c), values in agreement with GyPSM-S results. Subduction of younger slabs results in a fluid release pattern involving low- to mid-pressure dehydration of the AOC layers and the serpentinite layers within the slab, and a deep release from the serpentinite layer. However, due to the warmer thermal structure, the deepest reaction does not produce a similar intensity of fluid release as in the mature slab case, and the hydration structure is of approximately uniform thickness to the base of the model domain (LVC), with slight thickening directly over locations of fluid infiltration. Changing slab dip does not appear to impact the dehydration pattern, but does influence the geometry of the low-viscosity region generated.

The results of this study were influenced by the inclusion of the high-viscosity lid, background radial viscosity structure, low-density crustal model, and the higher-density eclogite layer within the slab, but not by the inclusion of the phase transformations associated with transition zone seismological boundaries. The background values for the transition zone and lower mantle viscosity ($100\times\eta_0$, $300\times\eta_0$) are relatively high, compared with previous studies [24].

For this study, we imposed an uniform, average value for water content in olivine over the entire low-viscosity region of either 1000 ppm (model ELVC4) or 2000 ppm (model ELVC5). GyPSM-S calculated water contents in olivine over the shallow water-saturated wedge (< 200 km depth) for the NIB model range from 150 - 1400 ppm, increasing with pressure, and so this average value does not reflect the more complex hydration structure of the wedge and may have an impact on the results. The basis for the compositional part of the viscosity law (Eq. 5) is water in olivine, based on experimental results involving dislocation creep in olivine, and on the assumption of an olivine-dominated rheology, which is appropriate for the mantle. However, a significant fraction of the mantle includes other nominally anhydrous minerals which can accommodate high water contents (clinopyroxene: 600-3000 ppm H_2O). Additional water-weakening due to these minerals may be a factor as well, making the high modeled water contents in the shallow wedge not as extreme. Assuming a peridotite assemblage of 57% olivine, 8% garnet, 16% orthopyroxene, and 16% clinopyroxene, the LVC can potentially hold ~2200 ppm H_2O at the base of the GyPSM-S model domain (200 km). We observe a significant influence on the topography with decreasing viscosity within the hydrated zones caused by increasing average water contents in olivine.

4.2. Comparison with previous regional models of low-viscosity zones

Billen and Gurnis [22] modeled potential low-viscosity, low-density zones corresponding to two model regions (Tonga-Kermadec and Central Aleutians) with differing subduction parameters. However, the mechanism by which such a zone would form was not directly addressed, and the ultimate geometry of the low-viscosity region was inferred by comparison of regional datasets with computed values for topography and geoid height. Results indicated that both subduction wedges included low-viscosity, low-density regions, but the the size of the region and magnitude of the density anomaly within the Tonga-Kermadec subduction zone was greater than that for the Central Aleutians. The primary difference between the two subduction zones is the age of the subducting slab. Tonga-Kermadec involves an older slab (~105 Ma), while the Central Aleutians involves a significantly younger slab (~55 Ma) [52]. Calculations made by [52] of the depth of the slab beneath the volcanic front (H') may indicate that the Central Aleutians may involve shallower fluid release (and melting) than Tonga-Kermadec, with H' of ~90 km and ~115 km, respectively. GyPSM-S modeling indicates that subduction of a more mature slab results in deeper fluid releases, and the possibility for the development of a larger low-viscosity region, in agreement with the results from [22].

5. Conclusions

Inclusion of a localized low-viscosity, low-density zone in subduction zone modeling is required in order to match geophysical surface observations. Coupled geochemical and geophysical modeling (GyPSM-S) allows for a fluid-source-based approach to determining a particular low-viscosity geometry based on changing subduction parameters, spatial location of the water-saturated solidus, and the water contents of nominally anhydrous minerals. Subsequent modeling of the topography and gravity and geoid anomalies with inclusion of the particular low-viscosity geometry can then be performed and compared with observed values. For the NIB system, comparison of the observed topography signal with computed values results in the conclusion that fluid release occurs within the interval ~150-350 km depth, forming an extended low-viscosity zone (ELVC) with an associated density reduction within the ELVC of ~ -10 kg/m^3, values in general agreement with GyPSM-S results emphasizing deep dehydration from subducting lithospheric serpentinite.

Acknowledgments

The authors would like to thank P. Antoshechkina, P. Asimow, and C. Hall for collaboration with the GyPSM-S modeling effort, and L. DiCaprio and E. Tan for helpful discussions and technical advice. Support provided through the Tectonics Observatory by the Gordon and Betty Moore Foundation.

References

[1] D. R. Bell and G. R. Rossman (1992) Water in Earth's mantle: the role of nominally anhydrous minerals. Science **255** (5050), 1391-1397.

[2] J. H. Davies and D. J. Stevenson (1991) Physical model of source region of subduction zone volcanics. Journal of Geophysical Research **97**(B2), 2037-2070.

[3] T. L. Grove et al. (2006) The influence of H_2O on mantle wedge melting. Earth and Planetary Science Letters **249**, 74-89.

[4] H. Iwamori (1998) Transportation of H_2O and melting in subduction zones. Earth and Planetary Science Letters **160**, 65-80.

[5] H. Kawakatsu and S. Watada (2007) Seismic evidence for Deep-Water Transportation in the Mantle. Science **316**, 1468-1471.

[6] P. D. Asimow, J. E. Dixon, C. H. Langmuir (2004) A hydrous melting and fractionation model for mid-ocean ridge basalts: Application to the Mid-Atlantic Ridge near the Azores. Geochemistry, Geophysics, Geosystems **5**(1), Q01E16, doi:10.1029/2003GC000568.

[7] G. A. Gaetani and T. L. Grove (2003) Experimental constraints on melt generation in the mantle wedge. Geophysical Monograph **138**, 107-134.

[8] G. Hirth and D. L. Kohlstedt (1996) Water in the oceanic upper mantle; implications for rheology, melt extraction, and the evolution of the lithosphere. Earth and Planetary Science Letters **144** (1-2), 93-108.

[9] D. Arcay et al. (2005) Numerical simulations of subduction zones: Effect of slab dehydration in the mantle wedge dynamics. Physics of the Earth and Planetary Interiors **149**, 133-153.

[10] T. V. Gerya and D. A. Yuen (2003) Rayleigh-Taylor instabilities from hydration and

melting propel 'cold plumes' at subduction zones. Earth and Planetary Science Letters **212**, 47-62.

[11] S. King et al. (1990) ConMan; vectorizing a finite element code for incompressible two-dimensional convection in the Earth's mantle. Physics of the Earth and Planetary Interiors **59**(3), 195-207.

[12] P. M. Smith and P. D. Asimow (2005) Adiabat_1ph: A new public front-end to the MELTS, pMELTS, and pHMELTS models. Geochemistry, Geophysics, Geosystems **6**(2), Q02004, doi:10.1029/2004GC000816.

[13] M. S. Ghiorso and R. O. Sack (1995) Chemical mass transfer in magmatic processes; IV, A revised and internally-consistent thermodynamic model for the interpolation and extrapolation of liquid-solid equilibrium magmatic systems at elevated temperatures and pressures. Contributions to Mineralogy and Petrology **119**(2-3), 197-212.

[14] A. Hasegawa et al. (2005) Deep structure of the northeastern Japan arc and its implications for crustal deformation and shallow seismic activity. Tectonophysics **403**, 59-75.

[15] V. Manea and M. Gurnis (2007) Subduction zone evolution and low viscosity wedges and channels. Earth and Planetary Science Letters **264**(1-2), 22-45.

[16] M.W. Schmidt and S. Poli (1998) Experimentally based water budgets for dehydrating slabs and consequences for arc magma generation. Earth and Planetary Science Letters **163**, 361– 379.

[17] K. M. Cooper et al. (2004) Oxygen isotope evidence for the origin of enriched mantle beneath the mid-Atlantic ridge. Earth and Planetary Science Letters **220**, 297-316.

[18] K. E. Donnelly et al. (2004) Origin of enriched ocean ridge basalts and implications for mantle dynamics. Earth and Planetary Science Letters **226**, 347-366.

[19] J. E. Dixon et al. (2002) Recycled dehydrated lithosphere observed in plume-influenced mid-ocean-ridge basalt. Nature **420**, 385-389.

[20] P. J. le Roux et al. (2002) Mantle heterogeneity beneath the southern Mid-Atlantic Ridge: trace element evidence for contamination of ambient asthenospheric mantle. Earth and Planetary Science Letters **203**, 479-498.

[21] M. I. Billen and M. Gurnis (2001) A low viscosity wedge in subduction zones. Earth and Planetary Science Letters **193**, 227-236.

[22] M. I. Billen and M. Gurnis (2003) Comparison of dynamic flow models for the Central Aleutian and Tonga-Kermadec subduction zones. Geochemistry, Geophysics, Geosystems **4**(4), 1035, doi:10.1029/2001GC000295.

[23] G. F. Davies (1981) Regional compensation of subducted lithosphere: effects on geoid, gravity and topography from a preliminary model. Earth and Planetary Science Letters **54**, 431-441.

[24] B. H. Hager (1984) Subducted slabs and the geoid: Constraints on mantle rheology and flow. Journal of Geophysical Research **89**(B7), 6003-6015.

[25] S. Zhong and M. Gurnis (1992) Viscous flow model of a subduction zone with a faulted lithosphere: Long and short wavelength topography, gravity and geoid. Geophysical Research Letters **19**(18), 1891-1894.

[26] M. I. Billen et al. (2003) Multiscale dynamics of the Tonga-Kermadec subduction zone. Geophysical Journal International **153**, 359-388.

[27] L. Moresi and M. Gurnis (1996) Constraints of the lateral strength of slabs from three-

dimensional dynamic flow models. Earth and Planetary Science Letters **138**, 15-28.

[28] N. H. Sleep (1975) Stress and flow beneath island arcs. Geophysical Journal International **42**, 827-857.

[29] S. Zhong et al. (1998) Role of faults, nonlinear rheology, and viscosity structure in generating plates from instantaneous mantle flow models. Journal of Geophysical Research **103**(B7), 15255-15268.

[30] R. J. Stern et al. (2003) An Overview of the Izu-Bonin-Mariana Subduction Factory. Geophysical Monograph 138, 175-222.

[31] K. Suyehiro et al. (1996) Continental crust, crustal underplating, and low-Q upper mantle beneath an oceanic island arc. Science **272**, 390-392.

[32] N. Takahashi et al. (1998) Implications from the seismic crustal structure of the northern Izu-Bonin arc. The Island Arc **7**, 383-394.

[33] N. Takahashi et al. (2007) Crustal structure and evolution of the Mariana intra-oceanic island arc. Geology **35**(3), 203-206.

[34] K. Kitamura et al. (2003) Petrological model of the northern Izu-Bonin-Mariana arc crust: constraints from high-pressure measurements of elastic wave velocities of the Tanzawa plutonic rocks, central Japan. Tectonophysics **371**, 213-221.

[35] N. I. Christensen and W. D. Mooney (1995) Seismic velocity structure and composition of the continental crust: A global view. Journal of Geophysical Research **100**, 9761-9788, doi: 10.1029/95JB00259.

[36] R. Van der Hilst et al. (1991) Tomographic imaging of subducted lithosphere below northwest Pacific island arcs. Nature **353**, 37-43.

[37] Y. Fukao et al. (1992) Subducting slabs stagnant in the mantle transition zone.

Journal of Geophysical Research **97**, 4809-4822.

[38] S. Widiyantoro et al. (1999) Seismic tomography with P and S data reveals lateral variations in the rigidity of deep slabs. Earth and Planetary Science Letters **173**(1-2), 91-100.

[39] Y. Fukao et al. (2001) Stagnant slabs in the upper and lower mantle transition region. Reviews of Geophysics **39**(3), 291-323.

[40] A. Gorbatov and B. L. N. Kennett (2003) Joint bulk-sound and shear tomography for Western Pacific subduction zones. Earth and Planetary Science Letters **210**, 527-543.

[41] D. T. Sandwell and W. H. F. Smith (1997) Marine Gravity from Geosat and ERS-1 Altimetry. Journal of Geophysical Research **102**, 10039-10054.

[42] F. G. Lemoine et al. (1998) The Development of the Joint NASA GSFC and NIMA Geopotential Model EGM96. NASA Goddard Space Flight Center, Greenbelt, Maryland, 20771 USA.

[43] A. N. Brooks and T. J. R. Hughes (1982) Streamline Upwind Petrov-Galerkin Formulations for Convection Dominated Flows with Particular Emphasis on the Incompressible Navier-Stokes Equations. Computer Methods in Applied Mechanics and Engineering **32**(1-3), 199-259.

[44] G. K. Batchelor (1967) An Introduction to Fluid Dynamics. Cambridge University Press.

[45] G. Hirth and D. Kohlstedt (2003) Rheology of the Upper Mantle and the Mantle Wedge: A View from the Experimentalists. Geophysical Monograph 138, 83-105.

[46] S. Zhong et al. (1993) Accurate determination of surface normal stress in viscous flow

from a consistent boundary flux method. Physics of the Earth and Planetary Interiors **78**, 1-8.

[47] F. Pribac (1991) PhD thesis: Superswells due to mantle convection. Australia National University.

[48] W. Schroeder (1984) The empirical age-depth relation and depth anomalies in the Pacific Ocean Basin. Journal of Geophysical Research **89**, 9873-9883.

[49] B. Blankenbach et al. (1989) A benchmark comparison for mantle convection codes. Geophysical Journal International **98**, 23-38.

[50] R. Jeanloz (1989) High pressure chemistry of the Earth's mantle and core, in Mantle Convection, edited by W. R. Peltier, Pergamon, New York, 203-260.

[51] S. D. King (2002) Geoid and topography over subduction zones: The effect of phase transformations. Journal of Geophysical Research **107**(0), doi: 10.1029/2000JB000141.

[52] E. M. Syracuse and G. A. Abers (2006) Global compilation of variations in slab depth beneath arc volcanoes and implications. Geochemistry, Geophysics, Geosystems **7** (5), Q05017, doi: 10.1029/2005GC001045.

[53] R. D. Müller et al. (1997) Digital isochrons of the world's ocean floor. Journal of Geophysical Research **102**(B2), 3211-3214.

[54] R. Arko et al. (2007) The Global Multi-Resolution Topography (GMRT) Synthesis. EOS Trans. AGU, **88**(52), Fall Meet. Suppl. Abstract IN51B-0405.

[55] S. Zhong and M. Gurnis (1994) Controls on trench topography from dynamic models of subducted slabs. Journal of Geophysical Research **99**(B8), 15,683-15,695.

Figure Captions

Figure 1: (a) Observed free air gravity for the northern Izu-Bonin region [41]; (b) Geoid east-west profile extracted from EGM96 dataset [42] using terms from degree and order 2 to 70 (note that the *x*-scale extends from 120 ºE to 150 ºE to show long-wavelength features); (c) East-west bathymetric profile extracted from the GMRT dataset [54] across 32 ºN, and does not vary appreciably from actual bathymetry; (d) Free air gravity anomaly east-west profile extracted from dataset of [41] (version 15.1).

Figure 2: GyPSM-S results for the viscosity structure of the shallow (< 200 km) mantle wedge for the NIB model calculation showing the influence of the high water contents in NAM as a localized zone of viscosity reduction. The geometry of the low-viscosity region is directly influenced by the vertical migration of water from the dehydrating subducting slab (shown as blue lines), the majority of which is released at depths ≥ 150 km from the lithospheric serpentinite layer.

Figure 3: Uncoupled model setup for calculation of topography, geoid height, and gravity anomalies: (a) schematic representation of calculation domain; (b) schematic representation of model geometries in association with fluid release locations.

Figure 4: Model viscosity structure with addition of parameterized low-viscosity regions: (a) no LV, corresponds to a lack of an imposed low-viscosity zone; (b) LVC, corresponds to a slab-adjacent uniform 50 km thick low-viscosity channel that extends to the top of the

transition zone, or where the slab begins to flatten (note change in viscosity scale); (c) ELVC, corresponds to an "extended" LVC approximating a wedge geometry in the shallow regions of the mantle wedge, but remaining a uniform channel as greater depths due to the near slab-parallel flow field, and (d) LVW, corresponding to a full "wedge"-type geometry.

Figure 5: Results of NIB model calculations (Table 3) for geoid height, gravity anomaly, and topography (thick black lines) compared with regional dataset profiles (thin gray lines) for (a, e, i) no LV; (b, f, j) LVC1 with 1000 ppm H_2O in olivine as an average value; (c, g, k) ELVC4 with 1000 ppm H_2O in olivine as an average value ($\eta_{LV} = 3.3\times10^{19}$-$4.0\times10^{20}$ Pa s); (d, h, l) LVW2 with 1000 ppm H_2O in olivine as an average value. Note that all models shown have zero density contrast between the LV region and the nominally anhydrous mantle wedge.

Figure 6: Independently varying model parameters. (a, d, b, e) Different lateral extents of models for the ELVC/LVW, corresponding to the depth of fluid release from the slab: (a, d) ELVC1: 100 km extent (black), ELVC2: 150 km extent (red), and ELVC24: 250 km extent (blue), all models having $\Delta\rho = 0$ kg/m^3 between the LV region and the nominally anhydrous mantle wedge and arrows indicating the changing peak position in the calculated topography; (b, e) ELVC9: 100 km extent (blue), ELVC12: 150 km extent (red), and ELVC25: 250 km extent (black), all models having $\Delta\rho = -10$ kg/m^3 between the LV region and the nominally anhydrous mantle wedge. (c, f) Different density contrast between the ambient nominally anhydrous wedge and the ELVC region on calculated topography and gravity anomalies: (c, f) ELVC24: $\Delta\rho = 0$ kg/m^3 (blue), ELVC25: $\Delta\rho = -10$ kg/m^3 (red),

and ELVC26: $\Delta\rho$ = -20 kg/m^3 (black), all models having a lateral LV extent of 250 km. The observed profiles are indicated by thinner gray lines in all panels.

Figure 7: Comparison of the result of variation of parameters, specifically the density contrast between the LV zone and the nominally anhydrous mantle wedge and the lateral extent of the LV zone, to the regional profiles for gravity anomalies and topography using RMS error estimates to establish goodness of fit (where darker colors indicate a better fit): (a) normalized RMS error calculated for misfit of calculated topography to that observed; (b) normalized RMS error calculated for misfit of calculated gravity to that observed; and (c) combined normalized RMS error calculated for the misfit of both gravity and topography where dotted lines indicate transects in Fig. 6.

Appendix IV-A: Benchmarking

We applied benchmarking to compare the results for surface observables (topography, geoid) that were produced by this code (ConMan plus Fourier transform analysis). Using Blakenbach et al. [49] cases 1a-c, we put together four models with varying grid resolution and Rayleigh number (Table 4). All models represent a single convection cell with constant viscosity in a square domain. The non-dimensional temperature is fixed to zero at the top and to ΔT = 1.0 at the base. There is reflecting symmetry at the sidewalls and zero shear stress along all boundaries [49]. The benchmarking exercise was successful in reproducing published results.

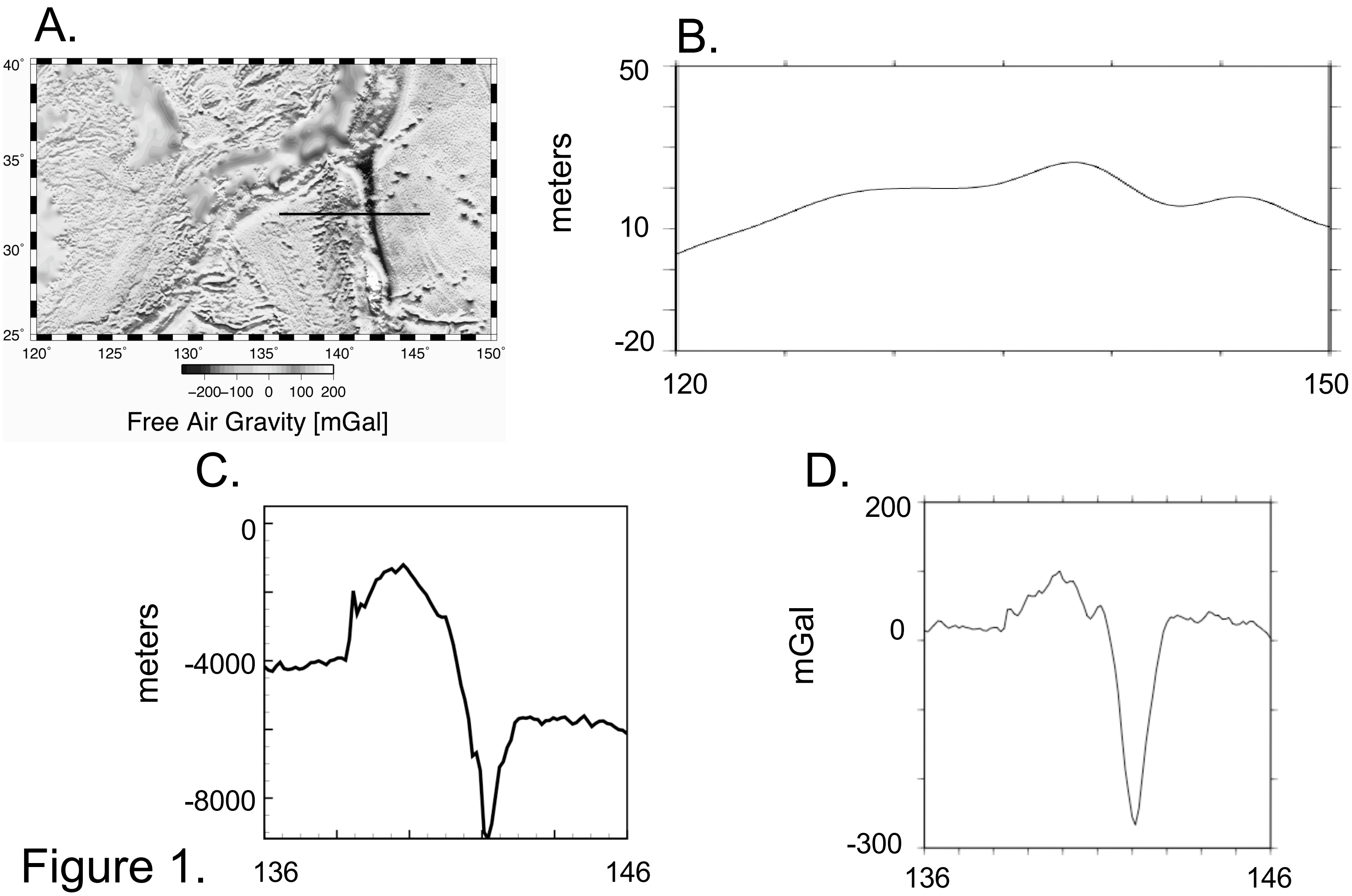
A.
40°
35°
30°
25°
120°
125°
130°
135°
140°
145°
150°
−200−100 0 100 200
Free Air Gravity [mGal]
B.
50
10
-20
meters
120
150
C.
0
-4000
-8000
meters
136
146
D.
200
0
-300
mGal
136
146

Figure 1.

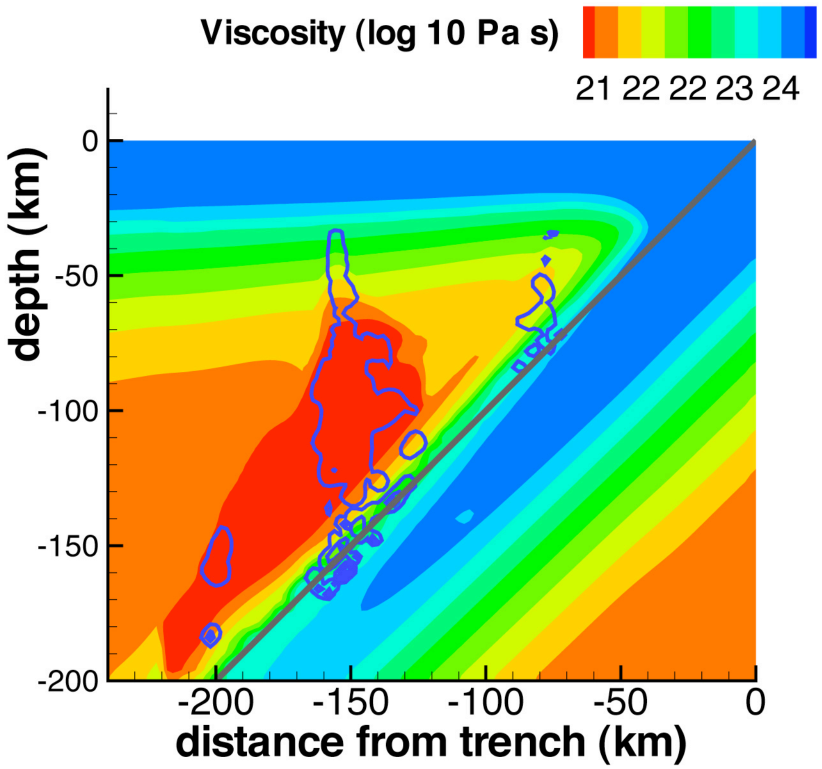
Viscosity (log 10 Pa s)
21 22 22 23 24
depth (km)
0
-50
-100
-150
-200
-200
-150
-100
-50
0
distance from trench (km)

Figure 2.

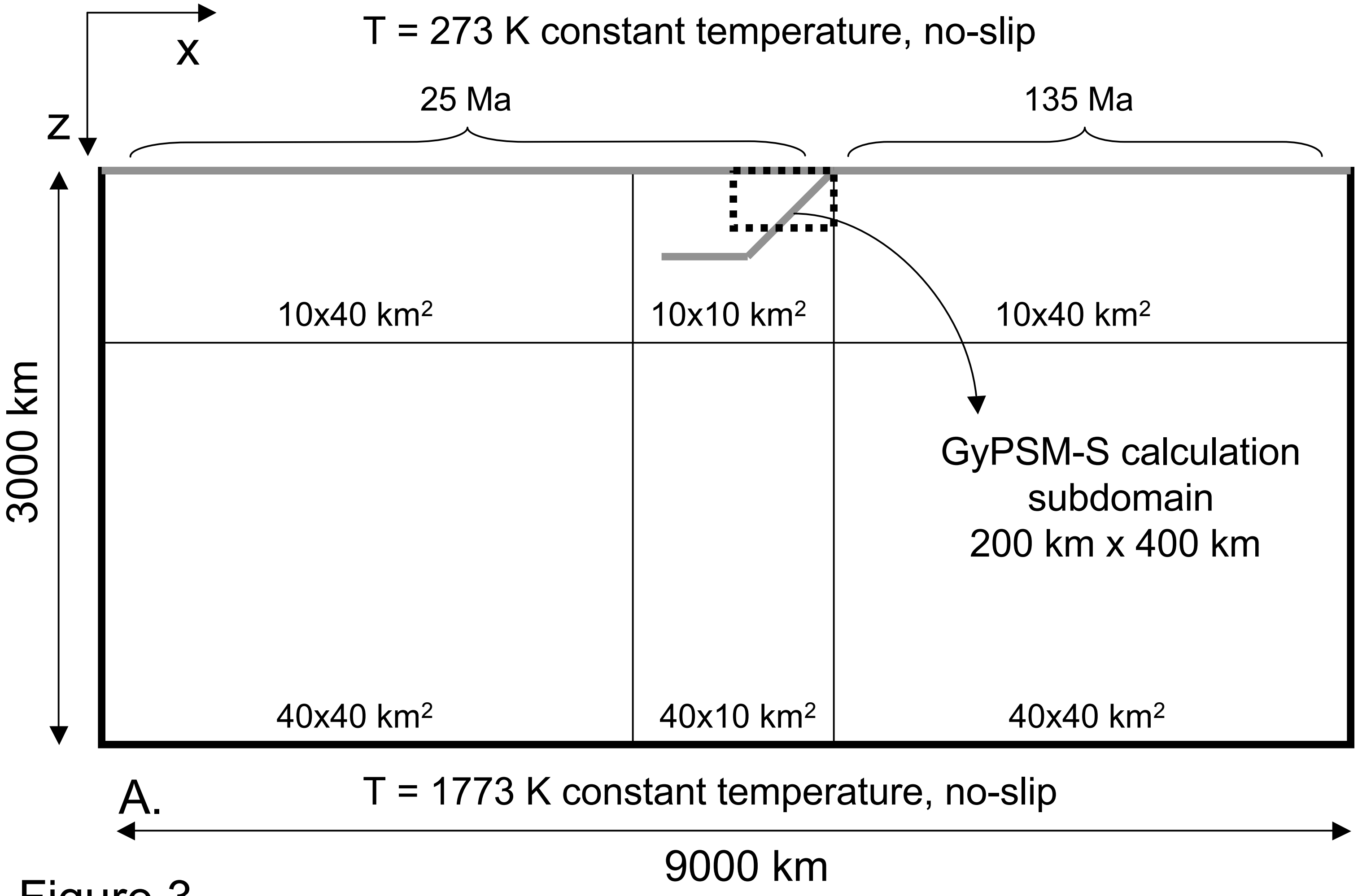
x
z
T = 273 K constant temperature, no-slip
25 Ma
135 Ma
10x40 km²
10x10 km²
10x40 km²
GyPSM-S calculation subdomain 200 km x 400 km
3000 km
40x40 km²
40x10 km²
40x40 km²
A.
T = 1773 K constant temperature, no-slip
9000 km

Figure 3.

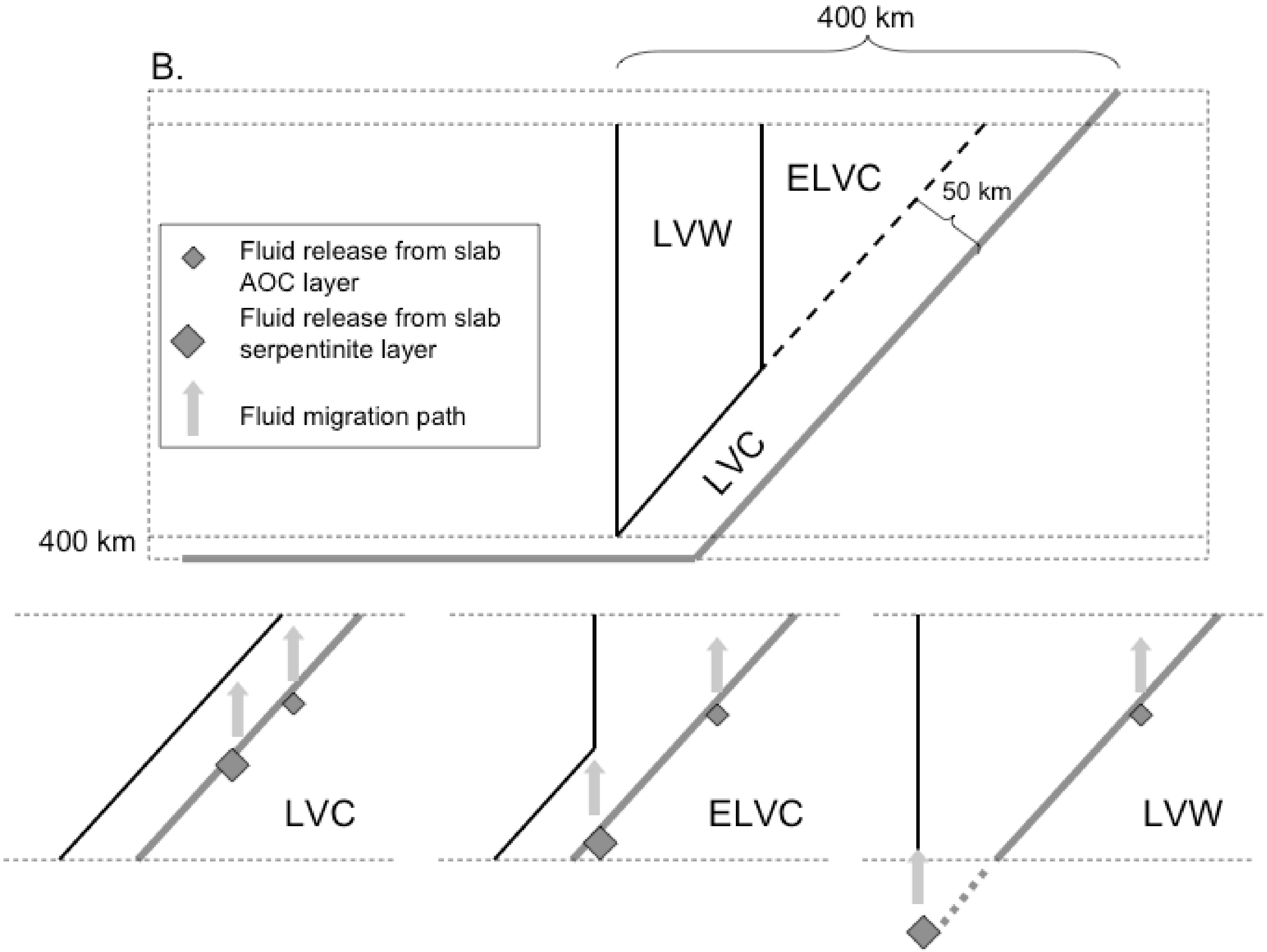
B.
400 km
400 km
LVW
ELVC
50 km
LVC
Fluid release from slab AOC layer
Fluid release from slab serpentinite layer
Fluid migration path
LVC
ELVC
LVW

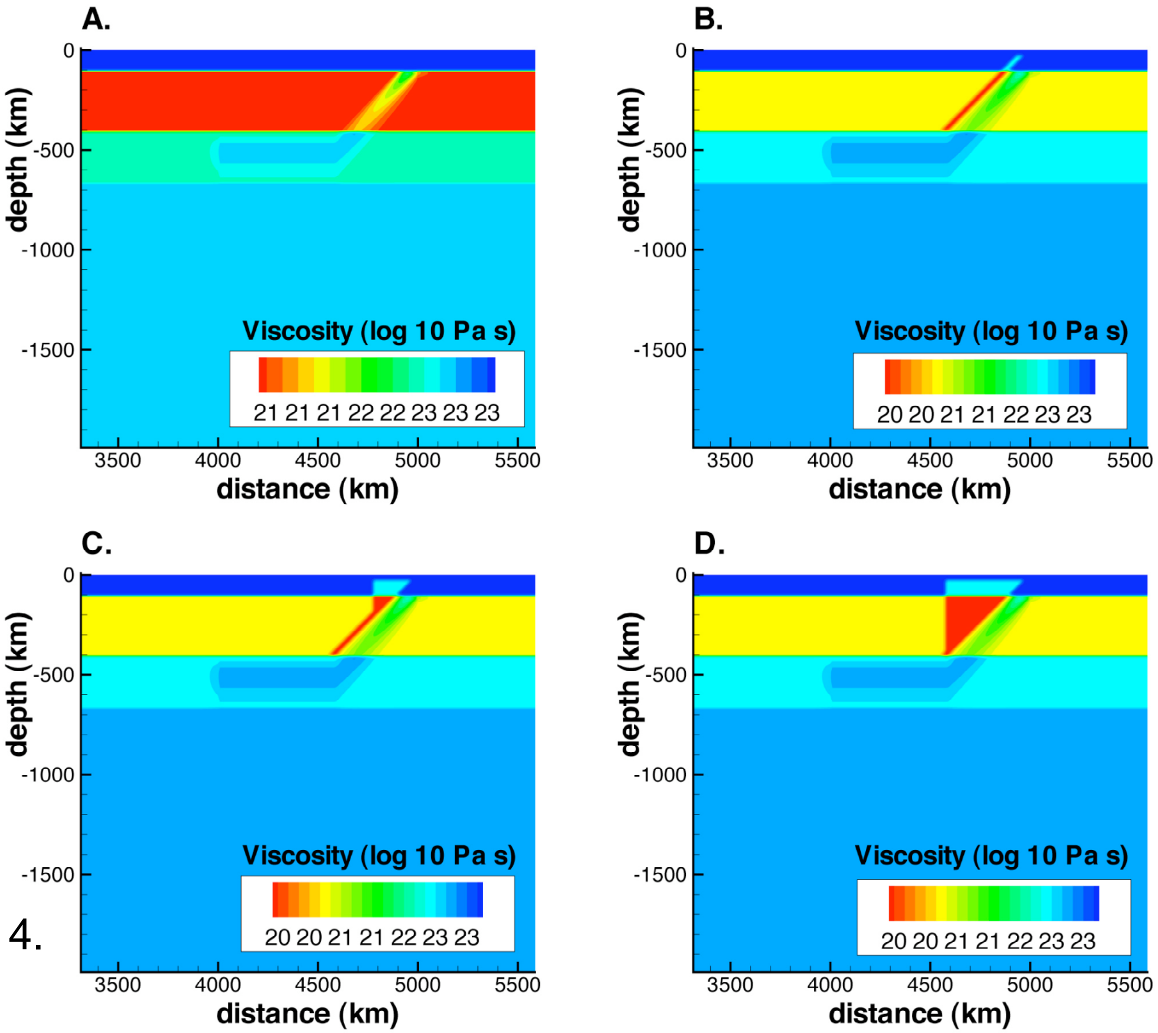
A.
B.
C.
D.
depth (km)
0
-500
-1000
-1500
distance (km)
3500
4000
4500
5000
5500
Viscosity (log 10 Pa s)
21 21 21 22 22 23 23 23
20 20 21 21 22 23 23
20 20 21 21 22 23 23
20 20 21 21 22 23 23

Figure 4.

Figure 5.

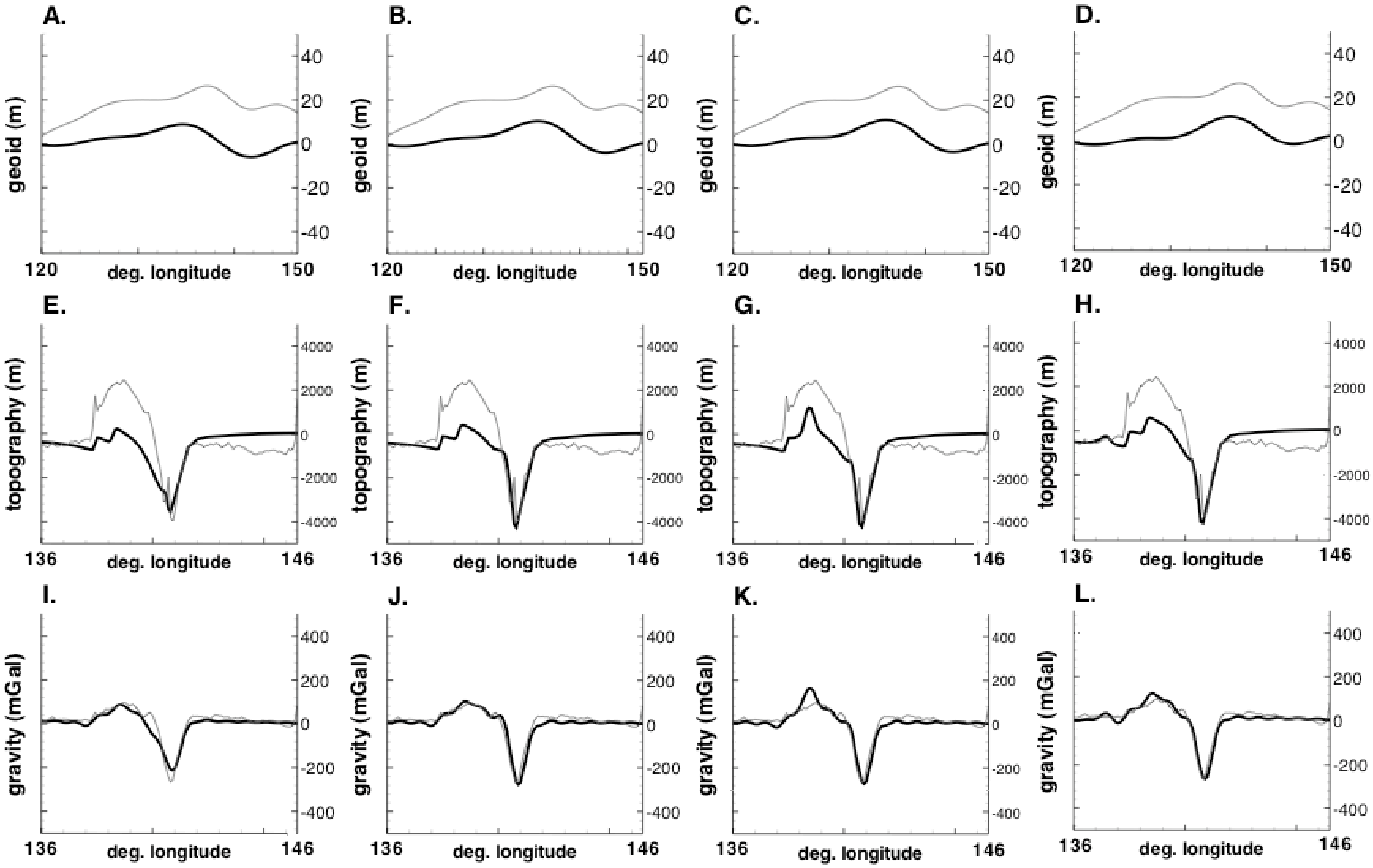
A.
B.
C.
D.
geoid (m)
40
20
0
-20
-40
120
deg. longitude
150
E.
F.
G.
H.
topography (m)
4000
2000
0
-2000
-4000
136
deg. longitude
146
I.
J.
K.
L.
gravity (mGal)
400
200
0
-200
-400
136
deg. longitude
146

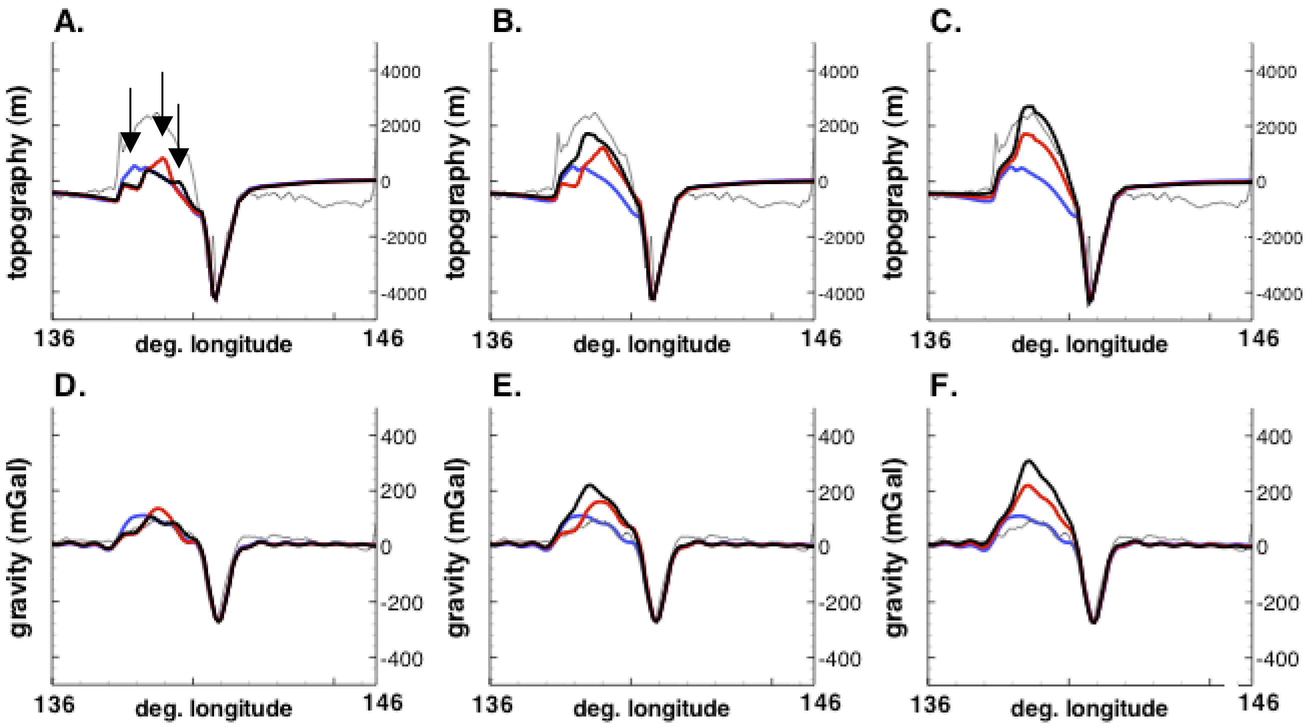
A.
B.
C.
D.
E.
F.
topography (m)
gravity (mGal)
deg. longitude
136
146
4000
2000
0
-2000
-4000
400
200
0
-200
-400

Figure 6.

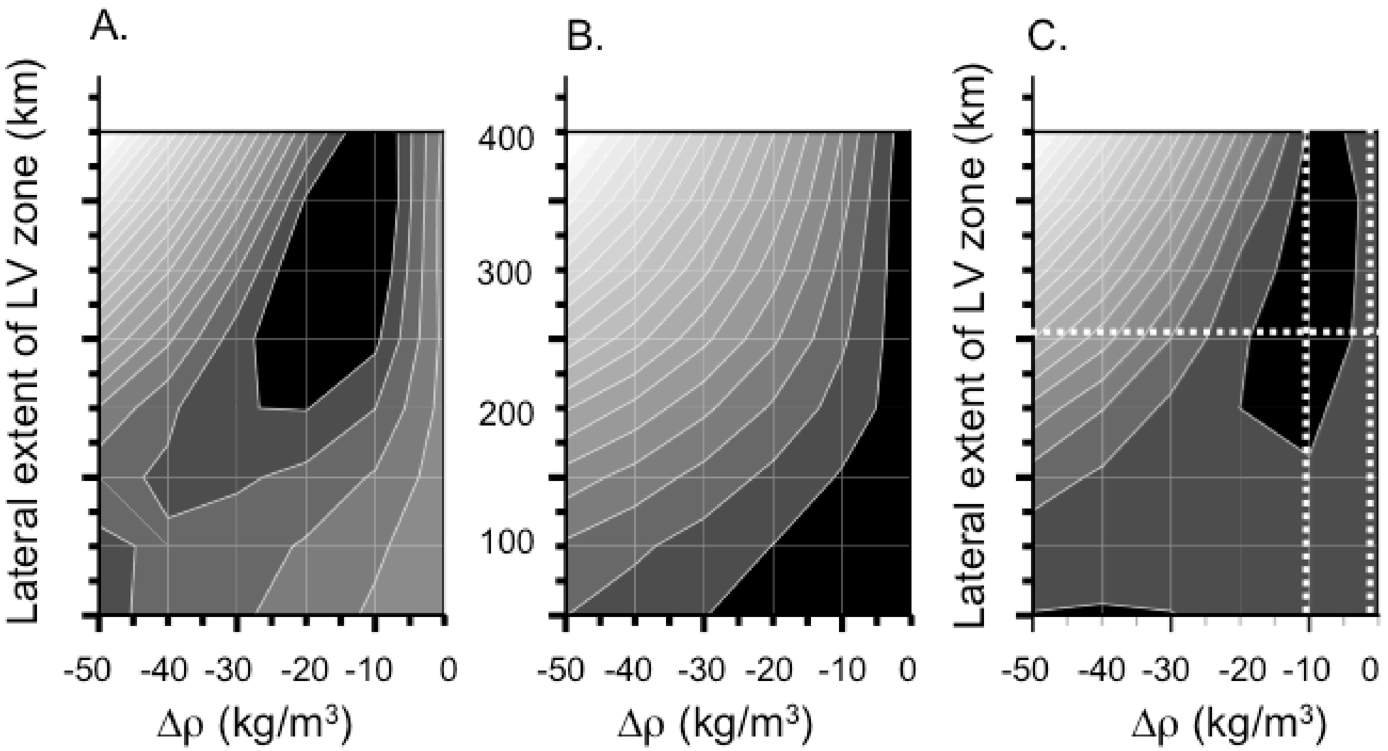
A.
B.
C.
Lateral extent of LV zone (km)
400
300
200
100
-50
-40
-30
-20
-10
0
Δρ (kg/m³)

Figure 7.

Table 1: Model parameters held constant

parameter	*value*	*units*
ΔT	1500	K
Ra	1.40E+08	*
η_0	3.0E+20	Pa s
Q	500	kJ/mol
$A_{Philippine}$	24 [53]	Myr
$A_{Pacific}$	141 [53]	Myr
κ	1.0E-06	m^2/s
α	2.5E-05	K^{-1}
g	10.0	m/s^2
G	6.67E-11	$N\ m^2/kg^2$
d	3000	km
R	8.31	J/K mol

** dimensionless quantity*
numbers in square brackets indicate references

Table 2: Summary of GyPSM-S subduction zone model parameters for initial calculation

subduction region	Northern Izu-Bonin
abbreviation	NIB
latitude range	~32 ºN
longitude range	~136-146 ºE
rate of convergence (mm/yr)	50.0 [30]
slab dip angle	45º
slab thermal age (Ma)	135 [30]
rigid lithospheric thickness (km)	32
thermal lithospheric thickness (km)	66

numbers in square brackets indicate references

Table 3: Summary of low-viscosity (LV) region model cases

model	*depth extent of channel section (km)*	*depth extent of wedge section (km)*	*width of channel (km) from top of slab*	*width of wedge (km) at top*	*average water content in olivine (ppm)*	*Δρ (LVZ-wedge) (kg/m^3)*
no LV	N/A	N/A	N/A	N/A	N/A	N/A
LVC1	400	0	50	0	1000	0
LVC2	400	0	50	0	1000	-10
LVC3	400	0	50	0	1000	-20
LVC4	400	0	50	0	1000	-50
ELVC1	400	100	50	100	1000	0
ELVC2	400	150	50	150	1000	0
ELVC3	400	180	50	180	1000	0
ELVC4	400	200	50	200	1000	0
ELVC5	400	200	50	200	2000	0
ELVC6	400	200	50	200	1000	-10
ELVC7	400	200	50	200	1000	-20
ELVC8	400	200	50	200	1000	-50
ELVC9	400	100	50	100	1000	-10
ELVC10	400	100	50	100	1000	-20
ELVC11	400	100	50	100	1000	-50
ELVC12	400	150	50	150	1000	-10
ELVC13	400	150	50	150	1000	-20
ELVC14	400	150	50	150	1000	-50
ELVC15	400	180	50	180	1000	-10
ELVC16	400	180	50	180	1000	-20
ELVC17	400	180	50	180	1000	-50
LVW1	400	300	50	300	1000	0
LVW2	N/A	400	N/A	400	1000	0
LVW3	400	300	50	300	1000	-10
LVW4	400	300	50	300	1000	-20
LVW5	400	300	50	300	1000	-50
LVW6	N/A	400	N/A	400	1000	-10
LVW7	N/A	400	N/A	400	1000	-20
LVW8	N/A	400	N/A	400	1000	-50
ELVC18	400	100	50	100	1000	-30
ELVC19	400	100	50	100	1000	-40
ELVC20	400	150	50	150	1000	-30
ELVC21	400	150	50	150	1000	-40
ELVC22	400	200	50	200	1000	-30
ELVC23	400	200	50	200	1000	-40
LVC5	400	0	50	0	1000	-30
LVC6	400	0	50	0	1000	-40
LVW9	400	300	50	300	1000	-30
LVW10	400	300	50	300	1000	-40
LVW11	N/A	400	N/A	400	1000	-30
LVW12	N/A	400	N/A	400	1000	-40
ELVC24	400	250	50	250	1000	0
ELVC25	400	250	50	250	1000	-10
ELVC26	400	250	50	250	1000	-20
ELVC27	400	250	50	250	1000	-30
ELVC28	400	250	50	250	1000	-40
ELVC29	400	250	50	250	1000	-50
LVW13	400	350	50	350	1000	0
LVW14	400	350	50	350	1000	-10
LVW15	400	350	50	350	1000	-20
LVW16	400	350	50	350	1000	-30
LVW17	400	350	50	350	1000	-40
LVW18	400	350	50	350	1000	-50

Table 4: Summary of benchmark cases

case	*resolution (x,y)*	*Ra*
bm1	32×32	10^5
bm2	64×64	10^5
bm3	64×64	10^4
bm3	64×64	10^6

Chapter V:

Greenish Quartz from the Thunder Bay Amethyst Mine Panorama, Thunder Bay, Ontario, Canada

Laura Baker Hebert and George Rossman

Published as:

L. B. Hebert and G. R. Rossman (2008) Greenish Quartz from the Thunder Bay Amethyst Mine Panorama, Thunder Bay, Ontario, Canada. The Canadian Mineralogist **46**, 61-74, doi: 10.3749/canmin.46.1.000.

Abstract

Naturally occurring greenish quartz found within the context of amethyst-bearing deposits is not simply the result of the exposure of amethyst to thermal bleaching or exposure to the sun. Rather, it can represent a set of distinct color varieties resulting from the changing chemical and thermal nature of the precipitating solution. Greenish quartz occurs at the Thunder Bay Amethyst Mine Panorama (TBAMP), Thunder Bay, Ontario, Canada, in several distinct varieties. Yellowish green quartz and dark green quartz with purple hues occur as loose detritus, and pale greenish gray quartz occurs as part of a color-gradational mineralization sequence involving macrocrystalline quartz of other colors and chalcedony. The TBAMP system contains a number of color varieties of quartz including greenish, amethyst, colorless, and smoky. Spectroscopic, irradiation, and controlled heating studies show that changes in salinity and temperature of the hydrothermal system that produced the TBAMP deposit are reflected in the changing coloration of the quartz. The greenish quartz, especially the greenish gray variety, has increased turbidity and fluid inclusions when compared with the adjacent amethyst. Analysis of different colors on major ($r = \{10\text{-}11\}$) and minor ($z = \{01\text{-}11\}$) rhombohedral sectors within the quartz indicates that changes in the growth rate also have influenced color development. As the system evolved, two factors contributed to the color changes: (i) a minor ferric component appears to change position from interstitial to substitutional within specific growth sectors and (ii) the trace element composition of the quartz evolved. The samples from the TBAMP deposit are compared to isolated samples of greenish quartz collected from three other amethyst-bearing localities: Farm Kos and Farm Rooisand (Namibia), Kalomo-Mapatiqya (Zambia), and Southern Bahia (Brazil). All included similar greenish hues with the exception of the yellowish green variety. Colors within the quartz are consistently correlated with the speciation of hydrous components. Darker green samples incorporate larger amounts of molecular water than either pale greenish gray samples, colorless samples, or amethyst. The appearance of strong hydroxyl peaks in the infrared spectra is limited to amethyst and colorless varieties.

Keywords: amethyst, green quartz, Thunder Bay, Ontario

1. Introduction

The Thunder Bay Amethyst Mine Panorama (TBAMP) deposit is the site of an extinct hydrothermal system that flowed through a fault and led to mineralization primarily by quartz [1]. Although most of the quartz is amethystine, greenish quartz has been found in the TBAMP in several distinct varieties. Yellowish green quartz and dark green quartz with purple hues are found as loose detritus within the TBAMP (originating from outcroppings), and pale greenish gray quartz is found as part of an outcropping color-gradational sequence involving macrocrystalline quartz of other colors, including colorless, smoky gray, and chalcedony (Fig. 1). The color-gradational sequence occurs solely in a localized zone, which may be the site of initial influx of fluids into the fault. Distally, the color of the *in situ* quartz is dominantly dark violet amethyst. In some cases, this dark violet amethyst, when cut perpendicular to its *c* axis, is found to be composed of alternating sectors of colorless and dark purple quartz.

It is important to understand the origin of the greenish gray color because it is ubiquitously present within a progressive color sequence in quartz. Clues in the chemical and spectroscopic variations within the sequence may provide an increased understanding of the development and persistence of radiation-induced color centers in quartz within the context of changing chemical, thermal, and kinetic factors in a hydrothermal system. The yellowish green and dark green varieties, while not observed *in situ*, will still allow inferences to be made about origins of natural green color in quartz.

2. Background Information

A greenish coloration in synthetic quartz can arise from irradiation of quartz, heating of quartz originally of another color, or from the presence of ferrous iron within the structure [2-5]. However, natural examples of greenish coloration in quartz are rare [6-8], and have not been fully discussed within the context of their environment of formation or in relation to other associated colors of quartz. To initially characterize the greenish color variety, spectroscopic examination of both the greenish and associated color varieties of quartz must be carried out. Additionally, visual observations and spectroscopic analyses of the different color varieties in the TBAMP system should be interpreted specifically in association with radiation exposure and heat-treatment experiments.

In all the samples included in this study, amethyst is consistently associated with the greenish quartz. The violet coloration in amethyst is due to the removal of an electron by high-energy radiation that results in oxidation of ferric iron within the quartz structure to Fe^{4+} [9]. It has been argued that the ferric iron impurity can be present as either a substitutional or interstitial species, and that its particular structural environment may have an influence on color-center development. In addition to amethyst, smoky quartz was found at the TBAMP associated with the greenish quartz. Commonly characterized by a brownish gray hue, smoky quartz represents another color variety of quartz produced by ionizing radiation. The smoky color center is modeled as Al^{3+} substituting into the Si^{4+} tetrahedral site, with associated charge-balance fulfilled by a nearby positively charged ion (such as Li^{+}) in an interstitial site. Upon irradiation, an electron will migrate away, leaving a “hole center,” and the associated charge-compensating cation will migrate away through the structure as well [10]. The source of the ionizing radiation is readily available as ^{40}K within the Archean granitic country-rock surrounding the TBAMP deposit.

McArthur et al. [1] proposed that greenish coloration at TBAMP is heat-induced “bleaching” of amethyst. Heating of quartz can thermally activate color centers and encourage migration of species within the structure. By destroying color centers, heat treatment can selectively eliminate components of coloration associated with exposure to ionizing radiation. We tested this hypothesis by subjecting the amethyst in the TBAMP system to carefully designed heating experiments. Because the presence of molecular H_2O within the quartz structure has been found to be detrimental to the development of certain colors and may allow other colors to emerge instead [11], it is also necessary to examine the incorporation of H_2O in TBAMP quartz.

3. TBAMP Geological Setting and Sample Description

Approximately 1.1 × 10^9 years ago, the development of the Mid-continent Rift initiated the intrusion of mafic dike swarms [12] followed by faulting in the region of the TBAMP [13]. The hydrothermal vein system utilized by the TBAMP is hosted within an Archean intrusion of granitic rocks located on the boundary between the Quetico and Wawa subprovinces [1]. The amethyst-bearing veins occur within a strike-slip fault, and are part of a chain of amethyst deposits associated with silver and lead-zinc-barite deposits that form along the contact between the Mesoproterozoic Sibley Group and the Archean granite-greenstone assemblage [1]. The timing of events in this region is disputed. Heat derived from the initiation of Keeweenawan rifting and associated intrusions may have mobilized and expelled brines from Sibley Group sediments and driven the fluids parallel to major faults, giving rise to the development of the hydrothermal systems responsible for quartz and ore-deposit mineralization [14]. Alternatively, mineralization may be associated with the formation of the Sibley Basin, wherein diagenetic expulsion of pore waters in conjunction with a thermal anomaly may have contributed to forming the lead-zinc-barite and quartz deposits [1].

The greenish quartz occurs in a range of shades from pale greenish gray to dark translucent green with purple hues to pale greenish yellow, and occurs exclusively in a centralized brecciated zone in the East Pit of the TBAMP, approximately 10 meters in diameter. This zone may have served as the location of initial influx of fluid into the fault. The breccia consists of pebble to small boulder-scale angular fragments of granite, greenstone, laminated chert, and potassium feldspar-rich pegmatite. The brecciation event may have been initiated by hydrofracture, as brecciated fragments tend to be well-sorted and subangular to subrounded, a consequence of fluid transport [1]. The breccia has been mineralized by quartz in a color sequence that includes the greenish gray coloration. Brecciated pieces are jumbled together, and the mineralized sequence, which nucleated on the breccia surface, has grown outward from that surface, commonly resulting in the abutment of different sequences of quartz. Loose pieces were found consisting of amethyst and greenish gray quartz adjacent to each other, but separated by a millimeter-scale chalcedony horizon. Vein mineralization tens of meters from this zone includes dominantly the color-zoned dark purple amethyst above a thin (2 mm ± 0.5 mm) layer of colorless quartz and dark purple amethyst capped by yellowish white fluid-inclusion-rich quartz. Late-stage amethyst in some areas is capped by dark red hematite flakes. The macrocrystalline varieties of quartz in the mineralization sequence have subparallel directions of growth, with the greatest variations in consistent orientation of the *c* axis found in the early (greenish gray and colorless) sections. Sub-millimeter euhedral grains of pyrite and chalcopyrite are consistently associated with the chalcedony layers.

Samples representative of the color sequence were taken from a single block, 006, from which a vertical section could be selected containing all the color variations in the sequence. Samples were taken from the macrocrystalline sections, focusing on the greenish gray, colorless to brownish gray, and bicolored sections. Detrital samples representative of the dark green and yellowish green varieties were chosen for their internal quality and uniformity of color. Samples characteristic of the dark purple amethyst and common pale purple amethyst were also collected from loose detritus. Most samples were cut so that spectroscopic analyses could be performed with the light polarized to be either parallel or perpendicular to the *c* axis, and others were cut in a plane perpendicular to the *c* axis, so that sector coloration could be observed. The samples were then doubly polished using alumina polishing paper. For infrared and near-infrared studies, samples were cut to less than 1 mm in thickness; for visible spectroscopic analyses, samples were cut to 2-10 mm in thickness. Polished sections of the collected samples allowed high magnification optical observation of fluid inclusions on the order of 1-5 μm diameter. The greenish gray samples, colorless samples, and greenish gray sectors of the bicolored sections all have similarly poor optical quality, with multiple visible inclusions and cracks and high turbidity. The amethyst sectors of the bicolored sections, and the amethyst found elsewhere in the mine, are all of comparatively high optical quality, with low turbidity. The yellowish green samples are of intermediate optical quality, with less turbidity than the greenish gray samples, but not as clear as the amethyst sections.

4. Descriptions of Samples from Other Localities

We obtained a limited sample set of greenish quartz from other amethyst localities. Samples from the Farm Rooisand (FR), Namibia, include amethyst and pale greenish gray quartz (Fig. 2a). Additionally, colorless varieties occur adjacent to amethyst. There is evidence for the changing state of the crystallizing system, as samples include colorless, high-turbidity generations overlain by pale greenish gray quartz, amethyst generations overlain with pale greenish gray quartz, and greenish gray generations overlain with high-turbidity, colorless generations. FR-3(6) is an example of a colorless vug that appears at the top of an amethyst crystal. FR-3(3) is an example of the greenish gray coloration. FR-3(5) is a section cut perpendicular to the *c* axis that shows an older greenish gray tip overgrown by a colorless generation of high turbidity. FR-3(2) is a section cut perpendicular to the *c* axis that shows an amethyst inner core, and a greenish gray overgrowth. Samples from Bahia, Brazil (GRR 2350) are uniformly dark green (Fig. 2b), but when cut parallel to the *c* axis, there appear sections of colorless quartz alternating with sections of dark green coloration.

5. Experimental Methods

5. 1.Spectroscopy

Infrared (IR) spectra were obtained at room temperature on doubly polished samples at 2 cm^{-1} resolution for up to 1000 scans using a Nicolet 860 FTIR instrument with a CaF_2 or KBr beam splitter, a liquid-nitrogen-cooled MCT-A detector, and Globar source. Near-infrared (NIR) spectra were obtained on the same instrument, but with an InGaAs detector, a SiO_2 beam splitter, and a visible (W-halogen) light source. A lithium iodate Glan-Foucault prism polarizer (Inrad 703-150) was used to obtain polarized spectra on oriented samples. Visible spectra were obtained at 1 nm resolution for 100 scans with a diode-array spectrometer system consisting of an EG&G PAR detection system with Si and InGaAs diode arrays and Acton triple grating spectrometers, in addition to an Oriel Q-housing tungsten lamp. A subjectively determined sloping baseline correction was applied to define peak positions and to correct for wavelength-dependent scattering effects due to internal defects in the crystal.

5.2.Radiation and thermal experiments

Radiation experiments were performed at room temperature using a ^{137}Cs source, which allows doses of 0.84 Mrads/day. Color change was visually estimated on the basis of comparison with an untreated standard sample.

Heating experiments were performed in air using a Lindberg furnace. The samples were subjected to temperatures from 100 to 500°C in 100°C steps over time intervals of 1 hour between temperature steps. The change in color was visually estimated on the basis of a comparison with an unheated standard sample.

6. Results

6.1.Optical spectroscopy

A background that rises toward shorter wavelengths, attributable to scattering from the internal turbidity of the samples, dominates all optical spectra. The absorption is anisotropic: being more intense if light is polarized parallel to the *c* axis. All the samples have a pale hue, and the absorption bands are superimposed on the scattering curve, with a tail from strong absorption in the ultraviolet. In samples with two colors present, such as the bicolored samples and samples 002, an effort was made to isolate regions of uniform color suitable for spectroscopic analysis, but some interference with other colors was unavoidable.

All greenish gray TBAMP samples are turbid, with low to moderate intensity of color. Absorption spectra consist of a broad band centered at approximately 900 nm, with a weak superimposed band centered at approximately 620 nm defining transmittance at green wavelengths and a further weak band at 520 nm in the perpendicular to *c* polarization (Fig. 3). The spectra of the yellowish green TBAMP samples have a band centered at 710 nm with a sharp increase into the ultraviolet region consistent with transmittance at greenish yellow wavelengths (Fig. 4). The dark green samples from the various localities have almost identical spectra: bands centered at 710 and 930 nm, with a weak band at 540 nm (associated with amethyst coloration) showing greater intensity in the perpendicular to c polarization (Fig. 5). The green color is defined by the transmission window in the 540 nm region. Greenish gray sample FR-3(3) shares the major absorption bands with the dark green samples (Fig. 6): we observed absorption centered at ~940 nm, which has been previously indicated for the interstitial ferrous iron impurity associated with synthetic green quartz (Rossman, 1994). Visible spectra obtained for late-stage dark amethyst samples at TBAMP show only the characteristic absorption bands of amethyst.

The samples were analyzed in the 6000 to 2000 cm^{-1} range to examine contributions from fluid inclusions and structurally bound hydroxyl groups. Quartz IR absorption spectra (Fig. 7) include two types of contributions: broad-band contributions, generally from molecular H_2O (broad-band in the 3440 cm^{-1} region), and sharp peak contributions, from hydroxyl groups (peak at 3585 cm^{-1}, for example).

All samples studied have an anisotropic orientation of hydroxyl groups within the structure, but the samples that contain molecular H_2O show isotropic absorption, which commonly indicates its presence as microscopic or macroscopic fluid inclusions distributed throughout the structure. Indeed, the greenish gray and colorless varieties at TBAMP contain visible fluid inclusions that were verified by Raman spectroscopy to be mostly H_2O.

The IR spectra for late-stage, dark purple amethyst at TBAMP appear very similar to previously published spectra for amethyst from various localities, with a strong dominance of hydroxyl peaks. The greenish samples, colorless samples, and *both* sectors of the bicolored samples all show greater amounts of H_2O present in the structure as both molecular H_2O and hydroxyl groups. The greenish samples have the greatest H_2O contents relative to the other color varieties, a phenomenon that persists even where differently colored sectors are directly adjacent to one another (Fig. 8).

Figure 9a shows that the relative depth of hue has a correlation with the content of molecular H_2O. The "flat top" spectra in Figure 9a for the Namibian and Brazilian samples suggest that the size and distribution of fluid inclusions may be different in the TBAMP samples. It is apparent in the spectra of samples from all localities that quartz with greenish gray coloration, even when in immediate proximity to other colors, consistently has the highest molecular H_2O content.

6.2. Chemical analysis of TBAMP samples

Chemical analyses of quartz from the TBAMP were performed on the Plasma 54 LA-ICP-MS at Ecole Normale Supérieure de Lyon (Table 1). Sodium is a likely constituent based on its common occurrence in other studies and on the composition of the brine from which the quartz precipitated at TBAMP. Microthermometric fluid-inclusion analysis by [1] showed that the eutectic temperatures in the initial stages of quartz growth are indicative of a brine in the system $CaCl_2$-NaCl-H_2O, whereas late-stage, high-clarity amethyst was most likely representative of a brine system of $CaCl_2$-NaCl and an iron or zinc salt. The concentration of iron in our samples was not measured, but as it is well understood that the mechanism of amethyst color generation requires iron, we assumed that the quartz in the TBAMP system contains iron.

The samples are heterogeneous on a millimeter scale with regard to their trace-element distribution. All samples contain Ga and S (which is most likely derived from fluid inclusions), and the samples within the color sequence all contain Li, but only the dark green samples (002) contain appreciable Na. It appears that the presence of Ca as a trace constituent is limited to the purple varieties and the darkest green samples. Indeed, the composition of the yellowish green variety would most closely match that of the dark amethyst but for the lack of appreciable Ca. The greenish color is associated with Al in all cases except the yellowish green variety. There is a similarity in coloration between the greenish gray samples and the greenish gray sectors of the bicolored samples, but the chemical analysis reveals the absence of K within the greenish gray samples, perhaps accounting for differing behavior during the heating and radiation experiments.

6.3.Heating experiments on TBAMP samples

Heating can lead to thermal activation of electrons or defect species (vacancies or impurity atoms), resulting in color change. For example, citrine (yellowish quartz) is produced by heating amethyst to 300-500°C, which Stock & Lehmann [15] proposed causes the iron in the amethyst to precipitate as ferric-iron-oxide clusters. Heating caused some color varieties in our study samples to gradually change color (with color change commencing after reaching 300°C), but others showed only an increase in turbidity, with gradually increasing internal cloudiness indicative of cracks developing through decrepitation of fluid inclusions. Optical observation using a petrographic microscope at high magnification revealed the lack of visible (micron-scale) fluid inclusions in samples after heat treatment. The results are summarized in Table 2.

Heating to temperatures of 500°C did not have an appreciable effect on the height or position of the broad band of molecular H_2O absorption centered at 3440 cm^{-1} for the colorless samples or for the greenish gray samples. Where the larger-scale fluid inclusions rupture during heating (leading to the increase in turbidity observed during the experiments), signs of H_2O remain in the IR spectrum, suggesting that some molecular H_2O is trapped within nanoscale fluid inclusions that do not rupture during heating, owing to the mechanical strength of quartz.

6.4.Radiation experiments on TBAMP samples

The results of the radiation experiments are summarized in Table 2. Samples lower in the color sequence (greenish gray and colorless samples) developed a brownish smoky color with the further darkening and development of purple overtones as exposure increased. Notably, for the colorless sample, the color on the *r* and *z* sectors alternated between brownish smoky and pale purple. This finding emphasizes the existence of different patterns of chemical behavior associated with the major and minor rhombohedral sectors that manifest themselves as color changes, a phenomenon that becomes more significant further up in the color sequence.

Irradiation of the thermally treated samples provides a way to understand the thermally induced destruction or movement of color centers within the crystals. The lack of development of purple coloration in the greenish samples from the color-gradational sequence is interesting because the other greenish varieties in the system did develop it. More specifically, the most H_2O-rich samples (greenish gray) seem to have the least likelihood of developing a purple color upon exposure to radiation after the heating step.

7. Discussion

In this study, we demonstrate that heating of amethyst from the TBAMP system does not produce the greenish coloration in quartz as a secondary effect, as was originally hypothesized by [1]. Instead, the greenish coloration appears to be intrinsic to the development of the system. The amethyst and smoky coloration in quartz, consistently associated with the greenish varieties in the TBAMP system, are produced by ionizing radiation. Irradiation of the system thus is a major factor in the development of coloration, and the greenish color may be attributable to radiation-induced color centers. It is most likely that the source of radiation was ^{40}K decay to ^{40}Ar, with associated emission of a 1.46 MeV gamma ray. Potassium is abundantly present in the granitic host-rock, and this gamma ray has sufficient energy to penetrate several centimeters into the crystals [16].

7.1.The greenish color in quartz: A radiation-induced color center involving aluminum?

There are brownish gray tones in the greenish gray quartz that may be indicative of the presence of aluminum impurities. Furthermore, the laboratory exposure of the greenish gray samples of the TBAMP suite to ionizing radiation induced yet stronger brownish gray overtones and the development of an optical absorption band centered at 660 nm, which is found in the spectrum of smoky quartz. The trace-element analysis confirms the presence of aluminum in all but one of the greenish varieties. This, and the proximity of the greenish gray quartz to the colorless-to-brownish layer in the color sequence, implies that the greenish gray coloration is possibly another variant of smoky coloration in quartz, caused by the interaction of ionizing radiation with substitutional aluminum and charge-balancing cations.

Both Li^+ and Al^{3+} (and significant molecular H_2O) are associated with IR bands found in the colorless, greenish gray, dark green, and bicolored (only in the greenish gray sector) sections of the TBAMP sequence and the presence of these elements are confirmed by chemical analysis. The identity of the smoky color center in this system may be that proposed by Maschemeyer et al. [17], who used EPR data to describe a color center composed of a Li-Al “hole” center adjacent to a silicon vacancy (smoky color), whereby the vacancy is generated by the incorporation of H_2O in the Si site. The persistence of the brownish gray coloration within the radiation-treated colorless and greenish gray quartz at room temperature and above (to 300°C) indicates that the identity of the possible contributing “smoky” color center may be associated with a charge-compensating cation other than H^+. This is indicated because Al-H color centers are unstable at room temperature owing to the rapid diffusion of the proton within the structure [18]. However, despite the association of the greenish gray varieties with smoky quartz, we find no definite evidence for any of the specific component bands for smoky quartz: A1, 670 nm; A2, 486 nm; A3, 427 nm; B, 314 nm; and C < 270 nm [6] in the untreated samples.

The dark green samples can be described qualitatively as an overprint of amethyst coloration on a greenish smoky background, resulting in a darkening of the color. The dark green TBAMP samples contain both Al and Ca impurities, which may contribute to the combination of greenish smoky and amethyst components. The heating of TBAMP dark green samples produces citrine (a result similar to the heating of dark purple amethyst), and upon exposure to radiation of the thermally bleached samples, a brownish coloration developed over the citrine.

7.2. The importance of H_2O to the development of greenish color

Rossman [5] observed that the amethyst coloration dominates in nature over the smoky coloration even where the aluminum content exceeds the iron content. There may be a similar phenomenon here, whereby the development of the amethyst color has been inhibited in the natural environment in favor of another color component; in this case, greenish. Aines & Rossman [11] discussed quartz crystals with both amethyst and citrine zones in which molecular H_2O is the dominant species associated with citrine and hydroxyl group is dominant in the amethyst zones. A feature of the dark green quartz is the dominance of molecular H_2O bands in the infrared spectrum. Molecular H_2O contained in these samples has a significant effect on coloration, as irradiation may dissociate it into free radicals, specifically H^0, which could migrate through the structure and allow reaction with electron hole centers [11, 19]. The amethyst coloration darkened in amethyst sectors upon irradiation in bicolored sample 006-BI, with a simultaneous apparent decrease in the intensity of the broad band for molecular H_2O at 3440 cm^{-1} (measured at the same spot). The dissociation of molecular H_2O into free radicals thus may not have a significant color-dilution effect for amethyst color centers in this system. However, a strongly negative correlation of natural amethyst color with molecular H_2O content is seen in all localities. The amethyst color in the TBAMP bicolored variety of quartz, where there is a strong band due to molecular H_2O, is relatively weak, and hydroxyl peaks dominate the IR spectra of late-stage amethyst, where the amethyst color is the most intense.

In all types of quartz except for amethyst (later-stage distal generation in the TBAMP suite), the IR spectra show both structurally bound H_2O and molecular H_2O that can be interpreted as fluid inclusions. The greenish gray samples, dark green samples, and the yellowish green samples all exhibit IR spectra that are dominated by the presence of the broad peak due to molecular H_2O. The presence of molecular H_2O is not a distinguishing factor among the three “types” of greenish quartz, but rather it is the relative amount of H_2O. For all localities, the dark green samples have higher contents of H_2O than the paler green varieties. The increase in turbidity upon heating of the yellowish green samples is not as strong as with the greenish gray samples. The persistence of the molecular H_2O bands during the heating experiments suggests that even though the macro- to micro-scale fluid inclusions rupture during heating, leading to an increase in turbidity, molecular H_2O is trapped within nano-scale fluid inclusions that do not rupture during heating, owing to the mechanical strength of quartz. Perhaps there is an increased distribution of fluid inclusions as nano-inclusions within the yellowish green quartz compared with the greenish gray quartz.

The appearance of truncated molecular H_2O bands in the Namibian and Brazilian samples (Fig. 9a) does not appear in the TBAMP samples. This truncation may have to do with the size and distribution of fluid inclusions within the quartz structure. Because of their size, and possibly because of a more uniform distribution, nano-inclusions would be much less prone to produce truncated H_2O bands in the infrared when compared to macro-inclusions. Along with the results of the heating experiments, this argument leads us to assert that the fluid-inclusion population within the TBAMP quartz may include a significant nano-inclusion subset, but that the presence of nano-scale inclusions is not a requirement for the development of the greenish coloration. It may, however, allow some insights about the conditions of crystallization of quartz in the TBAMP system.

7.3.The role of iron in the development of color

The yellowish green quartz of the TBAMP suite qualitatively shows no brownish smoky component, and further exposure to ionizing radiation has no affect on coloration. The trace-elements present in the yellowish green type are different from the other types of greenish quartz. In particular, the yellowish green quartz contains K, but no Al, Li, Na, or Ca. This agrees with the lack of observable brownish coloration (due to Al, or Li and Al). The presence of ferrous iron in the yellowish green quartz would inhibit the generation of violet tones upon exposure to radiation of the original sample. An explanation put forth for the strong greenish coloration of a form of synthetic quartz ("prasiolite") has been the reduction of an interstitial ferric iron impurity, which migrates to form ferrous iron in an interstitial channel site characterized by a distorted octahedral symmetry [2]. A transmission window defined by an absorption band centered at 741 nm [20] arises from interstitial Fe^{2+} [21]. A weak absorption can be seen at 950 nm for the yellowish green variety, another band position associated with the interstitial ferrous iron impurity in synthetic green quartz [5]. In addition, the color change upon heating is different than that seen for the other greenish varieties. For the early-stage greenish gray samples, heating produces colorless crystals with increased turbidity, and exposure to radiation produces smoky coloration, both demonstrating the relative lack of iron. In contrast, heating of the yellowish green samples produces strongly yellow citrine, a color that is due to the precipitation of iron oxide clusters in the quartz structure. Cohen & Hassan [3] argued that only interstitial iron is a candidate for precipitation of the clusters as a new phase, and heating in an oxidizing environment can result in the change in oxidation state of the iron from ferrous to ferric. Interestingly, when a *thermally bleached* sample of the yellowish green quartz is subsequently exposed to radiation, a faint purplish color is developed, confirming the presence of ferric iron in the thermally produced citrine (the ferric iron would be a likely precursor to amethyst coloration during subsequent irradiation).

In addition to the yellowish green samples, the amethyst sectors of the TBAMP bicolored generation, the greenish gray sectors of the bicolored generation, the dark green TBAMP samples, and some of the TBAMP dark purple amethyst changed color to citrine when heated. We find some evidence for absorption bands associated with interstitial ferrous iron (at about 950 nm) in the dark green samples and in the Namibian greenish gray samples. The dark greenish coloration could be indicative of the oxidation state of the formative environment. These materials thus also may contain interstitial iron.

We observed Brazil twinning and biaxial optics on greenish gray sectors in a bicolored sample from the TBAMP suite, but because of sample imperfections, it was difficult to verify a persistence of this phenomenon throughout the TBAMP section. In "ametrine," a naturally occurring bicolored variety of quartz that exhibits amethyst and citrine coloration on the *r* and *z* sectors, respectively, amethyst is normally associated with polysynthetic (Brazil) twinning, which is usually restricted to the major rhombohedral sector *r*. Cohen & Hassan [3] noted that with X-irradiation, synthetic, ferric-iron-doped quartz developed a smoky amethyst color on the *r* sectors and only smoky coloration on the *z* sectors. They also observed that the amethyst-colored regions are biaxial and the dominantly smoky sectors are uniaxial. The presence of polysynthetic twinning has been interpreted as a response by the crystal to strain initiated by the interstitial incorporation of ferric iron in channels perpendicular to the major rhombohedral face, a phenomenon which is presumed to be the precursor to the development of amethyst color [22, 23].

The absence of ferrous iron absorption bands in the greenish gray TBAMP quartz, and the existence of the biaxial character of the greenish gray sectors, may indicate that primarily ferric iron may be present in the structure, though not enough to influence color development when compared to Al impurities. Alternatively, the higher molecular H_2O content in the greenish gray zones could discourage development of the amethyst coloration. Irradiation of the greenish gray sectors produces no change in color. Though qualitatively identical in color, there is an inherent difference between the early-generation greenish gray quartz in the TBAMP suite and the greenish gray variety that appears in the bicolored generation. The early samples become more turbid and colorless when heated, whereas the bicolored greenish gray samples change to citrine. This may be indicative of the introduction of significant amounts of iron into the system as precipitation of quartz commenced, without an observable qualitative effect on the greenish gray coloration. The biaxial character of the originally greenish gray sectors persists through heating, suggesting that ferric iron remains in an interstitial location within the structure.

7.4. Color as an indicator of the dynamic state of the early TBAMP system

The kinetics of quartz formation has an impact on the generation of color. The formation of bicolored synthetic "ametrine" was evaluated [24] in terms of critical rates of growth of the rhombohedral faces *r* and *z*. As the growth rate increases, the intensity of the amethyst color in both sectors increases, and then the intensity of coloration of the major rhombohedral faces, *r*, decreases relative to *z* as the amethyst is increasingly replaced by citrine [24]. This analysis may define a region that is relevant to the transitional bicolored type of quartz in the TBAMP suite. Major rhombohedral sectors, in both the synthetic cases [24], and perhaps in the bicolored quartz generation at the TBAMP, contain polysynthetic twinning according to the Brazil law.

Crystals of synthetic quartz will incorporate greater amounts of H_2O at higher growth-rates, and the production of flawless synthetic amethyst requires lower growth-rates [25]. Indeed, a negative correlation between content of molecular H_2O and intensity of amethyst color (measured by comparative peak intensity) has been demonstrated in natural "ametrine" [26] and seems to apply in the TBAMP system as well. In the TBAMP sequence, the highest growth-rates may have existed in the earliest generations of quartz, exclusively greenish gray in color, where the greatest amount of molecular H_2O is found. The presence of an OH band at 3543 cm^{-1} may indicate the formation of a new OH^- defect in the quartz structure due to the influence of a high growth-rate [27]. Colorless sample 006-C has an OH band centered at 3530 cm^{-1} (Fig. 9b, I). During evolution of the system, growth rates decreased, as indicated by the slightly lower contents of molecular H_2O and the presence of very pale amethyst forming on the minor rhombohedral sectors. Finally, the amethyst color dominates, and H_2O is dominantly present as OH groups, possibly indicating the lowest growth-rates. Balitsky et al. [24] described these growth rates to be on the order of 0.3-0.8 mm/day for synthetic quartz.

In the bicolored generation, we contend that ferric iron is present dominantly in substitutional sites (with a minor interstitial component) in the amethyst sectors, and interstitially in the greenish gray sectors. The amethyst sectors in the bicolored section do not seem to exhibit Brazil-law twinning. Ferric iron in a substitutional site should not produce substantial distortion of the structure, and would be consistent with the mechanism understood to lead to color generation in amethyst. Another possibility is that the amethyst sectors of the bicolored section contain a low enough ferric iron content as to not produce significant distortion of the structure, or that only minor amounts of ferric iron are present interstitially.

An additional consideration for the growth of flawless synthetic amethyst is that it requires a Na-free solution [25]. The dominant hydrous component is hydroxyl in a Na-free solution; when Na is included in the solution, additional assimilation of molecular H_2O occurs [28]. This analysis is applicable to the TBAMP system, where salinity drops as the hydrothermal system persists, supposedly because of progressive mixing of the basinal brine with a meteoric H_2O component [1]. Measurements of the final melting temperatures of the fluid inclusions conducted by McArthur et al. [1] indicate that the TBAMP system experienced a decrease in salinity as the crystals grew, such that the earlier greenish gray generation had a relatively high salinity (approximately 20 equiv. wt. % NaCl) and that the dark amethyst generation had a very low salinity. It is apparent that the evolution of the system from quartz precipitation at a high growth-rate with high amounts of incorporated molecular water and high salinity, to quartz precipitation at a low-growth rate with lower amounts of molecular H_2O and low salinity, contributed to the gradual appearance of amethyst in the sequence. It is significant to conclude that the source of the greenish coloration is definitely not thermal bleaching of amethyst in this system, as previously thought. Indeed, the amethyst color does not begin to fade until temperatures of 300°C are reached, well above the approximately 145°C attained by hydrothermal heating in the TBAMP system.

8. Conclusions

(1) The evolution of color in a particular zone of the TBAMP system allows an examination of the chemical and kinetic factors acting during the early stages of quartz precipitation in the hydrothermal system. Interpretation of the color variations in quartz as environmental indicators stresses the importance of viewing color as a consequence of a system.

(2) The TBAMP quartz deposit, an economical source of dark purple amethyst, has a localized zone, interpreted as an area of initial hydrothermal influx that exhibits a consistent color-gradational mineralization sequence of quartz. This sequence includes naturally occurring greenish gray quartz.

(3) We present a comprehensive series of spectroscopic analyses of the quartz color sequence, supplemented by additional analyses of a limited sample set from similar amethyst-bearing localities worldwide, noting the importance of incorporation of water as hydroxyl and molecular species on color development.

(4) We conclude that the greenish gray coloration is not a secondary result of heating of pre-existing amethyst, but another radiation-induced color variant, which developed its particular color as a result of specific chemical constituents, exposure to radiation, and incorporation of molecular water both as nano-scale and micro- to macro-scale inclusions.

(5) We also conclude that interpretation of color is an important factor in deriving the changing state of early stages of this system, as we use our data to confirm that the hydrothermal system experienced a gradual decrease in salinity and quartz growth rate as deposition proceeded.

Acknowledgments

The authors gratefully acknowledge Stephen Kissin (Lakehead University) for providing the initial sample that led to this project and for his helpful comments and invaluable support during the field stages of the project. We acknowledge Steve and Lorna Lukinuk of TBAMP for their hospitality and for permission to sample in the mine. G.

Niedermayr (Vienna) is thanked for providing the Namibian and Zambian samples. Additional thanks go to Elizabeth Johnson and to Elizabeth Miura Boyd for discussion and assistance with analyses and Francis Albarède (Lyon) for LA-ICP-MS analyses. Funding from NSF (USA) grant EAR-0337816 and the White Rose Foundation are especially appreciated.

References

[1] J. R. McArthur et al. (1993) Stable-isotope, fluid inclusion, and mineralogical studies relating to the genesis of amethyst, Thunder Bay Amethyst Mine, Ontario. Canadian Journal of Earth Sciences **30***,* 1955-1969.

[2] G. Lehmann and H. Bambauer (1973) Quarzkristalle und ihre Farben. Angew. Chem. **85***,* 281-289; Quartz crystals and their colors. Angew. Chem. Int'l Edn. **12***,* 283-291.

[3] A. J. Cohen and F. Hassan (1974) Ferrous and ferric ions in synthetic alpha-quartz and natural amethyst. American Mineralogist **59***,* 719-728.

[4] E. Neumann and K. Schmetzer (1984) Mechanism of thermal conversion of colour and colour centres by heat treatment of amethyst. N. Jb. Miner. Mh. **6***,* 272-282.

[5] G. R. Rossman (1994) Colored Varieties of the Silica Minerals. In P.J. Heaney, C.T. Prewitt, G.V. Gibbs (eds.), Reviews in Mineralogy, Mineralogical Society of America, Washington, 1994, p. 433.

[6] K. Nassau and B. E. Prescott (1977) A unique green quartz. American Mineralogist **62**, 589-590.

[7] T. R. Paradise (1982) The natural formation and occurrence of green quartz. Gems and Gemmology **18**, 39-42.

[8] A. N. Platonov et al. (1992) Natural prasiolite from Lower Silesia, Poland. Z. Dt. Gemmol. Ges. **41**, 21-27.

[9] R. T. Cox (1977) Optical absorption of the d^4 ion Fe^{4+} in pleochroic amethyst quartz. Journal of Physics, C: Solid State Physics **10**, 4631-4643.

[10] J. A. Weil (1975) The aluminum centers in alpha-quartz. Radiat. Eff. **26**, 261-265.

[11] R. D. Aines and G. R. Rossman (1986) Relationships between radiation damage and trace water in zircon, quartz, and topaz. American Mineralogist **71**, 1186-1986.

[12] P. C. Thurston (1991) Chapter 13. In P.C.Thurston, H.R. Williams, R.H. Sutcliffe, G.M. Stott (eds.), Geology of Ontario. Ontario Geological Survey, Special Volume 4, Part 2, 1991.

[13] H. R. Williams (1991) Chapter 25. In P.C.Thurston, H.R. Williams, R.H. Sutcliffe, G.M. Stott (eds.), Geology of Ontario. Ontario Geological Survey, Special Volume 4, Part 2, 1991.

[14] S. A. Kissin and R. L. Sherlock (1989) Geoscience Research Grant program, Summary of Research 1988-1989, Ontario Geological Survey Miscellaneous Paper **143**, 33-41.

[15] H. D. Stock and G. Lehmann (1977) Phenomena associated with diffusion of trivalent iron in amethyst quartz. J. Phys. Chem. Solids **38**, 243-246.

[16] I. M Reinitz and G. R. Rossman (1988) Role of natural radiation in tourmaline coloration. American Mineralogist **73**, 822-825.

[17] D. Maschemeyer et al. (1980) Two modified smoky quartz centeres in natural citrine. Phys. Chem. Mineral. **6**, 145-146.

[18] J. H. Mackey (1963) An EPR study of impurity related colour centres in aluminum-doped quartz. J. Chem. Phys. **39**, 74-83.

[19] A. M. Hofmeister and G. R. Rossman (1985) A model for the irradiative coloration of smoky feldspar and the inhibiting influence of water. Phys. Chem. Mineral. **12**, 324-332.

[20] H. Rose and J. Lietz (1954) Ein grun verfarbbarer Amethyst. Naturwiss **41**, 448.

[21] G. Lehmann (1967) Farbzentren des Eisens als Ursache der Farbe von Amethyst. Zeit Naturforsch. **22a**, 2080-2086.

[22] A. C. McLaren and D. R. Pitkethly (1982) The twinning microstructure and growth of amethyst quartz. Phys. Chem. Min. **8**, 128-135.

[23] A. J. Cohen (1989) New data on the cause of smoky and amethystine color in quartz. The Mineralogical Record **20**, 365-367.

[24] V. S. Balitsky et al. (2000) Industrial growth, morphology, and some properties of Bi-colored amethyst-citrine quartz (ametrine). Journal of Crystal Growth **212**, 255-260.

[25] V. S. Balitsky (1977) Growth of large amethyst crystals from hydrothermal fluoride solutions. Journal of Crystal Growth **41**, 100-102.

[26] R. D. Aines and G. R. Rossman (1984) Water in minerals? A peak in the infrared. Journal of Geophysical Research **89**, 4059-4071.

[27] Personal communication, V. S. Balitsky (2003)

[28] R. D. Aines et al. (1984) Hydrogen speciation in synthetic quartz. Phys. Chem. Minerals **11**, 204-212.

Figure Captions

Figure 1: Block 006. The color sequence containing the greenish quartz is nucleated on brecciated fragments and consists of (1) reddish chalcedony, (2) macrocrystalline quartz grading from colorless to greenish gray over 2.0 cm ± 0.5cm, (3) a fine (0.5 cm ± 0.2 cm) layer of white chalcedony, (4) macrocrystalline quartz grading from colorless to brownish gray over 2.0 cm ± 1.0 cm, (5) an 8.0 cm ± 3.0 cm "bicolored" generation of pale amethyst and greenish gray quartz color-zoned on minor and major rhombohedral sectors, respectively, and finally, (6) dark purple amethyst with sectors color-zoned to colorless and dark violet.

Figure 2: Greenish samples: (a) Namibian greenish gray sample GRR 2477(1); (b) Brazil dark green samples GRR 2350 (1), and GRR 2350 (2).

Figure 3: Optical spectrum of greenish gray TBAMP sample 006-G showing a band centered at 620 nm. There is a weak band at 520 nm visible in the perpendicular to c polarization direction. The spectra, normalized to 1.0 mm thickness, show a significant increase in scattering from long to short wavelengths.

Figure 4: Unpolarized optical spectrum of yellowish green sample 001 that shows a broad, weak band at 710 nm in addition to a sharp increase into the ultraviolet region consistent with transmission at greenish yellow wavelengths. Plotted at 10.17 mm thick.

Figure 5: Polarized spectra covering the visible and near-infrared regions for dark green sample GRR 2350. Broad bands centered at 710, 930, and 1140 nm with transmittance at 547 nm are correlated with the greenish coloration of the sample.

Figure 6: Spectrum for greenish gray sample FR-3(3) showing broad bands at 710 and ~940 nm similar to the dark green samples. The absorption centered at ~940 nm has been previously indicated for the interstitial ferrous iron impurity associated with synthetic green quartz (Rossman, 1994).

Figure 7: Polarized IR spectra of TBAMP samples 002 (Top: dark green quartz), 001 (Center: yellowish green quartz), and 003 (Bottom: amethyst quartz) demonstrating the broad molecular water band intensity in the greenish samples contrasted with the hydroxyl (OH) peaks dominating the spectrum of the amethyst sample. All spectra are normalized to 1.0 mm thickness and vertically offset for clarity. Solid line: E parallel c; dashed line: E perpendicular c.

Figure 8: IR spectra of different color varieties of TBAMP sample 006 (see Figure 1 for reference) polarized E⊥c. Greenish gray is sample 006-G; colorless is sample 006-C; bicolored quartz is sample 006-BI represented by both a greenish gray sector and an

amethyst sector. All spectra are normalized to 1.0 mm thickness and are offset vertically for clarity. It can be seen qualitatively that the greenish samples have the greatest H_2O contents relative to the other color varieties, even in the case of the bicolored generation when the sectors are adjacent to one another.

Figure 9: IR spectra of different color varieties of Farm Rooisand and Brazil samples polarized E⊥c. All spectra are normalized to 1.0 mm thickness: (a) A comparison of greenish colored samples: I: TBAMP sample 002 (dark green); II: TBAMP sample 001 (yellow green); III: Brazilian sample GRR 2350 (dark green); IV: Namibian sample FR-3 (5) (greenish gray); V (dashed): Namibian sample FR-3(3) (greenish gray). The relative depth of hue has a correlation with the content of molecular H_2O. (b) A comparison of colorless samples: I: TBAMP sample 006-C-3; II: Brazilian sample GRR 2350; III (dashed): Namibian sample FR-3(6); IV: Namibian sample FR-3(5). The colorless samples have qualitatively significant H_2O content, but in comparison with the greenish gray samples in (a), there is an increasing resolution of hydroxyl peaks (labeled) superimposed over the broad band at 3400 cm^{-1}.

Figure 1.

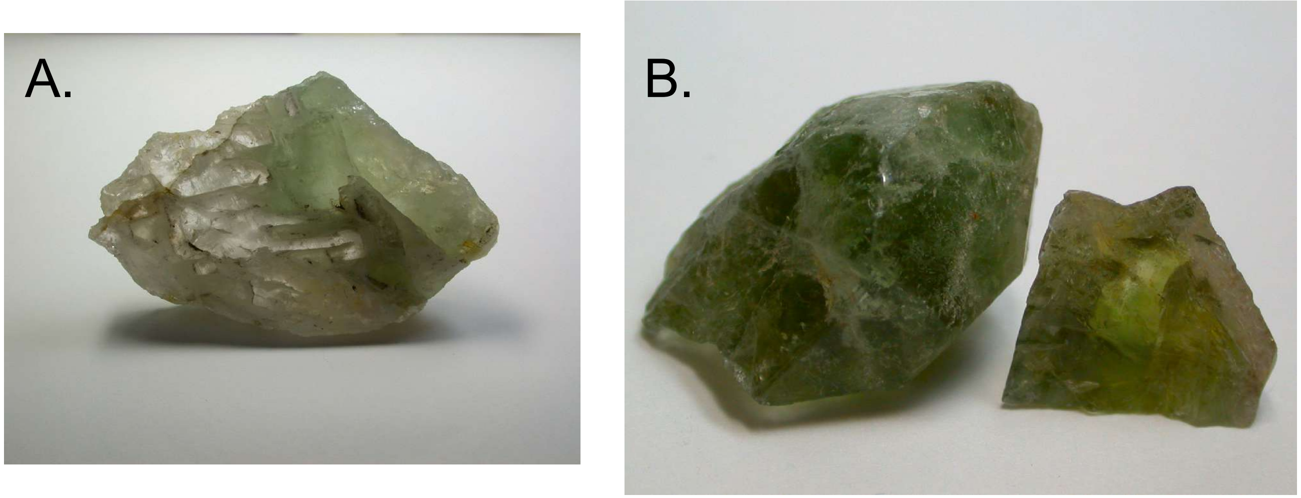

Figure 2.

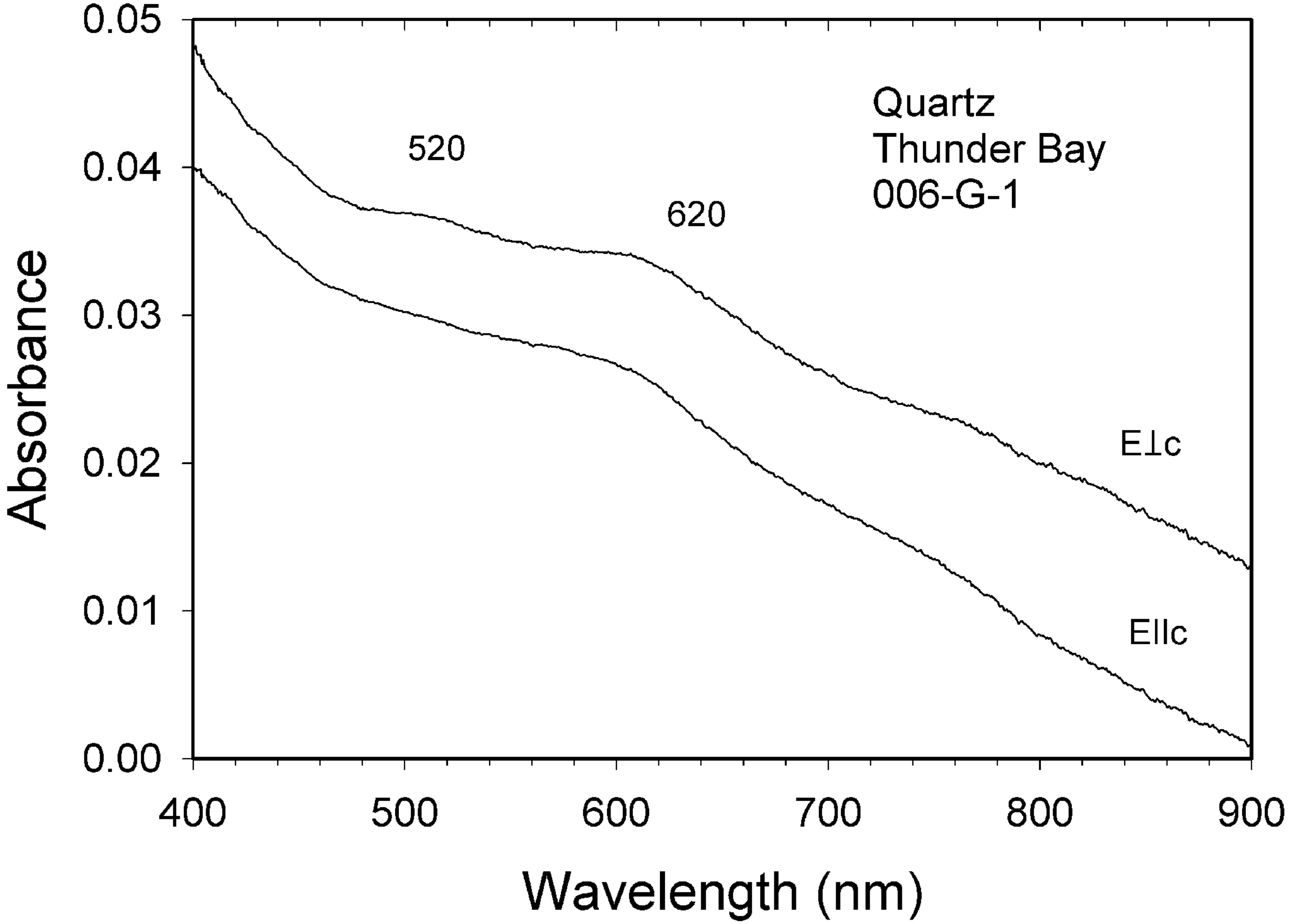
0.05
0.04
0.03
0.02
0.01
0.00
Absorbance
400
500
600
700
800
900
Wavelength (nm)
Quartz
Thunder Bay
006-G-1
520
620
E⊥c
E||c

Figure 3.

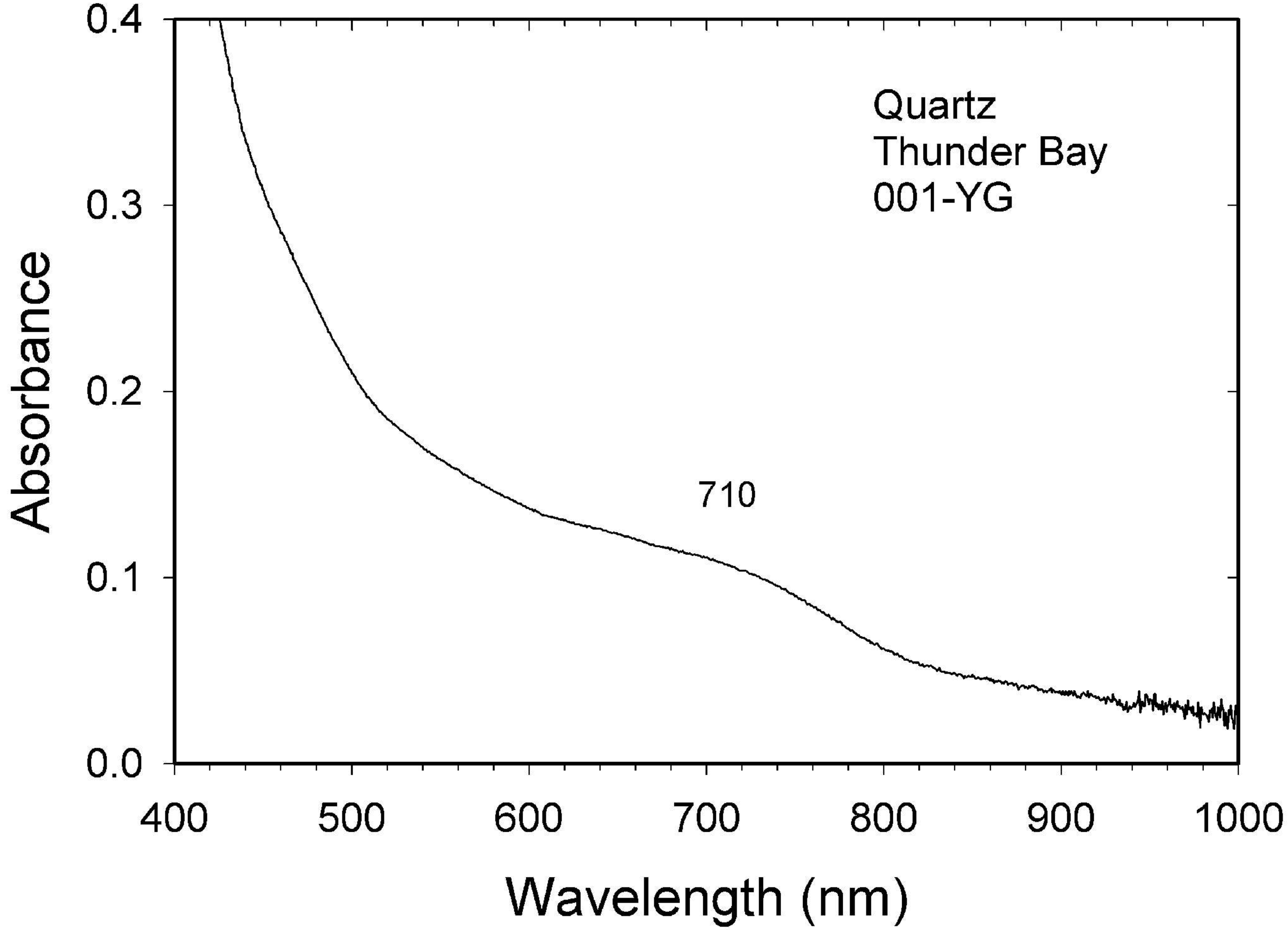
Quartz
Thunder Bay
001-YG
710
Absorbance
0.0
0.1
0.2
0.3
0.4
Wavelength (nm)
400
500
600
700
800
900
1000

Figure 4.

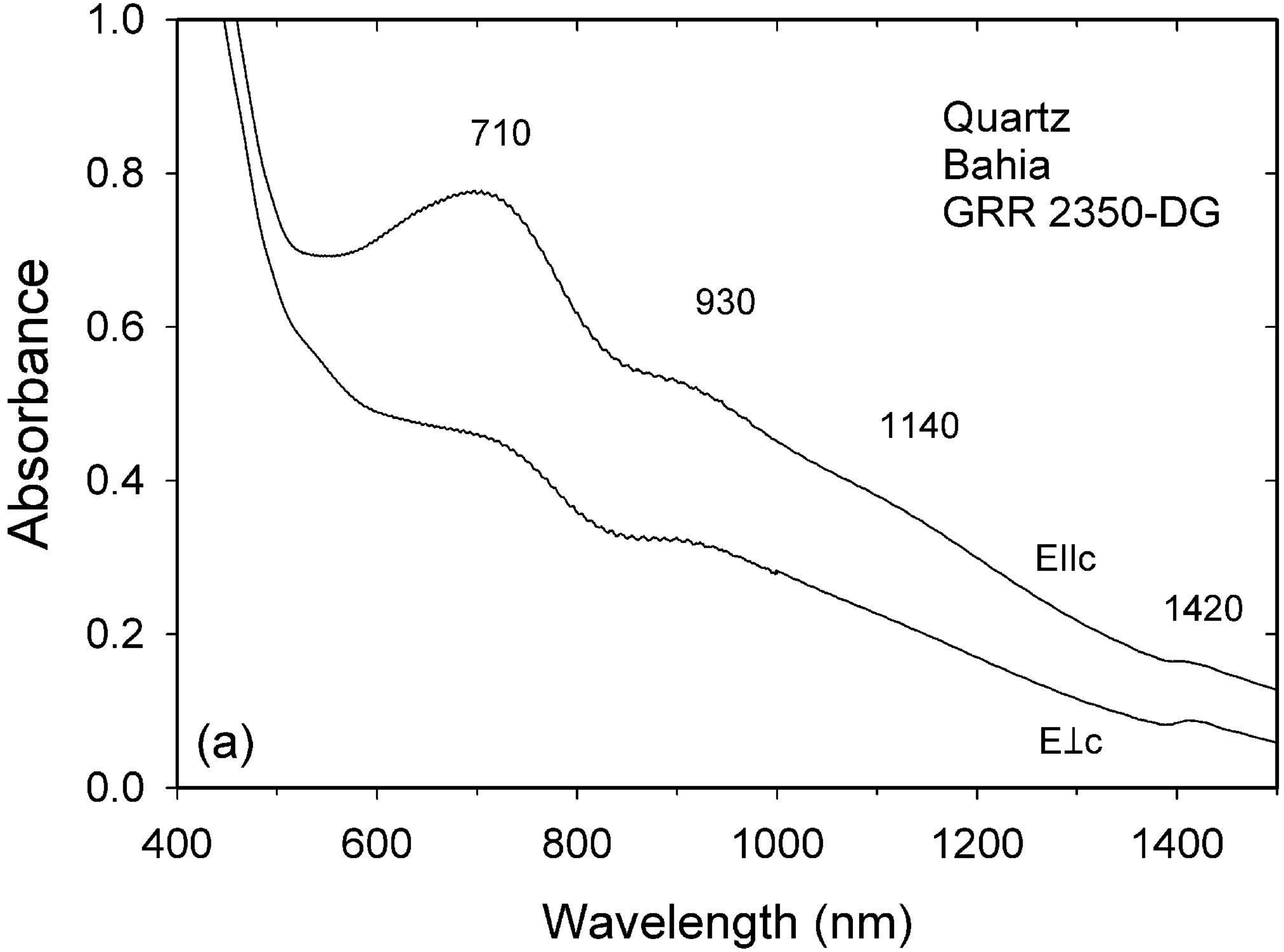
Quartz
Bahia
GRR 2350-DG
710
930
1140
1420
E||c
E⊥c
(a)
Absorbance
Wavelength (nm)
0.0
0.2
0.4
0.6
0.8
1.0
400
600
800
1000
1200
1400

Figure 5.

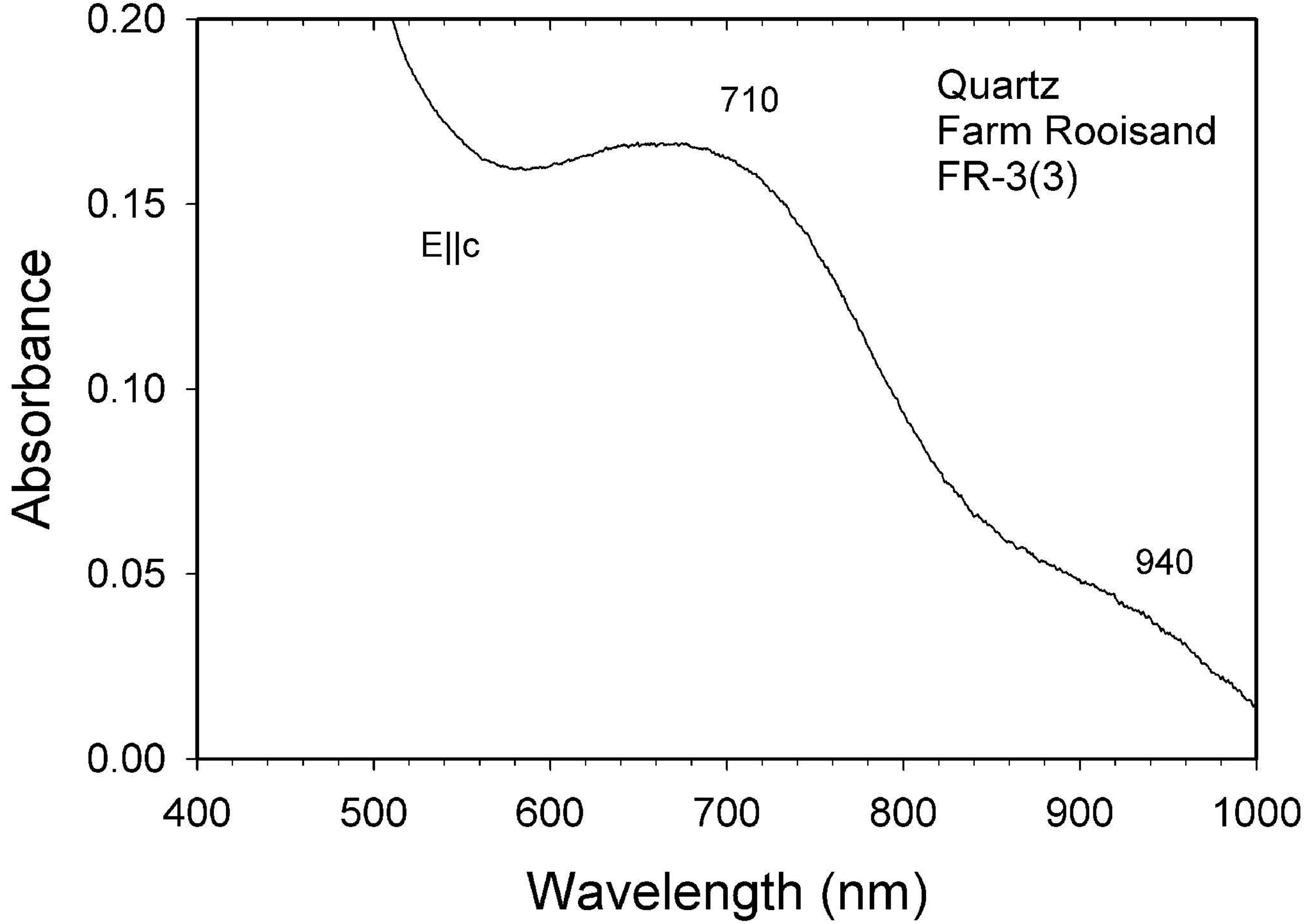
0.20
0.15
0.10
0.05
0.00
Absorbance
400
500
600
700
800
900
1000
Wavelength (nm)
710
940
E||c
Quartz
Farm Rooisand
FR-3(3)

Figure 6.

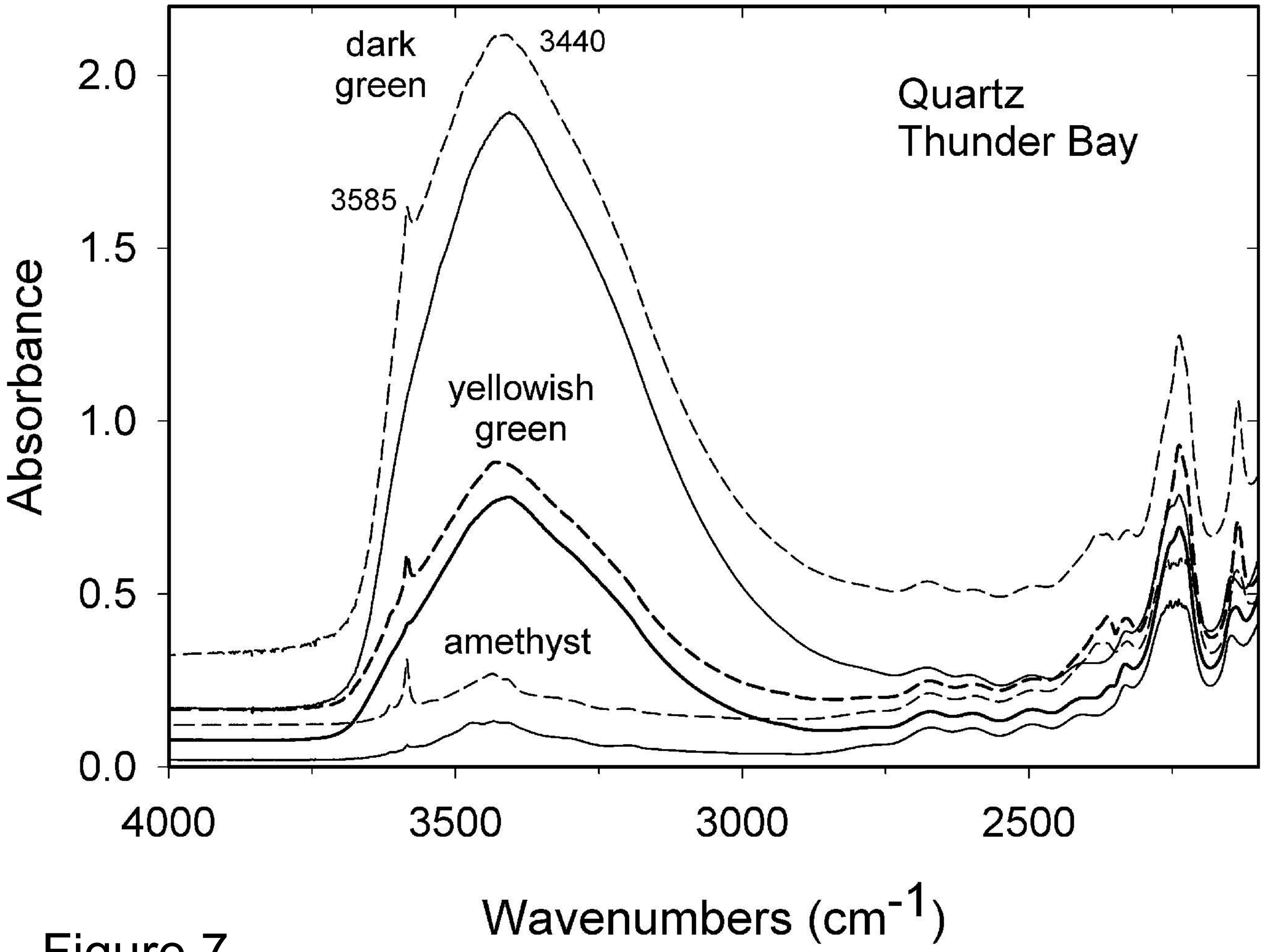
dark
green
3440
3585
Quartz
Thunder Bay
yellowish
green
amethyst
Absorbance
0.0
0.5
1.0
1.5
2.0
4000
3500
3000
2500
Wavenumbers (cm^{-1})

Figure 7.

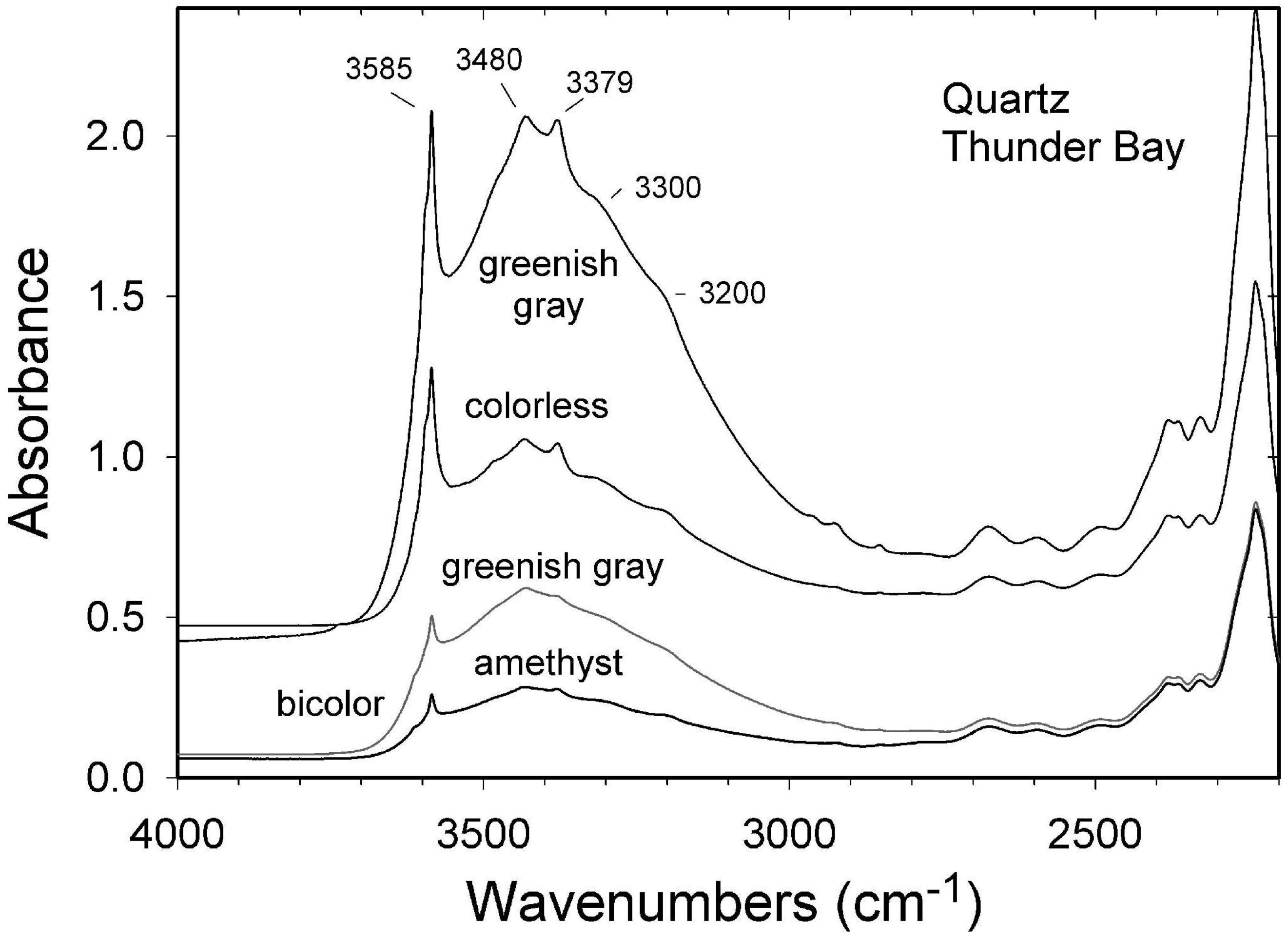
3585
3480
3379
3300
3200
Quartz
Thunder Bay
greenish
gray
colorless
greenish gray
amethyst
bicolor
Absorbance
2.0
1.5
1.0
0.5
0.0
4000
3500
3000
2500
Wavenumbers (cm-1)

Figure 8.

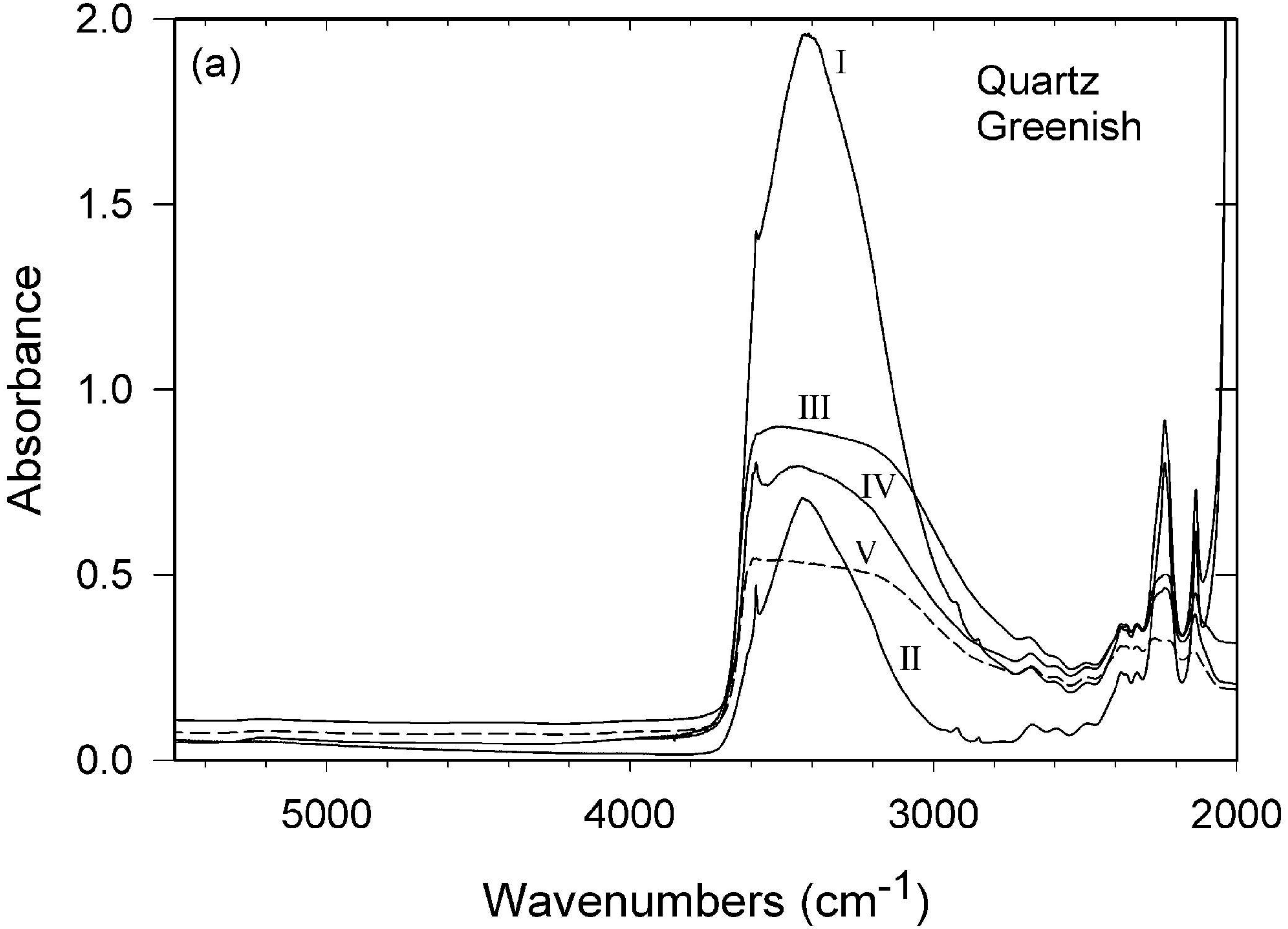
(a)
Quartz
Greenish
I
II
III
IV
V
Absorbance
2.0
1.5
1.0
0.5
0.0
5000
4000
3000
2000
Wavenumbers (cm-1)

Figure 9.

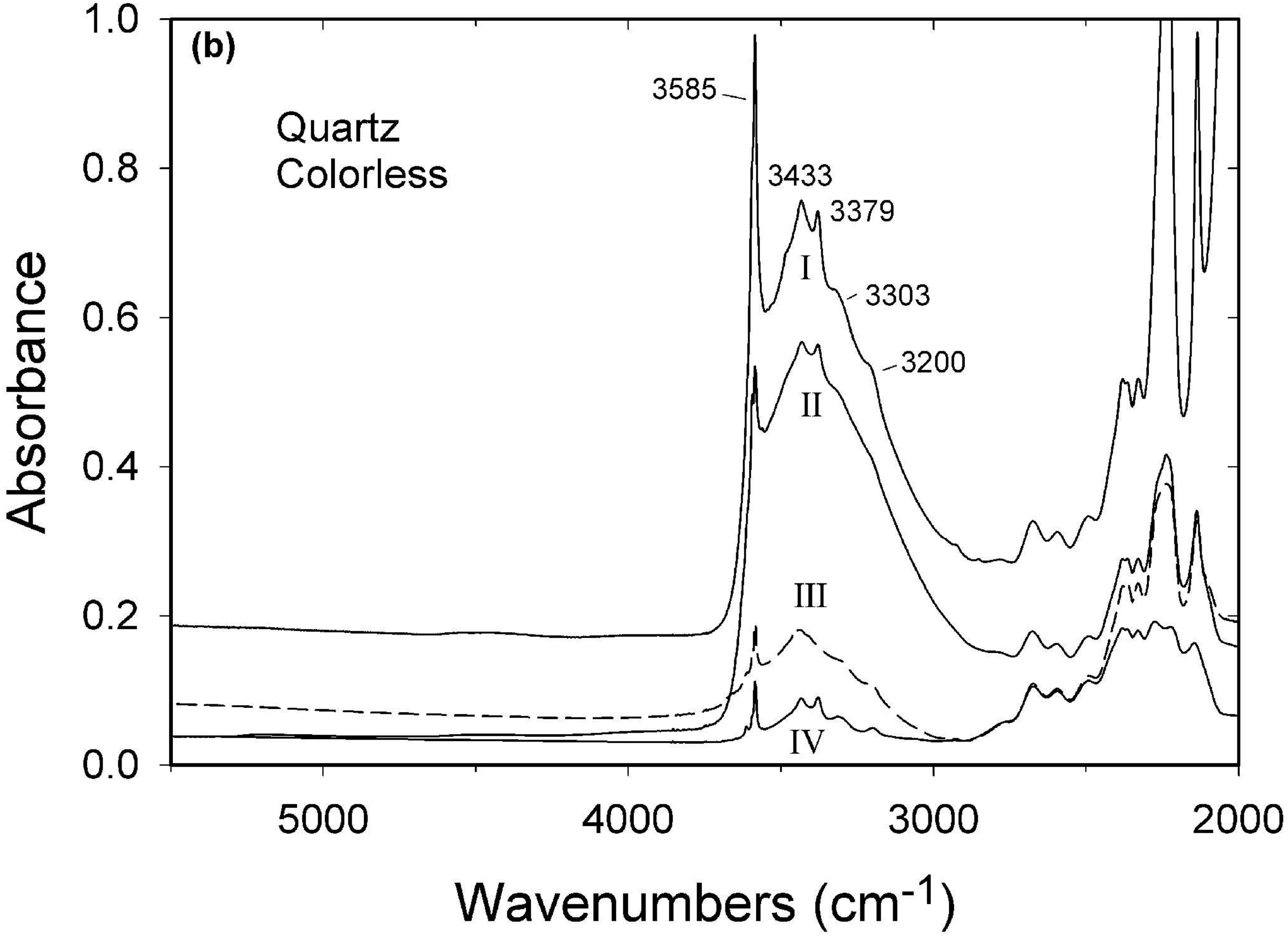
(b)
Quartz
Colorless
3585
3433
3379
3303
3200
I
II
III
IV
Absorbance
0.0
0.2
0.4
0.6
0.8
1.0
5000
4000
3000
2000
Wavenumbers (cm-1)

Table 1: LA-ICP-MS analysis results for TBAMP samples

Sample	original color	^{9}Be	^{11}B	^{23}Na	^{44}Ca	^{27}Al	^{39}K	^{7}Li	^{33}S	^{69}Ga	Position in sequence
003-1	dark amethyst	7	-	-	4166	-	14	2	29	3	top
006-BI	bicolored amethyst	-	-	-	1464	-	-	32	11	15	
006-BI	bicolored greenish gray	-	-	-	-	275	-	22	35	15	
006-C3	colorless	-	-	-	-	262	-	24	35	4	
006-G1	greenish gray	-	-	-	-	187	63	6	22	9	bottom
001-1	yellowish green	-	-	-	-	-	12	-	25	11	detrital
002-1	dark green	-	0.8	38	3987	218	-	8	27	15	detrital

- indicates levels below detection

Table 2: Summary of heating and radiation experiment results for TBAMP samples

Sample	original color	after heating	after irradiation of heated	after irradiation of original	position in sequence
003	dark purple amethyst	citrine	original amethyst color superimposed over citrine		top
006	bicolored amethyst	pale yellow	original amethyst color	no change	
006	bicolored grayish green	pale yellow	original grayish green		
006-base-2	bicolored greenish gray	turbid, colorless			
006-C	colorless	opaque white	dark smoky greenish purple	color on *r* and *z* sectors alternates between brownish and pale purple (24 hour exposure, darkening with additional exposure)	
006-G	greenish gray	turbid, colorless	dark brownish gray	dark brownish gray, smoky color (48 hour exposure) with slight purple overtones (72 hour exposure)	bottom
No number	pale purple amethyst	colorless	original pale purple		detrital
001	yellowish-green	citrine	brownish with purple overtones	no change (30 day exposure)	detrital
002	dark green	dark citrine	brownish with purple overtones		detrital

Chapter VI:

Conclusions

(PART I)

The ability to simultaneously explain geophysical and geochemical observations is essential to demonstrate certain behaviors such as the development of boundary features along the slab-mantle interface, and is a primary reason for using a coupled scheme such as GyPSM-S. The development of the low-viscosity channel (LVC) is a consequence of the migration of slab-derived fluids into the mantle wedge and reaction with peridotite to produce hydrous phases and higher water contents in nominally anhydrous minerals (NAM). The spatial extent of the low-viscosity region of the wedge may be a large-scale volume extending from the slab-mantle interface to the back-arc [1] or a relatively thin, continuous channel defined by water-saturated NAM and hydrous phases along the slab-mantle interface, depending on changing subduction parameters (slab age, convergence velocity, slab dip angle). It is limited by the onset of melting, and its geometry is therefore dependent on the position of the water-saturated solidus, which changes spatial position within the wedge due to source depletion (prior melt extraction) and/or the thermal evolution of the wedge (latent heat of melting). The zone of active melting within the mantle wedge exists at the upper surface of the LVC, and is restricted in our models by assumptions of iterative near-fractional melt extraction and water transport via a hydrous fluid only (as opposed to a hydrous melt).

Despite changing subduction parameters, the geometry of the melting region is quite similar in all models: discontinuous lenses inclined to the slab surface and displaced from it by tens of kilometers, geometries in agreement with results from tomographic imaging [2, 3]. The persistence of the LVC would provide a mechanism by which hydrated slab-adjacent mantle material (consisting of a significant reservoir of water and potentially very low-degree mantle melts) is transported to the deep mantle without melting, providing a source for enriched OIB magmas. The LVC is also significant because of the effect it has on the large-scale flow field within the wedge, possibly leading to slab decoupling [1] and changes in slab dip [4].

Changing subduction parameters have significant impacts on the source lithology and intensity of fluids originating from the slab as a function of distance along the subducting slab. Modeling of fluid migration through the LVC provides evidence for a limited fluid-rock interaction, preserving the fluid-mobile trace element chemistry associated with the original slab lithology to the active melting region. This suggests the potential for either a rapid fluid transport scenario or a fluid-dominated trace element budget within the LVC. Comparison with interpretations of along-arc trends suggest that changing subduction parameters lead to a varying fluid flux and fluid chemistry reaching the active melting region, which can be manifested in erupted lavas. By comparison with interpretations of cross-arc [5-7] trends, we find that a simple melt migration scheme which preserves spatial heterogeneity of initial melts towards eruption is likely. Melts associated with low- to mid-pressure fluid release will erupt towards the volcanic front and melts associated with higher-pressure fluid release will erupt towards the rear-arc. Interpretations of these results lead to several potential mechanisms to explain hydrous inputs to back-arc source regions [8].

Inclusion of a localized low-viscosity, low-density zone in modeling the subduction zone wedge is required in order to match geophysical surface observations of dynamic topography and geoid and gravity anomalies [1, 9]. Coupled geochemical and geophysical modeling using GyPSM-S allows for a fluid-source-based approach to determining a particular low-viscosity geometry based on changing subduction parameters. Subsequent modeling of geophysical surface signals with inclusion of the particular low-viscosity geometry can then be performed and compared with observed values. For the northern Izu-Bonin (NIB) subduction system, comparison of computed signals with those observed results in the conclusion that fluid release from the slab occurs within the interval ~150-350 km depth, forming an extended low-viscosity channel (ELVC) ($\eta_{LV} = 3.3\times10^{19}$-$4.0\times10^{20}$ Pa s) with an associated density reduction within the ELVC of -10 kg/m^3 relative to the ambient nominally anhydrous mantle wedge, values in agreement with GyPSM-S results.

Thus, the development of a coupled geochemical and geodynamic model for subduction (GyPSM-S) results in a greater understanding of the role that changing subduction parameters (slab age, convergence velocity, slab dip angle) play in the hydration of the mantle wedge. The dominant control on fluid release into the wedge is the thermal state of the slab, defined primarily by slab age and secondarily by convergence velocity. As water transits the near-slab wedge, a water-saturated zone (LVC) emerges, composed of hydrated NAM and hydrous phases, and necessarily truncated by the crossing of the water-saturated peridotite solidus further into the wedge. Slab age and slab dip angle are the primary controls on the geometry of this hydrated slab-adjacent region. As water in NAM additionally has a water-weakening effect, this water-saturated zone has important consequences for the force balance within the wedge as well. The chemical composition of melts changes along the active melting region at the top of the LVC as a function of the fluid source lithology, fluid flux, and degree of prior depletion of the melt source region. At the surface, as demonstrated by comparison with datasets from the NIB and central Costa Rican (CCR) systems, geochemical and geophysical modeling can be used to strengthen the arguments for the existence of the particular low-viscosity geometries solved by GyPSM-S.

(PART II)

The evolution of color, including a naturally occurring greenish gray variety, in a particular zone of the Thunder Bay Amethyst Mine Panorama (TBAMP) system allows an examination of the chemical and kinetic factors acting during the early stages of quartz precipitation in the hydrothermal system. Interpretation of the color variations in quartz as environmental indicators stresses the importance of viewing color as a consequence of a system. We present a comprehensive series of spectroscopic analyses of the quartz color sequence, supplemented by additional analyses of a limited sample set from similar amethyst-bearing localities worldwide, noting the importance of incorporation of water as hydroxyl and molecular species on color development. The greenish gray coloration is not a secondary result of heating of pre-existing amethyst, but another radiation-induced color variant, which developed its particular color as a result of specific chemical constituents, exposure to radiation, and incorporation of molecular water both as nano-scale and micro- to macro-scale inclusions. Interpretation of color is an important factor in deriving the changing state of early stages of this system, as we use our data to confirm that the hydrothermal system experienced a gradual decrease in salinity and quartz growth rate as deposition proceeded.

References

[1] M. I. Billen and M. Gurnis (2001) A low viscosity wedge in subduction zones. Earth and Planetary Science Letters **193**, 227-236.

[2] A. Hasegawa et al. (2005) Deep structure of the northeastern Japan arc and its implications for crustal deformation and shallow seismic activity. Tectonophysics **403**, 59-75.

[3] D. P. Zhao et al. (2001) Seismological structure of subduction zones and its implications for arc magmatism and dynamics. Physics of the Earth and Planetary Interiors **127**, 197-214.

[4] V. Manea and M. Gurnis (2007) Subduction zone evolution and low viscosity wedges and channels. Earth and Planetary Science Letters **264**(1-2), 22-45.

[5] A. Hochstaedter et al. (2001) Across-arc geochemical trends in the Izu-Bonin arc: contributions from the subducting slab. Geochemistry, Geophysics, Geosystems 2:2000GC000105.

[6] R. J. Stern et al. (2006) Subduction factory processes beneath the Guguan cross-chain, Mariana Arc: no role for sediments, are serpentinites important? Contributions to Mineralogy and Petrology, doi: 10.1007/s00410-005-0055-2.

[7] L. H. Rupke et al. (2002) Are regional variations in Central American arc lavas due to differing basaltic versus peridotitic slab sources of fluids? Geology **30**(11), 1035-1038.

[8] C. H. Langmuir et al. (2006) Chemical systematics and hydrous melting of the mantle

in back-arc basins. Geophysical Monograph 166, 87-146.

[9] M. I. Billen and M. Gurnis (2003) Comparison of dynamic flow models for the Central Aleutian and Tonga-Kermadec subduction zones. Geochemistry, Geophysics, Geosystems **4**(4), 1035, doi:10.1029/2001GC000295.